INFORMATION TO USERS

This manuscript has been reproduced from the microfilm master. UMI films the text directly from the original or copy submitted. Thus, some thesis and dissertation copies are in typewriter face, while others may be from any type of computer printer.

The quality of this reproduction is dependent upon the quality of the copy submitted. Broken or indistinct print, colored or poor quality illustrations and photographs, print bleedthrough, substandard margins, and improper alignment can adversely affect reproduction.

In the unlikely event that the author did not send UMI a complete manuscript and there are missing pages, these will be noted. Also, if unauthorized copyright material had to be removed, a note will indicate the deletion.

Oversize materials (e.g., maps, drawings, charts) are reproduced by sectioning the original, beginning at the upper left-hand corner and continuing from left to right in equal sections with small overlaps. Each original is also photographed in one exposure and is included in reduced form at the back of the book.

Photographs included in the original manuscript have been reproduced xerographically in this copy. Higher quality 6" x 9" black and white photographic prints are available for any photographs or illustrations appearing in this copy for an additional charge. Contact UMI directly to order.

UMI

A Bell & Howell Information Company
300 North Zeeb Road, Ann Arbor MI 48106-1346 USA
313/761-4700 800/521-0600

The Formation and Evolution of the Large Magellanic Cloud from Selected Clusters and Star Fields

by

Knut A. G. Olsen

A dissertation submitted in partial fulfillment
of the requirements for the degree of

Doctor of Philosophy

University of Washington

1998

Approved by Gaurav W. Harper

(Chairperson of Supervisory Committee)

E

Scott Anderson

Program Authorized
to Offer Degree ASTRONOMY

Date JUNE 5, 1998

In presenting this dissertation in partial fulfillment of the requirements for a Doctoral degree at the University of Washington, I agree that the Library shall make its copies freely available for inspection. I further agree that extensive copying of this dissertation is allowable only for scholarly purposes, consistent with "fair use" as prescribed in the U.S. Copyright Law. Requests for copying or reproduction of this dissertation may be referred to University Microfilms, 1490 Eisenhower Place, P.O. Box 975, Ann Arbor, MI 48106, to whom the author has granted "the right to reproduce and sell (a) copies of the manuscript in microform and/or (b) printed copies of the manuscript made from microform."

Signature Kurt A.G. Olsen

Date June 5, 1998

University of Washington

Abstract

The Formation and Evolution of the Large Magellanic Cloud from Selected Clusters and Star Fields

by Knut A. G. Olsen

Chairperson of Supervisory Committee
Professor Paul W. Hodge
Astronomy Department

We have obtained deep *Hubble Space Telescope* color-magnitude diagrams of fields centered on the six old LMC globular clusters NGC 1754, NGC 1835, NGC 1898, NGC 1916, NGC 2005, and NGC 2019. The data have been carefully calibrated and the effects of crowding on the photometric accuracy have been thoroughly investigated. The observations have been used to produce $V-I$,V color-magnitude diagrams of the clusters and of the background field stars, which we have separated from each other through a statistical cleaning technique.

The cluster color-magnitude diagrams show that the clusters are old, with main sequence turnoffs at $V \sim 22.5$ and well-developed horizontal branches. We used the slopes of the red giant branches to measure the abundances, which we find to be 0.3 dex higher, on average, than previously measured spectroscopic abundances. In two cases there is significant variable reddening across at least part of the image, but only for NGC 1916 does differential reddening preclude accurate measurements of the CMD characteristics. The mean reddenings of the clusters, measured both from the

color of the red giant branch and through comparison with Milky Way clusters, are $\leq$0.10 magnitudes in $E(B-V)$ in all cases.

By matching the color-magnitude diagrams of the clusters to fiducial sequences of the Milky Way globular clusters M3, M5, and M55, we find that the mean difference of the LMC and Milky Way cluster ages is 1.0 $\pm$ 1.2 Gyr, calculated such that a positive difference indicates that the LMC clusters are older. Through Monte Carlo simulations, errors in the individual measurements of the ages relative to Milky Way clusters are found to be $\lesssim$1.0 Gyr. We find a similar chronology by comparing the horizontal branch morphologies and abundances with HB evolutionary tracks, assuming that age is the "second parameter". These results imply that the LMC formed at the same time as the Milky Way Galaxy.

The evolution of the LMC following its formation has been studied through an analysis of the field star CMDs. We used an automated technique to disentangle the evolutionary tracks of varying age and composition that are represented in the CMDs. We computed star formation rates as a function of age for a number of models having different initial mass function slopes, distances, and uniform reddenings, assuming that the chemical evolution follows that implied by LMC clusters. We additionally assumed that there is no abundance spread at any age, that binary stars may be neglected, and that differential reddening may be ignored; the last of these assumptions excludes the NGC 1916 field from our analysis. By minimizing a robust fit parameter, we solved for the best-fit reddening, distance modulus, and star formation history. Errors in the best-fit parameters are calculated through Monte Carlo simulations of the technique.

Our results show that the LMC has been actively forming stars over the last 4 Gyr, with evidence for a decline in the last 0.5$-$1 Gyr. While the NGC 1754 field, which lies in the disk, has had only a low level of star formation after the globular cluster

formation epoch until 4 Gyr ago, we find that the bar has been actively forming stars for the past 6–8 Gyr. We find that these qualitative results are robust against errors in the model parameters.

The poor fit of the models to the old red giant branches in the bar fields implies that the abundances we measured for the globular clusters are too high by $\sim$0.5 dex or that the models incorrectly reproduce the color of the red giant branch. While tentative, this result provides a hint that LMC field star CMDs may be a useful way to test stellar evolution models.

TABLE OF CONTENTS

LIST OF FIGURES

LIST OF TABLES

ACKNOWLEDGMENTS

My deepest thanks go to Paul Hodge, my advisor, for leading me down the path of research in star formation and stellar populations, a subject that provoked some of my earliest interest in astronomy. His subtle guiding hand has considerably smoothed the path before me, yet still instilled in me a sense that the real effort and progress made was my own. I can only hope that some of his generosity, integrity, kindness, and brownie-making ability have rubbed off on me while he has been my mentor.

My heartfelt thanks go to the participants of our weekly "Hodge meetings", where the details presented here were hammered out and where I sought the advice that has kept me on track. I thank John Collier, Andy Dolphin, Karl Krienke, Luis Mendoza, Brooke Skelton, Ted Wyder, Dan Zucker, Gene Magnier, and, of course, Paul Hodge, who led the forum and fed us with coffee and cookies. Eric Deutsch, while not an attendant of these meetings, nevertheless also helped solve many technical details through generously sharing his expert knowledge of computers, algorithms, and IDL.

Many others have helped show me the ropes as I have tried my hand at research. Nick Suntzeff's scrutiny of the reduction and analysis of the globular cluster data showed me what comprises a finished piece of work and has given me confidence that the work presented here is sound. Alistair Walker contributed generously with his time in doing all of the ground-based reductions and with helpful comments along the way. Bob Schommer, Mario Mateo, and Ed Olszewski also contributed useful comments. George Lake, Karl-Heinz Böhm, and Scott Anderson gave me some of my first research opportunities, for which I am grateful. George was especially generous with his support, even as I discovered that my biggest interests lie outside his fields

of expertise.

I would never have had the energy to finish this dissertation were it not for the continual reaffirmation of the purpose of studying astronomy that I got from the informal discussions that popped up at various times with various people, but especially with Dara Norman, Bernhard Beck, Dave Reiss, Dan Zucker, Jeff Gardner, Andy Becker, Eric Deutsch, Luis Mendoza, Ted Wyder, Mark Hammergren, the other graduate students of Johnson Hall and the PAB, and my family. I hope that these discussions have given not just me but also others a clearer idea of why studying astronomy is not a waste of time.

While graduate school has been hard work, there has been plenty of time for goofing around. I will look back fondly on all the frisbee games below Drumheller Fountain and on the poop-soaked fields of the IMA (for which we got t-shirts!), volleyball and softball games, hikes in the Cascades (especially around Mt. Rainier), Whine Times, trips to the pub, and afternoon "Q"-fests. I deeply appreciate the friendships I have forged in Seattle through these and many other activities. I especially thank Dara for her friendship, as she let me bother her on a daily basis and lent me many forks.

Finally, I want to thank my family for all of the support they have given me while I have been in graduate school. Over the past few years I have begun to know my parents as adults, watched my sister finish medical school and get engaged to a wonderful guy, and seen my brother grow up at a startling rate. I am sure that these trends will continue over the next years.

Chapter 1

INTRODUCTION

Studying the formation and evolution of any particular galaxy is an exciting and important pursuit simply because there are very few galaxies for which such studies are possible, and the rewards for helping to understand the galaxy formation process are great. We thus have ample motivation for seeking to chronicle the formation and evolution history of the Large Magellanic Cloud. However, the unique properties of the LMC make the pursuit an especially exciting and important one. Its proximity, low reddening, and nearly face-on inclination have made it an object of intense scrutiny by astronomers of this century. As a result, we have as many pieces of the puzzle of galaxy formation and evolution assembled for the LMC as for any other galaxy, including the Milky Way.

The LMC fills a number of roles in the galaxy formation and evolution picture. In hierarchical galaxy formation scenarios (e.g. White & Rees 1978), the numerous 1– and 2–σ peaks in the primordial fluctuation spectrum collapse first, forming objects with masses similar to dwarf galaxies. The LMC thus represents a large number of galaxies having similar properties. However, due to its larger mass compared to the majority of dwarf galaxies, the LMC also plays a somewhat unusual role, having properties that are transitional between low-mass and high-mass galaxies. For instance, while the photoionizing background radiation from quasars and the first generations of stars might have kept low-mass dwarfs from collapsing until $z\sim1$ (Quinn, Katz & Efstathiou 1996), the LMC was probably only moderately affected. The LMC is sim-

ilar to lower-mass dwarfs in having been profoundly affected by the energy feedback generated from supernovae and winds from massive stars. The resulting structure of the interstellar medium, spectacularly shown in the most recent HI map (Kim & Staveley-Smith 1997), is one pockmarked with holes, yet still superposed on a spiral pattern. It is unlike the dwarf spheroidals, however, which are thought to have lost the majority of their gas in single starbursts (Smecker-Hane 1997). The LMC also plays a role as a test case for the effect of interactions with neighboring galaxies on the development of a galaxy. The result of these interactions is clearly seen in the Magellanic Stream, which was either tidally stripped from the LMC-SMC system by the Galaxy or ram-pressure driven by hot gas in the Milky Way halo (Murai & Fujimoto 1980, Moore & Davis 1994), and in the star formation occurring in the region between the LMC and the SMC (Demers & Irwin 1991).

Many aspects of these roles have been explored through the study of the stellar populations of the LMC, a subject that is the focus of this dissertation. Unlike gas, stars retain many of the properties given to them upon their births, making them tracers of the past history of the galaxy in which they formed. As stars are responsible for stirring and enriching the interstellar medium, they are also key for understanding the structure of the ISM, through which we can hope to develop a self-consistent picture of star formation and chemical evolution. Through studying their kinematics, we may also be led to an understanding of the physical origins of stellar populations and the effects of external influences on star formation.

The LMC contains many different tracers of stellar populations, the bulk of which are discussed in the excellent review by Olszewski, Suntzeff, & Mateo (1996). This dissertation presents results of a study of two such tracers, the old globular clusters in the inner regions of the LMC and their background field stars. We will thus only discuss how studies of the clusters and field stars have advanced our knowledge of the LMC's formation and evolution, rather than duplicate the enormous effort of Olszewski et al. (1996) by discussing all of the stellar population studies that have

led to our current understanding of the LMC.

1.1 The Clusters of the LMC

For studying the evolution of a galaxy, clusters have the distinct advantage of having formed at discrete times, making it relatively easy to measure their ages and abundances. The LMC is rich with clusters, with ~6500 estimated to exist (Hodge 1986). A fraction of these clusters have been studied to reveal the age distribution, abundance distribution, and kinematics of the LMC cluster system.

1.1.1 Age Distribution

Ages are best measured by comparing photometry of the main sequence and its turnoff to stellar evolution models. This preferred approach is time consuming in that it requires photometry of many individual stars. However, the LMC contains many blue clusters with bright main sequence turnoffs for which measuring the age through color-magnitude diagrams is relatively easy. The large number of these young clusters shows that the LMC has recently been a very active star-forming galaxy. Some of these clusters are so densely populated and concentrated that they were first mistakenly thought to be similar to the Milky Way globular clusters, until it was noticed that their spectra were very different from the globulars of the Milky Way (Shapley 1930). These clusters have no known counterpart in the Milky Way, revealing a strong difference between the current state of evolution of the LMC and our Galaxy.

The LMC also has old clusters, although they are much rarer than the young ones. These "red" clusters were first identified by Shapley (1930), based on integrated spectra and their appearance on plates. Measuring ages from their color-magnitude diagrams has proved to be difficult, however. The distance of the LMC puts the old main sequence at a magnitude where crowding in the dense fields of the LMC severely limits ground-based photometry. In addition, the surrounding field includes

many blue main sequence stars which can easily confuse the identification of the cluster main sequence. These difficulties have been somewhat overcome through careful photometry, studying the clusters that lie in the least crowded regions of the LMC, and by employing statistical field subtraction techniques.

Since the early color-magnitude diagrams of Hodge (1960), who estimated that at least 35 LMC clusters were similar to Galactic globular clusters, the list of truly old clusters has been reduced to a handful. Table 1.1 shows the most current list and some of their known properties, adapted from Olszewski et al (1996). Many of these have been studied for the presence of RR Lyrae variables, which have been found in seven clusters. Some have been studied with 4-m-class telescopes in the southern hemisphere, producing deep color-magnitude diagrams. Walker (1992) showed that NGC 1466 has blue horizontal branch stars as well as some red ones, and was almost able to reach the main sequence, which is at the level expected for an ancient population. Brocato et al. (1996) achieved photometry of the turnoff for three clusters, NGC 1786, NGC 1841, and NGC 2210. Each of these clusters was shown to be as old as Milky Way globular clusters, although the errors in the age comparison are $\sim$3 Gyr. The deep color-magnitude diagram of Testa et al. (1995) also revealed an old cluster in NGC 2257. By comparing it to the sequence of a Milky Way globular cluster and measuring its age through comparisons to isochrones and through the gap between the horizontal branch and the main sequence turnoff, they found that it is 2-3 Gyr younger than the oldest Galactic globular clusters. Mighell et al. (1996), using WFPC2 on the *Hubble Space Telescope*, found that Hodge 11 is the same age as M92 to within 10$-$20%.

The accuracy with which ages of the old clusters are currently known is sufficient to study the evolution of cluster formation in the LMC. The age distribution of LMC clusters, shown in Olszewski et al. (1996), clearly demonstrates the paucity of older clusters compared to young ones. There are a small number of clusters with ages similar to the oldest Galactic clusters, one cluster, ESO 121+SC03, in the

age range 8-10 Gyr (Mateo et al. 1986, Sarajedini, Lee, & Lee 1995), and many young clusters with ages less than 4 Gyr. This age distribution cannot solely be accounted for by the destruction of older clusters by dynamical forces. Hodge (1988), by studying color-magnitude diagrams of a complete sample of clusters, showed that the destruction time scale for clusters is ~5 times larger in the LMC than in the Milky Way, and similar to that in the SMC. As the SMC has a much more uniform distribution of cluster ages than than the LMC, the dearth of clusters in the LMC with ages 4-10 Gyr must partly be intrinsic to the cluster population. The failure of Geisler et al. (1997), who produced color-magnitude diagrams of many clusters thought to be old based on integrated photometry and abundance measurements, to find any previously unidentified old clusters reinforces the suspicion that the cluster age distribution reflects the cluster formation history.

While ancient clusters are one of the few ways in which the formation epoch of the LMC can be studied directly, the accuracy with which the ages have so far been measured is insufficient for any definitive statement to be made. As mentioned previously, the NGC 2257 CMD of Testa et al. (1995) suggests that this cluster is younger than the oldest Milky Way globular clusters by 2–3 Gyr. A similar result is obtained for all of the outer LMC globular clusters on the basis of their horizontal branch morphologies, assuming that age is responsible for the second parameter effect seen in many globular clusters (Da Costa 1993). However, these tentative results need to be verified through main sequence photometry of all LMC globular clusters.

1.1.2 Abundance Distribution

Measuring abundances of clusters is a useful way of studying the relationship between the star formation history and chemical evolution. The most complete set of abundances comes from the medium-resolution Ca-triplet spectroscopy of Olszewski et al. (1991), although abundances have also been measured from color-magnitude diagrams. While the interpretation of the Ca abundances depends somewhat on the

current value and evolution of the Ca/Fe ratio (Wallerstein, personal communication), they are useful for studying the chemical evolution history. The results suggest that the metallicity has risen steadily from a value -2.0≤[Fe/H]≤-1.5 for the oldest clusters to [Fe/H]∼-0.3 for the young clusters. It is puzzling that such large enrichment occurred during a period when very few clusters were formed. While star formation bursts can explain some of the enrichment by delaying it through supernovae Ia, it has not been possible to explain all of the enrichment this way (Olszewski et al. 1996).

1.1.3 Spatial Distribution and Kinematics

The spatial distribution and kinematics of star clusters have also been useful in studying the evolution of the LMC. Recent cluster formation appears to have taken place in localized clumps, with the distribution of clumps changing over time (Hodge 1986). One such site of cluster formation that is currently active is 30 Doradus, the largest HII region in the LMC. A possibility is that the sites of cluster formation are triggered into activity by the bar of the LMC, as suggested by Dottori et al. (1996).

The kinematics of even the oldest clusters follow the rotation of the HI disk, although with slightly higher velocity dispersion and slower rotation (Schommer et al. 1992). The LMC is thus very different from the Milky Way in not having and old, dynamically hot halo. It appears that the LMC had already collapsed to a disk at the onset of star formation.

1.2 The Field Stars of the LMC

As the LMC is easily resolved into stars, its field stars comprise the biggest fossil record of the formation and evolution of the LMC. It is of strong interest to unravel their star formation and chemical evolution histories, so that the age and abundance distributions may be compared to those of the clusters. While studying them is made much easier by the low inclination and foreground reddening of the LMC, it is a

challenge to disentangle the mix of properties represented by stars in the field.

1.2.1 An Intermediate-Age Population

The first studies of LMC field stars examined the color-magnitude diagrams with an eye towards determining the broad characteristics of the populations represented. The studies unanimously found the LMC field to be dominated by an intermediate-age stellar population. Butcher (1977), comparing the luminosity function of a field near NGC 1866 to that of the solar neighborhood, concluded that the majority of stars in the field have ages of 3-5 Gyr. Hardy et al. (1984) studied a field in the LMC bar, using the main sequence luminosity function, the red clump stars, and the subgiant branch stars to estimate the contributions of populations of various ages. In rough agreement with the result of Butcher (1977), they found that little star formation took place in the field before 3 Gyr ago. Stryker (1984) and Hodge (1987) showed that even in fields far from the LMC bar, intermediate age stars dominate the color-magnitude diagrams. The lack of blue horizontal branch stars in Stryker's (1984) CMDs rules out a sizable old-metal poor component, as does the poor fit of the giant and subgiant branches to the fiducial of NGC 2257. Similar results were found by Hodge (1987), who showed that the giant branch in his southwest field matches that of an intermediate age population, with little evidence for significant star formation before 3 Gyr ago.

More recently, efforts have been made to explain the distribution of numbers of stars in field star CMDs by comparison with models constructed from a superposition of stellar isochrones. Bertelli et al. (1992) did this in a rough way, separating main sequence stars, red giant branch stars, and red horizontal branch stars into three areas of the CMD, which they found could be used as indicators of the star formation history. By comparing the ratios of the number of stars in each area from three different fields to the expectations of evolutionary tracks, and using different assumptions of the distance modulus, IMF, and stellar abundances, they found evidence that the LMC

experienced a strong burst in its recent star formation history. They found that the star formation burst, which proceeded at a rate ~10 times higher than earlier star formation, began 3-4 Gyr ago, in agreement with the earlier studies.

1.2.2 Results from HST

Even more sophisticated techniques strive to explain the detailed distribution of stars in the color-magnitude diagrams or luminosity functions of field stars. These studies are made possible by the recent improvement in telescope, instrument, and computing power. In particular, *HST* has made it possible to produce field star color-magnitude diagrams of unprecedented quality, with the observations extending to ~0.6 $M_{\odot}$ stars deep on the unevolved main sequence. Holtzman et al. (1997), using *HST* WFPC2 observations of a field near NGC 1866 presented by Gallagher et al. (1996), fit the luminosity function of the field stars with model star formation histories containing stars in three age ranges having different metallicities. They found that with a Salpeter IMF, the luminosity function fits implied only a modest factor ~3 increase in the star formation rate in the past 2-3 Gyr. This result stands in contrast to the previous ground-based field star work, which showed the field stars to be strongly dominated by an intermediate-age population. Geha et al. (1998) analyzed additional WFPC2 star fields using the ratio method developed by Bertelli et al. (1992). Their results for the fields confirm those of Holtzman et al. (1997), showing significant numbers of older stars. A hint that the LMC bar may contain more stars with ages ~1 Gyr than these outer fields of the LMC was found in the WFPC2 observations of Elson, Gilmore, & Santiago (1997).

1.2.3 Developing Work

The recent work with *HST* has thus questioned whether the LMC is as dominated by intermediate-age stars as previously thought. Fortunately, continuing advances in both the observations and analysis techniques promise to help sort out the mess.

The development of the analysis techniques is being strongly driven by the desire to understand the unique star formation histories of all Local Group dwarf galaxies. Gallart et al. (1996) developed a set of template star formation histories using large numbers of stars sampled from stellar isochrones to study the star formation history of NGC 6822. The templates were designed to select differing contributions from stellar populations of different ages. Combined with a full understanding of the photometric errors through extensive artificial star tests, the templates were fit to the distribution of stars in the CMDs and the best fit evaluated. Aparicio, Gallart, & Bertelli (1997) used the same technique with a larger number of templates to study the star formation history of the Pegasus dwarf.

For more detailed studies of the star formation histories of Local Group dwarf galaxies, it becomes necessary to use an automatic approach that is not limited by the number of template star formation histories it is possible to produce. Tolstoy & Saha (1996) provided the basis for such an analysis by providing an automatic technique for evaluating the goodness of fit of a model to an observed data set. Dolphin (1997) took a further step by developing a method by which the best linear combination of an input set of models containing stars in various age ranges is fit to observed multi-color CMDs, yielding a solution of the star formation history implied by the models. A similar technique using a different algorithm was discussed by Ng (1998).

These new techniques will be powerful when combined with existing and future *HST* studies of LMC field stars. Combined with two new large surveys of the LMC, the drift-scan survey of Zaritsky et al. (1997) which has so far collected photometry of $\sim 10^6$ stars, and the 9 million star CMD of the MACHO collaboration (Alves et al. 1997), LMC field stars may be used not only to study the star formation history but to provide strong tests of the details of stellar evolutionary theory.

1.3 Goals of the Dissertation

As demonstrated by the work cited in this Introduction, the epoch of formation of the LMC is unknown to an accuracy of better than 2-3 Gyr, while the age of the dominant population formed during the subsequent evolution is a controversial issue. This dissertation aims to address these questions with new observations from *HST*. We have observed the six inner globular clusters NGC 1754, NGC 1835, NGC 1898, NGC 1916, NGC 2005, and NGC 2019 with WFPC2, for which ground-based data would be especially difficult to interpret because of the photometric effects of crowding. The locations of these clusters projected on the face of the LMC are shown in Fig. 1.1, demonstrating the high background star density that accompanies them. The environment of these inner clusters is quite different from that of the outer clusters, which lie several degrees away from the bar, as illustrated in Fig. 1.2. The inner clusters are thus important objects of study, as they probe the early formation of the main mass of the LMC. Our observations reach below the main sequence turnoff of the clusters, making it possible to establish their ages accurately based on fundamental stellar evolutionary theory.

While the dense background has previously been a plague for studying the LMC's inner globular clusters, we will take advantage of the good statistics it provides to study the color-magnitude diagrams of the field stars. These fields are of particular interest as 5 are located in the bar while one, the NGC 1754 field, lies $\sim$1°outside the bar, making them useful for comparing the spatial distributions of field star populations. For our analysis of the CMDs, we will employ the ideas generated by the recent work on star formation histories cited above to study them in detail.

Table 1.1: Basic LMC Globular Cluster Parameters[a]

Cluster	RA (2000.0)	Dec	V (int.)	n(RR)	CMD[b]
NGC 1754	04h55m	-70°31′	11.4	–	10,11
NGC 1835	05h05m	-69°28′	9.5	35	10
NGC 1898	05h17m	-69°43′	11.1	–	10
NGC 1916	05h19m	-69°27′	9.9	–	–
NGC 2005	05h30m	-69°45′	11.2	–	–
NGC 2019	05h32m	-70°12′	10.7	0	–
Hodge 11	06h14m6s	-69°52′	11.3	0	3,5,6,10,12,13,17,20,25
NGC 1466	03h44m34s	-71°40′24″	10.7	38	6,12,14,23
NGC 1786	04h59m08s	-67°44′42″	10.6	9	4,10
NGC 1841	04h45m10s	-83°59′42″	11.0	22	1,2,4,6,9,22
NGC 2210	06h11m28s	–69°08′	10.4	12	2,4,8,9,10,15
NGC 2257	06h30m28s	-64°19′	11.5	37	6,9,12,16,18,19,21
Reticulum	04h36m11s	-58°51′48″	12.4	32	7,24

[a]Adapted from Olszewski et al. (1996)

[b]Published color-magnitude diagrams:

1. Alcaino et al. (1996) 2. Andersen, Blecha, & Walker (1985) 3. Andersen, Blecha, & Walker (1984)
4. Brocato et al. (1996) 5. Freeman & Gascoigne (1977) 6. Gascoigne (1966) 7. Gratton & Ortolani (1987)
8. Harris, Hesser, & Atwood (1983) 9. Hesser, Ugarte, & Hartwick (1976) 10. Hodge (1960)
11. Jensen, Mould, & Reid (1988) 12. Johnson & Bolte (1997) 13. Mighell et al. (1996)
14. Penny (1975) 15. Reid & Freedman (1994) 16. Stryker (1983) 17. Stryker et al. (1984) 18. Testa et al. (1995)
19. Walker (1972) 20. Walker (1979) 21. Walker (1989) 22. Walker (1990) 23. Walker (1992a)
24. Walker (1992c) 25. Walker (1993)

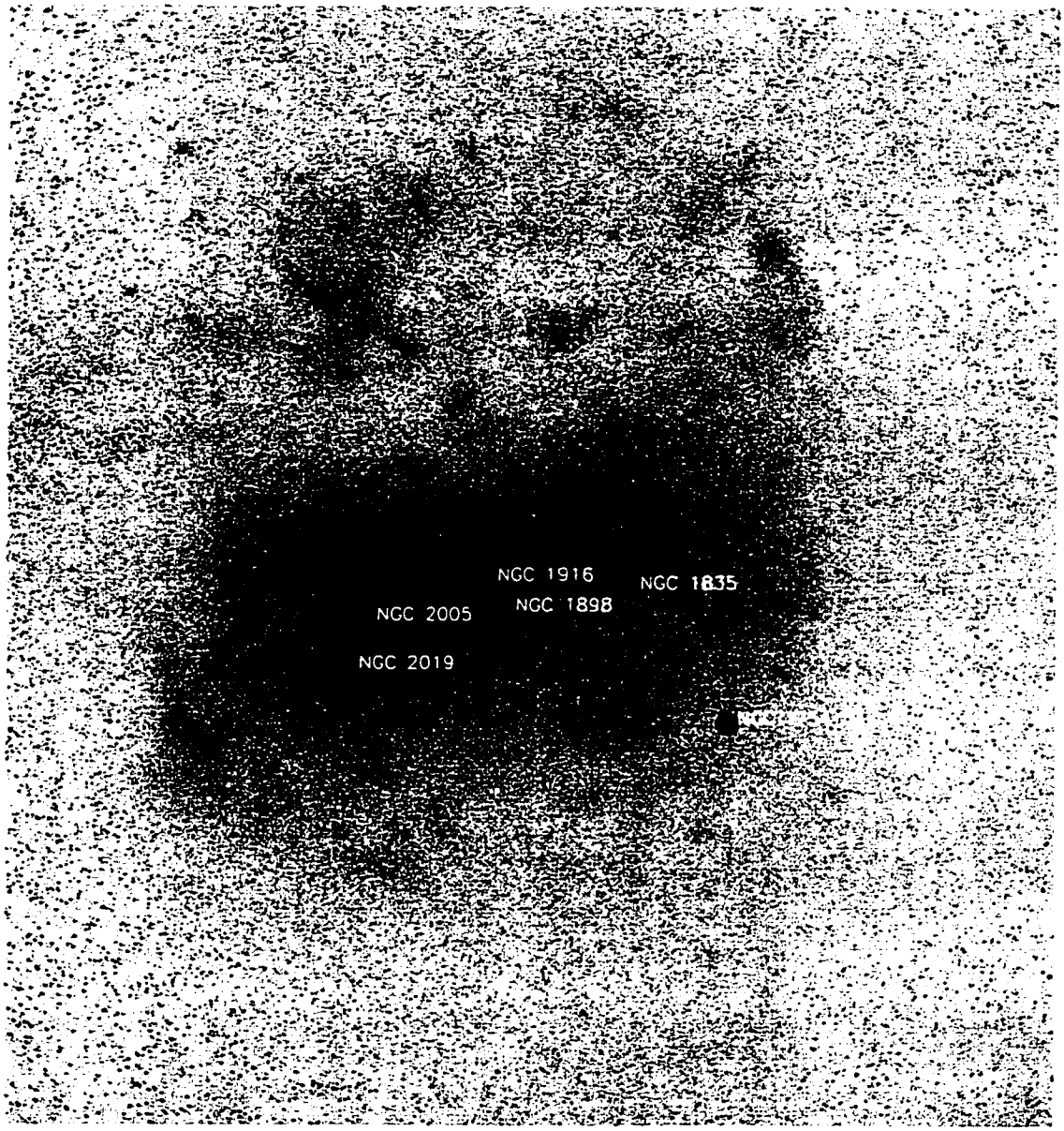

Figure 1.1: This image shows the positions of the target LMC globular clusters with respect to the parent galaxy. The circles represent the clusters NGC 1754, NGC 1835, NGC 1898, NGC 1916, NGC 2005, and NGC 2019. Plate courtesy of Harlow Shapley, Harvard College Observatory, Boyden Observatory photograph.

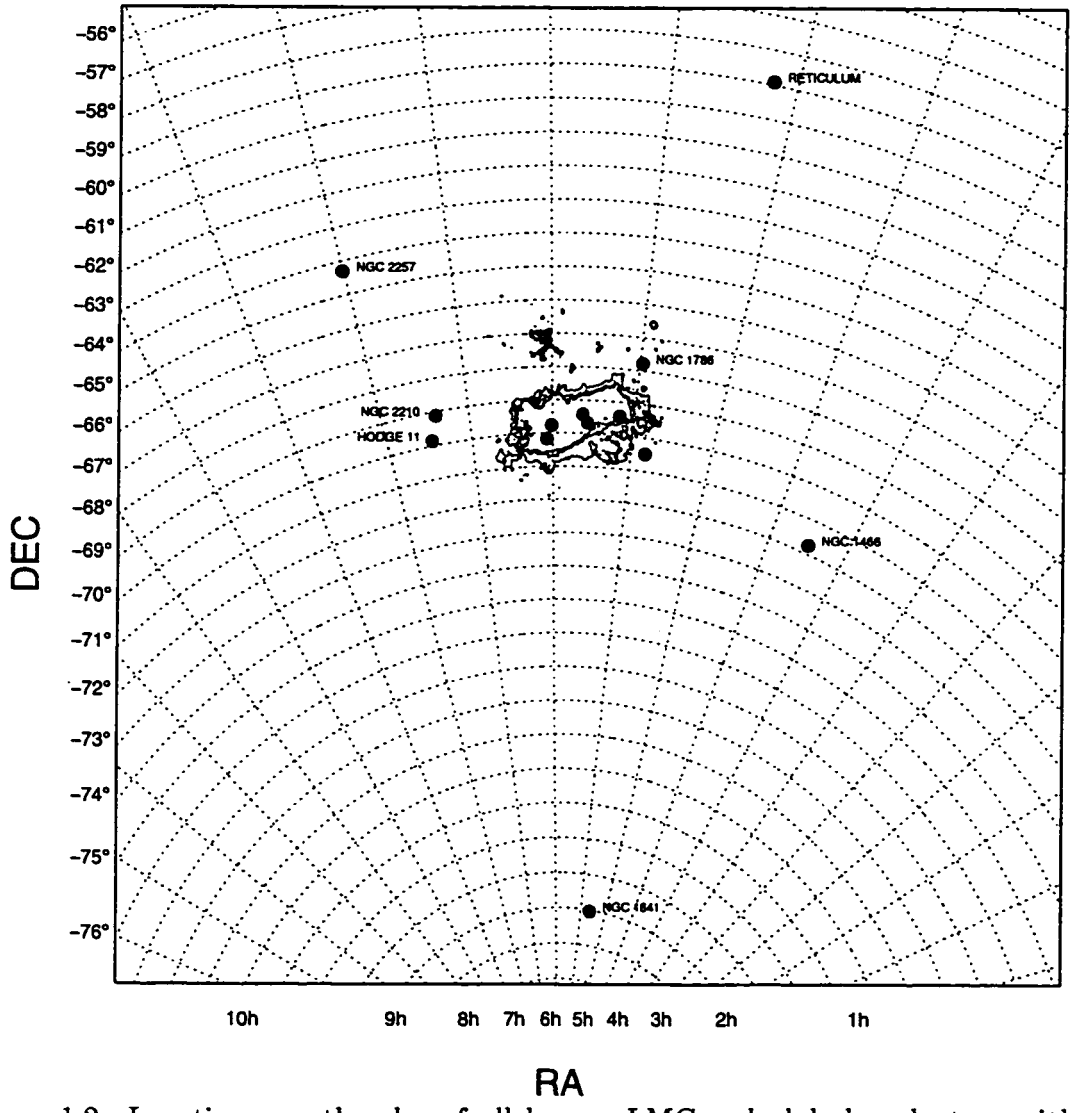

Figure 1.2: Locations on the sky of all known LMC red globular clusters with respect to the bar, the main optical feature of the LMC. The figure demonstrates the large difference in environments sampled by the outer clusters compared to the inner clusters. To avoid confusion, labels are excluded for the clusters shown in Fig. 1.1.

Chapter 2

WFPC2 OBSERVATIONS, REDUCTIONS, AND PHOTOMETRY

2.1 Introduction

Seasoned astronomers often remark that while the use of modern technology in astronomical observations has vastly improved our ability to study the Universe in detail, the time spent analyzing the data taken by modern telescopes using CCD detectors has greatly increased. This adage is especially true of the *Hubble Space Telescope.* While *HST* offers the best available resolution in optical bands, calibrating the data involves a number of time-consuming steps. As the goal of this project is to discriminate between stellar populations with only small differences in age, we desire high photometric accuracy, requiring careful calibration of the data. The focus of this Chapter is to describe the observations, the photometry, and the steps in the calibration. The background cleaning technique used to produce the final product color-magnitude diagrams is also discussed.

2.2 Observations

Observations of six fields, each containing a globular cluster and background field stars, were taken during Cycle 5 of HST. Each field was observed for the duration of one orbit of the spacecraft, with the cluster centered on the Planetary Camera (PC). For these observations, we used the low gain setting of the WFPC2 camera (GAIN=7). Each field was observed in 11 frames; the breakdown of exposure times and filters is listed in Table 2.1. Multiple exposures were taken through each filter to

aid in cosmic ray removal, but no dithering technique was used. We took both long and short exposures to provide unsaturated photometry of as many stars as possible. The images were processed through the standard STScI reduction pipeline, which includes bias subtraction, dark current subtraction, flat field correction, and a small shutter shading correction, prior to our receipt of them.

The accuracy of the photometric zero points of the WFPC2 instrument is currently in debate, with possible errors in the zero point of $\lesssim$0.05 magnitudes (Suntzeff, personal communication). In order to check the zero point of the WFPC2 photometry, A. Walker obtained images of each cluster with the CTIO 1.5-m and Tek 2048 CCD. The field of view of this camera is 8.'3, or $\sim$3 times the size of the WFPC2 field of view. Images were taken through CTIO copies of the *HST* F555W and F814W filters on the nights of January 23-26, 1995 under photometric conditions and in good seeing (FWHM$\sim$1″). Standard stars from Landolt (1992) and from the ω Cen field used to calibrate WFPC2 photometry were observed. While the majority of the stars in the LMC fields studied here are too crowded with neighboring stars for reliable photometry from the ground, a few stars appeared isolated enough to provide a useful comparison with the WFPC2 photometry. Careful photometry of these stars using DAOPHOT/ALLSTAR was performed by Walker and the photometry transformed to Johnson/Kron-Cousins V and I. The comparison of the photometry from these ground-based images with the HST photometry is described in section 2.4.5.

2.3 Image reduction and corrections

Our first step was to check the image alignment for each set of exposures in each filter. In all cases, the alignment is better than a fraction of pixel. We made no attempt to align the images further.

We combined multiple images and removed cosmic rays in one step with the IRAF[1]

[1]IRAF is written and supported by the IRAF programming group at the National Optical As-

STSDAS task *crrej*. From multiple equal-length exposures of the same field in each filter, *crrej* produces a cosmic ray-free image by averaging the stack of exposures after rejecting pixels with values too high compared to an initial guess at the uncontanimated pixel values. The threshold outside of which pixels are rejected is set by the noise characteristics of the image and through adjustable parameters. Because there are fractional pixel offsets between successive frames, the sharp cores of stars illuminate the pixels of the successive frames differently, and are often interpreted as cosmic rays by the standard rejection procedure. By setting the parameter *scalenoise* to 10%, which raises the rejection threshold by 10% of the pixel value, we insured that the cores of stars were left unaltered while still removing many cosmic rays.

As described by Holtzman et al. (1995a), the WFPC2 CCD chips have a charge transfer problem which, while readily observed, is not yet fully understood. The fundamental cause of the problem is charge traps (impurities) in the silicon wafers that capture passing electrons during the readout of the chips. The rows which are read out last encounter a larger number of traps and, therefore, lose more electrons. We accounted for these CTE effects by using the corrections suggested by Holtzman et al. (1995a). The correction depends on the background level, as background light acts to partially fill in the traps. The backgrounds in the long exposures are in the 30-200 e^- range, while the short exposures have backgrounds of 2-10 e^-'s. For the short exposures, we multiplied an image containing a 4% ramp into the data frames, while we used a 2% ramp for the long exposures. Recently, Whitmore & Heyer (1997) published a report indicating that CTE corrections should be a function of x- and y-position on the chip as well as star counts and background counts. In section 2.4.3, we explore the effect of star counts on the CTE effect by comparing magnitudes measured in the long and short exposures. The other corrections suggested by Whitmore &

---

tronomy Observatories (NOAO) in Tucson, Arizona. NOAO is operated by the Association of Universities for Research in Astronomy, Inc. under cooperative agreement with the National Science Foundation.

Heyer (1997) should be small for this data, and we have not included them.

The WFPC2 focal plane is distorted, so that pixels near the edges of the chips view a smaller area of the sky (Holtzman et al. 1995a). An extended object of uniform surface brightness, such as the flat field source, therefore appears to have a lower surface brightness per pixel near the edges of the chips. However, since the flat fields are divided into the science images in the STScI reduction pipeline, the science images are corrected for this perceived lower "sensitivity" near the edges of the frames. Because we are doing point source photometry, we are interested in measuring the total amount of light received over all pixels spanned by the sources in the image. Sources near the edges of the images will be spread over a larger number of pixels than those near the center because of the geometric distortion, and so will appear brighter in the flat fielded images. To correct for this effect, we re-applied the geometric distortion effects to the images using maps generated by the coordinate transformations of Holtzman et al. (1995a).

The STScI reduction pipeline produces a list of bad pixels for each science image. We used these lists to create bad pixel masks for each group of exposures in each filter. These masks include macroscopic charge traps, bad columns, questionable pixels, and pixels saturated by stars in the field. By setting the masked pixels in the data frames to a low value, they are ignored during photometry.

2.4 Photometry and photometric calibration

2.4.1 DoPHOT photometry

Figs. 2.1a-b display mosaics of the WFPC2 images of each of the six fields. The images are crowded, even far away from the cluster centers, because of the high field star densities in these fields of the LMC. In order to combat the effects of crowding and to achieve the best photometry for the faint stars, which are crucial for determining the cluster ages and for studying the field star main sequence, it is necessary to resort

to profile-fitting rather than aperture photometry. For its speed and ease of use, we chose to use the program DoPHOT (Schechter, Mateo, & Saha, 1993), version 2.5, with modifications performed by Eric Deutsch to handle our floating point images. DoPHOT's operation is controlled by a file containing user-adjustable parameters, the most important of which are described in detail below.

DoPHOT generates object lists by identifying peaks above a model of the background in the image. We chose to use DoPHOT's median filter to generate the model background. We found that DoPHOT's other background options, the plane and Hubble models, did not adequately fit the background, becoming weighted too heavily by the bright cluster cores and causing stars at the outskirts of the clusters to escape detection. We used a minimum threshold for object detection of 2σ above the background.

After detecting objects, DoPHOT measures their magnitudes by fitting their profiles to a power-law point spread function (PSF) containing two adjustable coefficients. We adjusted these coefficients by simultaneously inspecting the fit of the PSF to a small sample of stellar radial profiles and by minimizing the aperture correction, described in Section 3.3. We fit the coefficients independently for each filter and chip. Table 2.2 contains the final adopted values of β_4 and β_6, and Fig. 2.2 shows a sample fit of the PSF to a stellar radial profile. Although the PSF fits well in the core of the star, the wing shows structure that is not fit by the PSF, most noticeably in the F814W filter. Hence, the PSF-subtracted image shows halos around the positions of subtracted stars. In order to prevent DoPHOT from identifying too many spurious objects in these residuals, we forced DoPHOT to add extra noise each time it subtracted a PSF from the image. This extra noise only affects the detection of objects, not the measurement of their magnitudes.

Finding the optimal size of the box within which the PSF is fit is a trade-off between the need to include pixels far from the core of the star for a proper fit to the background and the desire to exclude neighboring stars from the fit box. The issue

of crowding on the accuracy of the photometry is most critical in the crowded PC frames. Fig. 2.3 shows the distribution of sky levels with position on the PC chip for two fit box sizes, 9 and 25 pixels, and the resulting CMDs of NGC 1754. While the use of the larger 25-pixel fit box produces a much smoother sky distribution, the accompanying CMD shows much greater scatter. We settled on the 9-pixel fit box for both the PC and WF images, finding that this size produced adequate determinations of the background while avoiding, as much as possible, the effects of crowding.

When DoPHOT encounters objects that are significantly broader than the mean stellar profile, it makes a decision on whether to interpret the object as a single broad object ("galaxy") or as overlapping stars, in which case the object is split into multiple objects. The decision is weighted by the parameter *stargalknob*, which we set to a high value of 3.0 because these crowded frames likely contain many more overlapping stars than background galaxies. We encountered some problems with DoPHOT classifying some bright yet unsaturated stars in the long exposure frames as broad, and splitting them into pairs. Using the short exposure photometry for these cases solved this problem.

2.4.2 Aperture corrections

For absolute calibration of the photometry, we used the zero points reported by Holtzman et al. (1995b). These zero points are based on aperture photometry of standard stars using an aperture size of 0.″5, which encloses >99% of the WFPC2 PSF in both the PC and the WF chips. Because DoPHOT's model PSF is imperfect, the DoPHOT photometry produces systematically different results from aperture photometry. We therefore need to apply an aperture correction to the DoPHOT photometry to calibrate it properly. Because the PSF changes between different chips and filters, the aperture corrections were calculated independently for each set of observations. Moreover, because the WFPC2 PSF varies with position on the chip, while DoPHOT assumes that the PSF is uniform with position, we applied an aperture correction

that depends on position in the frame as well as the chip and filter used.

For these aperture corrections, it was necessary to find several bright, isolated stars in order to be able to do aperture photometry out to a 0.″5 radius. While we found a few such isolated stars in the WF frames, there were practically none in the PC frames. To increase the number of stars available for the aperture corrections, we used a PSF to subtract all stars but a few bright ones and performed aperture photometry on the subtracted image. Because DoPHOT's PSF is uniform in position and leaves halos in the subtracted image, we chose to use PSFs kindly provided by Peter Stetson and DAOPHOT/ALLSTAR to produce the subtracted images. These PSFs, derived from multiple WFPC2 observations of ω Cen, are "perfect" PSFs, in that they average over time-dependent effects such as focus variations. We found that ALLSTAR photometry using the ω Cen PSFs had greater scatter than our DoPHOT photometry, although the PSF-subtracted images are cosmetically cleaner.

Choosing 200 bright stars to be left untouched in each frame, we used the ALLSTAR photometry to subtract the remaining stars. We inspected the profiles of each of the 200 stars in the subtracted frame, discarding stars that had significant unsubtracted companions or deviant pixels within a 0.″5 radius. With DAOPHOT's PHOTOMETRY routine, we performed aperture photometry on each of the 200 stars out to 0.″5. After matching the aperture photometry lists with the DoPHOT photometry list, we fit the aperture corrections as a function of x and y on the chip with an appropriate polynomial. Figs. 2.4–2.7 show the fits of the aperture correction surfaces for all chips and for both long and short exposures. In all of the WF frames, a 2nd order polynomial surface fits well. The residuals of the points around the mean surfaces are generally Gaussian-distributed with dispersions similar to those expected from errors in the combined aperture and PSF photometry, implying that we were successful in removing the stars neighboring to those used in calculating the aperture corrections. However, in the PC frames we find no clear dependence of the aperture correction on position, which we interpret as the result of the severe crowding

and the difficulty of doing reliable aperture photometry in the PC frames. Instead of using the questionable PC aperture photometry, we generated approximate aperture corrections by inserting artificial stars into the original frames (using Stetson's WFPC2 PSFs), performing DoPHOT photometry on these frames, and comparing the DoPHOT magnitudes to the aperture magnitudes of the artificial stars. These artificial star tests, which were used for a variety of purposes in the analysis, are described in section 1.5. Fig. 2.5 shows the comparison between the aperture correction surfaces generated using our own data with artificial surfaces. For the WF frames, the agreement is generally good, although some of them disagree at the level of $\sim$0.05 mag. In the PC frames, the disagreement is large, and suggests that aperture photometry in the PC is too difficult to produce reliable aperture corrections. Since we are uncertain of the PC aperture corrections generated from our own data at a level of $\gtrsim$0.05 mag, we chose to use the artificially generated surfaces to correct the PC photometry. For the WF frames, the aperture corrections derived from the original frames were used. After applying the aperture corrections, we added the zero points appropriate for each chip and filter used to the raw counts for each star, following equation 7 and Table 9 of Holtzman et al. (1995b).

2.4.3 CTE effects in short exposure photometry

As a check on the photometry, we compared the measurements of unsaturated stars common to the long and short exposure frames. As reported by Whitmore & Heyer (1997), among others, we find an offset between magnitudes measured in the long exposure frames compared to those measured in the short exposure frames. Figs. 2.6 show the comparisons. The differences increase as the magnitudes of the stars increase, typically reaching a maximum of $\sim$0.1 magnitudes at F555W = 21.5. As the offsets are due to a CTE effect which worsens at low background and count levels, we chose to trust the long exposure photometry and apply a correction to the short exposure photometry. Within broad magnitude bins, we calculated the

average difference between the long and short exposure magnitudes and subtracted this difference from all of the short exposure magnitudes in the bin. The use of broad magnitude bins assumes that the offset changes slowly with magnitude, with no erratic behavior hidden by the scatter in the plots. We checked this assumption by comparing the distribution of points about the mean within each bin to similar distributions generated by comparing the photometry of simulated long and short exposure stars, using the artificial star tests described in Section 1.5. The application of a Kolmogorov-Smirnov statistic shows that in all cases the distributions are nearly identical, implying that the assumption that the offset changes slowly with magnitude is well-justified.

2.4.4 Final calibrated photometry

After correcting the short exposure photometry for the CTE effect described in the previous section, we merged the short and long exposure photometry lists. First, we removed stars near saturated and bad pixels from the lists. Stars within five pixels of a saturated pixel were assumed to lie in the wings of the saturated star and were removed, while stars within 1.5 pixels of an otherwise bad pixel were also removed. Next, we matched the lists according to position of the stars. When we plot the distribution of pixel offsets between stars found in both the short and long exposure lists, we find that most of the distribution lies within 0.6 pixels of the origin, so matches outside this range were considered spurious. For all matching pairs, we kept the photometry for the star having the smallest photometric error. Sometimes, a star identified as single on the short exposure image was split into two stars by the long exposure reduction. In these cases, we compared the photometric error of the single star with the error of the split pair member with the position closest to the single star, and kept the data for the star having the smallest error. In most cases, this procedure rejected the photometry of the split pair member in favor of the single star and generally eliminated the previously mentioned difficulty of having bright stars

split into two in the long exposures. We also added stars found in the short exposure frames but not in the long exposures to the final combined list, as these stars were generally saturated in the long exposures.

Next, we matched the merged photometry lists from the two different filters, again using a 0.6 pixel matching radius. We kept only stars having a DoPHOT object type of 1 ("perfect" star), 2 ("galaxy"), 3 (member of overlapping stellar group), or 7 (faint but measurable object) for the final list. Using equation 9 and the zero points from Table 10 of Holtzman et al. (1995b), we transformed our magnitudes to Johnson V/Kron-Cousins I, as this is the photometric system on which stellar evolutionary models are generally tabulated. Figs. 2.7–2.8 show the CMDs generated from the photometry. As expected from a glance at the images (Figs. 2.1), the PC CMDs are dominated by the globular cluster sequences while the WF CMDs contain predominantly field stars, which have a range of ages. However, the PC CMDs are clearly contaminated with field stars, while blue horizontal branch stars, some of which are presumably cluster stars, contaminate the WF CMDs. Our technique for cleaning the CMDs of these contaminating stars is discussed in section 1.6. Table 2.3 contains a sample of our photometric data, the rest of which is not reproduced here because of its excessive size.

2.4.5 Comparison with ground-based photometry

In order to check the Holtzman et al. (1995b) zero points, we compared our calibrated WFPC2 photometry with photometry from our V and I CTIO 1.5-m observations of the cluster fields. The seeing in the 1.5-m images is generally $\sim 1''$, corresponding to 22 pixels on the PC and 10 pixels on the WF chips. Using approximate WFPC2 x and y positions of the ground-based stars, we identified stars from the 1.5-m and WFPC2 lists with positions matching within a radius equal to the radius of the 1.5-m seeing circle. For almost all of the stars appearing isolated on the 1.5-m images, we found several stars within the seeing circle on the WFPC2 frames. The correct match

was assumed to be with the brightest of the candidates in the WFPC2 frame. We inspected each matching star by eye on the WFPC2 frame, and eliminated any star with significantly bright companions within a 0.″7 radius from further consideration. The remaining matches were used to establish the comparison between the ground-based and WFPC2 photometry.

Table 2.4 lists the average difference in magnitude between the ground-based and HST photometry for the selected stars. The absolute differences are as large as 0.1 mag, and vary between different clusters and chips. Fig. 2.9 plots the data from Table 2.4 versus cluster for each chip, and shows that the differences in ground-based and WFPC2 photometry for different chips and filters are correlated. Because the four WFPC2 chips are essentially treated as different instruments in our reduction, such correlation is unlikely to be caused by a systematic error in the WFPC2 photometry. Rather, we attribute the correlation to the extreme difficulty of doing photometry in the severely crowded ground-based frames. We also find that the difference between the ground-based and WFPC2 magnitudes is correlated with distance from the cluster center, which we believe is due to the increased crowding towards the cluster core. After removing the cluster-to-cluster variations, the ground-based and WFPC2 zero points are found to agree to within $\sim$0.1 mag. We have thus not felt it necessary to adjust the Holtzman (1995b) zero points.

2.5 Artificial star tests

With artificial star tests, we explored a number of calibration issues as well as studied the completeness of the photometry and the effects of crowding. The crowding and completeness effects are expected to be a function of magnitude, color, and position in the frame. Therefore, we used a set of artificial stars with magnitudes, colors, and positions distributed similarly to those of the stars in our CMDs. We generated the magnitudes and colors of the input artificial star sets by dividing our combined WF

and PC CMDs into bins of 0.03-0.06 magnitudes in $V - I$ and 0.1-0.2 magnitudes in V. In each bin, we chose a number of random points to represent the artificial stars. The number of artificial stars in a bin was chosen to be 10 times the number of observed stars in that bin, with the constraint that no bin should contain more than 100 artificial stars. Figs. 2.10–2.11 show the input artificial star CMDs. We distributed the positions of the artificial stars randomly, weighting the distribution by the stellar density profile. We determined the stellar density profile by fitting the completeness-corrected combined PC and WF star counts to a King (1966) model plus a constant background, with completeness corrections measured from an earlier artificial star experiment in which the artificial stars were uniformly distributed in position. Although useful for estimating the completeness, this initial experiment was not otherwise helpful because of insufficient coverage in $V - I$. We refit the King models later from the updated completeness corrections of the new artificial star experiments.

Using the previously mentioned PSFs obtained from Stetson, we distributed the artificial star sets over multiple copies of the original images, with the density of artificial stars in a given image amounting to $\sim$5% of the original stellar density. Each artificial star was placed in both the long and short exposure frames and in both filters. In all, $\sim$7200 artificial star images were generated. The frames containing the artificial stars were reduced in exactly the same manner as the original images, although it was, of course, unnecessary to perform any CTE correction to the short exposure photometry. To recover the detected artificial stars, we searched the DoPHOT output lists for stars with positions matching to within 0.6 pixels to those of stars in the input artificial star list. The list of recovered stars was similarly compared with the list of stars from the original image. In cases where the recovered artificial star also matched a star in the original image, we considered the artificial star lost if the recovered magnitude was closer to the magnitude of the real star than to the magnitude of the artificial star. As with the real photometry, artificial stars placed too closely to bad

or saturated pixels were considered lost. We merged the lists of recovered artificial stars placed in the short and long exposure images, and matched the merged lists from the two filters. Also shown in Figs. 2.10–2.11 are the stars recovered from the input distributions.

2.5.1 The effects of crowding and incompleteness

Incompleteness, which we define as the missed detection of stars due to noise fluctuations, presence of bright nearby neighbors, or our selection criteria, must be accounted for before we use the CMDs for quantitative purposes, such as deriving the ages of the globular clusters or the star formation histories of the field stars. In addition, we must account for the photometric scatter and bulk photometric shifts introduced by crowding. By following the undetected stars and by comparing the input and recovered magnitudes of detected stars in our artificial star experiements, we quantified the crowding effects and measured the completeness of our photometry.

Figs. 2.12 show the completeness surfaces, which represent the probability that a star of a given position and actual V magnitude would be found in our CMDs. The surfaces demonstrate that the completeness and associated limiting magnitude are strong functions of position near the cluster center.

Figs. 2.13 present a visualization of the random errors and systematic shifts in the photometry. The arrows represent the average distance and direction over which stars placed in the associated bins drifted during the artificial star experiments, while the error bars are the robust standard deviations of the photometric drifts. While the size of the random errors depend mostly on V magnitude with very little, if any, color dependence, the systematic shifts depend on both $V-I$ and V. At faint V, this dependence of the shifts on both V and $V-I$ can be explained by the existence of a magnitude-limit in both the V and I filters. At brighter magnitudes, however, there remains a tendency for blue stars to be recovered redder than their true colors. This is likely an effect of crowding with redder neighboring stars.

For the purposes of later analysis, we incorporate the effects of crowding and incompleteness as a function of $V-I$ and V into a single surface, which we label $\Lambda(V-I,V)$ (Gallart, Aparicio, & Vilchez 1996, among others). Λ is defined as the ratio of the distribution of colors and magnitudes recovered from the artificial star experiments to the distribution of input colors and magnitudes.

2.6 Cleaning background stars from the CMDs

Our WFPC2 frames are a mix of cluster and background field stars, with no portion of the images containing only one type of star. However, because the cluster and field stars are distributed differently, we can still statistically separate the two populations. We are further aided by the fact that the PC frames contain more cluster stars than field stars, vice versa in the WF frames. Our approach is to use the WF frames to remove field stars from the PC frames, and use the cleaned PC frames to remove cluster stars from the WF frames. After a few iterations of this procedure, we will achieve satisfactorily clean cluster and field CMDs.

Our cleaning procedure accounts for the different crowding conditions and the different areas subtended by the cluster and field star distributions in the PC and WF frames. The following equation describes the number of contaminating background stars expected in the frame containing the stars of interest:

$$N(V,V-I)=\frac{\Lambda^p(V,V-I)}{\Lambda^c(V,V-I)}\frac{\int F(\vec{r})dA^p}{\int F(\vec{r})dA^c}D^c(V,V-I) \qquad (2.1)$$

where $\Lambda^p(V,V-I)$ is the surface describing crowding and incompleteness in the primary frame, $\Lambda^c(V,V-I)$ is the equivalent surface for the background frame, $F(\vec{r})$ is the spatial distribution of the background stars, dA^p and dA^c are area elements, and D^c is the distribution of stars in the CMD in the background frame. We assume the field stars are uniformly distributed, so that $F(\vec{r})$ =constant and the integrals reduce to the areas of the frames. For the cluster stars, we choose a King (1966) model to represent $F(\vec{r})$. The next section discusses these King model fits.

2.6.1 Cluster profiles

We determined the centers of the clusters through an algorithm developed by King and described in Mateo (1987). Briefly, the algorithm finds the center of symmetry of the clusters by extracting subimages on a grid of points in the image containing the cluster and correlating each subimage with itself, rotated 180 degrees. The value of the correlation is stored at each grid point, resulting in a surface whose maximum represents the center of symmetry. We measured the maximum by fitting this surface to a second order polynomial and computing the vertex. The algorithm worked well for the rich clusters, but was somewhat time-consuming and more difficult in the poorer clusters, particularly NGC 1898. Table 2.5 lists the cluster center positions calculated by the algorithm.

With the cluster centers established, we calculated the radial stellar distributions of each cluster. We transformed the coordinates of all the stars to a reference frame centered on the cluster and scaled to the size of PC pixels. We set up 30 logarithmically spaced annuli around the center of each cluster out to the edges of the WF chips and calculated the area of the portion of each annulus covered by the WFPC2 chips. We then summed up the number of stars within each annulus, divided the sum by the completeness appropriate to the stars' positions and magnitudes, and divided by the appropriate area. Because the magnitude limit is a function of position, we tried to restrict the radial distribution to contain only stars with completeness $\gtrsim 50\%$ at all radii. In order to have enough stars to define the profiles of NGC 1835, NGC 2005, and NGC 2019, however, we were forced to include stars with completenesses as low as 20%.

We fit King (1966) models with variable amounts of background to the radial distributions to determine the relative contribution of the cluster stars in each chip. First, we estimated the peak density from the profile close to the center and set the core radius, r_c to the radius at which the density reaches $\sim 1/2$ the peak radius. We

then tried different variations of r_c, concentration, and background level and chose the best fit by eye. We note that for NGC 1835, the innermost three points do not give a good fit, probably because of incompleteness problems near the cluster center. Figs. 2.14 show the observed background-subtracted profiles for each cluster and the adopted fits. The parameters of these fits are included in Table 2.5.

2.6.2 Cleaning Procedure

We began by removing a statistical sample of field stars chosen from the combined WF CMDs from the cluster-dominated PC CMD. Equation 1 becomes:

$$N^{PC}(V, V-I) = \frac{\Lambda^{PC}(V, V-I)}{\Lambda^{WF}(V, V-I)} \frac{A^{PC}}{A^{WF}} D^{WF}(V, V-I)$$

$N^{PC}(V, V-I)$ represents how the stars in the WF CMD would be distributed in the PC CMD, and are the stars we wished to subtract. However, because some areas of the CMDs are sparsely populated, not all of the bins in the PC CMD for which $N^{PC}(V, V-I)$ is positive contain stars. Therefore, rather than simply subtracting the $N^{PC}(V, V-I)$ stars from the appropriate bins, we subtracted stars based on the error ellipse at each point. At each point $(V, V-I)$, we gave the surrounding stars weights based on the error distribution at $(V, V-I)$, and chose the stars to be subtracted randomly from this weighted distribution. Stars outside the 3-σ error ellipse were given zero weight and were not considered. If no stars laid within the 3-σ ellipse, we subtracted the nearest available neighbor. We then used the cleaned PC CMDs to subtract cluster stars from the WF CMDs. The relevant equation is:

$$N^{WF}(V, V-I) = \frac{\Lambda^{WF}(V, V-I)}{\Lambda^{PC}(V, V-I)} \frac{\int F_{\rm King}(r) dA^{WF}}{\int F_{\rm King}(r) dA^{PC}} D^{PC}(V, V-I)$$

where $F_{\rm King}(r)$ is the King model fit from the completeness-corrected stellar density distribution and $D^{PC}(V, V-I)$ is the cleaned PC CMD. We used the same procedure described above to remove stars from the WF CMDs, producing CMDs with mostly cluster stars removed.

Because there are both cluster and field stars in both the PC and WF CMDs, we necessarily removed some cluster stars from the PC CMDs and some field stars from the WF CMDs in the first iteration of the subtraction procedure. Repeated iterations improved the separation, producing statistically cleaner cluster and field star CMDs. We found that the procedure converges in $\sim$5 iterations, as expected by the measured contamination levels and a simple calculation of the convergence rate. Figs. 2.15–2.16 show the cleaned cluster and field star CMDs. While the cleaning worked well for the cluster CMDs, the field star CMDs have a tattered appearance. This is probably because in some cases the cluster stars dominate the red giant branch, making the statistical errors along the RGB large.

2.7 Summary

This Chapter has followed the production of deep *HST* color-magnitude diagrams for six LMC globular clusters and the surrounding field stars, which form the basis for the bulk of the remaining analysis. Besides following standard WFPC2 reduction techniques, we took several steps to ensure a correct calibration of the photometry. Aperture corrections were constructed as a function of position in the frames using the brightest, most isolated stars. We compared these aperture corrections with ones derived from Peter Stetson's WFPC2 PSF observations, finding that our WF aperture corrections agreed well with Stetson's PSFs while our PC aperture corrections did not. Because our PC frames are very crowded, we adopted the aperture corrections based on Stetson's PSFs for the PC photometry. We compared stars measured in both the long and short exposures and found evidence for the magnitude-dependent CTE effect discussed by Whitmore & Heyer (1997). Finally, we checked our WFPC2 photometry against ground-based photometry of selected stars, but decided that the differences in the two sets of photometry are most likely explained by the extreme crowding of the ground-based images. On the basis of the comparison, however, we rule out errors of

$\gtrsim$0.1 magnitudes in the WFPC zero points.

Towards the end of the Chapter, we showed King (1966) model fits of the stellar density profiles of the globular clusters. These fits were used to produce uncontaminated cluster and field star CMDs, the analysis of which we discuss in the following chapters.

Table 2.1: Summary of Observing Log

Cluster	Files	Filter	Exp. time (sec.)	Date (DD/MM/YY)
NGC 1754	u2xq0101t_cvt.*, u2xq0102t_cvt.*	F555W	20	21/10/95
	u2xq0103t_cvt.*, u2xq0104t_cvt.*, u2xq0105t_cvt.*	F555W	500	21/10/95
	u2xq0106t_cvt.*, u2xq0107t_cvt.*, u2xq0108t_cvt.*	F814W	20	21/10/95
	u2xq0109t_cvt.*, u2xq010at_cvt.*, u2xq010bt_cvt.*	F814W	600	21/10/95
NGC 1835	u2xq0201t_cvt.*, u2xq0202t_cvt.*	F555W	20	18/10/95
	u2xq0203t_cvt.*, u2xq0204t_cvt.*, u2xq0205t_cvt.*	F555W	500	18/10/95
	u2xq0206t_cvt.*, u2xq0207t_cvt.*, u2xq0208t_cvt.*	F814W	20	18/10/95
	u2xq0209t_cvt.*, u2xq020at_cvt.*, u2xq020bt_cvt.*	F814W	600	18/10/95
NGC 1898	u2xq0301t_cvt.*, u2xq0302t_cvt.*	F555W	20	10/12/95
	u2xq0303t_cvt.*, u2xq0304t_cvt.*, u2xq0305t_cvt.*	F555W	500	10/12/95
	u2xq0306t_cvt.*, u2xq0307t_cvt.*, u2xq0308t_cvt.*	F814W	20	10/12/95
	u2xq0309t_cvt.*, u2xq030at_cvt.*, u2xq030bt_cvt.*	F814W	600	10/12/95
NGC 1916	u2xq0401t_cvt.*, u2xq0402t_cvt.*	F555W	20	10/12/95
	u2xq0403t_cvt.*, u2xq0404t_cvt.*, u2xq0405t_cvt.*	F555W	500	10/12/95
	u2xq0406t_cvt.*, u2xq0407t_cvt.*, u2xq0408t_cvt.*	F814W	20	10/12/95
	u2xq0409t_cvt.*, u2xq040at_cvt.*, u2xq040bt_cvt.*	F814W	600	10/12/95
NGC 2005	u2xq0501t_cvt.*, u2xq0502t_cvt.*	F555W	20	19/10/95
	u2xq0503t_cvt.*, u2xq0504t_cvt.*, u2xq0505t_cvt.*	F555W	500	19/10/95
	u2xq0506t_cvt.*, u2xq0507t_cvt.*, u2xq0508t_cvt.*	F814W	20	19/10/95
	u2xq0509t_cvt.*, u2xq050at_cvt.*, u2xq050bt_cvt.*	F814W	600	19/10/95
NGC 2019	u2xq0601t_cvt.*, u2xq0602t_cvt.*	F555W	20	18/10/95
	u2xq0603t_cvt.*, u2xq0604t_cvt.*, u2xq0605t_cvt.*	F555W	500	18/10/95
	u2xq0606t_cvt.*, u2xq0607t_cvt.*, u2xq0608t_cvt.*	F814W	20	18/10/95
	u2xq0609t_cvt.*, u2xq060at_cvt.*, u2xq060bt_cvt.*	F814W	600	18/10/95

Table 2.2: DoPHOT PSF Parameters

	F555W			F814W		
Chip	β_4	β_6	FWHM	β_4	β_6	FWHM
PC	4.5	4.5	2.0	4.5	4.5	2.0
WF2-4	2.2	2.2	1.2	2.5	2.5	2.0

Table 2.3: LMC WFPC2 Photometry

Star #	X (V)	Y	V	σ_V^a	I	σ_I^a	V type[b]	I type[b]	Removed[c]
NGC 1754 PC									
1	386.11	100.57	19.3881	0.038	18.3591	0.052	10	10	y
2	477.04	104.77	18.6639	0.042	17.5141	0.049	3	10	
3	491.68	112.58	19.6949	0.044	18.6781	0.049	1	10	
4	597.60	127.65	19.4229	0.050	18.3281	0.051	1	10	
5	233.08	129.43	19.6629	0.046	19.3249	0.054	1	1	
6	142.73	142.05	19.6841	0.039	19.5021	0.056	10	10	
7	753.78	153.25	19.3071	0.055	18.1461	0.050	30	10	
8	286.41	184.42	19.2699	0.046	18.8031	0.045	1	10	
9	105.07	203.56	19.6689	0.054	19.2081	0.052	3	10	
10	644.67	212.54	19.5009	0.0470	18.4271	0.0480	1	10	
.....									

[a]Photometric errors reported by DoPHOT

[b]Where the short exposure photometry was used, the DoPHOT object type has been multiplied by 10. See text for explanation of object types.

[c]Stars removed by cleaning procedure are marked with "y".

Table 2.4: Comparison of WFPC2 and Ground-based Photometry

Field	Chip	$V_{\rm ground} - V_{\rm HST}$	$\sigma_{\Delta V}$	$I_{\rm ground} - I_{\rm HST}$	$\sigma_{\Delta I}$	N
NGC 1754	PC	-0.053	0.035	-0.016	0.022	22
	WF2	-0.023	0.007	0.048	0.015	64
	WF3	0.028	0.008	0.102	0.018	55
	WF4	-0.027	0.009	0.029	0.015	59
NGC 1835	PC	-0.006	0.023	0.068	0.013	18
	WF2	0.067	0.018	0.142	0.022	36
	WF3	0.098	0.014	0.170	0.021	39
	WF4	0.024	0.019	0.112	0.026	34
NGC 1898	PC	-0.093	0.020	0.012	0.022	32
	WF2	0.007	0.012	0.108	0.018	11
	WF3	0.080	0.030	0.120	0.032	8
	WF4	-0.001	0.011	0.032	0.026	18
NGC 1916	PC	-0.154	0.073	-0.140	0.100	29
	WF2	0.020	0.023	0.111	0.025	18
	WF3	-0.010	0.036	0.144	0.033	11
	WF4	-0.154	0.089	-0.001	0.036	9
NGC 2005	PC	-0.177	0.064	-0.057	0.055	18
	WF2	-0.029	0.015	0.010	0.018	22
	WF3	0.061	0.026	0.076	0.023	21
	WF4	-0.116	0.025	-0.076	0.017	11
NGC 2019	PC	-0.066	0.023	-0.013	0.014	15
	WF2	0.076	0.024	0.118	0.015	19
	WF3	0.099	0.015	0.138	0.018	18
	WF4	0.037	0.016	0.053	0.011	22

Table 2.5: Cluster Centers and Structural Parameters

Cluster	RA (2000.0)	Dec	$r_c('')$	$\log_{10}(r_t/r_c)$
NGC 1754	$4^h54^m18^s.70$	-70°26′32″.1	3.6	1.5
NGC 1835	$5^h05^m6^s.44$	-69°24′14″.5	2.7	1.5
NGC 1898	$5^h16^m42^s.41$	-69°39′24″.6	5.2	1.9
NGC 2005	$5^h30^m10^s.36$	-69°45′9″.0	1.3	1.9
NGC 2019	$5^h31^m56^s.73$	-70°09′33″.3	0.9	2.2

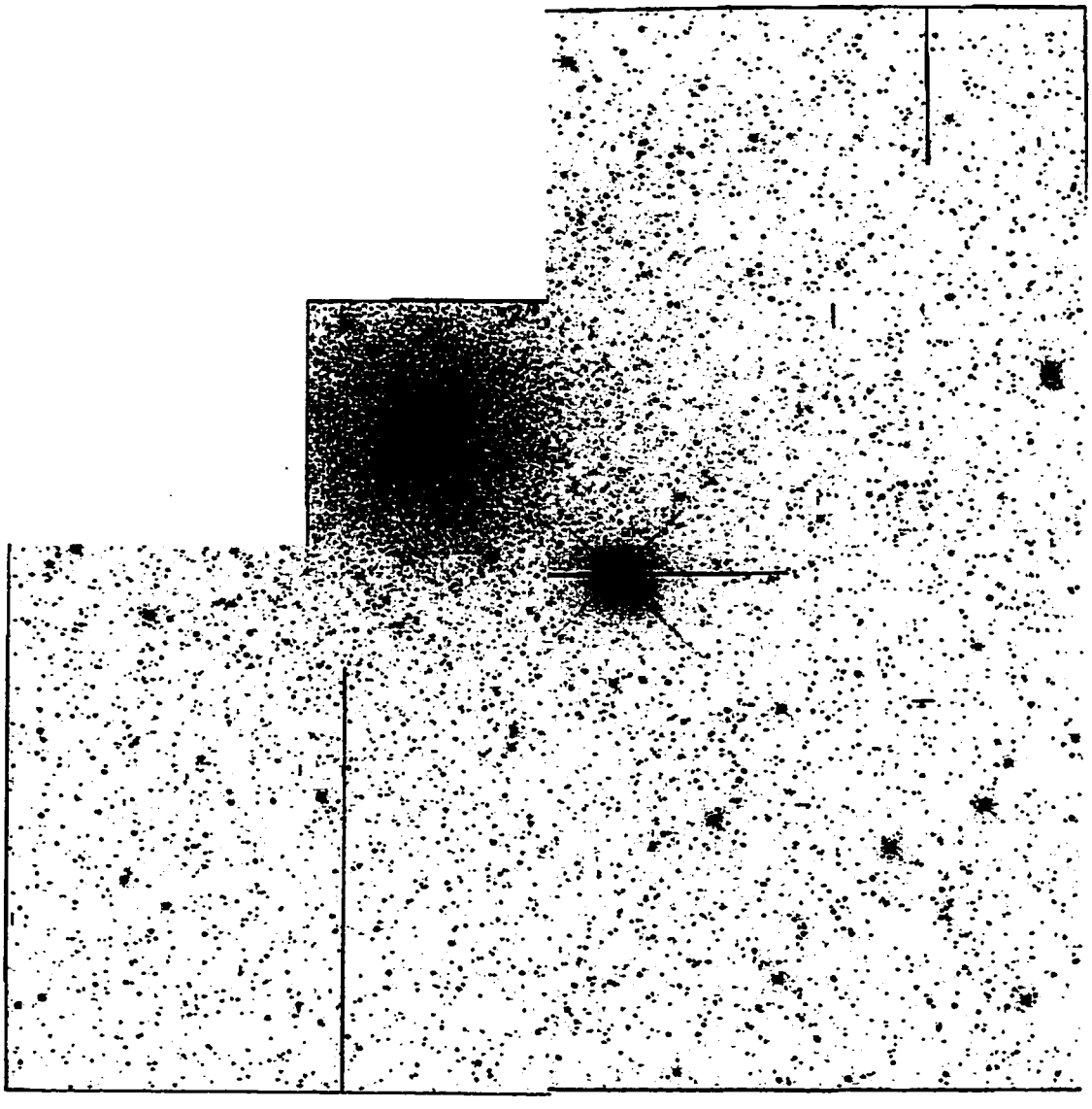

Figure 2.1a: WFPC2 mosaic of NGC 1754. Courtesy of Nick Suntzeff.

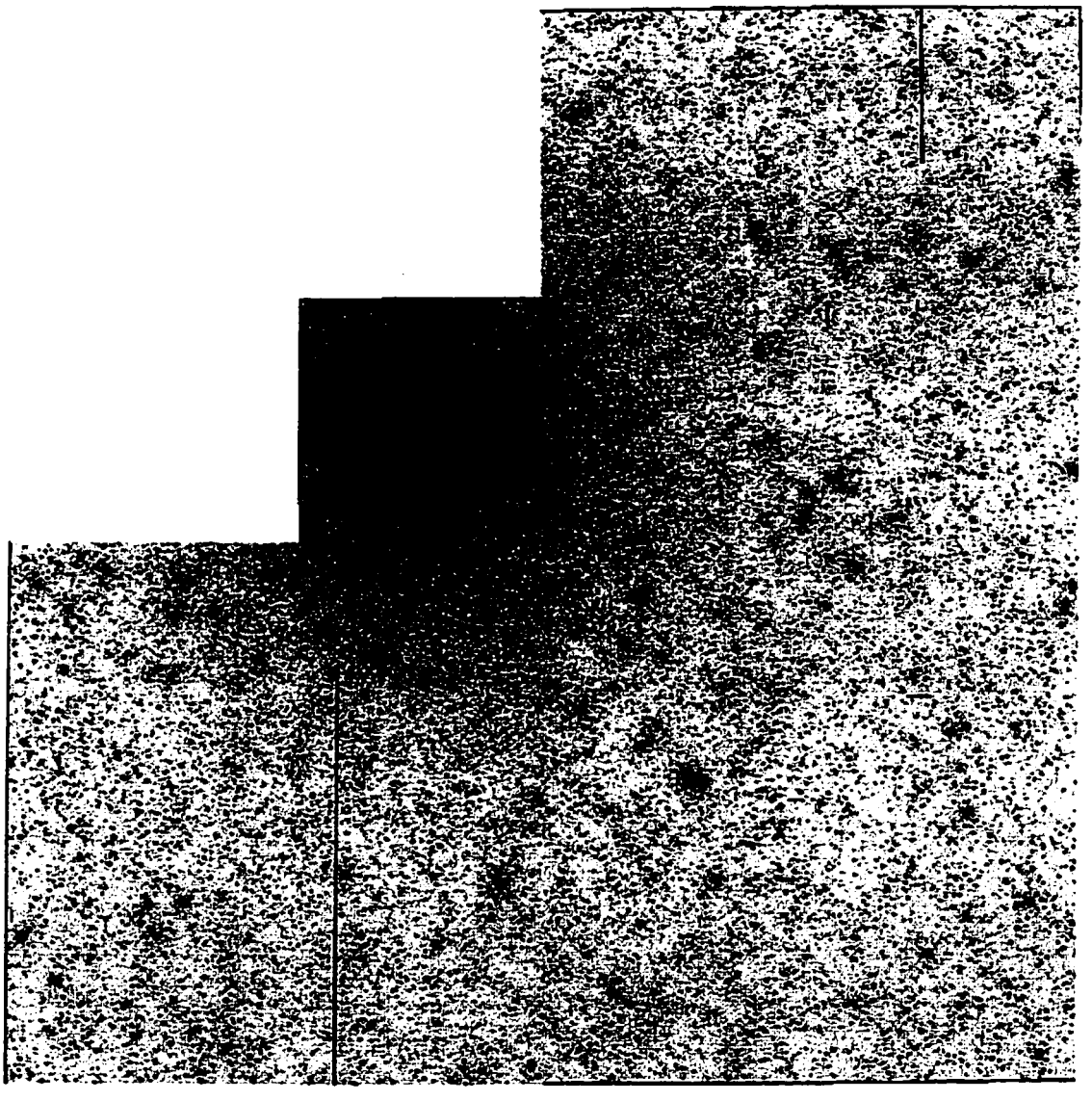

Figure 2.1b: WFPC2 mosaic of NGC 1835.

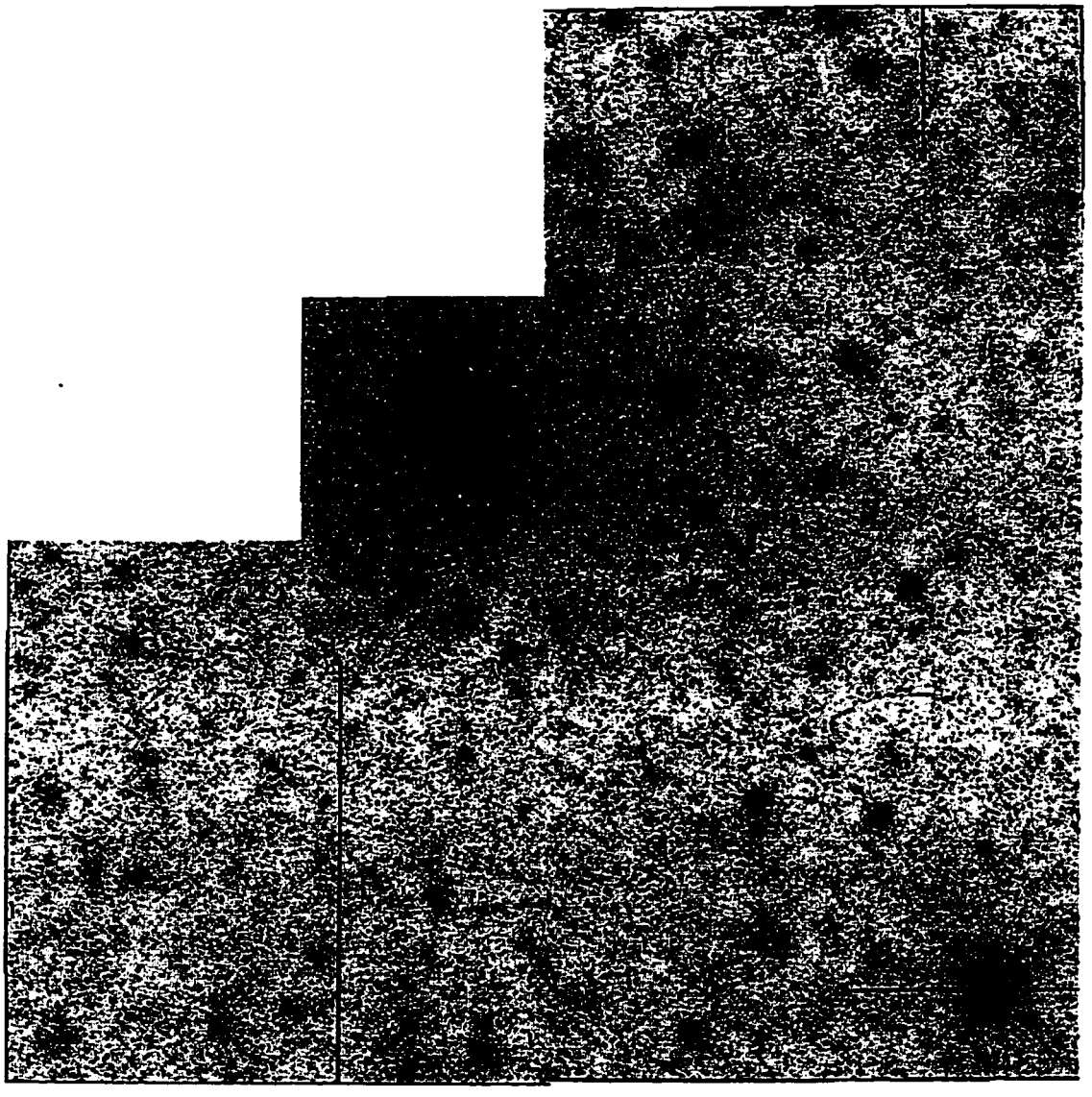

Figure 2.1c: WFPC2 mosaic of NGC 1898.

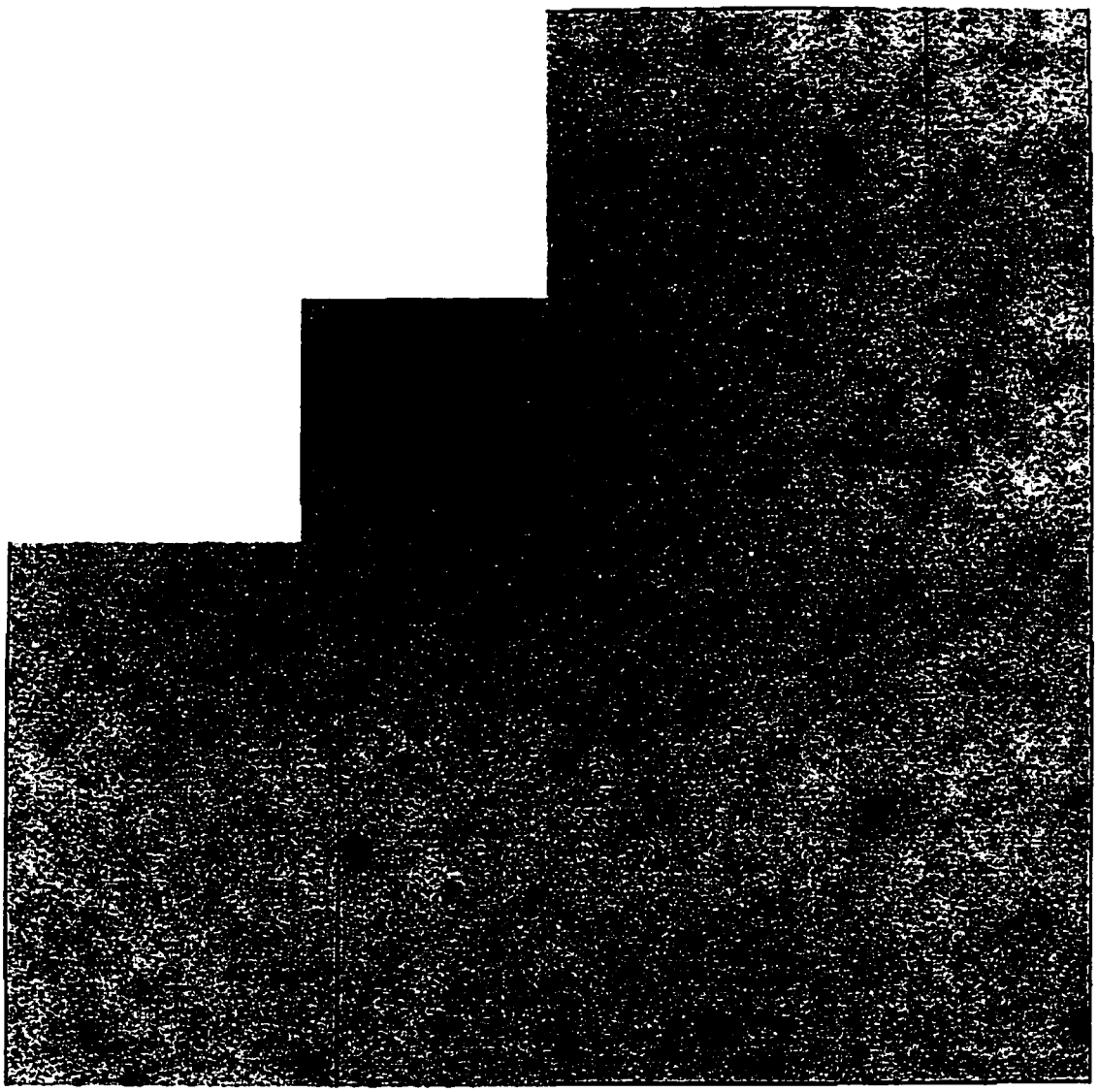

Figure 2.1d: WFPC2 mosaic of NGC 1916.

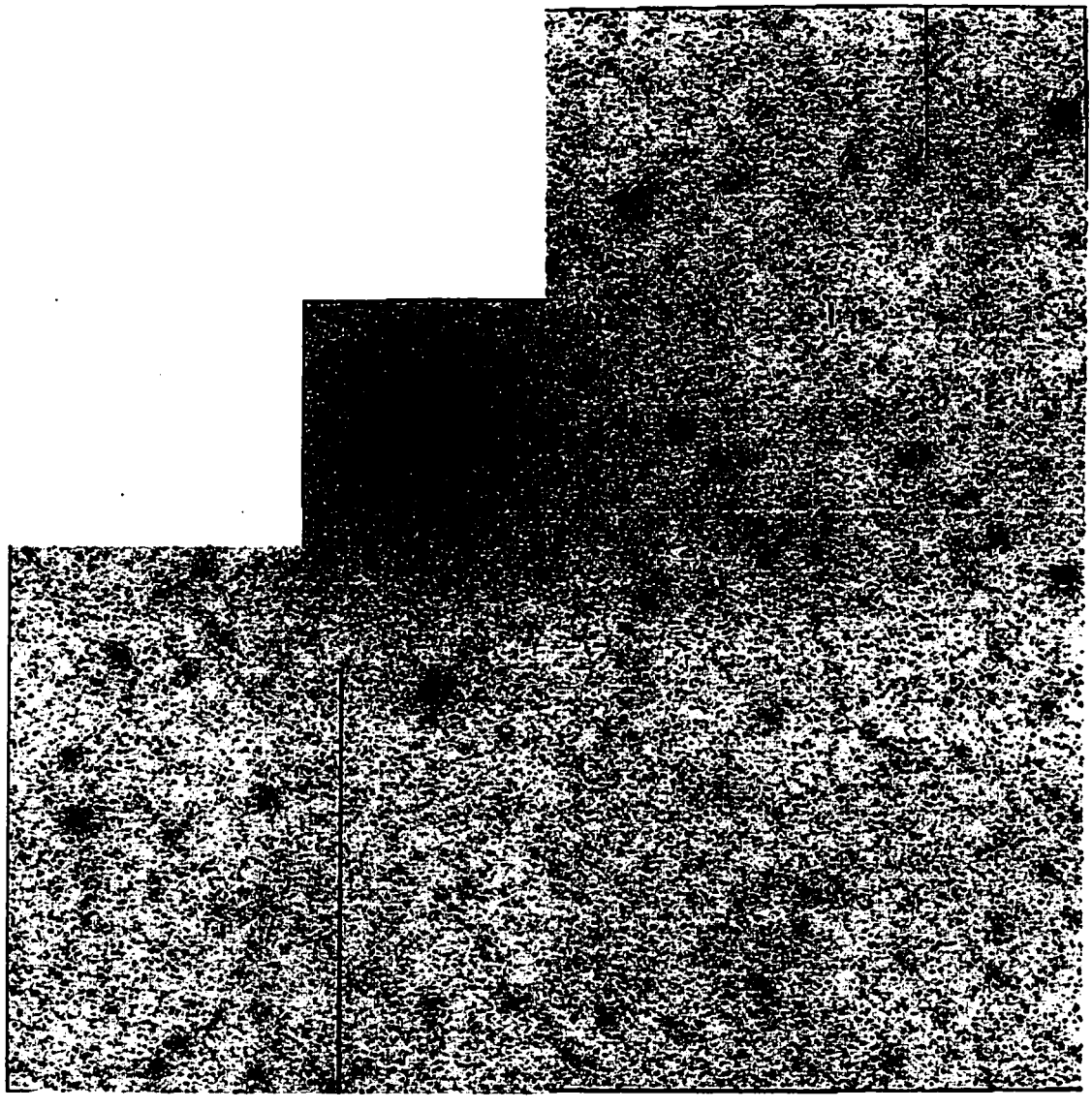

Figure 2.1e: WFPC2 mosaic of NGC 2005.

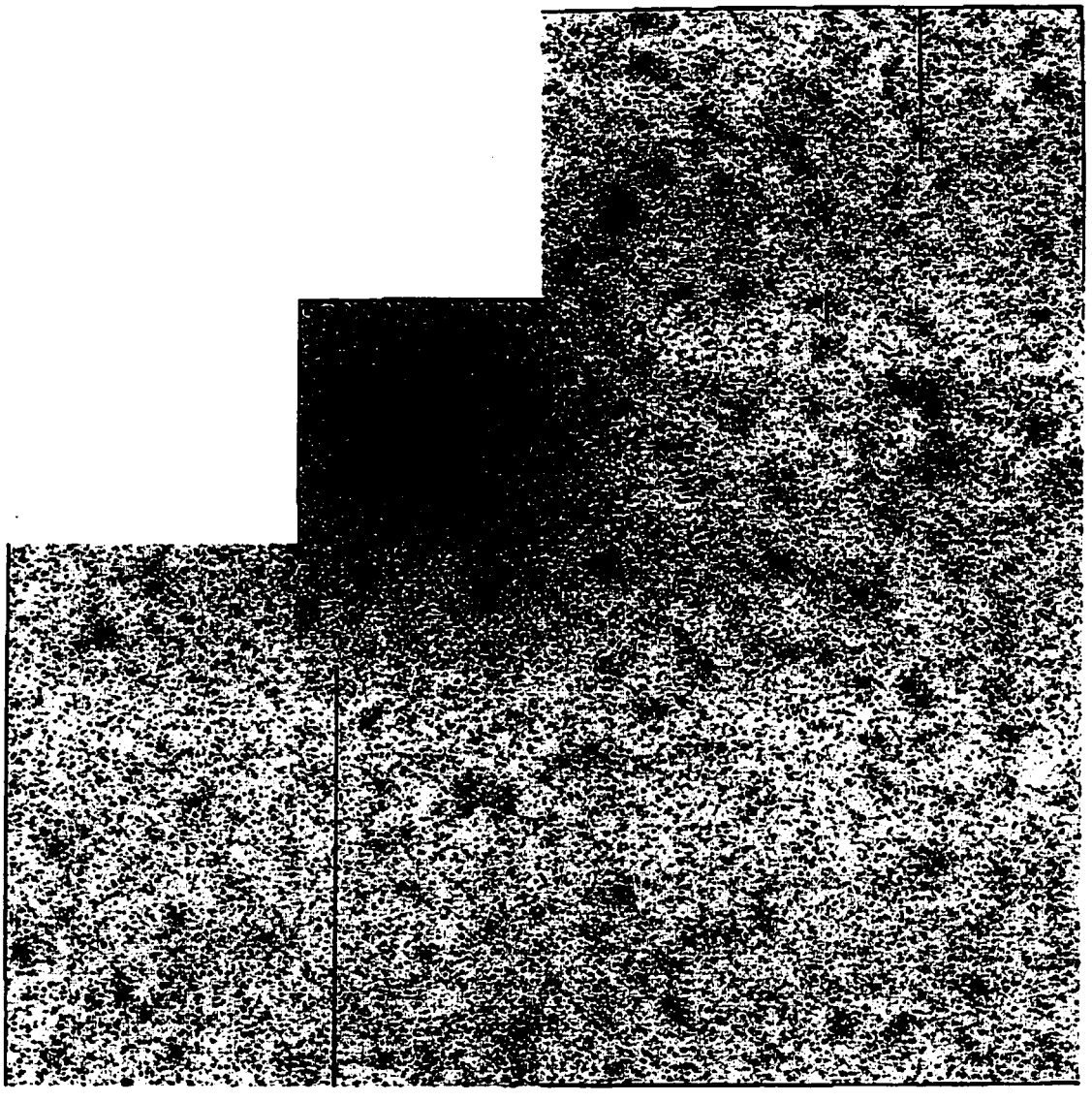

Figure 2.1f: WFPC2 mosaic of NGC 2019.

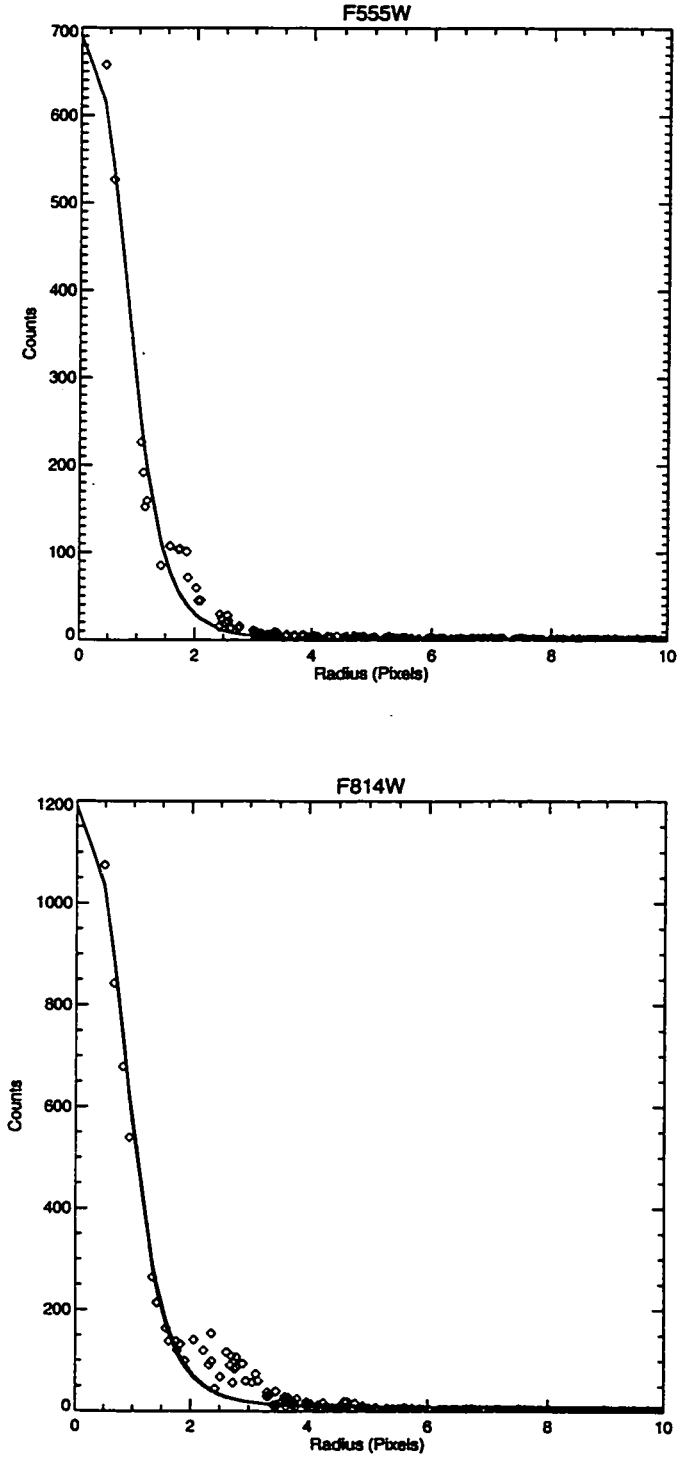

Figure 2.2: Fit of the DoPHOT analytical PSF used in the photometry to a sample star from the WFPC2 frames. While the PSF fits the core of the star and the background well, it does not fit the broad wings most prominent in the F814W images.

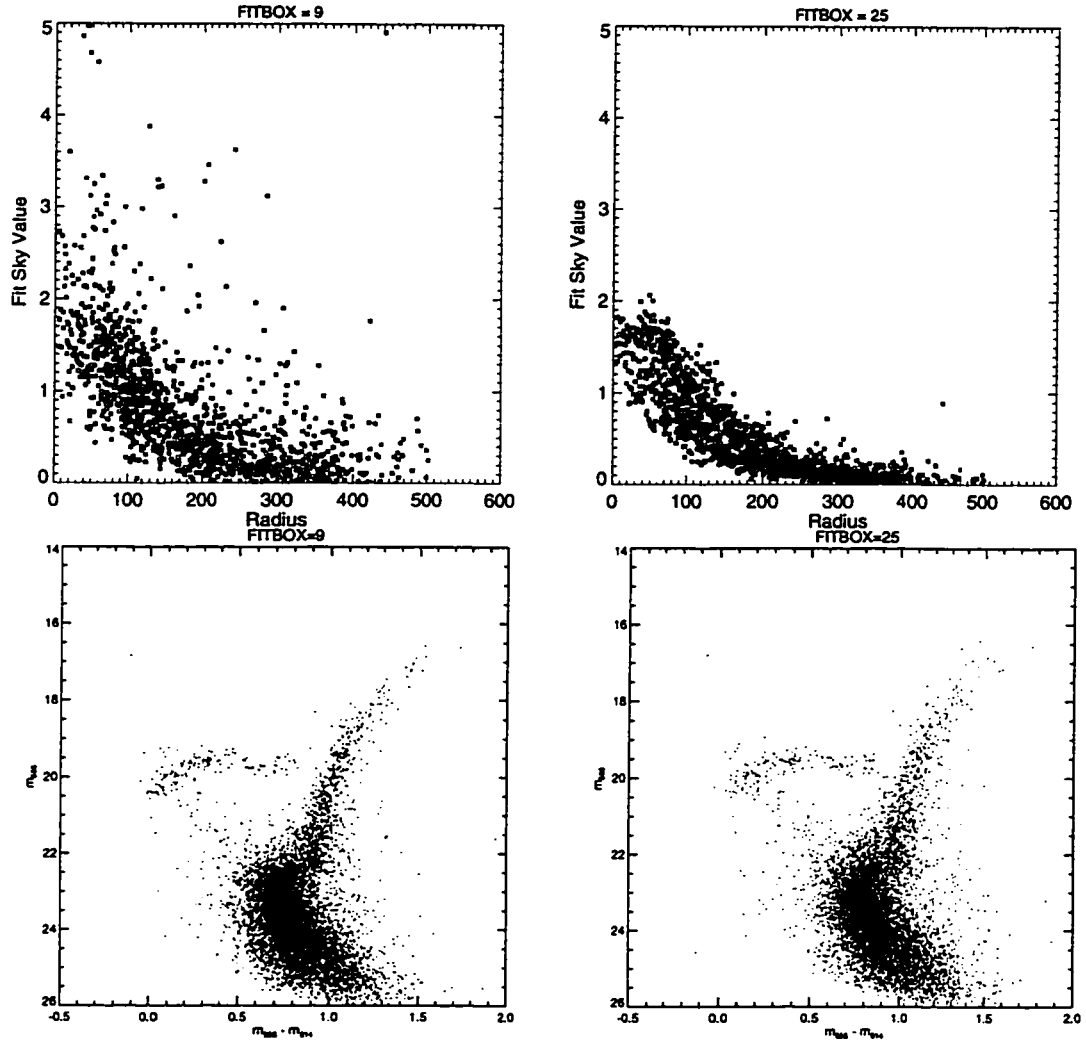

Figure 2.3: Plots showing the effect of different sizes of the fitting box used in the DoPHOT photometry. While using a larger fitting box produces better background fits, crowding limits the accuracy of the photometry.

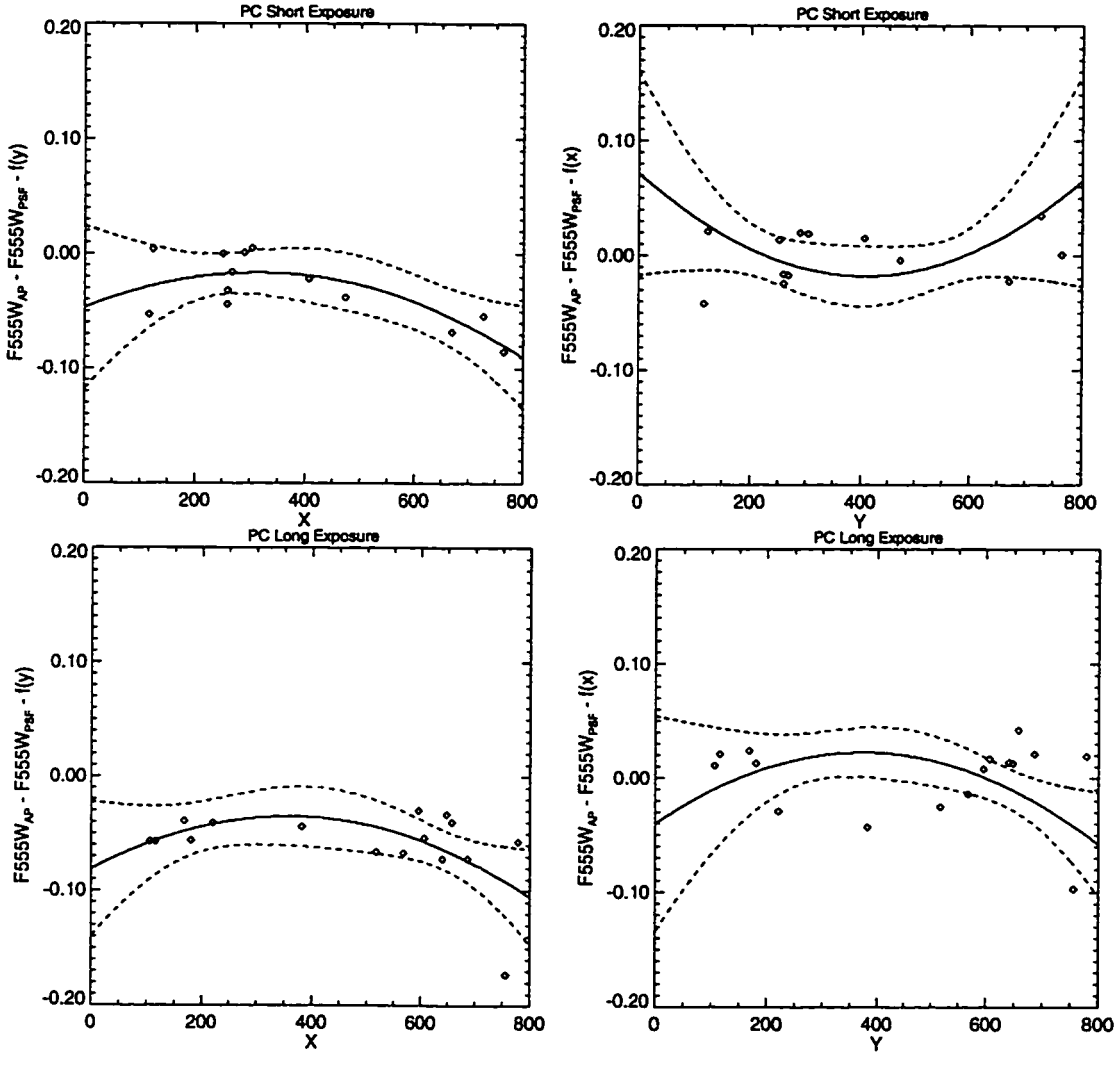

Figure 2.4a: Aperture corrections in the PC frame of the NGC 1754 field. The solid lines are weighted 2nd order polynomial fits while the dashed lines represent 1σ deviations from the fit. The poor fit demonstrates the difficulty of determining the aperture corrections in the PC frames.

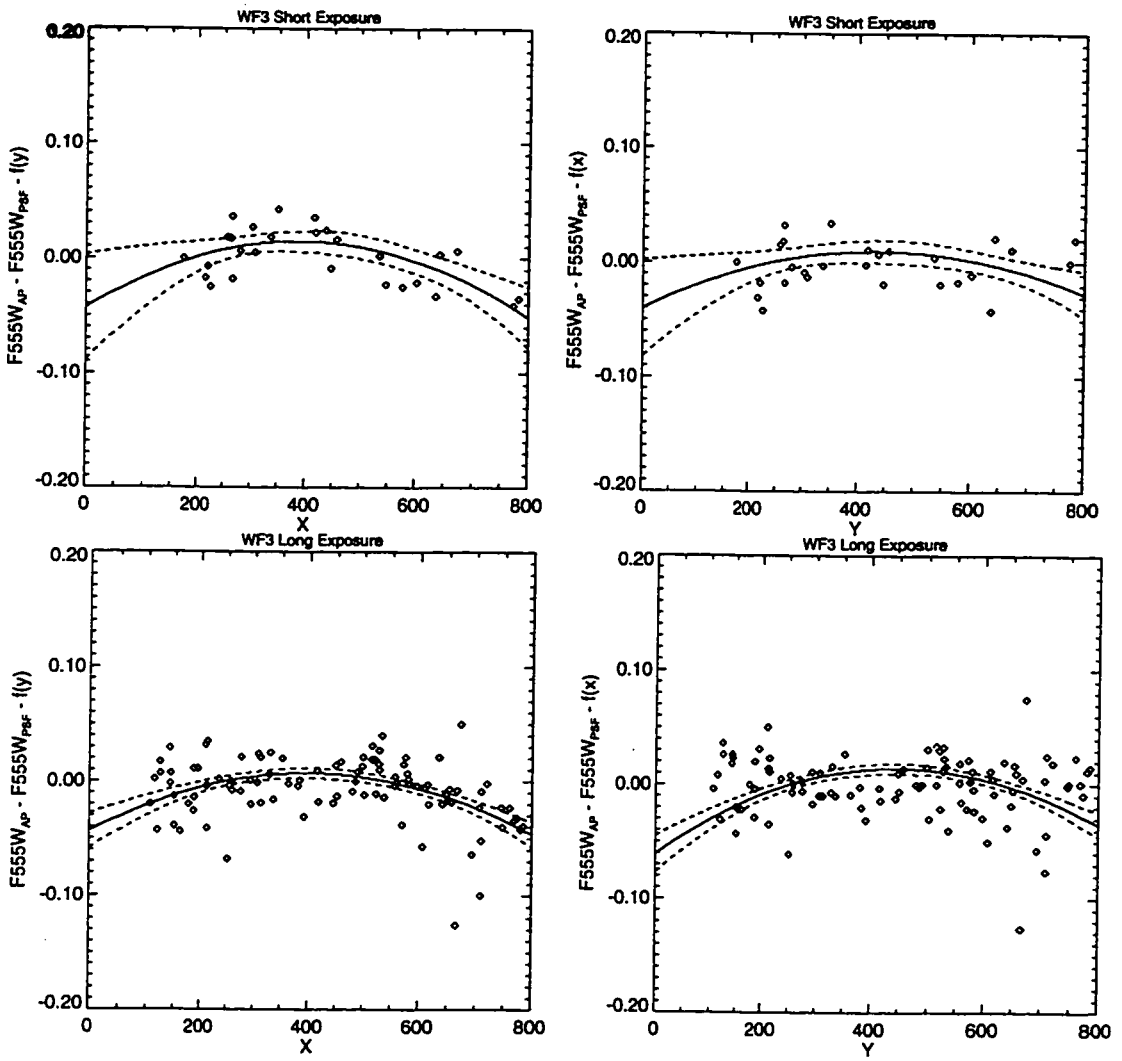

Figure 2.4b: Aperture corrections in the WF3 frame of the NGC 1754 field. These aperture corrections are much better fit by the second order polynomials than are the PC aperture corrections.

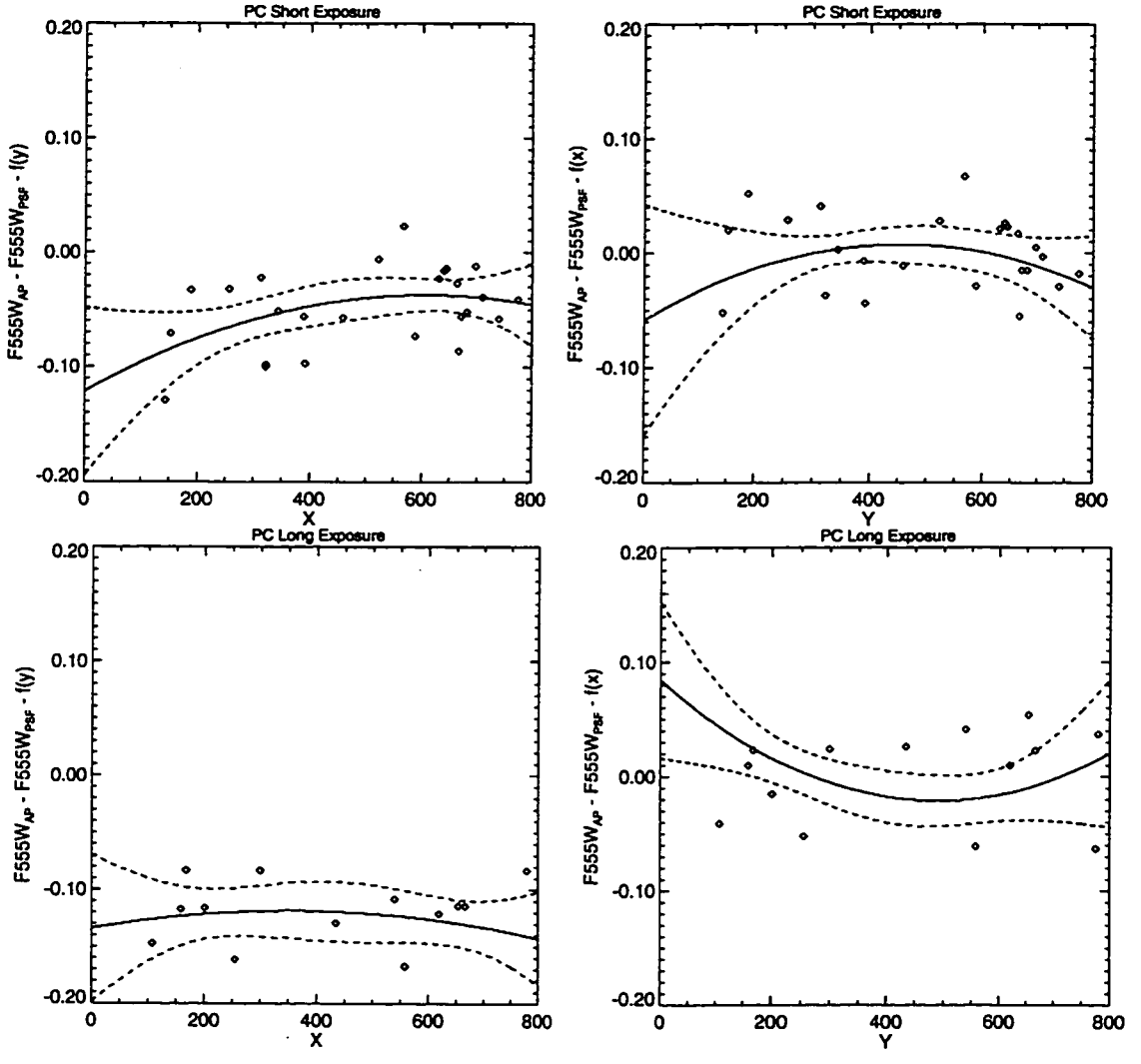

Figure 2.4c: Aperture corrections in the PC frame of the NGC 1835 field.

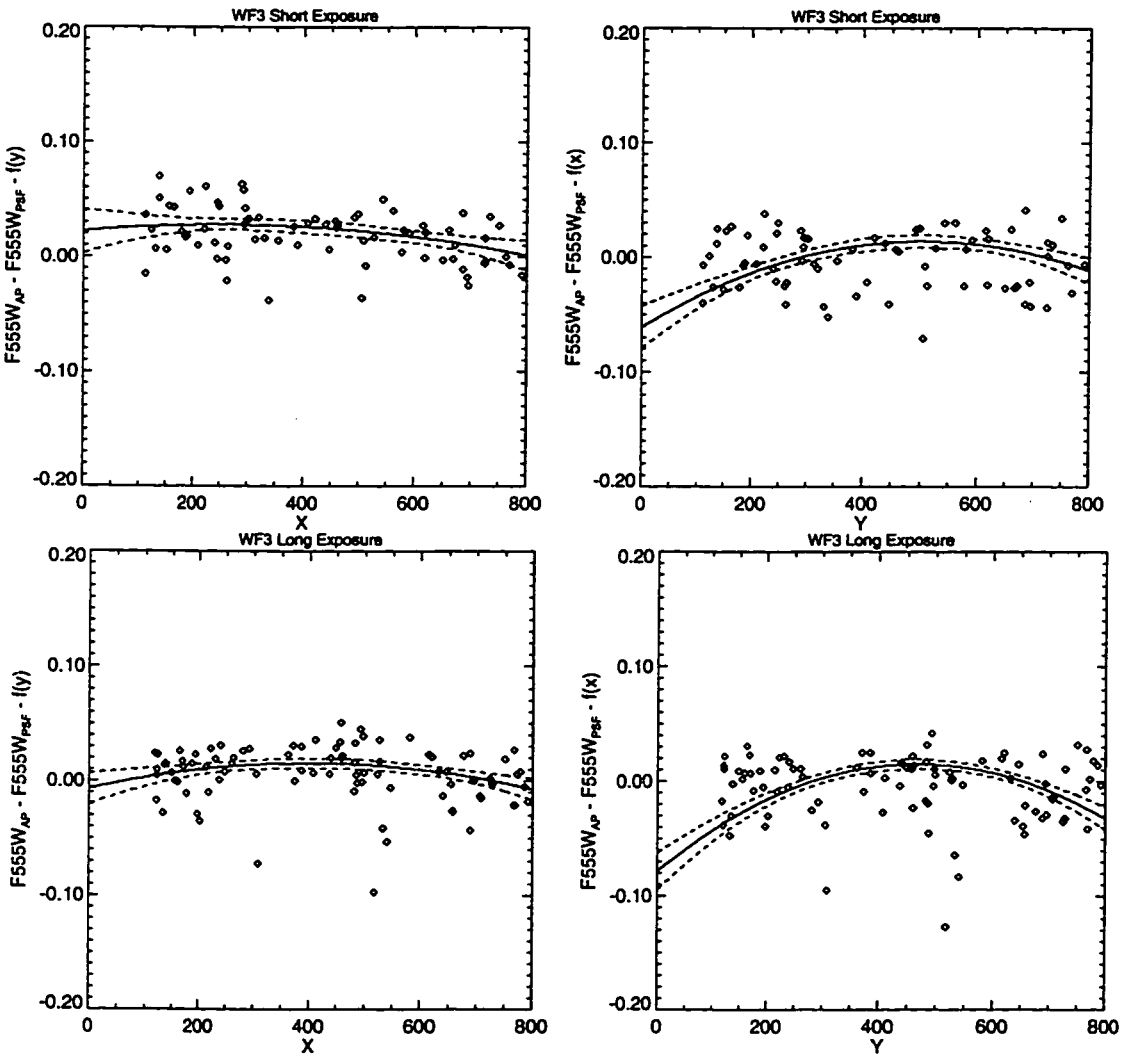

Figure 2.4d: Aperture corrections in the WF3 frame of the NGC 1835 field.

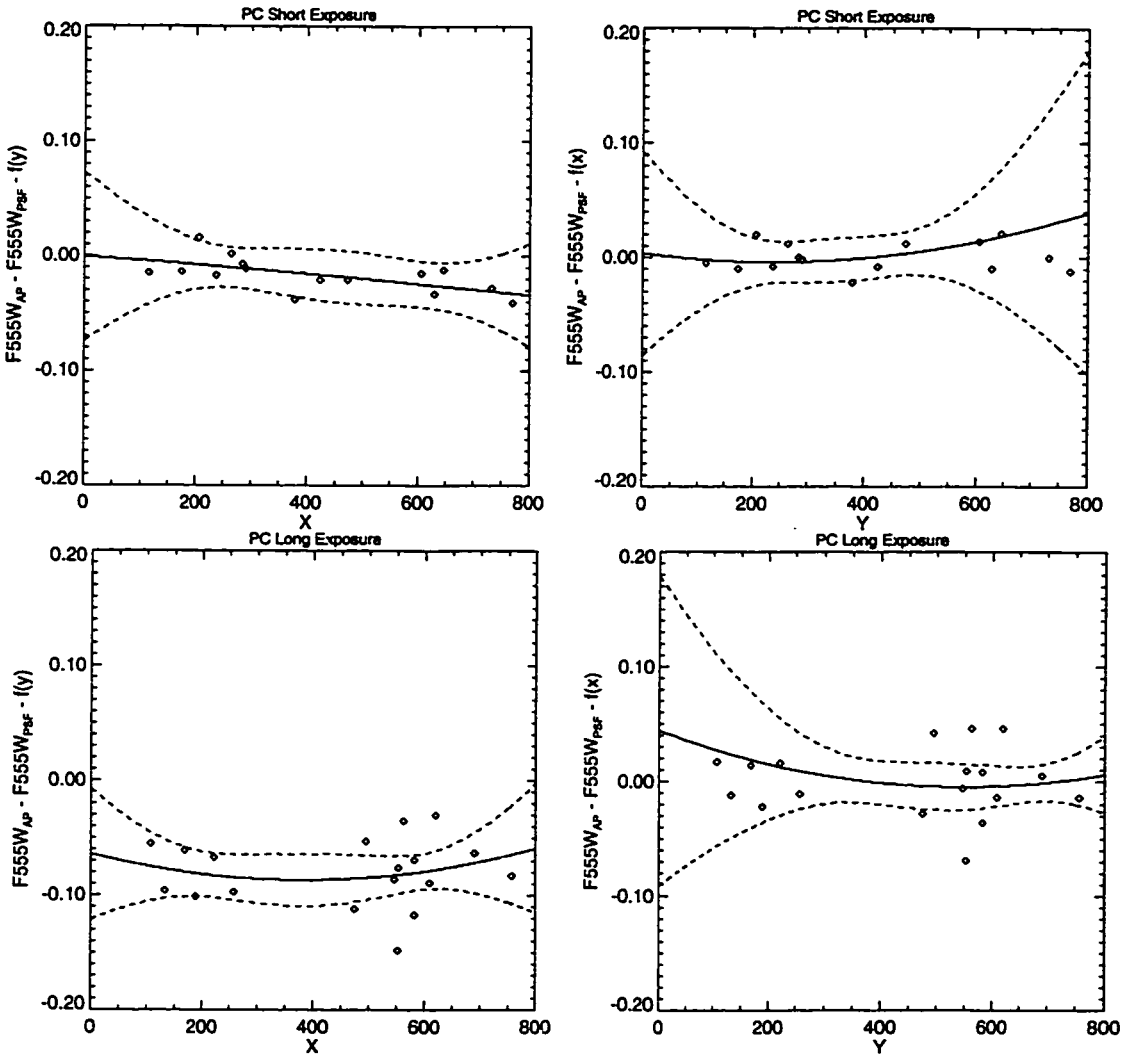

Figure 2.4e: Aperture corrections in the PC frame of the NGC 1898 field.

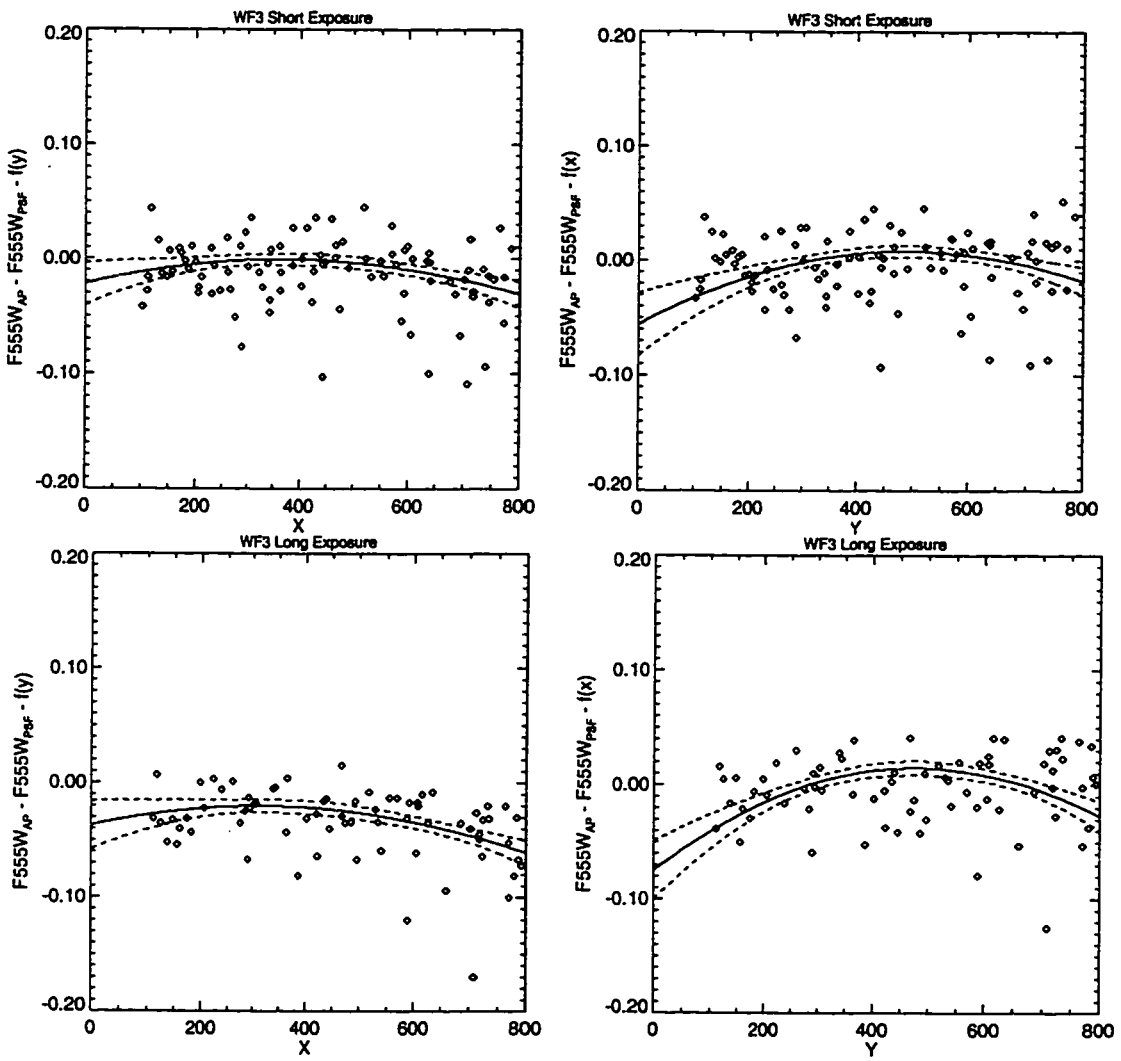

Figure 2.4f: Aperture corrections in the WF3 frame of the NGC 1898 field.

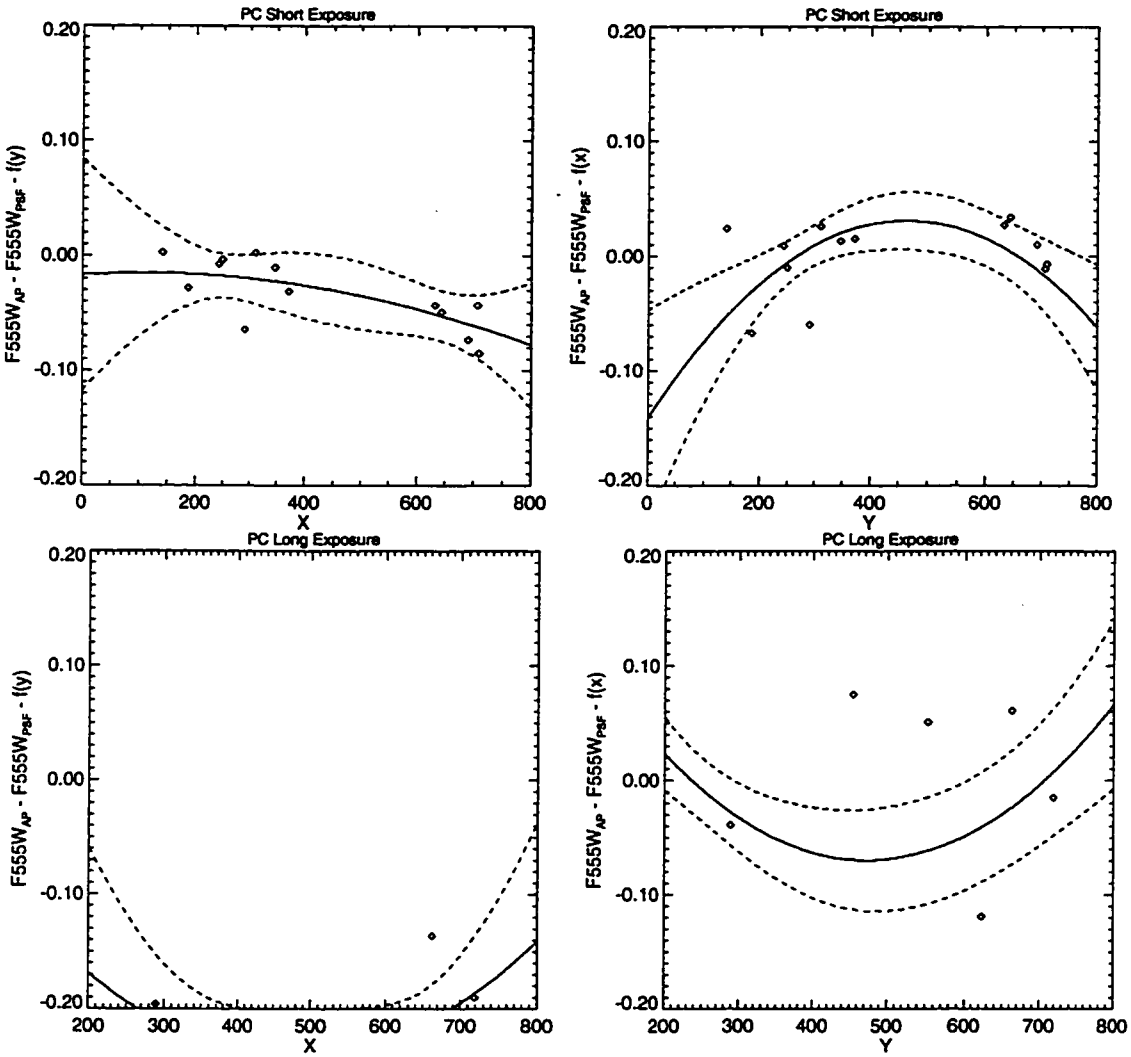

Figure 2.4g: Aperture corrections in the PC frame of the NGC 1916 field.

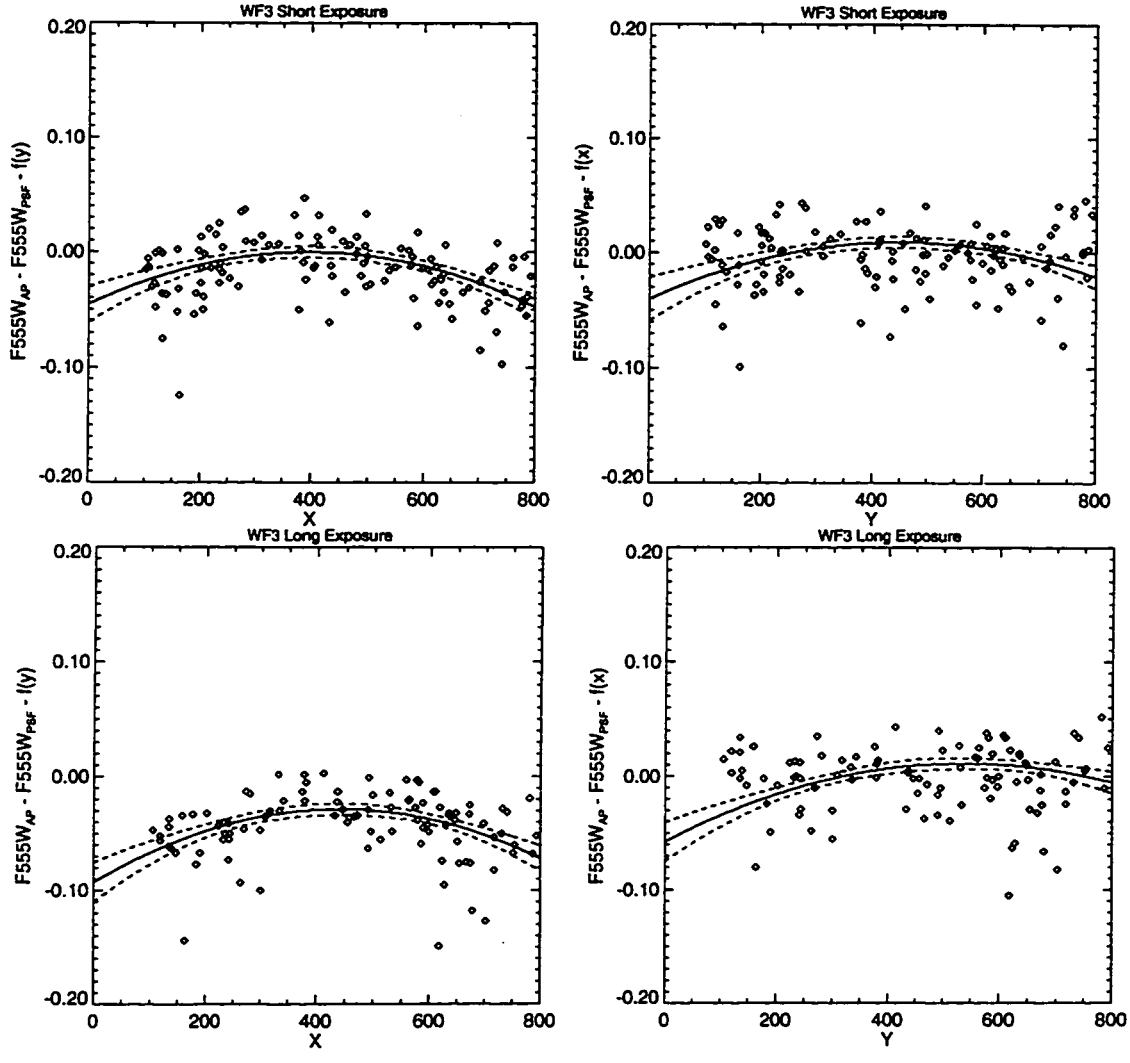

Figure 2.4h: Aperture corrections in the WF3 frame of the NGC 1916 field.

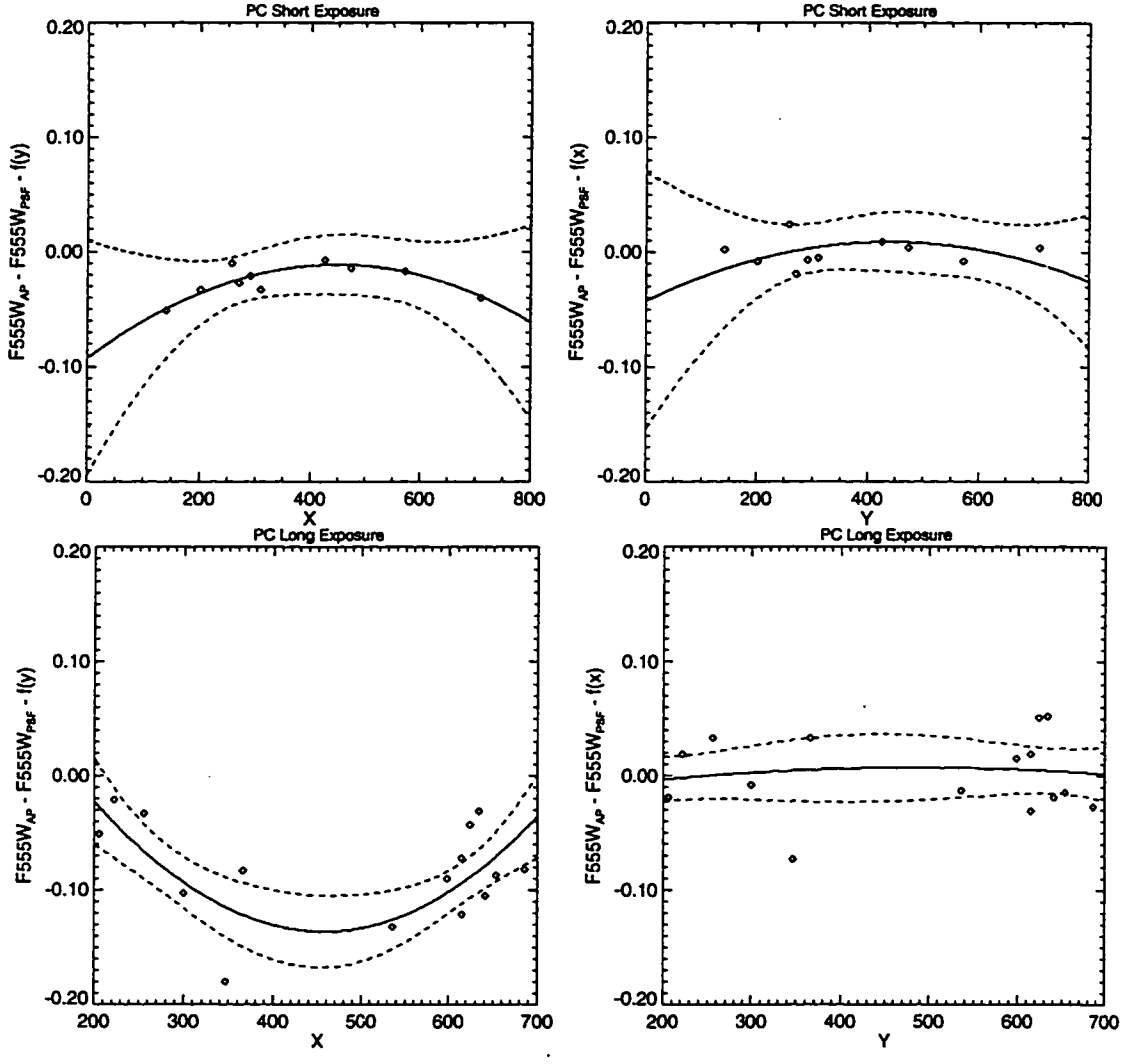

Figure 2.4i: Aperture corrections in the PC frame of the NGC 2005 field.

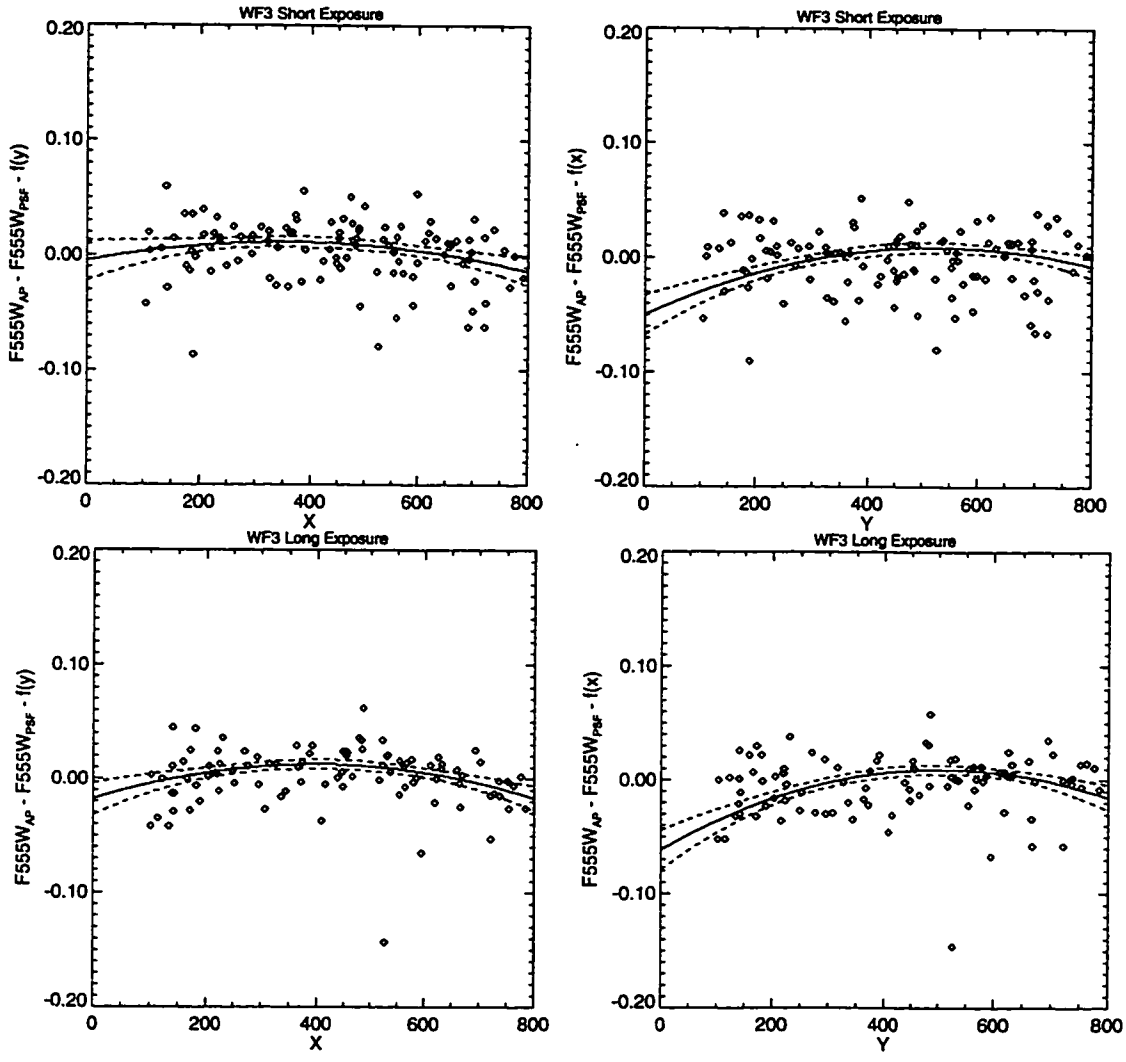

Figure 2.4j: Aperture corrections in the WF3 frame of the NGC 2005 field.

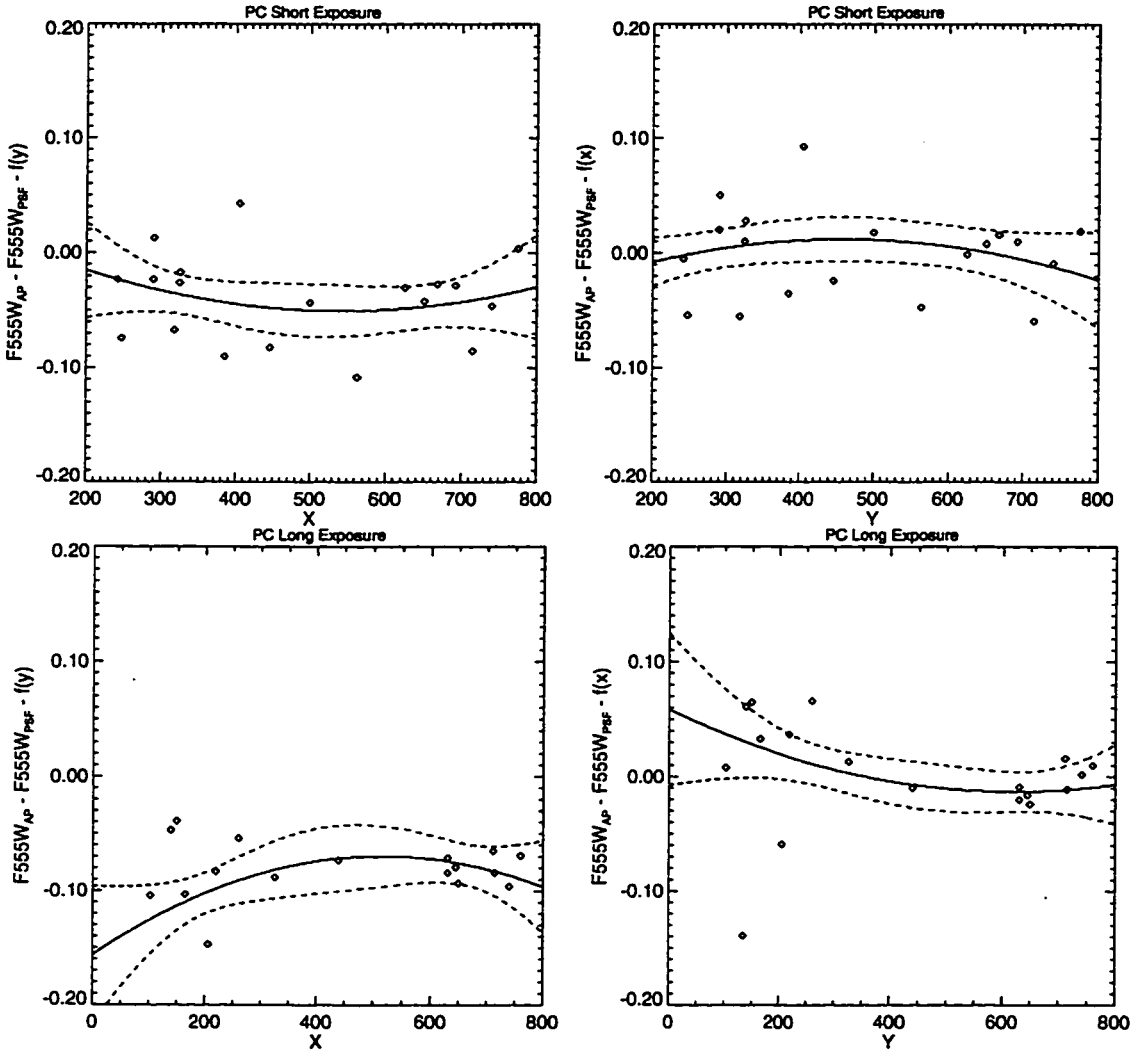

Figure 2.4k: Aperture corrections in the PC frame of the NGC 2019 field.

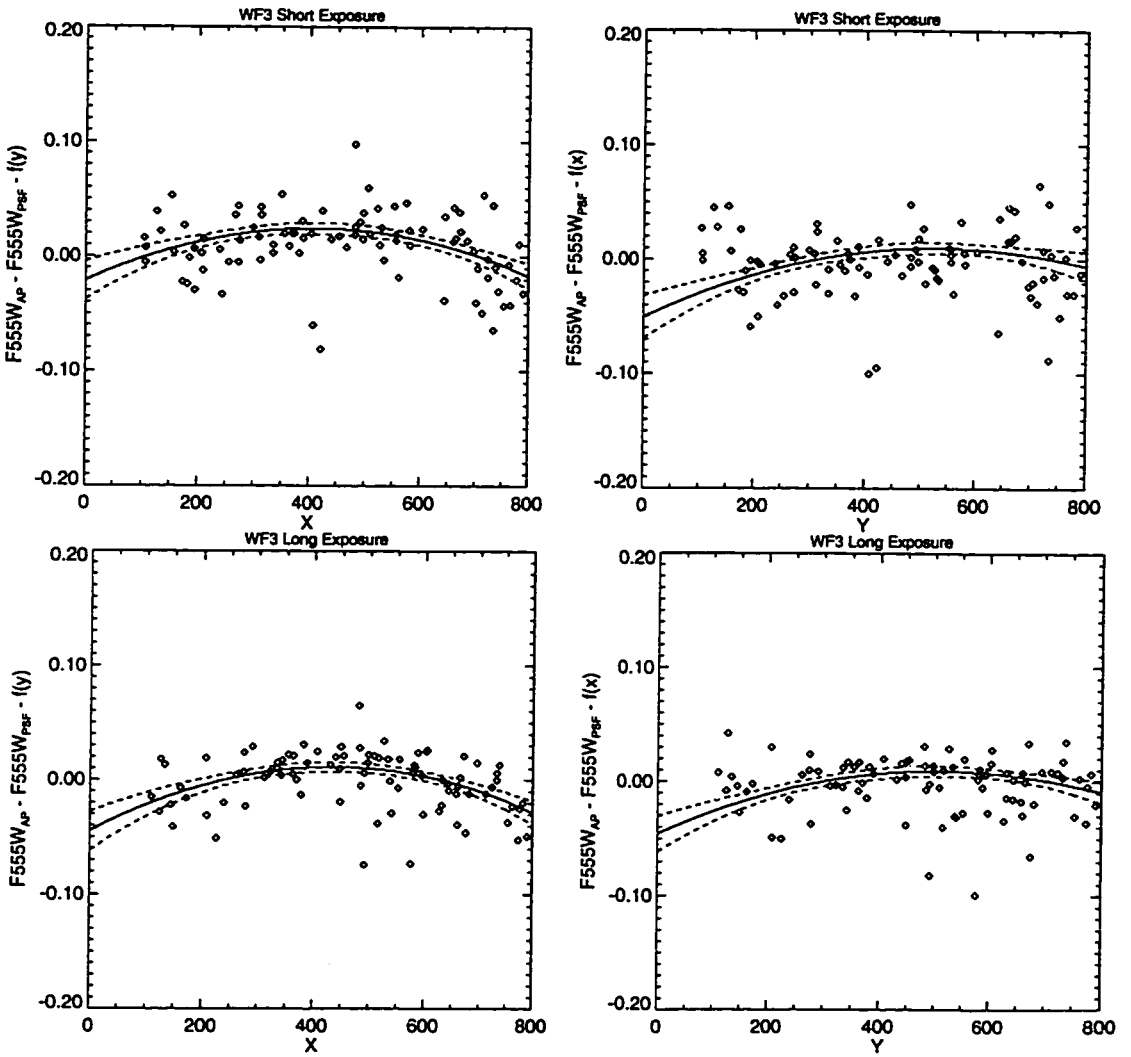

Figure 2.4l: Aperture corrections in the WF3 frame of the NGC 2019 field.

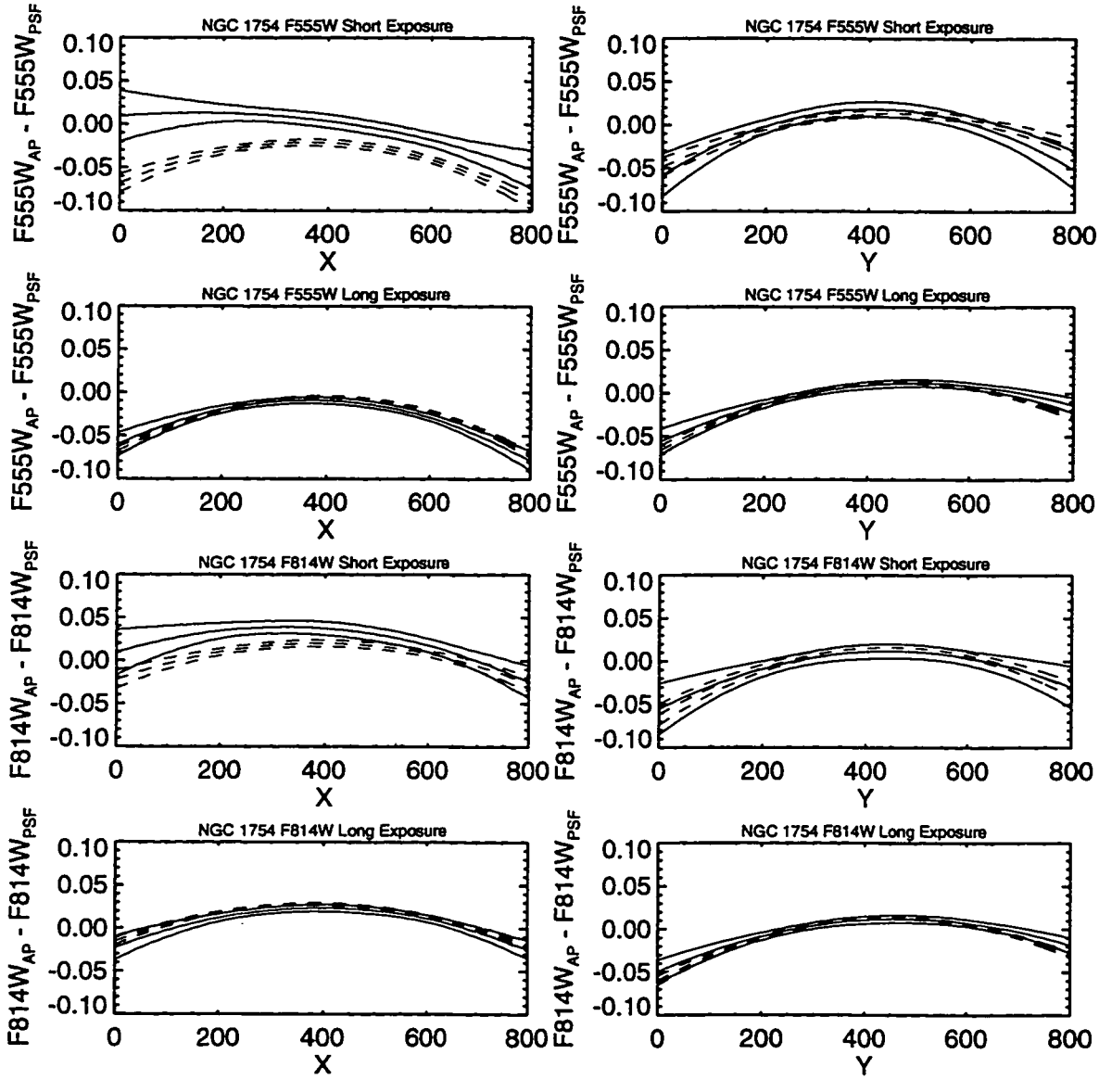

Figure 2.5a: Comparison of the aperture correction surfaces generated using Stetson's PSFs (dashed lines) with those derived from our WF2 frames (solid lines) for the NGC 1754 field, showing the generally good agreement between the two. Both the 2nd order polynomial fits to the surfaces and the 1σ deviations are shown.

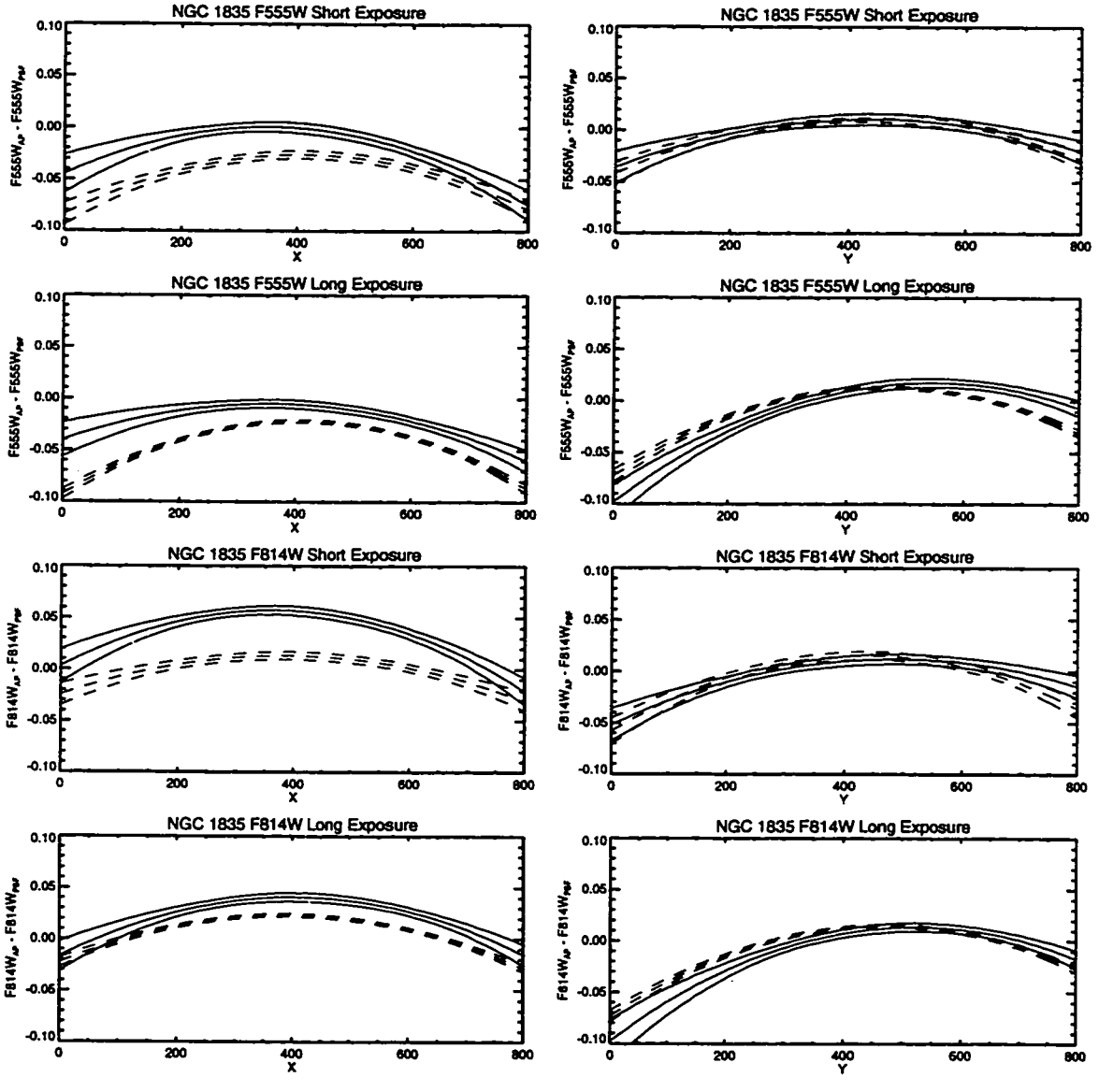

Figure 2.5b: Comparison of the aperture correction surfaces generated using Stetson's PSFs with those derived from our WF2 frames for the NGC 1835 field.

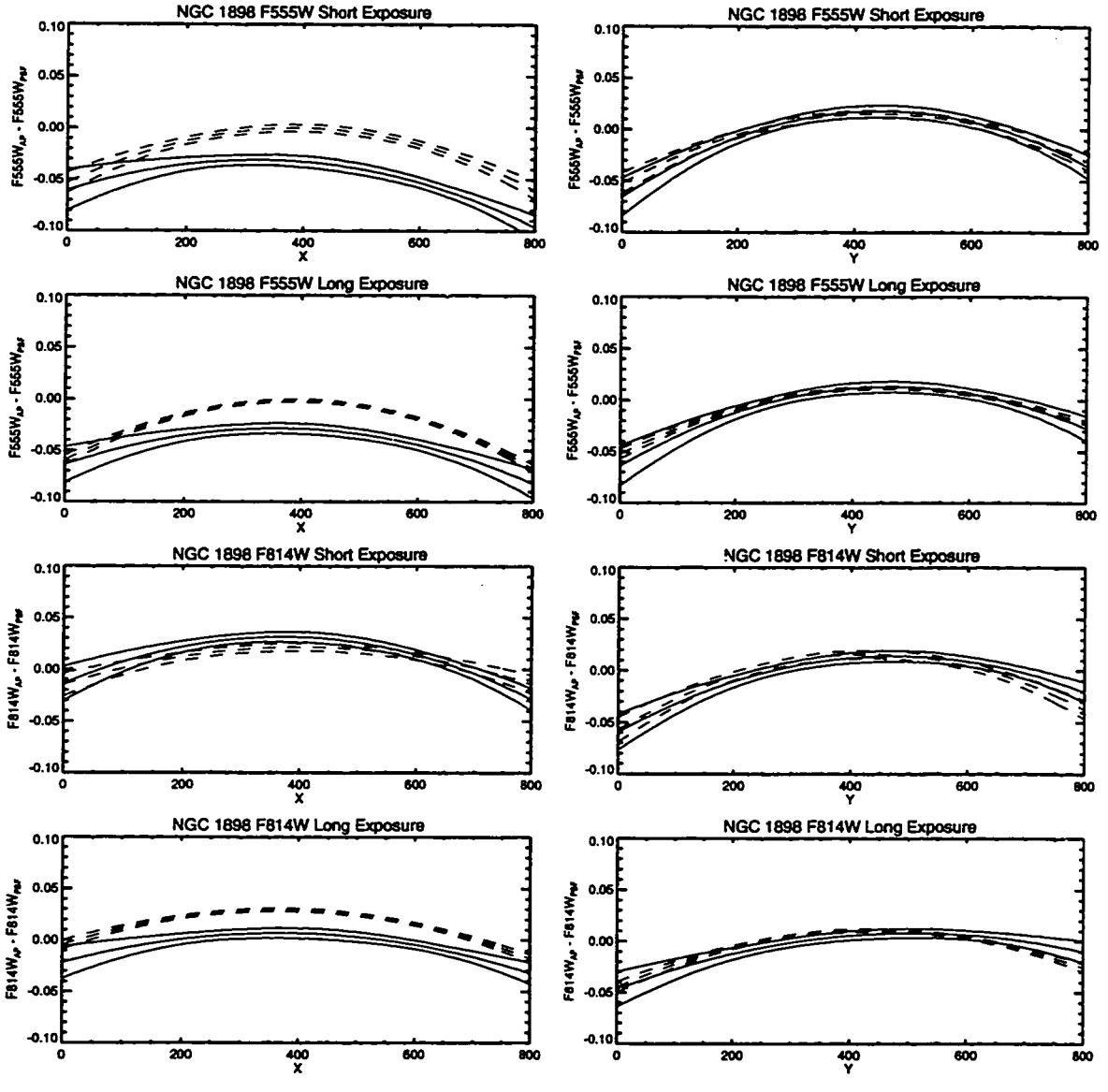

Figure 2.5c: Comparison of the aperture correction surfaces generated using Stetson's PSFs with those derived from our WF2 frames for the NGC 1898 field.

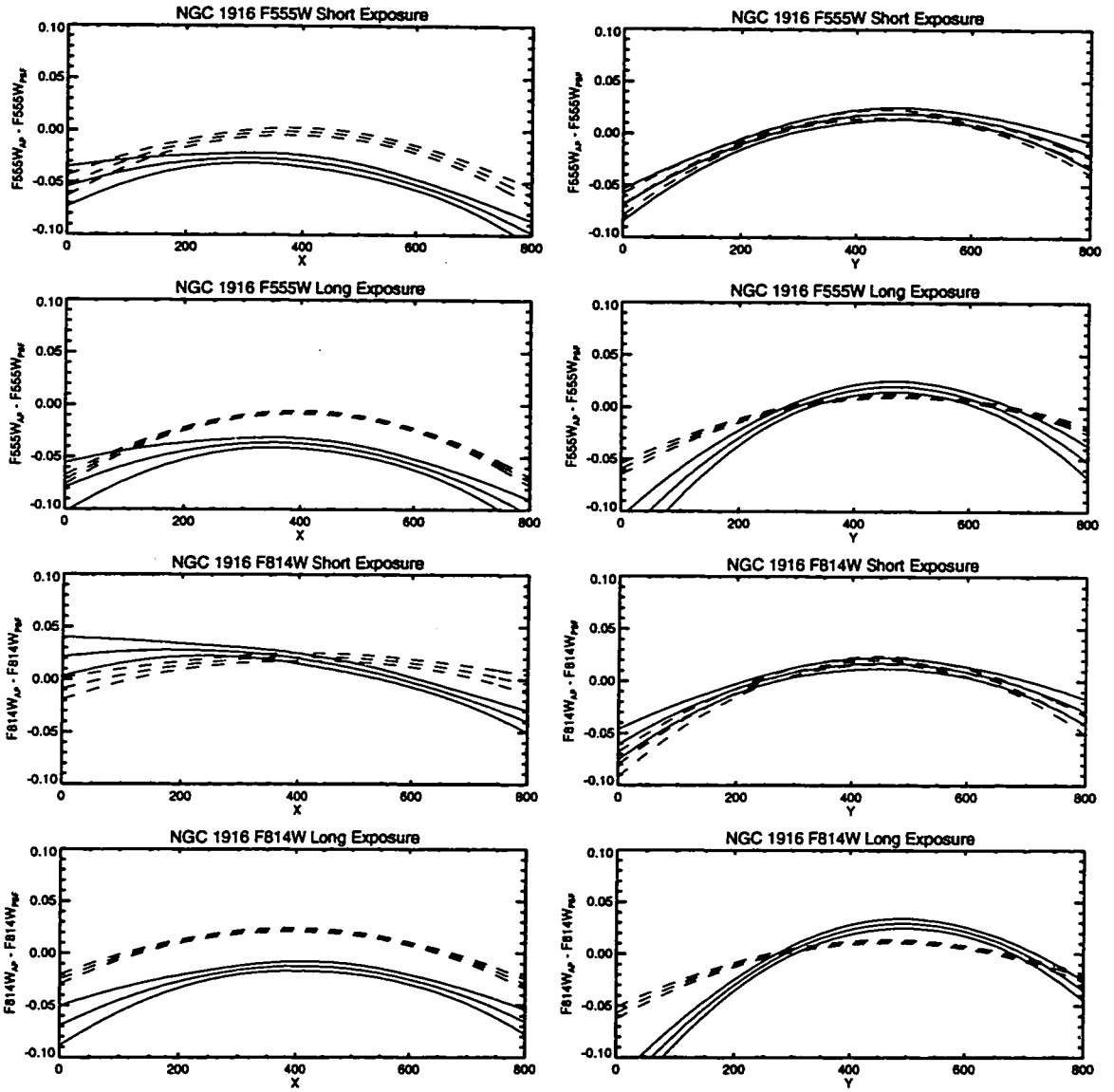

Figure 2.5d: Comparison of the aperture correction surfaces generated using Stetson's PSFs with those derived from our WF2 frames for the NGC 1916 field.

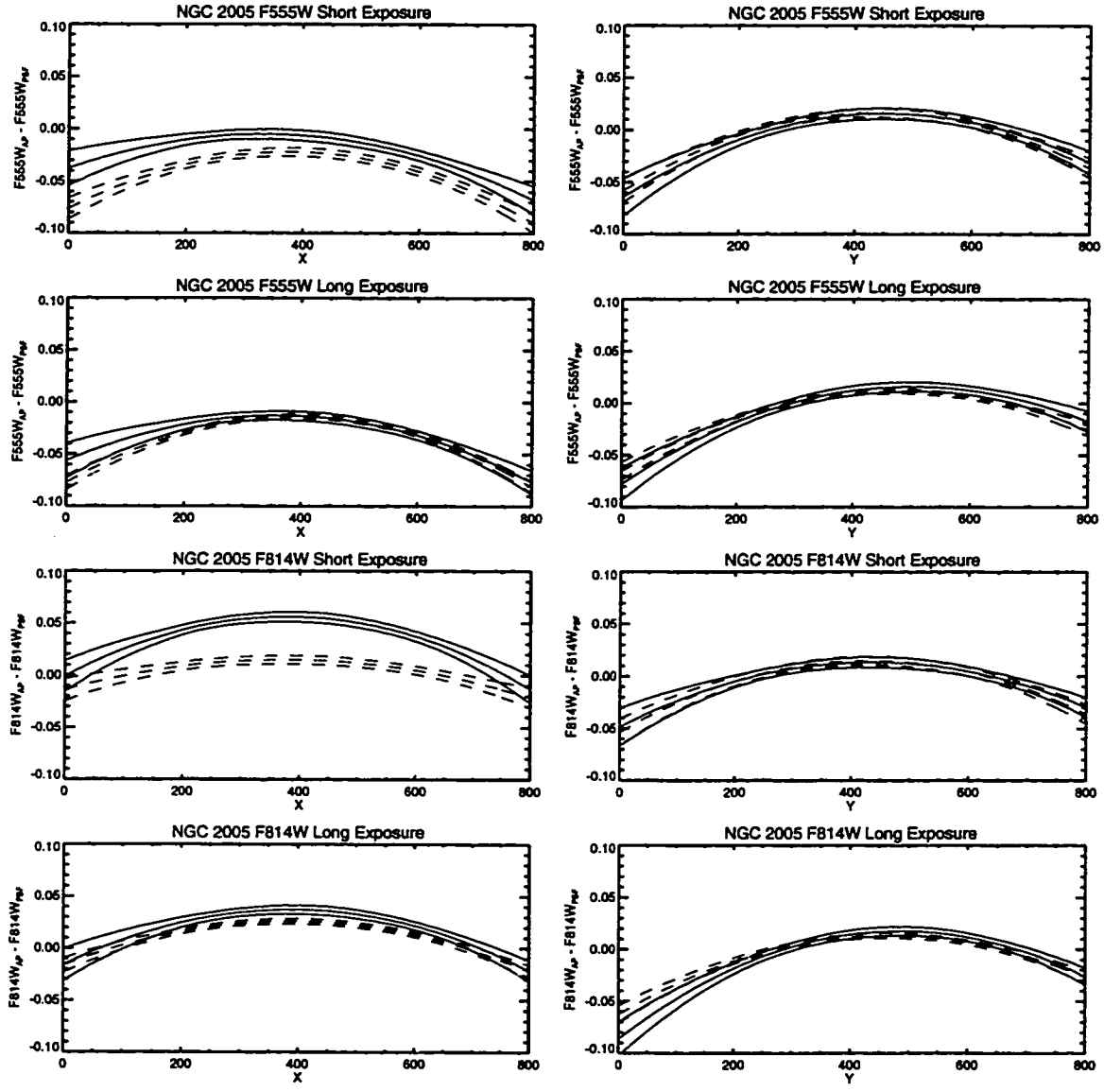

Figure 2.5e: Comparison of the aperture correction surfaces generated using Stetson's PSFs with those derived from our WF2 frames for the NGC 2005 field.

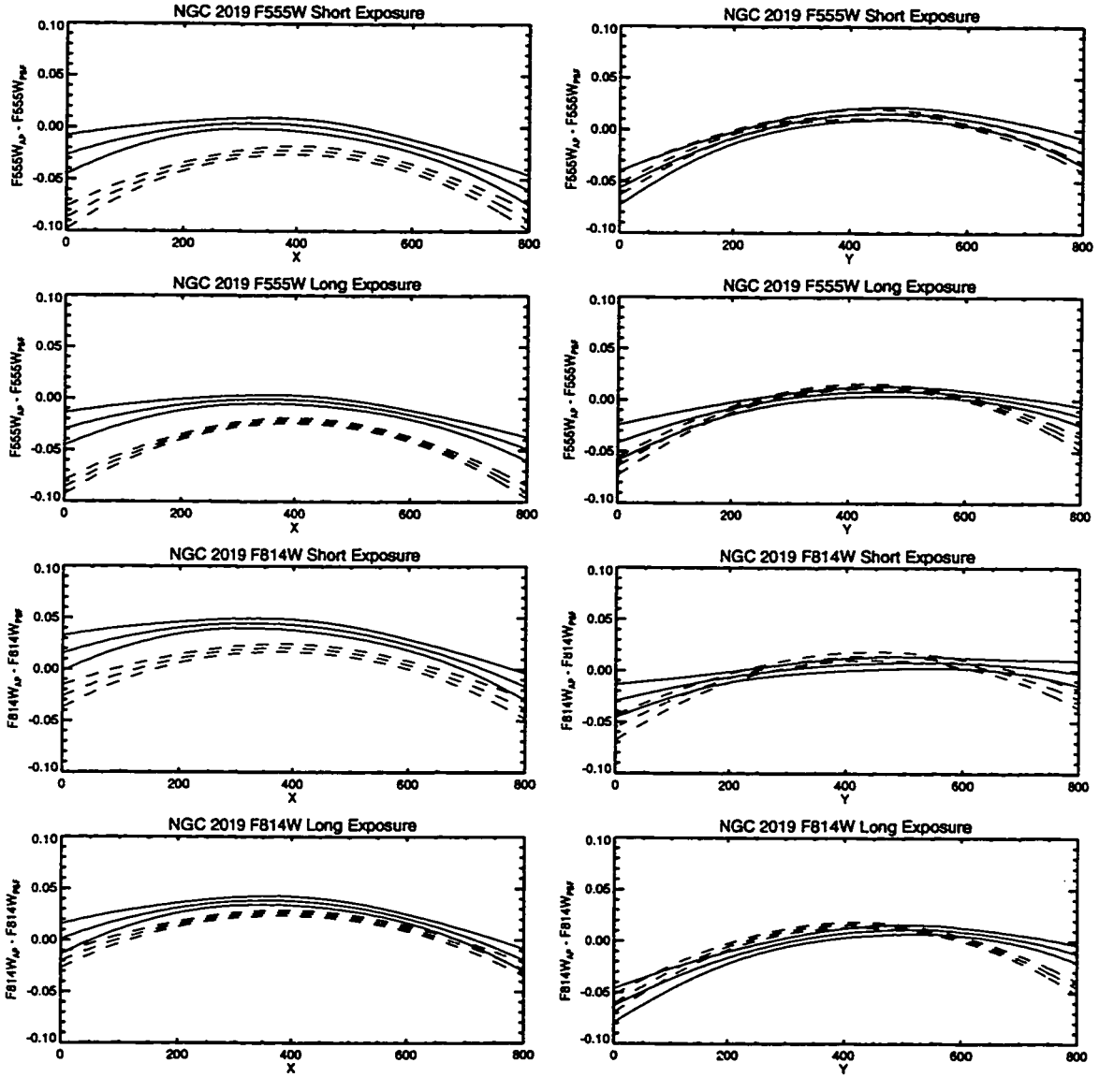

Figure 2.5f: Comparison of the aperture correction surfaces generated using Stetson's PSFs with those derived from our WF2 frames for the NGC 2019 field.

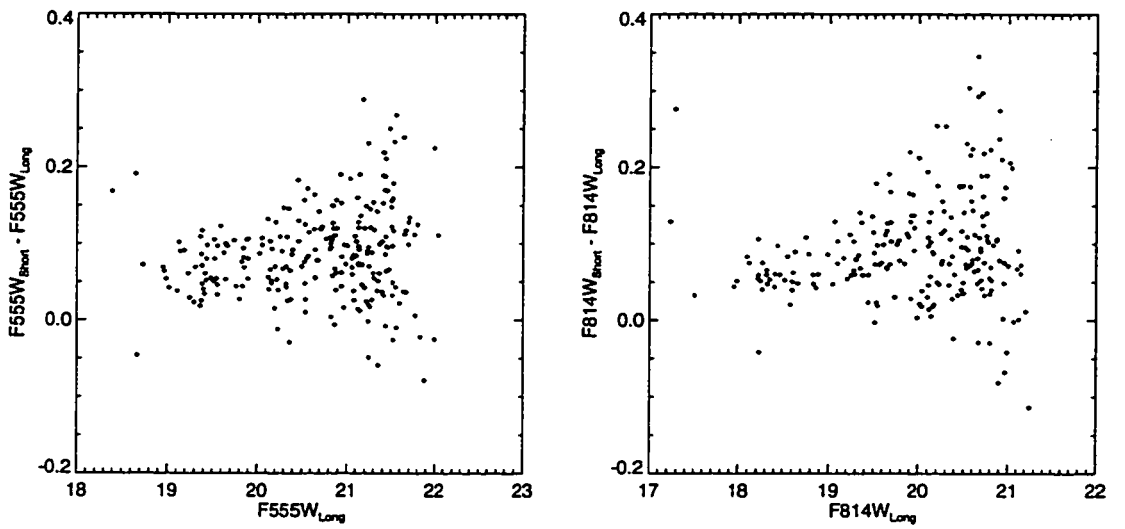

Figure 2.6a: Comparison of stellar magnitudes measured in the long (500, 600 s) WFPC2 exposures with the short (20 s) exposures of the NGC 1754 field, showing the CTE effect discussed by Whitmore & Heyer (1997).

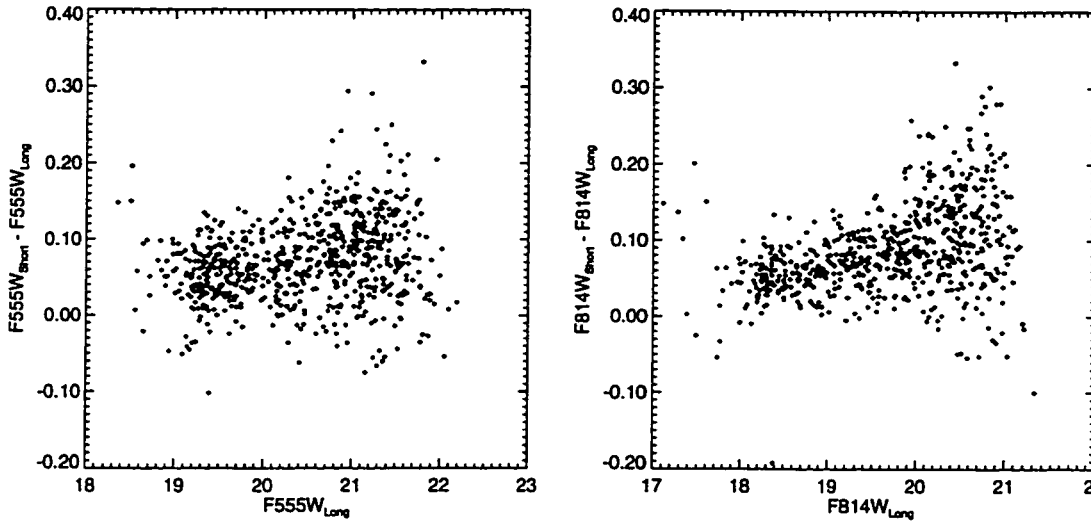

Figure 2.6b: CTE effect in NGC 1835 short exposure photometry.

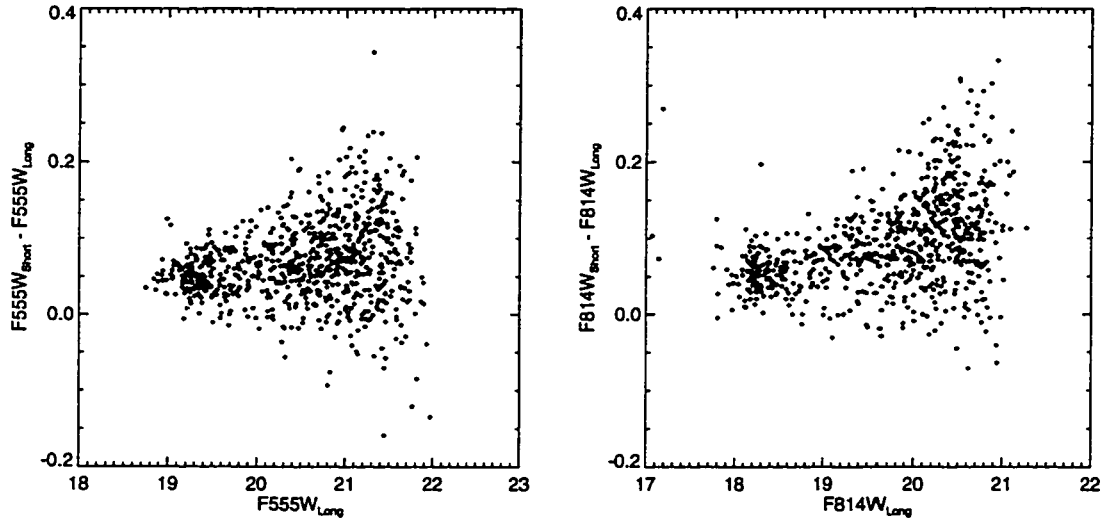

Figure 2.6c: CTE effect in NGC 1898 short exposure photometry.

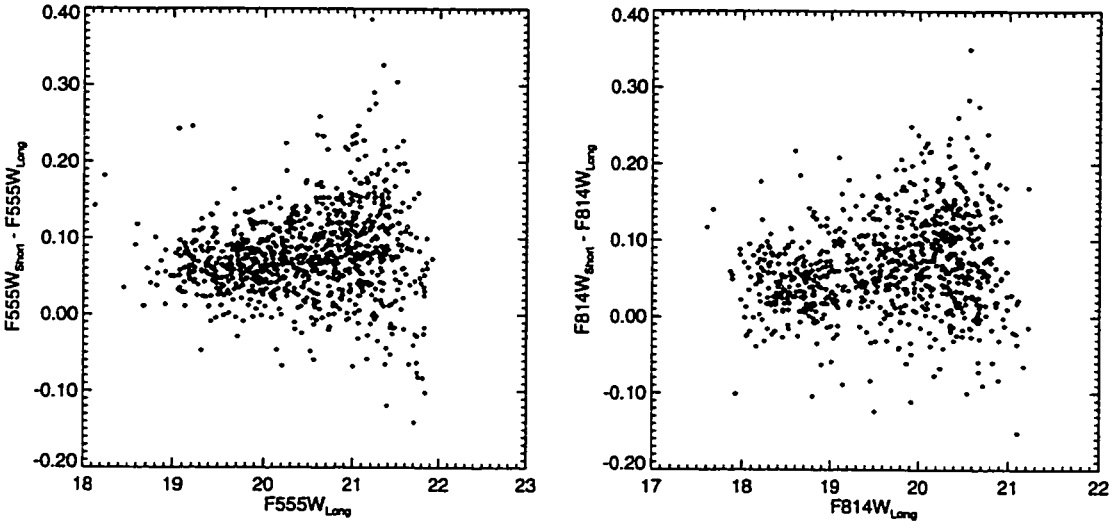

Figure 2.6d: CTE effect in NGC 1916 short exposure photometry.

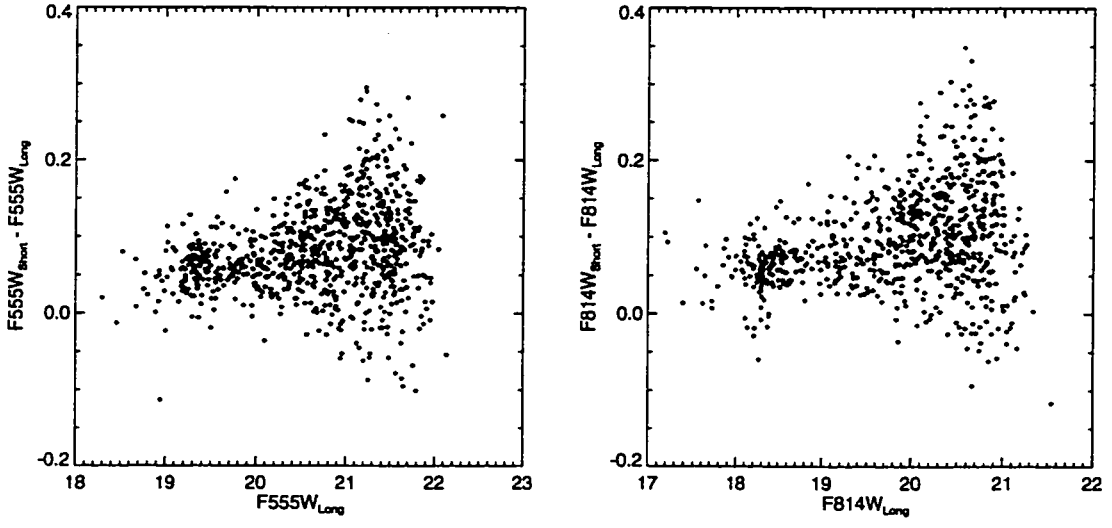

Figure 2.6e: CTE effect in NGC 2005 short exposure photometry.

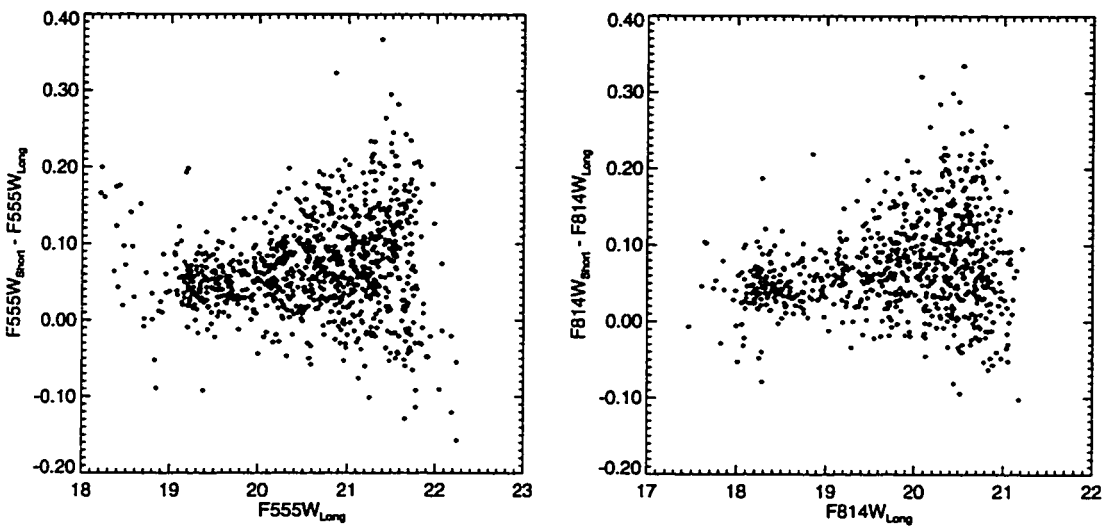

Figure 2.6f: CTE effect in NGC 2019 short exposure photometry.

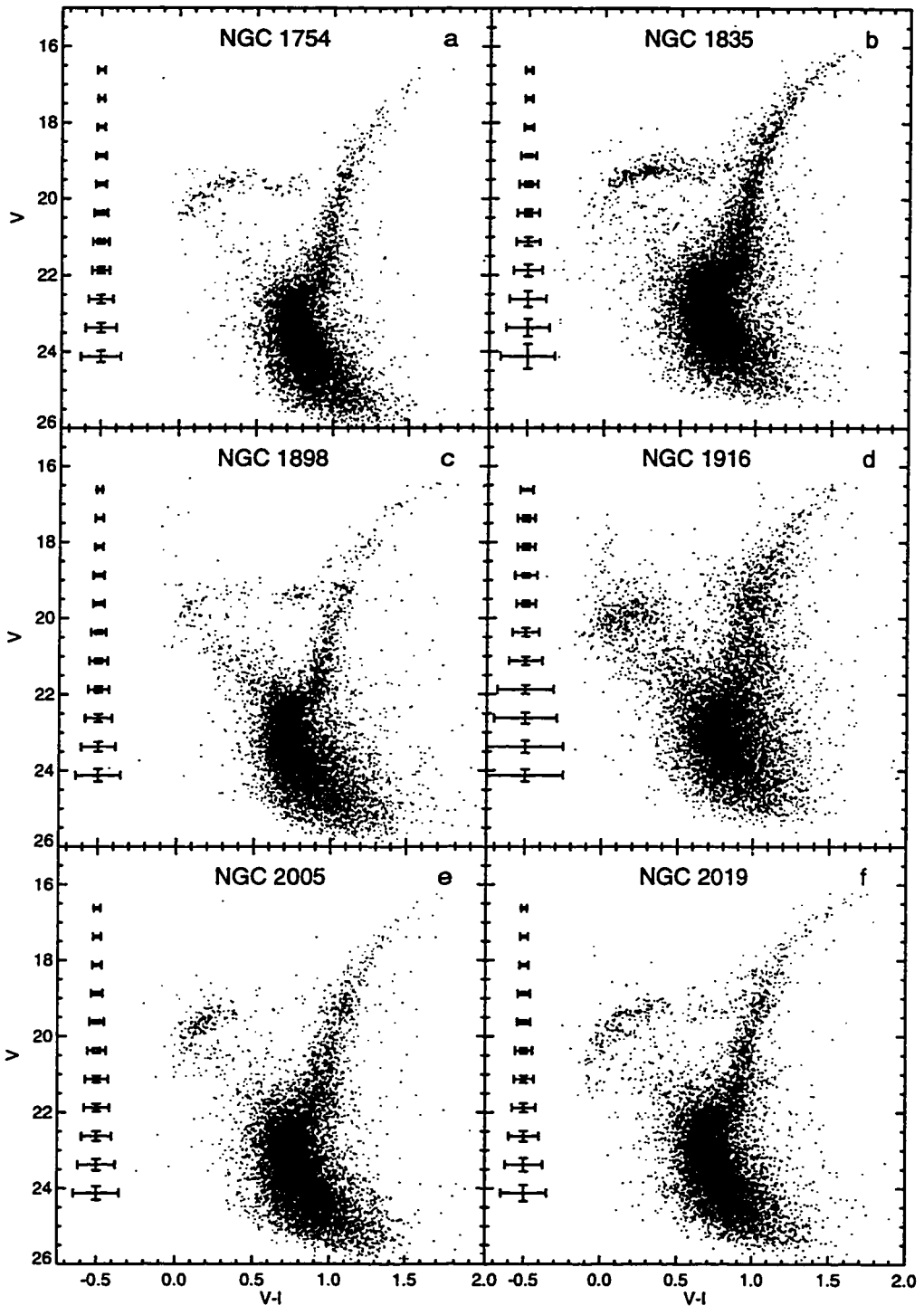

Figure 2.7: Color-magnitude diagrams of the PC frames of the six globular cluster fields. No field star subtraction or other selective removal of stars has been performed and the diagrams are uncorrected for reddening. The error bars are derived from the artificial star tests discussed in the text.

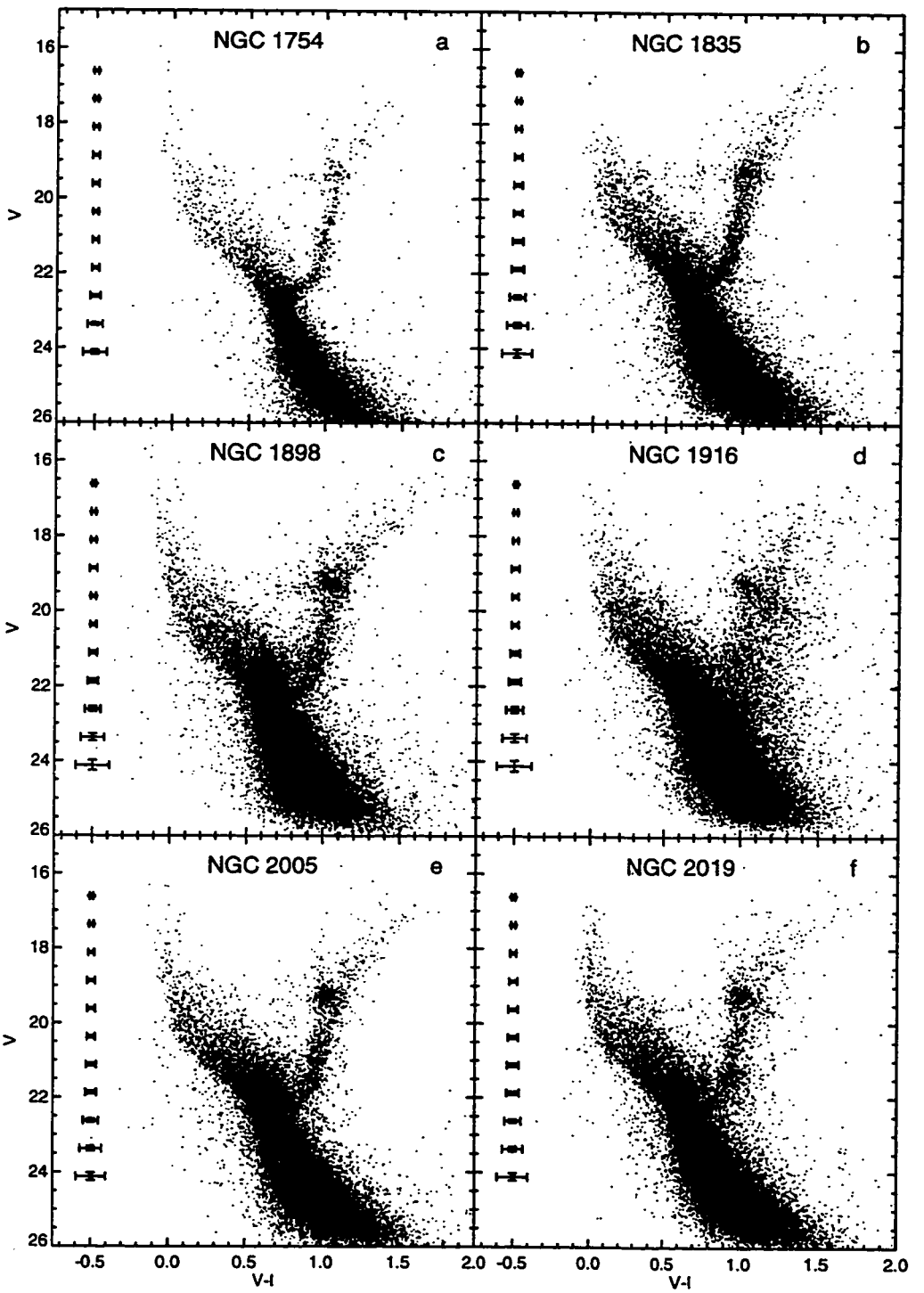

Figure 2.8: Color-magnitude diagrams of the combined WF frames of the six globular fields.

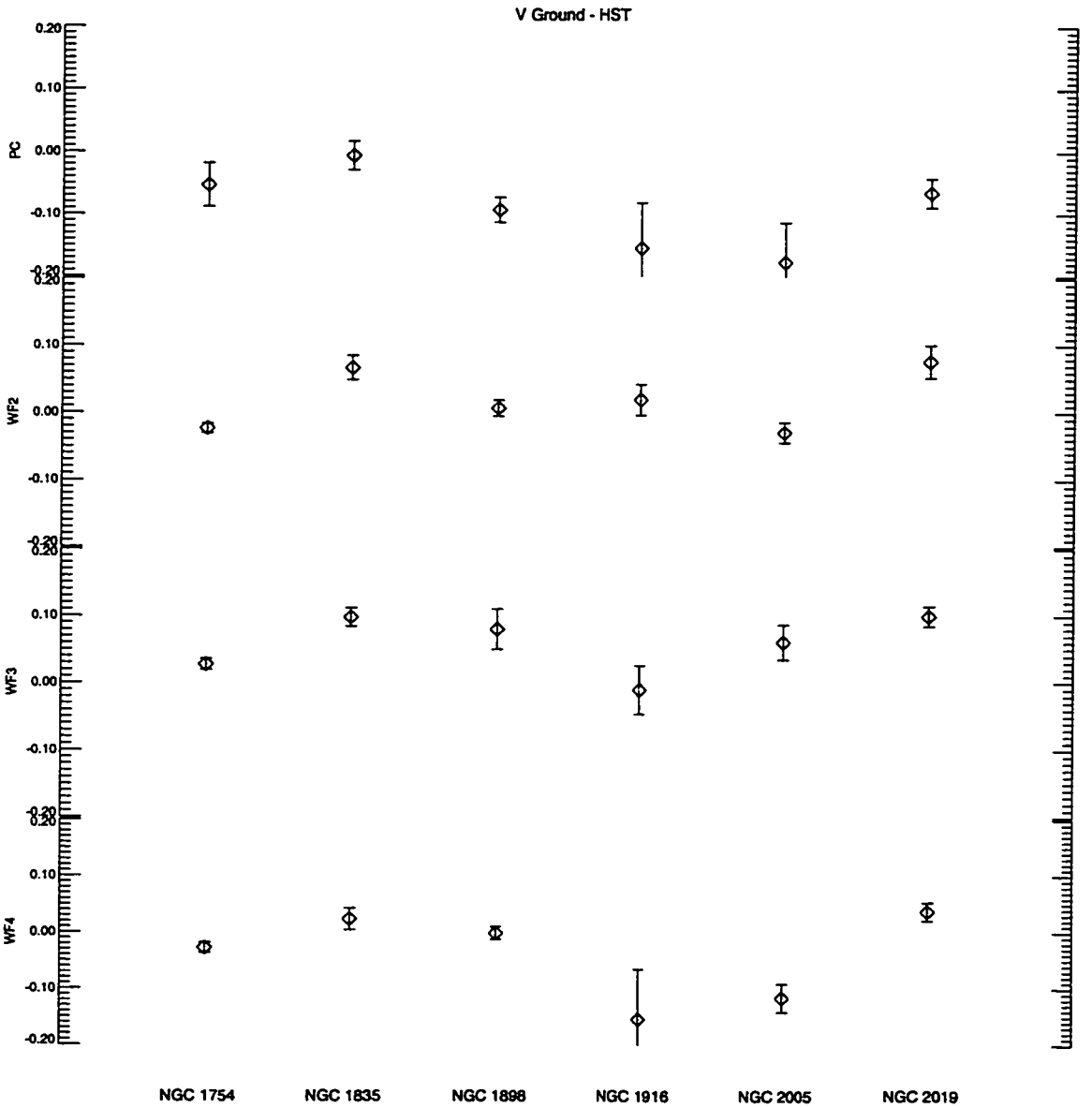

Figure 2.9a: Comparison of ground based photometry with WFPC2 photometry for four WFPC2 frames, all six fields, and F555W filter. The magnitude differences are plotted in the sense $V_{\mathrm{ground}} - V_{HST}$. Figures *a* and *b* show a clear correlation between the magnitude difference and the cluster in which it was measured, independent of chip and filter used.

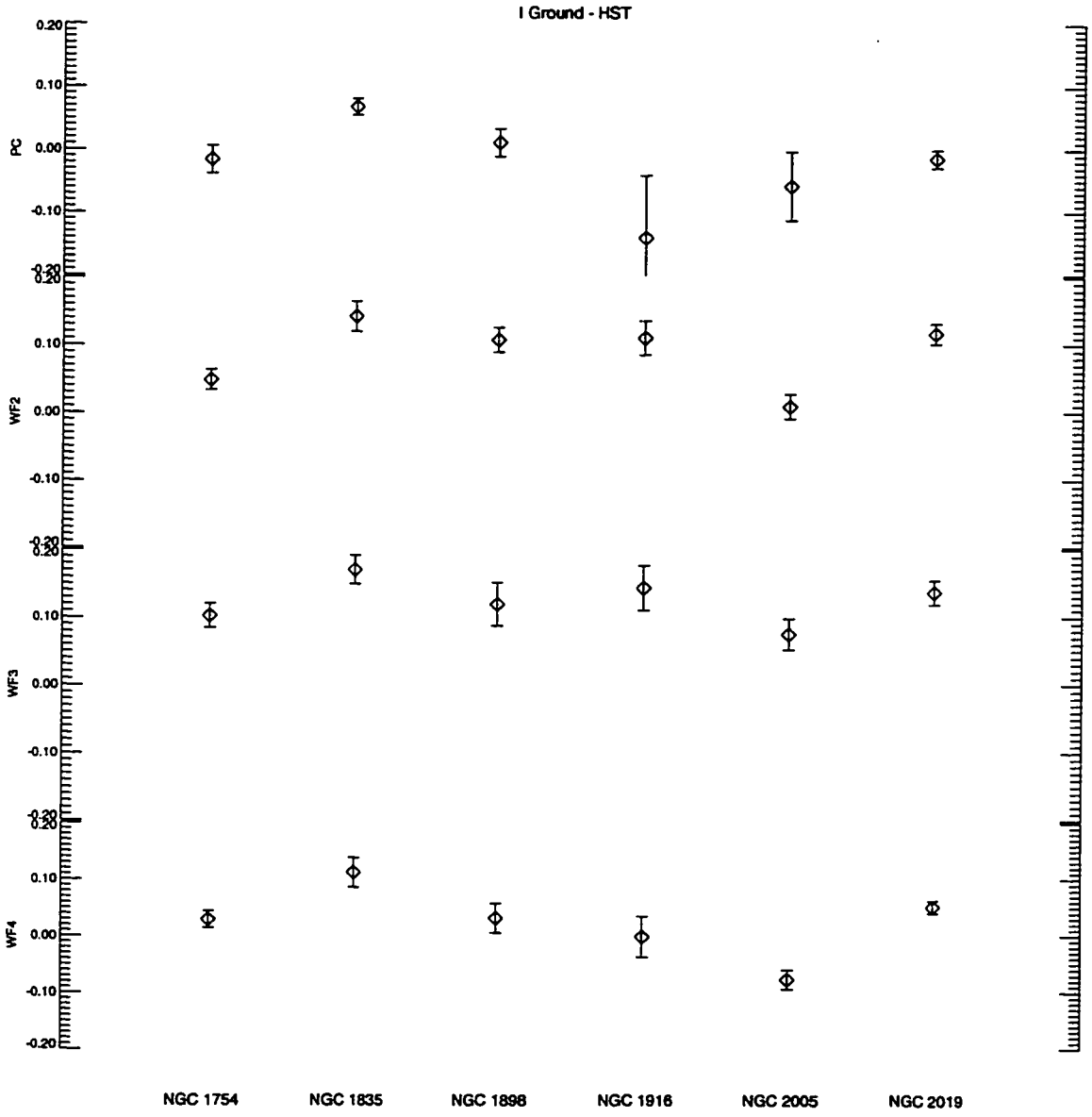

Figure 2.9b: Comparison of ground based photometry with WFPC2 photometry for F814W filter.

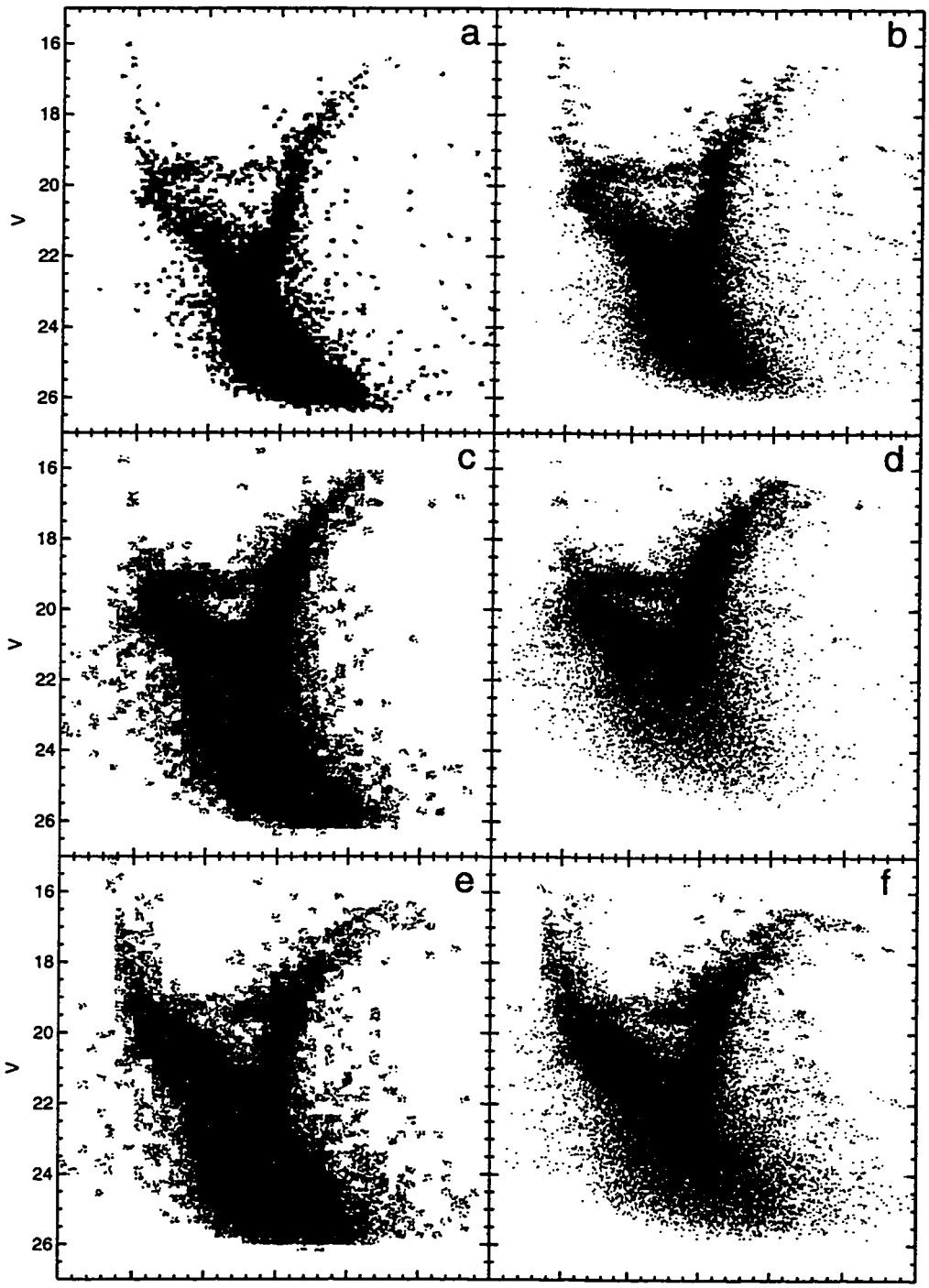

Figure 2.10: Input artificial star distributions (*a*, *c*, and *e*) used in the tests discussed in the text and the color-magnitude diagrams recovered after addition to and processing through the WFPC2 images (*b*, *d*, and *f*). Distributions shown are for the NGC 1754, NGC 1835, and NGC 1898 fields.

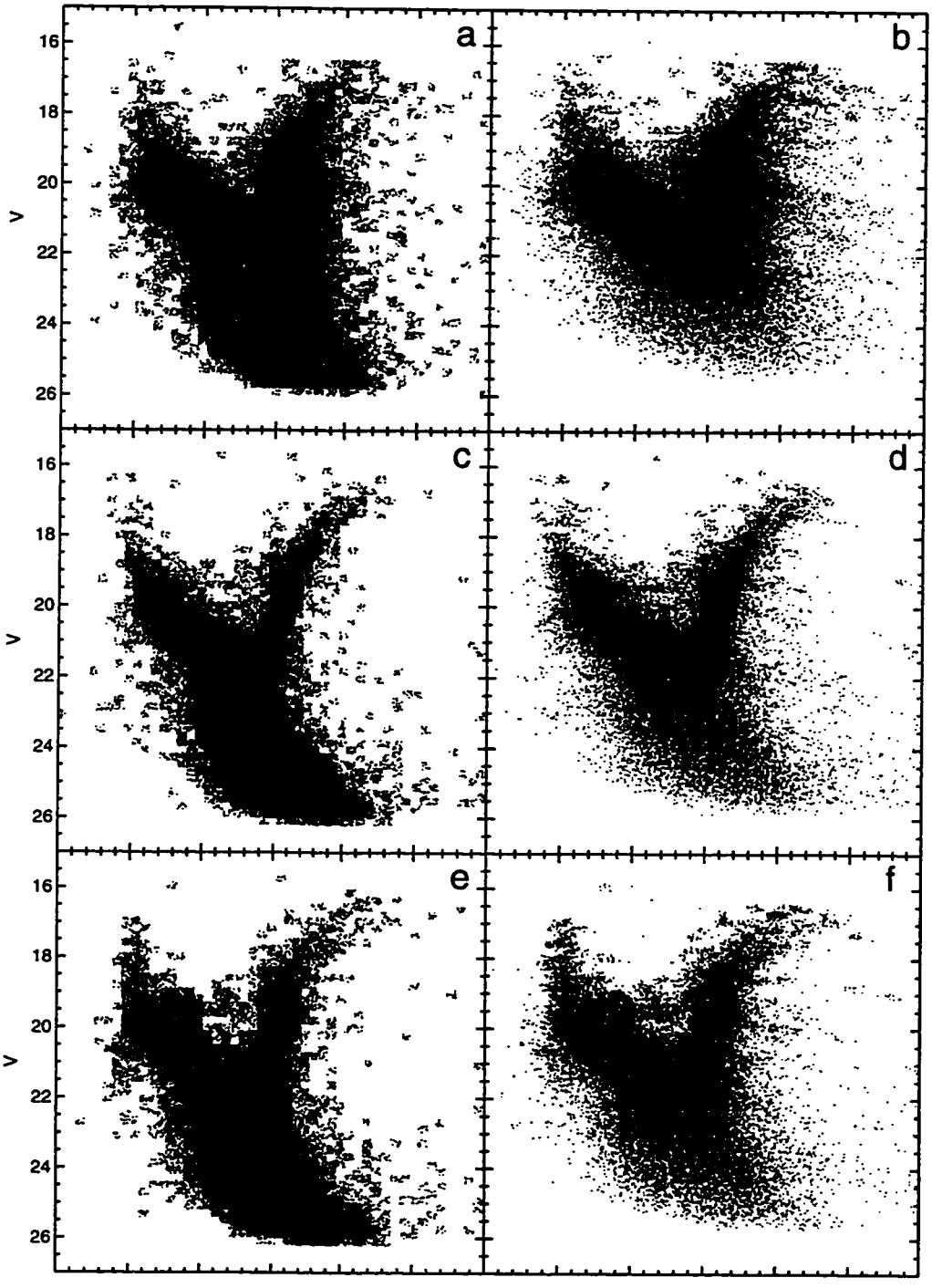

Figure 2.11: Input and recovered artificial star distributions for the NGC 1916, NGC 2005, and NGC 2019 fields.

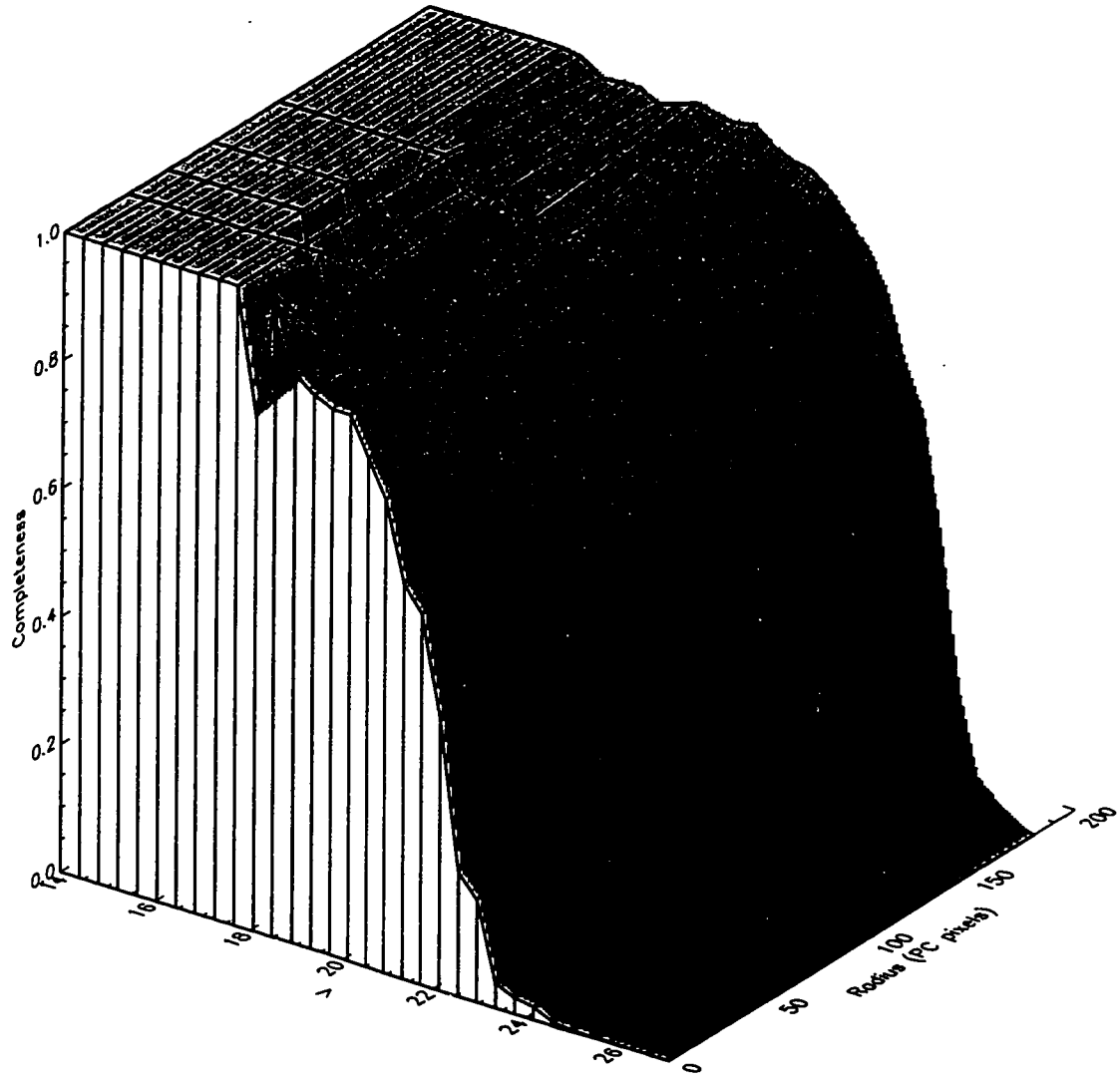

Figure 2.12a: Completeness as a function of V and radius from the cluster center for NGC 1754. The gray shadings are levels of constant completeness fraction. At bright V magnitudes, the completeness has been set to 1 where no artificial stars were placed to calculate the completeness.

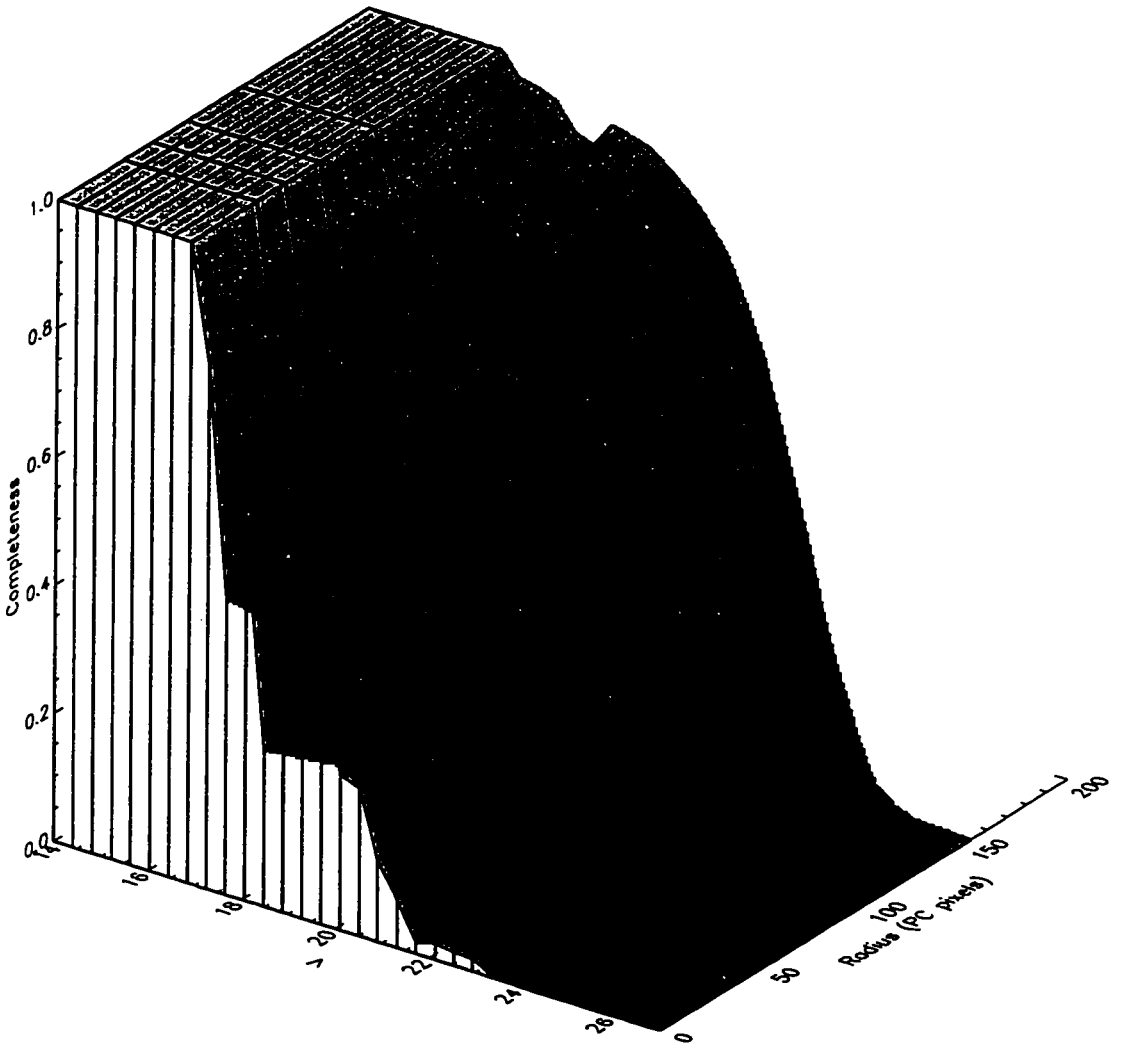

Figure 2.12b: Completeness as a function of V and radius from the cluster center for NGC 1835.

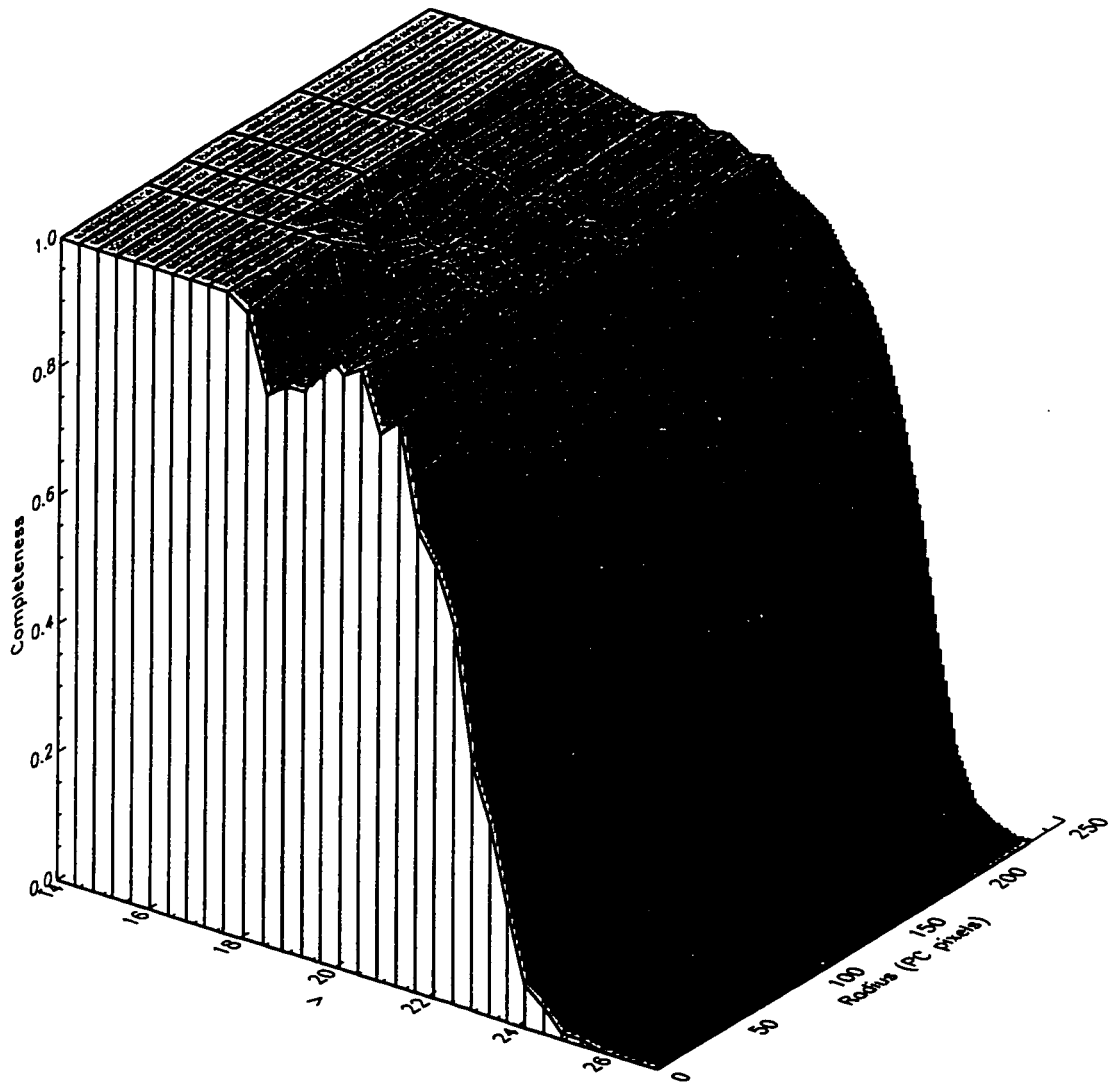

Figure 2.12c: Completeness as a function of V and radius from the cluster center for NGC 1898.

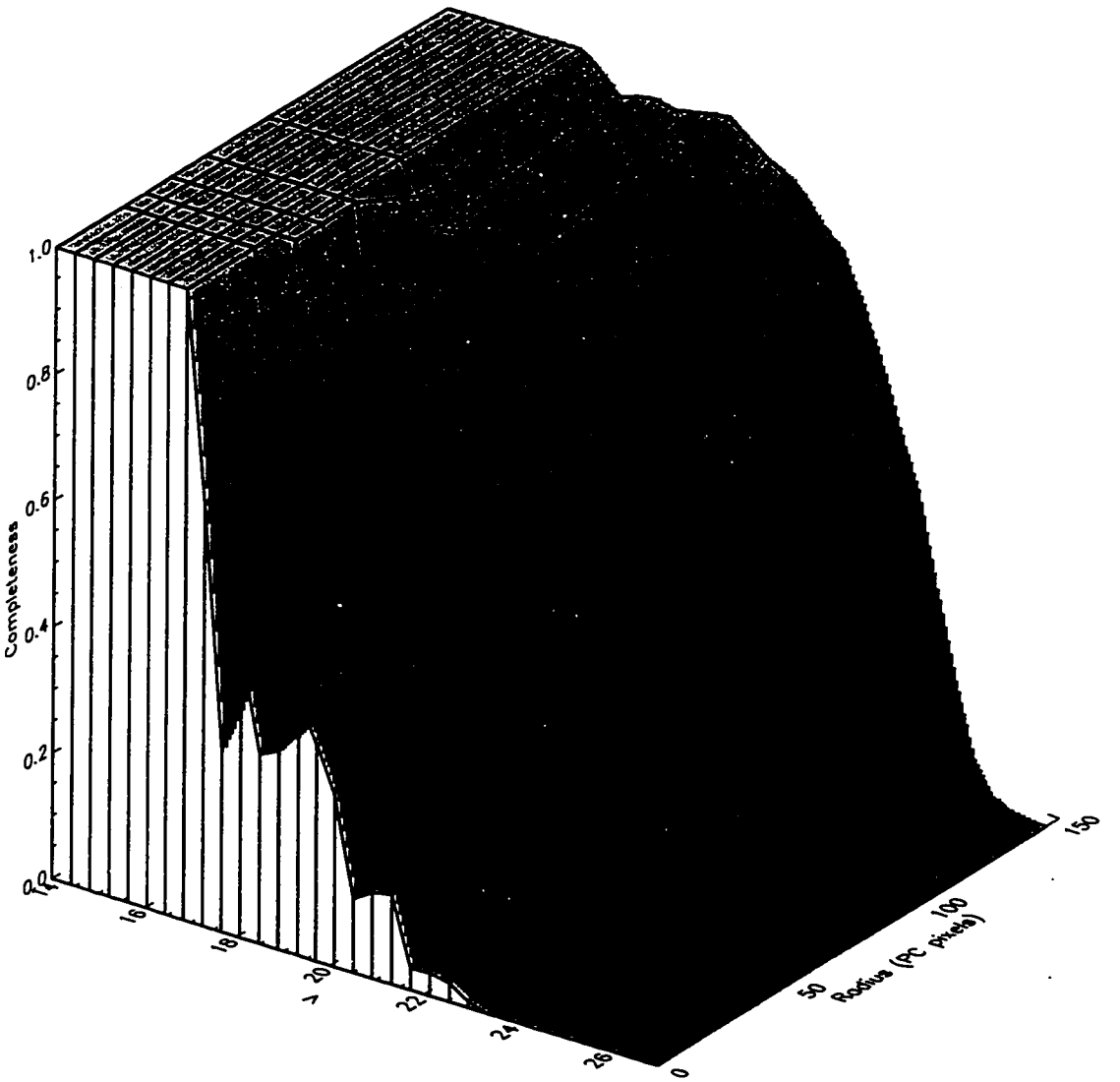

Figure 2.12d: Completeness as a function of V and radius from the cluster center for NGC 2005.

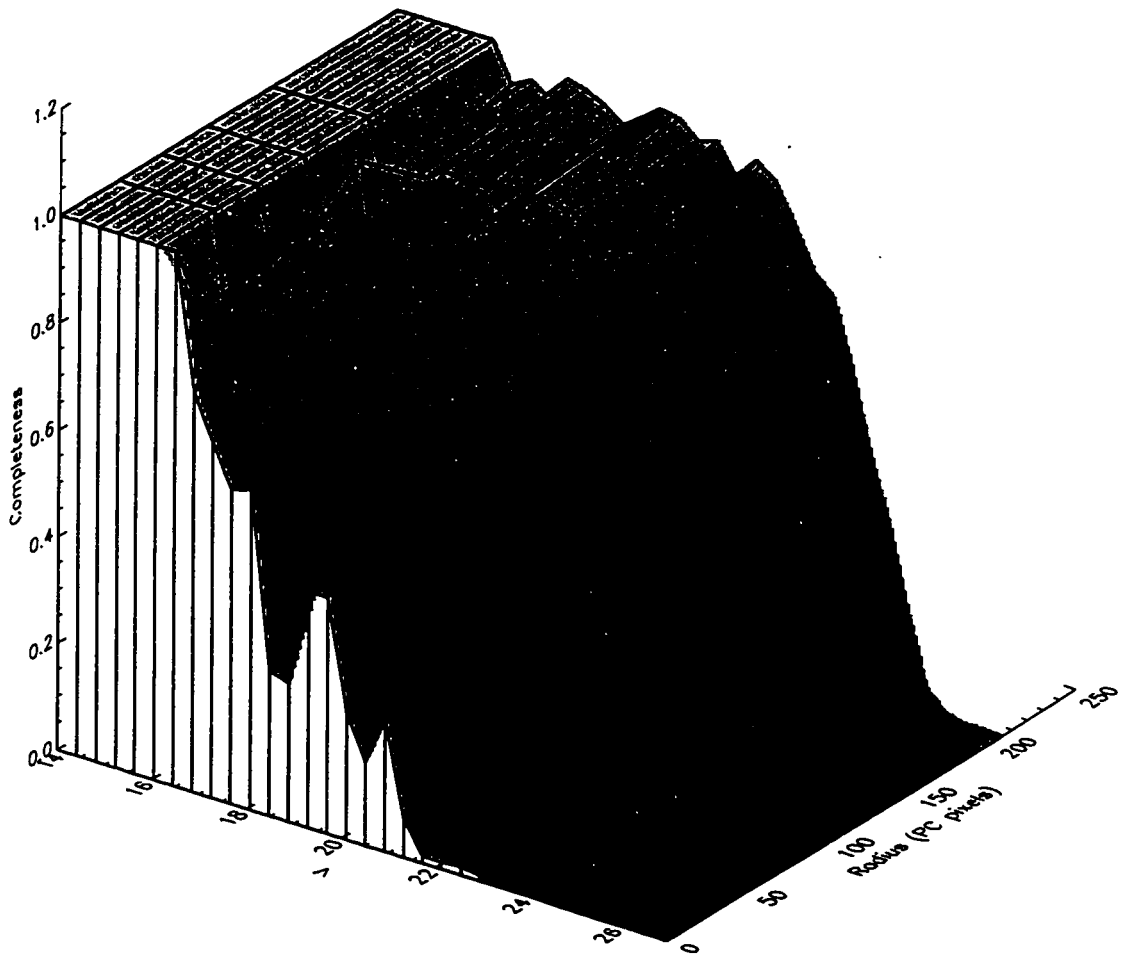

Figure 2.12e: Completeness as a function of V and radius from the cluster center for NGC 2019.

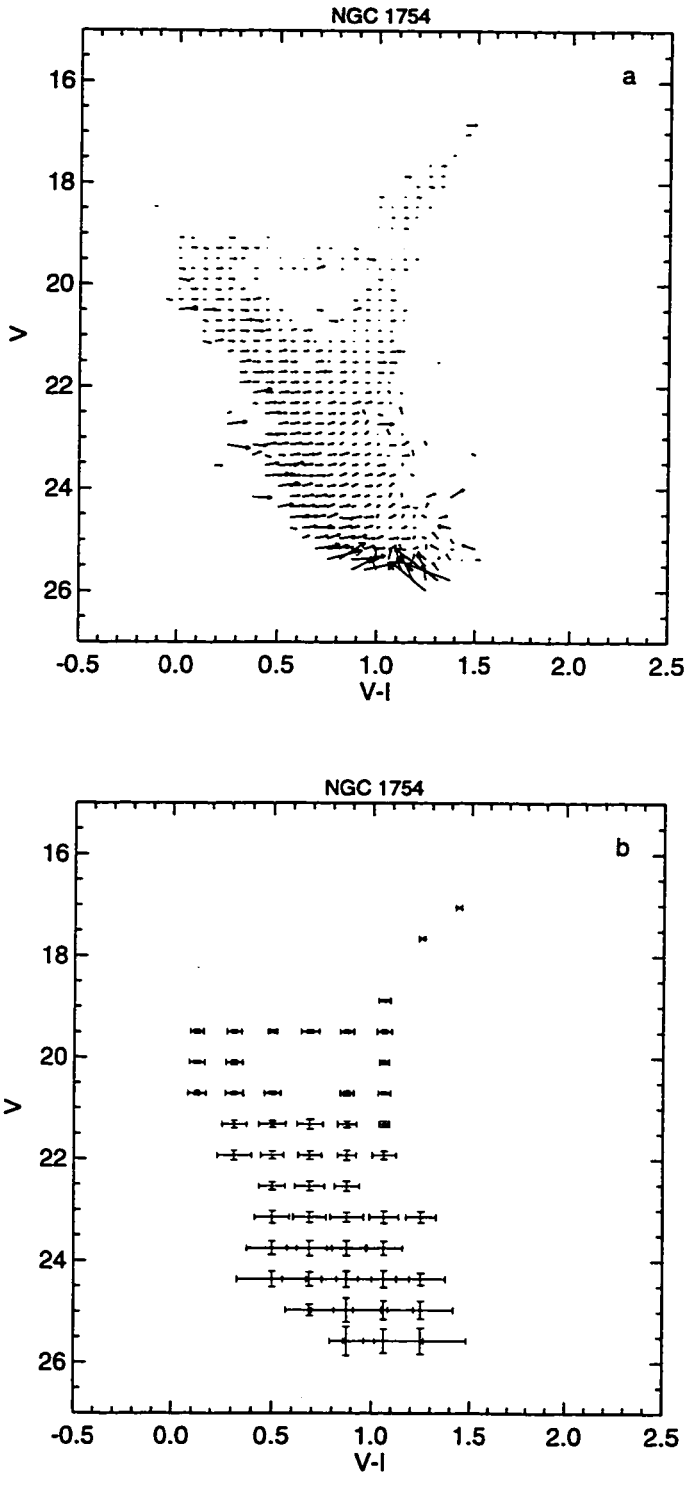

Figure 2.13a: Systematic and random photometric errors calculated through artificial star tests for the case of NGC 1754. In (*a*), the arrows show the mean direction and distance over which stars originating in the bin at the tail of the arrow drifted in the color-magnitude plane. In (*b*), the error bars show the 1σ robust standard deviations of the recovered colors and magnitudes of the artificial stars in each bin.

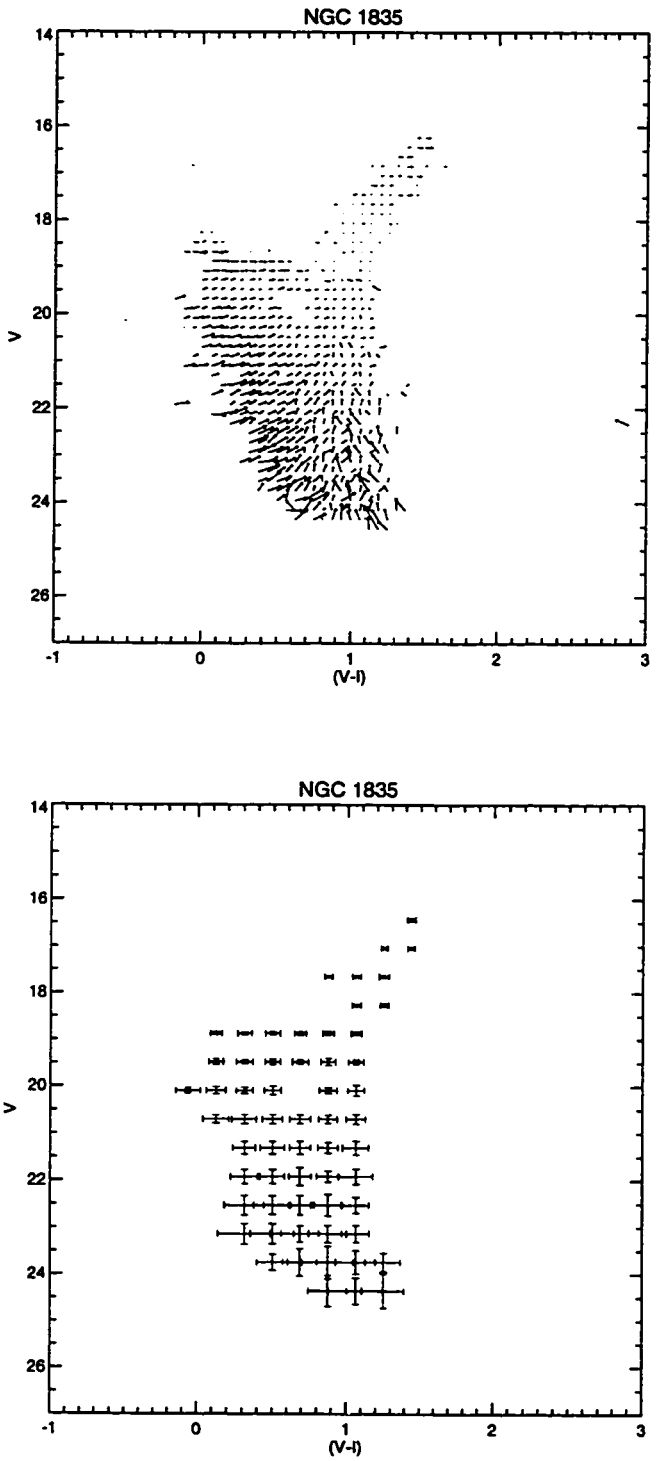

Figure 2.13b: Systematic and random photometric errors for NGC 1835.

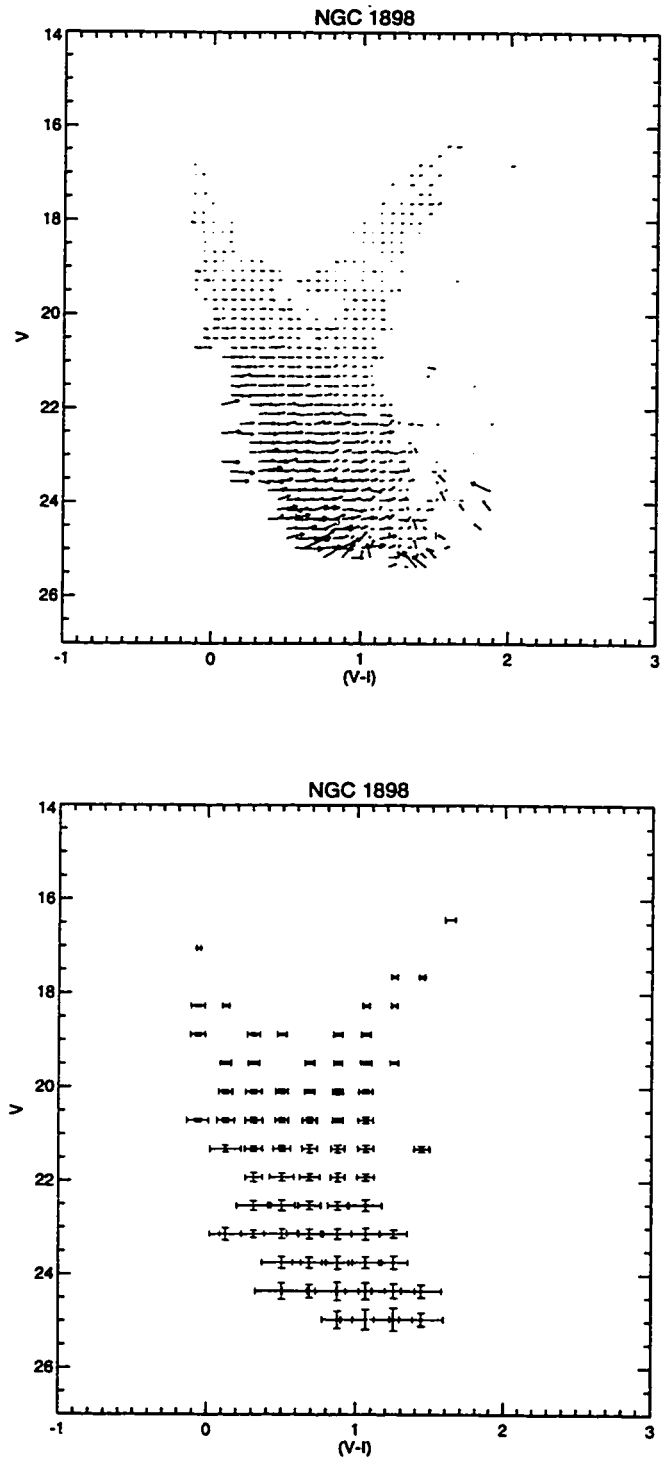

Figure 2.13c: Systematic and random photometric errors for NGC 1898.

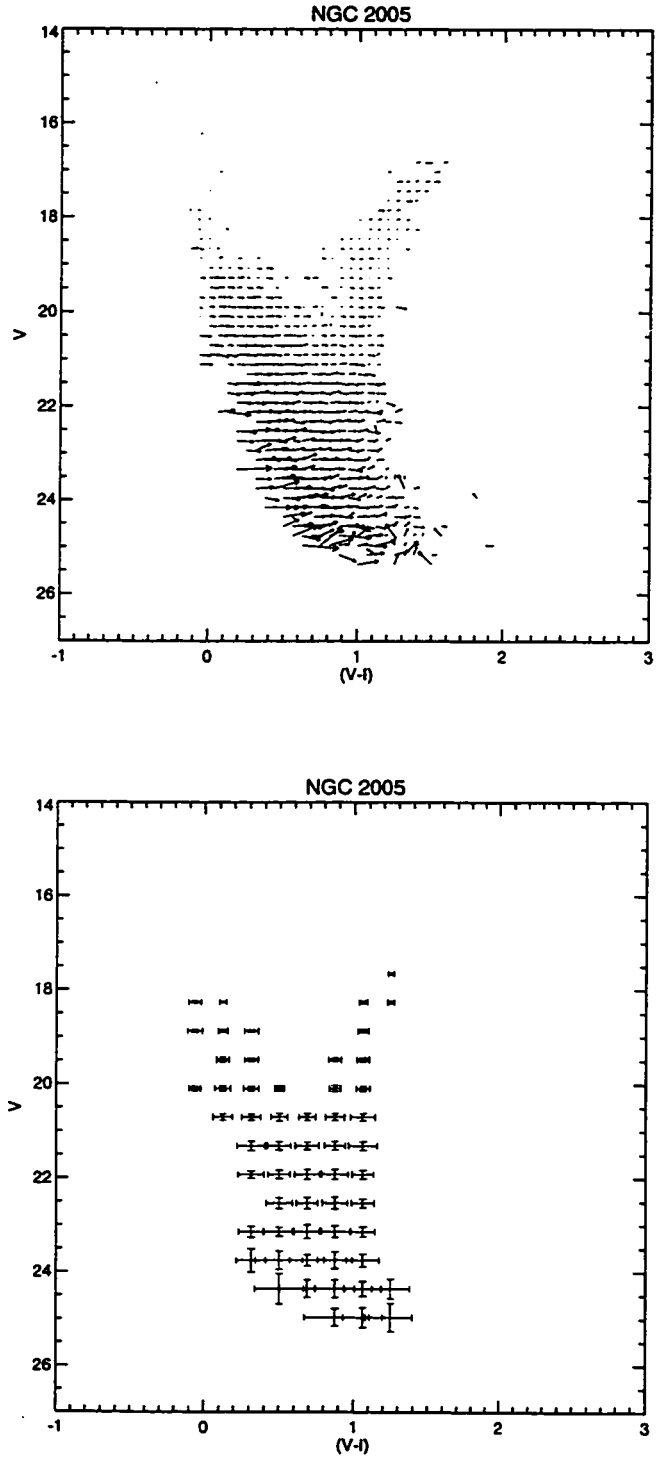

Figure 2.13d: Systematic and random photometric errors for NGC 2005.

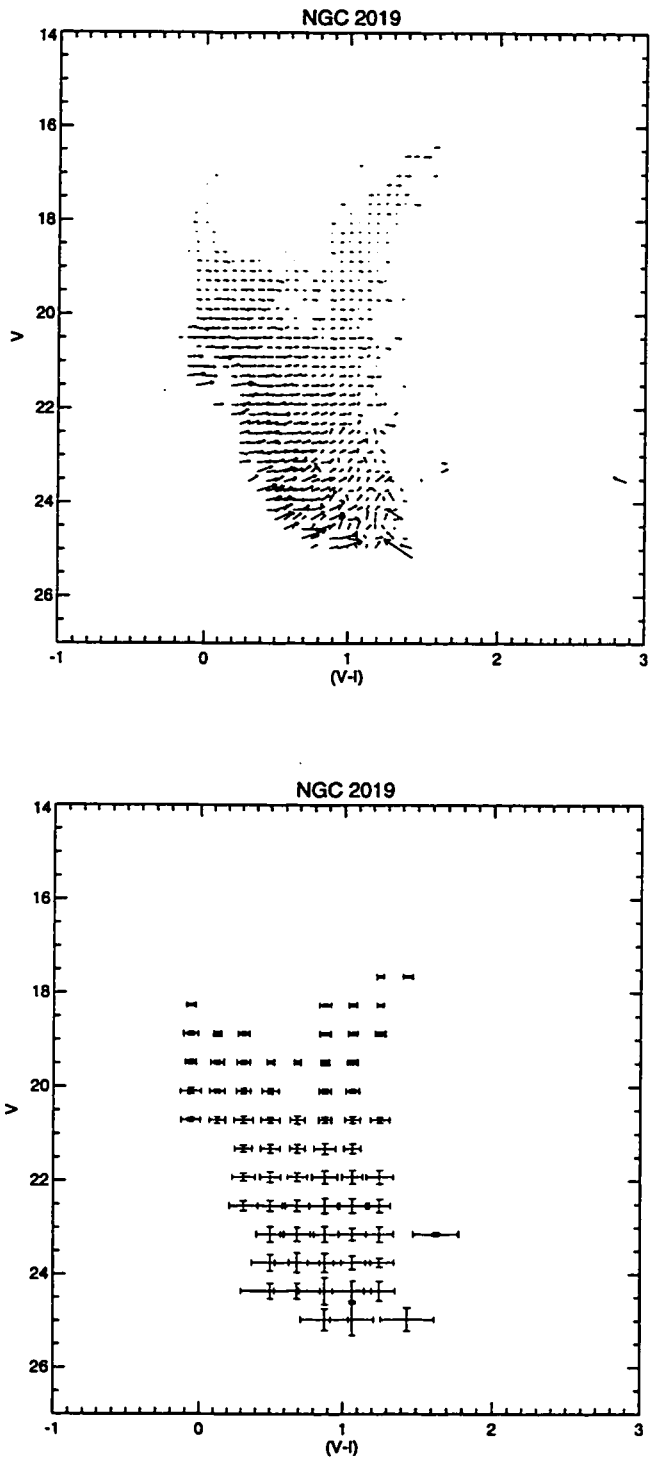

Figure 2.13e: Systematic and random photometric errors for NGC 2019.

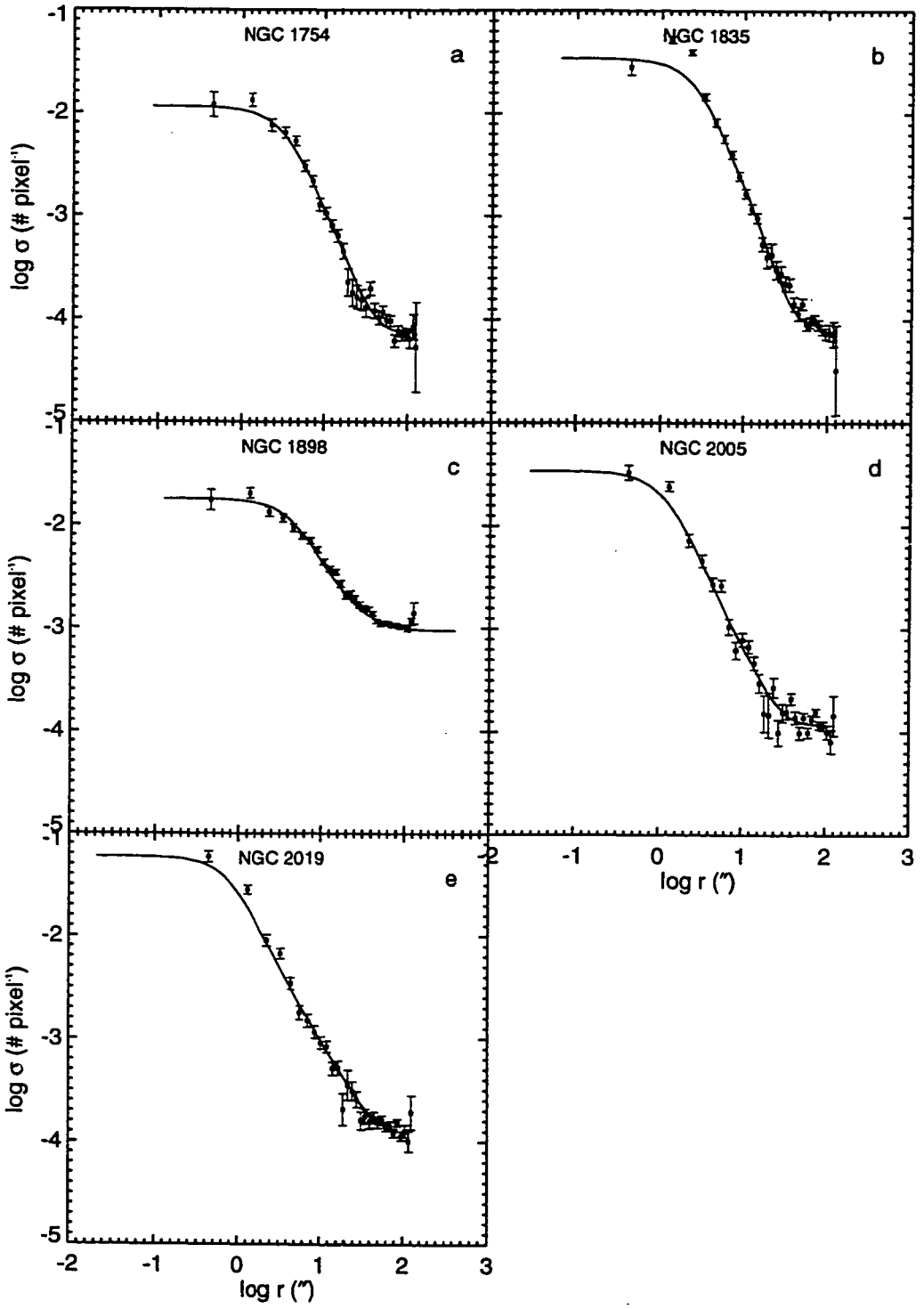

Figure 2.14: By-eye fits of King (1966) model profiles (solid lines) to the completeness-corrected stellar surface density profiles of each cluster (open squares). The error bars are due to counting statistics and uncertainty in the completeness corrections.

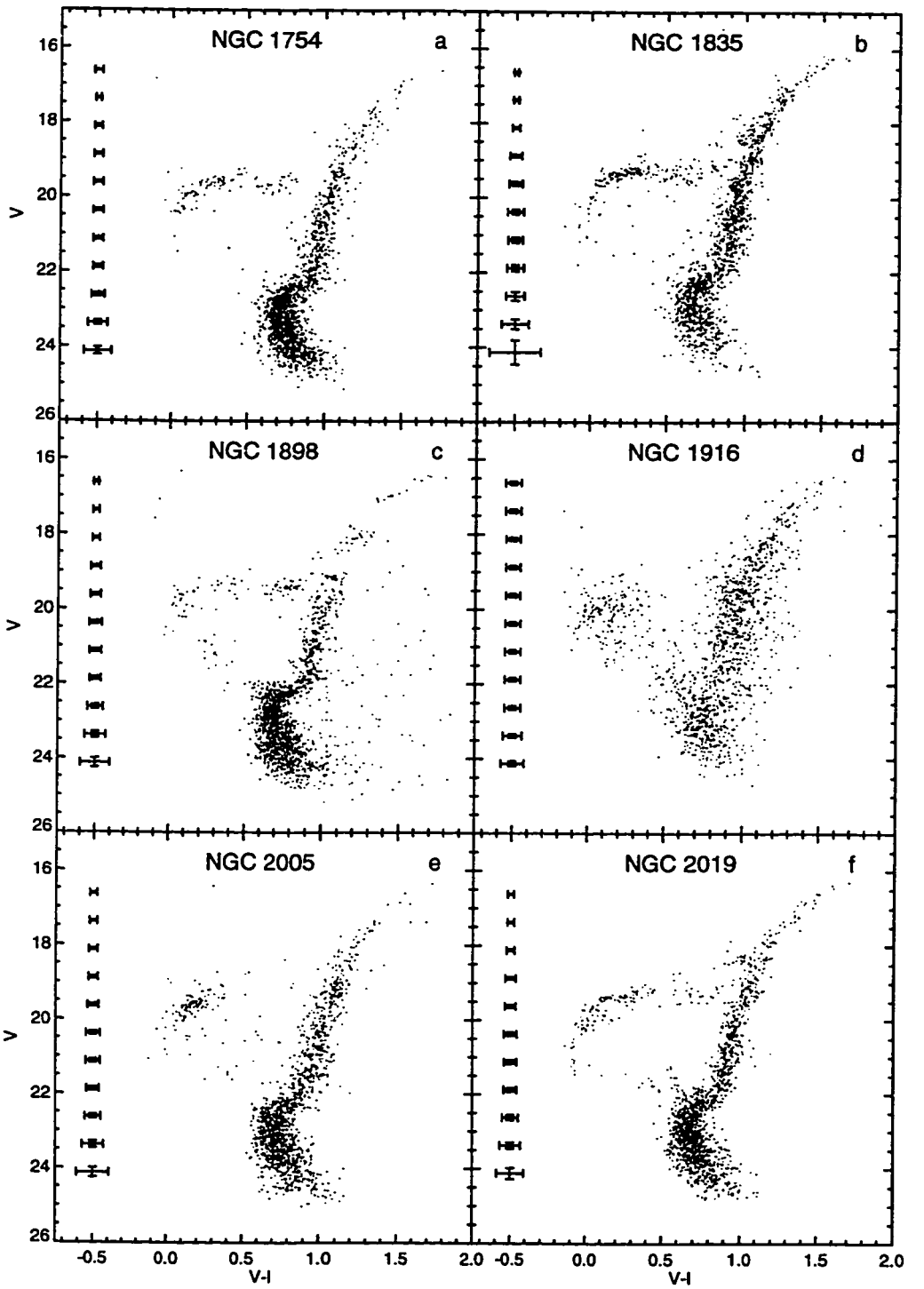

Figure 2.15: Color-magnitude diagrams of the LMC clusters after selection of stars of DoPHOT object type 1 with $r \gtrsim 9''$ from the cluster centers. For all of the clusters except NGC 1916, field stars have been statistically removed. The error bars are those calculated from the artificial star tests discussed in the text.

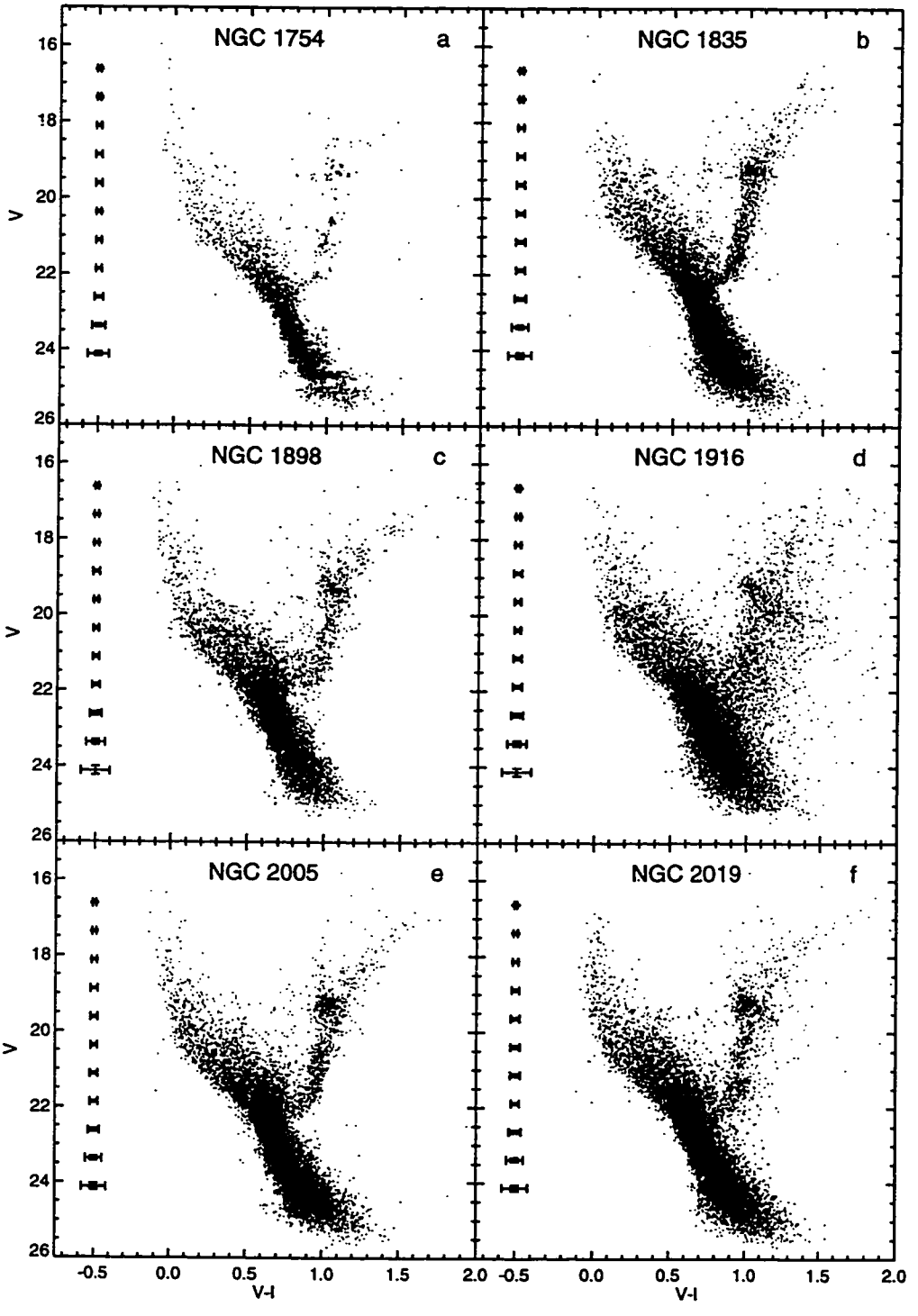

Figure 2.16: Field star color-magnitude diagrams after selection of stars of DoPHOT object type 1. For all of the fields except NGC 1916, cluster stars have been statistically removed. The error bars are those calculated from the artificial star tests discussed in the text.

Chapter 3

ANALYSIS OF CLUSTER COLOR-MAGNITUDE DIAGRAMS

3.1 Introduction

Since the middle of the century, color-magnitude diagrams of star clusters have been used as a straightforward way to compare theoretical stellar evolutionary models with observations. Once the distance, reddening, and abundance of a cluster are known, comparison with stellar isochrones yields the cluster age from the absolute magnitude of the main sequence turnoff. For globular clusters, the fitting of isochrones to CMDs in this fashion has established them as some of the oldest objects in the Universe.

However, because stellar isochrones lie very close together in the C-M plane for old ages, errors in the distance, reddening, or abundance can have a large effect on the derived age. The difficulty of finding the best match to the observations from closely spaced isochrones is compounded by our incomplete knowledge of the physics that governs the shapes and locations of the isochrones as well as uncertainties in the transformation from the theoretical $\log T_{eff} - \log L$ plane to observed broad-band colors and magnitudes. In particular, the best treatment for convection, which affects stars on the red giant branch as well as near the turnoff (Mazzitelli, D'Antona, & Caloi 1995, VandenBerg, Bolte, & Stetson 1996), remains unresolved while color$-T_{eff}$ relations and bolometric corrections continue to be updated from delicate observations and new work in stellar atmospheres. The shapes of isochrones, therefore, do not fit even the best color-magnitude diagrams perfectly, leaving the decision of identifying the best fit up to individual judgment. Unless the observations are of exceptional

quality and the distances, reddenings, and abundances are well-known, errors of ±2-3 Gyr in the ages of globular clusters derived from isochrone fits are typical.

Combined with the large number of globular clusters that have been observed, such precision in age has been sufficient to establish a meaningful lower bound on the age of the Universe. For the purpose of using globular clusters to trace the earliest stages of galaxy formation, however, errors of 3 Gyr in age wash out interesting information. Luckily, globular clusters can often be arranged by their relative ages to a higher degree of precision than their absolute ages can be measured. Relative age dating techniques use differences in easily identifiable features of the CMDs to quantify age differences between clusters, and have the advantage of being independent of distance and reddening. The V magnitude difference between the horizontal branch (HB) and the main sequence turnoff (TO), or $\Delta V_{\rm TO}^{\rm HB}$, is commonly used. It depends only weakly on abundance, as changes in abundance affect $V_{\rm HB}$ and $V_{\rm TO}$ in the same sense. While the calibration of absolute ages derived from $\Delta V_{\rm TO}^{\rm HB}$ depends on uncertain theoretical calculations such as the luminosity of the HB and the effect of convection near the TO, as a differential age indicator $\Delta V_{\rm TO}^{\rm HB}$ depends mainly only on the change of TO luminosity with age and abundance and the change of HB luminosity with abundance, which are fairly well-understood. The main practical disadvantages of the method are the difficulty of measuring $V_{\rm HB}$ for clusters with mainly blue HBs and the fact that the TO region is nearly vertical in V, making typical measurements of $V_{\rm TO}$ uncertain by $\gtrsim$0.1 magnitudes.

"Horizontal" techniques (e.g. VandenBerg, Bolte, & Stetson 1990, hereafter VBS) avoid the problems associated with measuring $\Delta V_{\rm TO}^{\rm HB}$ at the expense of relying on less fundamental physics. Following VBS, one registers the CMDs of two clusters being compared in the C-M plane by lining up the TO colors and the magnitudes of a fiducial point on the main sequence. The difference in the lengths of the subgiant branches can then be measured and converted to an age difference through calibration from theoretical isochrones. While the details of the treatment of convection strongly

affect the color of the red giant branch (RGB), the differential ages should not suffer as long as all cluster RGBs are affected the same way. Because of uncertainties in the dependence of convection on abundance, however, VBS caution that their technique should only be used to compare ages of clusters with similar metallicities.

An intriguing way to measure the relative ages of globular clusters stems from work on the "second parameter" problem of globular clusters. As is now well known, the morphologies of globular cluster HBs, while primarily governed by the cluster metallicity, are in certain cases observed to be very different for clusters of the same metallicity. Lee, Demarque, & Zinn (1994, hereafter LDZ), using evolutionary models of core He-burning HB stars that show the variation of the HB morphology index (B-R)/(B+V+R) with age and metallicity, have most recently argued that age is the second parameter. While this interpretation is currently in hot debate (cf. Stetson, VandenBerg, & Bolte 1996; Sarajedini, Chaboyer, & Demarque 1997), HB morphology remains a potentially powerful way of studying the chronology of globular cluster formation.

In this Chapter, we establish a comparison between the six LMC globular clusters we observed with the Milky Way globular cluster system. Through this comparison, we avoid the problems associated with determining absolute ages for the globular clusters while still addressing the very interesting question of the history of formation of some of the oldest objects in the Local Group. Because there is as yet no consensus on which method best describes the true distribution of Milky Way globular cluster ages, we will use each of the relative age-dating techniques mentioned in this Introduction to date the LMC clusters, with the hope that we can build a consistent (at least internally) picture of their properties.

3.2 Abundances

Each of the age-dating techniques described above depends, to some degree, on the assumed metallicities of the clusters. While we have available directly measured spectroscopic abundances of the clusters (O91), these abundances are based on difficult observations of only 1-2 giant stars per cluster. We therefore measured the abundance of each cluster from the CMD using the formalism of Sarajedini (1994, hereafter S94). This method is empirically calibrated against six Milky Way globular clusters with well-established metallicities and reddenings. It derives the metallicity of an old metal-poor cluster from the slope of its RGB and, as a byproduct, the reddening of the cluster from the color of the RGB after the effect of metallicity has been removed.

To determine the slopes of the RGBs of the clusters, we used the points on the RGB with V brighter than the HB and with $V-I$ bluer than 1.2 magnitudes plus the color of the RGB at the level of the HB ($(V-I)_g$). As suggested in S94, we fit this portion of the RGB with a 2nd order polynomial, which let us solve for $E(B-V)$ and [Fe/H] analytically. We determined the level of the HB ($V_{\rm HB}$) by taking the median of the points on the flat portion of the HB. For NGC 2005, which has mostly blue HB stars, this involves some guesswork, so its parameters are likely more uncertain than those of the other clusters. Our measurements of $V_{\rm HB}$ are shown in Table 3.2.

To calculate the uncertainties, we derived $E(B-V)$ and [Fe/H] from polynomial fits to the RGBs of a set of 100 Monte Carlo realizations of each CMD. These simulated CMDs were constructed by choosing an appropriate number of stars from the luminosity functions of Vandenberg (1997) isochrones with abundances, reddenings, and ages approximately matching the observed CMDs. We simulated the observational errors by applying the $V-I$ and V shifts calculated from our artificial star database to the chosen stars. Because we did not simulate HB stars, we used the measured $V_{\rm HB}$ in the calculations but added to it a random number selected from a Gaussian with a σ of 0.1 magnitudes. We then calculated $E(B-V)$ and [Fe/H] for

the simulated CMDs and compared the values to the input values. We found typical errors of 0.15 dex in [Fe/H] and 0.01 magnitudes in $E(B-V)$ with systematic biases of up to 0.1 dex in [Fe/H] and 0.025 magnitudes in $E(B-V)$. These biases are probably due to small scale changes in the photometry introduced by crowding, as illustrated in Figs. 2.13.

Table 3.2 contains the calculated $E(B-V)$ and [Fe/H] values for the clusters, after correction for the biases found in the Monte Carlo experiments. For NGC 1754, NGC 1835, and NGC 1898, the differences between the spectroscopic abundances and the CMD-based abundances are small. For NGC 2005 and NGC 2019, the CMD-based abundances are $\sim$0.6 dex higher than the spectroscopic ones. The high CMD-based abundance of NGC 2005 especially comes as a surprise because the cluster has a very blue HB morphology. While the discrepancy with the spectroscopic abundances is a cause for some concern, we again note that the spectroscopic abundances of NGC 2005 and NGC 2019 are based solely on measurements of a single star in each cluster, which could be in error, and on the assumed Ca/Fe ratio. In addition, because the CMD-based abundances are rooted in well-understood photometric data of a large number of stars, we regard them as more reliable than the currently available spectroscopic abundances.

3.3 Ages of the LMC Clusters

The CMDs of the clusters all clearly show that the clusters are old, with MSTOs at V$\sim$23 and blue HB stars along with red ones. It is tempting to suggest that some of the blue stars just above the MSTO in NGC 1898 and NGC 2019 may be true blue stragglers. However, considering the large numbers of young MS field stars in this region and the uncertainty in the statistical cleaning procedure, we make no such claim here. With the exception of NGC 2005 and possibly NGC 1916, (Fig. 2.15d), all of the clusters have HB stars both to the blue and to the red of the instability strip.

Both the NGC 1835 and NGC 2019 CMDs show a few AGB stars, as do possibly the other clusters. Comparing our CMD of NGC 1754 with the ground-based CMD of Jensen, Mould, & Reid (1988), we see the immense difference that the resolution of *HST* makes in these crowded fields. While Jensen et al.'s (1988) effort was valiant, their misidentification of the field main sequence and the HB of NGC 1754 with the cluster main sequence led them to suggest an age of only 0.8 Gyr for the cluster. In the following, we use the techniques discussed in section 3.1 to derive the ages of the clusters.

3.3.1 Relative ages from the horizontal method

We compared our LMC cluster CMDs to fiducial sequences of M3, M5, M13, M92 (Johnson & Bolte, 1997), and M55 (Mandushev et al., 1996 and personal communication), which span the range of metallicity $-1.4 \lesssim$ [Fe/H] $\lesssim -2.5$. For consistency, we adopt the Zinn & West (1984) abundances for all of the Milky Way clusters. The technique described by VBS was used to measure the relative ages between the LMC clusters and the Milky Way fiducials. We first attempted to register the LMC and Milky Way clusters in the C-M plane through the color of the TO ($(V-I)_{\rm TO}$) and the magnitude of the point 0.05 magnitudes redder than the TO ($V_{+0.05}$). For both the LMC and Milky Way sets of clusters, we determined these points from polynomial fits to the points in the appropriate regions. These fits were iterated until they converged, with outlying points rejected after each iteration. Because our photometry becomes substantially incomplete below the TO, however, we found it necessary to adjust the vertical registration to match the HB V magnitudes. While using $V_{\rm HB}$ instead of $V_{+0.05}$ makes our result more subject to photometric scale errors because of the large span in V between the HB and the TO, we feel we understand our photometry well enough to account for such effects.

As an alternative to the process described above, which is fairly automatic and unbiased, we also attempted to register the LMC clusters and Milky Way fiducials by

eye, involving both the disadvantage of possible subconscious bias and the advantage of judgement based on knowledge. Each of the six LMC cluster CMDs was compared to the fiducials of M3 and M13 and displacements in $V-I$ and in V were recorded for the best eye fits. (This was done by Paul Hodge, who had not, up to that time, been involved with the initial fitting process). Interestingly, the results were quite similar to those from the automatic comparison. The average difference in the derived $V-I$ was 0.01 magnitudes, while that in V was 0.11 mag. These by-eye measurements confirmed that the automatic method had not introduced any unrealistic data into the problem.

Figs. 3.1 show the comparison of our LMC clusters with Milky Way fiducials after registration. The dashed lines indicate the differences in position of the RGB that would be expected for a 2 Gyr age difference. NGC 1916 is not included because of its strong differential reddening. We also only show those comparisons for which the abundances of the fiducials most closely match either the spectroscopic or CMD-based abundances. The superior fits provided by matching the abundances of the Milky Way fiducials with the CMD-based abundances of the LMC clusters reinforces our greater confidence in these abundances.

Relative ages and age errors

To measure the difference in position of the RGBs in Figs. 3.1, we fit the piece of the fiducial extending from $-5 \leq \Delta V \leq -2$ to the CMD points in the same ΔV range. To map these differences in RGB position to age differences between the Galactic and LMC clusters, we used a calibration based on the new isochrones of VandenBerg (1997). These isochrones are calculated for more than a dozen metallicities in the range $-2.3 \leq$ [Fe/H] ≤ -0.3 for ages of 8-18 Gyr in 2-Gyr steps. The calibration was constructed by registering the six isochrones of a given metallicity in the $\Delta(V-I), \Delta V$ plane, and then fitting a piece of the 14 Gyr isochrone spanning the range $-5 \leq \Delta V \leq -2$ to similar pieces of the other five isochrones. To establish the calibration over a

continuum of age differences, we fit a 2nd order polynomial to the offsets needed to shift this portion of the RGB of the 14 Gyr isochrone to the RGBs of the other isochrones. The choice of the 14 Gyr isochrone as the fiducial for this calibration is inconsequential, as the change of the color of the RGB is nearly linear with age for ages between 12 and 18 Gyr, the likely age range of old globular clusters. Table 4.2 lists the polynomial coefficients of the fits to the equation $\Delta\mathrm{Age} = a + b\Delta(V-I) + c\Delta(V-I)^2$ for the range of metallicities considered in this paper. Fig. 3.2 shows our calibration for [Fe/H]=−2.14 compared to that of Harris et al. (1997). Over a range of age differences of ±1 Gyr, our calibration differs by ∼15% from that of Harris et al. (1997), which we attribute to the likely possibility that different portions of the RGB were used to measure the age differences. However, as the difference in the calibration will only produce differences in the relative age measurements of $\lesssim$0.2 Gyr, and Harris et al. (1997) do not specify what portion of the RGB their calibration is based on, we do not explore the cause any further.

Table 3.2 contains the ages we derive, in Gyr, for the LMC clusters relative to the appropriate comparison clusters, in the sense of $\mathrm{age}_{\mathrm{LMC}} - \mathrm{age}_{\mathrm{MW}}$. On average, the LMC clusters have the same ages as the Milky Way clusters to within 1.0 ± 1.3 Gyr, implying that the LMC old globular clusters formed at the same time as those in the Milky Way. In order to examine this global statement on a cluster-to-cluster basis, however, we need to establish the accuracy of the individual relative age measurements.

We calculated the uncertainties in the relative age measurements through the sets of 100 Monte Carlo realizations of each cluster described previously. For each simulated CMD, we first measured $(V-I)_{\mathrm{TO}}$ and $V_{+0.05}$ as for the observed CMD and registered the simulated CMD and the error-free input isochrone in the $\Delta(V-I), \Delta V$ plane. The simulated measurements of $V_{+0.05}$ confirm that low completeness affects this measurement, so we adjusted the vertical registration to match exactly the $V_{+0.05}$ values calculated from the isochrone, and then added a random offset selected from

a Gaussian with a 1-σ dispersion of 0.1 magnitudes. We then measured the age difference between the simulated CMD and the input isochrone as we did for the real clusters. Figs. 3.3 show the resulting distributions of age differences (in the sense of $\mathrm{age_{out}} - \mathrm{age_{in}}$ and the cumulative distributions of absolute age differences around the mean. The distributions of age differences are narrow, with 70% of the distributions enclosed within 0.7-0.8 Gyr of the mean. However, three of the clusters, NGC 1754, NGC 2005, and NGC 2019, show systematic biases towards recovering ages $\sim$1 Gyr younger than the age of the input isochrone, while NGC 1835 has a bias towards recovering ages $\sim$0.5 Gyr younger than the input. These biases are likely due to the systematic shifts in the photometry introduced by crowding, illustrated by Fig. 2.13. Although ignoring the biases would not significantly affect our results, we have corrected for them in the relative age measurements reported in Table 3.2.

3.3.2 Ages from $\Delta V_{\mathrm{TO}}^{\mathrm{HB}}$

To measure $\Delta V_{\mathrm{TO}}^{\mathrm{HB}}$ we used the values of V_{HB} measured in section 3.2 and the magnitude of the TO (V_{TO}) implied by the polynomial fit to the points near the turnoff, also described in section 3.2. Because the TO region is nearly vertical in the CMD and the measurement of V_{HB} is subject to some interpretation, the error in $\Delta V_{\mathrm{TO}}^{\mathrm{HB}}$ may be larger than reported here. We estimate the error in V_{HB} to be $\pm$0.1 magnitudes, while for the error in V_{TO} we adopt the error calculated from the covariance matrix of the polynomial fit.

To convert $\Delta V_{\mathrm{TO}}^{\mathrm{HB}}$ to age, we adopted the calibration of Chaboyer, Demarque, & Sarajedini (1996), which is based on a recent set of Yale isochrones (Chaboyer et al., 1995). The calibration depends on an assumed M_V(RR)$-$[Fe/H] relation; their preferred relation is $M_V(\mathrm{RR}) = 0.20[\mathrm{Fe/H}] + 0.98$. Recent work based on *HIPPARCOS* parallaxes and proper motions of field RR Lyrae (Tsujimoto, Miyamoto, & Yoshii, 1998) finds a similar slope and zero point, $M_V(\mathrm{RR}) = 0.20[\mathrm{Fe/H}] + 0.91$, albeit with large error. The independent analysis of Fernley et al. (1998) gives

M_V(RR) = 0.18[Fe/H] + 1.05, which agrees, within the error, with the Tsujimoto et al. (1998) result. As the Chaboyer et al. (1996) preferred zero point of the M_V(RR)–[Fe/H] relation is the exact average of the two available *HIPPARCOS*-based zero points, we adopt their preferred relation. An advantage of using this relation is that we can easily compare the ages we derive from $\Delta V_{\rm TO}^{\rm HB}$ with those that Chaboyer et al. (1996) derive for the Galactic globular clusters. As has been noted, however, this relation disagrees strongly with the distance to the LMC implied by the *HIPPARCOS* Cepheid work (Feast & Catchpole, 1997), but not with the recent *HIPPARCOS* Cepheid analysis of Madore & Freedman (1998). The $\Delta V_{\rm TO}^{\rm HB}$ ages we measure are listed in Table 3.2, for both the O91 and CMD-based abundances. We find that the average age of the clusters implied by $\Delta V_{\rm TO}^{\rm HB}$ is 15.3±1.5 Gyr, which agrees better with Chaboyer et al.'s (1996) age of the younger halo than with that of the old halo, although the errors are large.

3.3.3 Ages Implied by Horizontal Branch Morphology

An interesting question is whether the LMC clusters show a variation of HB morphology with metallicity similar to the Milky Way clusters. We measured the HB morphology of our clusters through the commonly used (B-R)/(B+V+R) index, where B is the number of stars to the blue of the instability strip, R the number of stars to the red of the instability strip, and V the number RR Lyrae variables. Because we do not have sufficient time resolution in our images to identify RR Lyrae variables from their light curves, we rely on the approximate location of the instability strip in the CMD plane to determine the boundaries of the B, V, and R zones. Our chosen boundaries are $V - I$=0.23 for the blue edge of the instability strip and $V - I$=0.57 for the red edge. Table 3.2 contains our measured values of (B-R)/(B+V+R) for each cluster, corrected for incompleteness, along with uncertainties calculated from Poisson counting statistics and the uncertainties in the completeness corrections.

In Figs. 3.4 we plot [Fe/H] vs. (B-R)/(B+V+R) for the LMC clusters studied

here, for the outer LMC clusters using data from Walker (1992), and for selected Milky Way clusters from Table 1 of LDZ. The HB evolutionary tracks from LDZ are also plotted, for a fiducial age and for ages 2 Gyr older and younger than the fiducial. We show separate plots for the O91 spectroscopic abundances and the CMD-based abundances. Depending on which set of abundance measurements is adopted, we arrive at slightly different conclusions. If we choose to adopt the spectroscopic abundances, we conclude that, based on the HB morphologies, our LMC clusters are similar to the "younger halo" of the Milky Way. On the other hand, if we adopt the CMD-based abundances, we find that the LMC clusters are similar to the oldest Milky Way globulars, with NGC 1835 perhaps being $\sim$2 Gyr younger. As we are more confident in the CMD-based abundances, the HB models suggest that the LMC is as old as the Milky Way. Independent of the abundances used, all of the clusters, with the possible exception of NGC 1835, fall on the same HB evolutionary sequence. The similarity in age of the clusters implied by the HB sequences agrees with the narrow age spread implied by both the comparison with Milky Way fiducials and the measurements of $\Delta V_{\rm TO}^{\rm HB}$. It is also interesting to note that none of the LMC clusters studied here bears similarity to Ruprecht 106 or Pal 12, which have been suggested to be captures from the Magellanic Clouds (Lin & Richer, 1992; cf. Rup 106 CMD of Buonanno et al., 1993).

3.4 Reddenings and Distances

We estimated the reddenings of the clusters in two ways. First, the horizontal shifts needed to register our CMDs with the the Milky Way fiducials yields the reddening difference between the LMC clusters and the Milky Way comparison clusters. As the reddenings of the Milky Way clusters are well known, we can calculate the reddenings of the LMC clusters. Second, as previously discussed, we use the S94 method to measure the reddening from $(V-I)_{\rm g}$, the color of the giant branch at the level of

the HB. Table 3.2 contains our measurements of $E(B-V)$ as well as the estimates of Suntzeff et al. (1992). For the Milky Way comparison method, we report separate values for the two possible abundance systems. In all calculations, we have used $E(B-V) = E(V-I)/1.3$ (Dean, Warren, & Cousins 1978). As the dispersion in the measurements is small, we adopt for the $E(B-V)$ of each cluster the average of our measurements, also listed in Table 3.2.

The NGC 1898 CMD is unique in containing a large number of stars to the red of the primary fiducial sequence. As we were puzzled by these stars, we selected them on the CMD and examined their locations in the image. Figs. 3.5 show the selected stars and their locations on the image. The majority of the stars lie in an area of the sky that contains relatively few stars–this plus the anomalously red colors of these stars indicates that the area is a patch of heavy obscuration. Amazingly, the rest of the cluster suffers only a modest of amount of reddening, comparable to that of the other clusters.

Our CMDs are not sufficiently deep to accurately measure the distances to the clusters directly from a fit to the unevolved main sequence. However, we can use the vertical shifts measured in Section 6.2.3 to measure the distances to the LMC clusters based on adopted distances to the Milky Way comparison clusters. In addition, by adopting an $M_V(\mathrm{RR}) - [\mathrm{Fe/H}]$ relation, we can measure the distances to the LMC clusters from V_{HB}. By demanding that the distances measured from our data should be consistent with those implied by observations of LMC field RR Lyrae, we can use the distance measurements to check the internal consistency of our measurements of the reddenings and abundances, in addition to establishing the relative distances between the clusters. For our calculations, we adopt distances to M3, M5, and M55 that are consistent with the LMC modulus of 18.5 used in Walker's (1992c) analysis of the zero point of the $M_V(\mathrm{RR})$–[Fe/H] relation; we use the preferred $M_V(\mathrm{RR}) - [\mathrm{Fe/H}]$ relation of Chaboyer et al. (1996), $M_V(\mathrm{RR}) = 0.20[\mathrm{Fe/H}] + 0.98$, which is consistent with the SN1987A distance to the LMC of 18.37 (Gould, 1995). While other analyses

of the SN1987A ring find larger LMC distances (Panagia et al. 1991, Sonneborn et al. 1997), the exact distance is irrelevant for the consideration of the *internal* consistency of our measurements.

Fig. 3.6 shows our distance modulus measurements for both the Milky Way comparison and V_{HB} methods and for both the O91 and CMD-based abundance sources. We compare our measurements with the distance modulus gradient across the LMC of Caldwell & Coulson (1986). In the top panels, (a) and (b), we have used the O91 abundances while in the lower panels, (c) and (d), we have used the CMD-based abundances. The panels on the left, (a) and (c), show the results derived from the comparison with Milky Way clusters while the panels on the right, (b) and (d), show the results of adopting $M_V(\mathrm{RR}) = 0.20[\mathrm{Fe/H}] + 0.98$ in conjunction with V_{HB}. We have subtracted an LMC distance modulus of 18.5 from the left panels and 18.37 from the right panels. While the errors are large, the plots suggest that the CMD-based abundances produce a greater consistency between the cluster distances and the LMC modulus. All of the distances, with the possible exception of NGC 1754, appear consistent with lying in the plane of the LMC.

3.5 Summary

The main results of our analysis of the cluster CMDs are that the six old LMC globular clusters NGC 1754, NGC 1835, NGC 1898, NGC 1916, NGC 2005, and NGC 2019 are clearly very similar in age, abundance, and HB morphology to the globular clusters of the Milky Way halo. Excluding NGC 1916 from the bulk of the analysis because of the difficulty of treating its differential reddening, we have explored the similarity in age through the use of three age-dating techniques: comparison of our CMDs with Milky Way globular cluster fiducial sequences through the "horizontal method" (VBS), measurement of ΔV_{TO}^{HB} ("vertical method"), and comparison of our HB data with HB evolutionary models from LDZ. While showing the clear similarity in age

with Milky Way globular clusters, each of these techniques additionally suggests that we detect no internal age spread in this set of LMC globular clusters. We have measured the abundances of the clusters from the slope of the RGB (S94). While the mean abundance that we derive is higher than that measured by O91, it is not grossly different. We have argued, however, that the CMD-based abundances should be considered more reliable.

Throughout our analysis, we have tried to be as careful as possible in identifying and measuring errors. In particular, we have extensively used Monte Carlo simulations to model both systematic and random errors in our measurements. Although we were unable to independently check the Holtzman (1995b) zero points to a precision of <0.1 magnitudes through our ground-based photometry, our measurements of the abundances and relative ages are differential, and so should not be affected by errors in the zero points. The reddenings and distance moduli that we derive, however, *are* subject to unknown zero point errors in the photometry.

Adopting the CMD-based abundances, the possibility that the old LMC globular clusters are younger than the oldest Milky Way globular clusters by 2-3 Gyr (Da Costa, 1993) appears not to be the case for the clusters studied here. This result is clear from the relative ages derived from the comparison of the clusters with Milky Way fiducials, the results of which are shown in Table 3.2. NGC 1754, NGC 1898, NGC 2005, and NGC 2019, which we find have abundances most closely matching that of the classical old Galactic globular cluster M5, are all of similar age or older than M5. NGC 1835, which we find has an abundance similar to M3, is $\sim$2 Gyr older. As LDZ consider M3 to be $\sim$2 Gyr younger than the oldest halo clusters, NGC 1835 appears to have an age similar to the oldest Milky Way clusters.

Interpreting our data through the HB models of LDZ, we paint a similar picture. As shown in Fig. 3.4, the clusters NGC 1754, NGC 1898, NGC 2005, and NGC 2019 all fall on the HB evolutionary track crossing through the oldest Milky Way halo clusters. Comparing our data with the HB data of Walker (1992) for the outer LMC

old globular clusters, we find that the HB models suggest that the earliest episode of cluster formation in the LMC spanned 2-3 Gyr. However, we find some problems with the ages implied by the HB models. The age of NGC 1835 suggested by the HB models is inconsistent with its age relative to M3. In addition, the age of NGC 1754 relative to M5 is slightly older than suggested by the HB models. These inconsistencies may indicate a difficulty with the interpretation that metallicity and age are the only parameters affecting HB morphology, as has been suggested by many authors (e.g. Buonanno et al. 1997, Catelan et al. 1997, Sweigart 1997). Given the currently large errors in the abundance measurements, however, we do not claim on the basis of our data that this interpretation needs to be modified.

The ages we derive from $\Delta V_{\rm TO}^{\rm HB}$ are marginally consistent with the picture that the LMC clusters studied here are as old as the oldest Milky Way clusters. Our measured values of $\Delta V_{\rm TO}^{\rm HB}$ imply an average age of 15.3 $\pm$ 1.5 Gyr, which is lower but within $\sim 1.5\sigma$ of the average age of the old halo quoted by Chaboyer et al. (1996), 17.8 $\pm$ 0.4 Gyr, measured from $\Delta V_{\rm TO}^{\rm HB}$.

In contrast to the globular clusters of the Milky Way halo, the old LMC clusters are not as clearly part of a distinct halo (O91; Schommer et al., 1992). Our results imply that at the time the Milky Way formed its first globular clusters, the LMC may have already collapsed to a disk and started forming clusters. Why there appears to be no clear halo component in the LMC (Olszewski, Suntzeff, & Mateo, 1996) remains an open question. However, by establishing that the oldest clusters in the LMC are truly as old as the Milky Way Galaxy, we have taken an important step towards understanding the formation of the LMC.

Table 3.1: Calibration of Relative Ages

[Fe/H]	a	b	c
-1.14	8.51×10^{-4}	9.70×10^{-3}	-5.25×10^{-4}
-1.31	7.80×10^{-4}	1.02×10^{-2}	-6.11×10^{-4}
-1.41	7.91×10^{-4}	1.05×10^{-2}	-6.59×10^{-4}
-1.54	9.71×10^{-4}	1.11×10^{-2}	-7.49×10^{-4}
-1.61	1.12×10^{-3}	1.14×10^{-2}	-7.95×10^{-4}
-1.71	1.44×10^{-3}	1.19×10^{-2}	-8.87×10^{-4}
-1.84	2.07×10^{-3}	1.26×10^{-2}	-9.68×10^{-4}
-2.01	2.51×10^{-3}	1.36×10^{-2}	-1.16×10^{-3}
-2.14	2.81×10^{-3}	1.45×10^{-2}	-1.28×10^{-3}

Table 3.2: Derived Parameters of LMC Globular Clusters

		NGC 1754	NGC 1835	NGC 1898	NGC 2005	NGC 2019
[Fe/H]	O91	-1.54 ± 0.2	-1.79 ± 0.2	-1.37 ± 0.2	-1.92 ± 0.2	-1.81 ± 0.2
	S94 method	-1.42 ± 0.15	-1.62 ± 0.15	-1.18 ± 0.16	-1.35 ± 0.16	-1.23 ± 0.15
E(B-V)	O91	0.08 ±0.02	0.13 ± 0.02	0.06 ± 0.02	0.12 ± 0.02	0.12 ± 0.02
	MW GC comp.					
	O91 abundance	0.10 ±0.02	0.07 ± 0.02	0.08 ± 0.02	0.12± 0.02	0.07 ± 0.02
	S94 abundance	0.09 ±0.02	0.12 ±0.02	0.08 ±0.02	0.09 ±0.02	0.05 ±0.02
	S94 method	0.082 ±0.01	0.036 ± 0.01	0.046 ± 0.01	0.068 ± 0.01	0.034 ± 0.01
	adopted	0.09 ±0.02	0.08 ±0.02	0.07 ±0.02	0.10 ±0.02	0.06 ±0.02
V_{HB}		19.57 ± 0.10	19.30 ± 0.10	19.41 ± 0.10	19.39 ± 0.10	19.24 ± 0.10
$(V-I)_{TO}$		0.72 ± 0.01	0.66 ± 0.02	0.69 ± 0.01	0.71 ± 0.01	0.68 ± 0.02
$\frac{(B-R)}{(B+V+R)}$		0.47 ± 0.07	0.48 ± 0.05	-0.08 ± 0.10	0.87 ± 0.04	0.56 ± 0.07
Ages						
Age (LMC–						
MW cluster)	O91 abundance					
(Gyr)	MW cluster: M3	2.56 ± 0.53	–	–	–	–
	MW cluster: M5	–	–	-0.45 ± 0.81	–	–
	MW cluster: M55	–	1.03 ± 0.76	–	0.35 ± 0.54	0.35 ± 0.66
	S94 abundance					
	MW cluster: M3	–	2.23 ± 0.76	–	–	–
	MW cluster: M5	2.42 ± 0.53	–	-0.45 ± 0.81	0.42 ± 0.54	0.53 ± 0.66
ΔV_{HB}^{TO} (mags.)		3.51 ± 0.13	3.54 ± 0.16	3.44 ± 0.15	3.51 ± 0.29	3.59 ± 0.17
Age(ΔV_{HB}^{TO}) ..	O91 abundance	15.6 ± 2.3	16.6 ± 2.9	14.0 ± 2.3	16.6 ± 5.1	17.8 ± 3.2
(Gyr)	S94 abundance	15.6 ± 2.2	16.2 ± 2.8	13.5 ± 2.2	15.5 ± 4.9	16.3 ± 3.1
Distances						
$(m-M)_V$	MW GC comp.					
	O91 abundance	19.00 ± 0.15	18.67 ± 0.15	18.69 ± 0.15	18.71 ± 0.15	18.64 ± 0.15
	S94 abundance	18.87 ± 0.15	18.77 ± 0.15	18.69 ± 0.15	18.69 ± 0.15	18.62 ± 0.15
$(m-M)_o$	MW GC comp.					
	O91 abundance	18.70 ± 0.16	18.46 ± 0.16	18.45 ± 0.16	18.31 ± 0.16	18.38 ± 0.16
	S94 abundance	18.60 ± 0.16	18.65 ± 0.16	18.45 ± 0.16	18.40 ± 0.16	18.46 ± 0.16
$(m-M)_V$	V_{HB}					
	O91 abundance	18.90 ± 0.11	18.68 ± 0.11	18.70 ± 0.11	18.79 ± 0.11	18.62 ± 0.11
	S94 abundance	18.87 ± 0.10	18.64 ± 0.10	18.67 ± 0.10	18.68 ± 0.10	18.51 ± 0.10
$(m-M)_o$	V_{HB}					
	O91 abundance	18.62 ± 0.12	18.43 ± 0.12	18.49 ± 0.12	18.48 ± 0.12	18.44 ± 0.12
	S94 abundance	18.60 ± 0.12	18.40 ± 0.12	18.45 ± 0.12	18.37 ± 0.12	18.32 ± 0.12

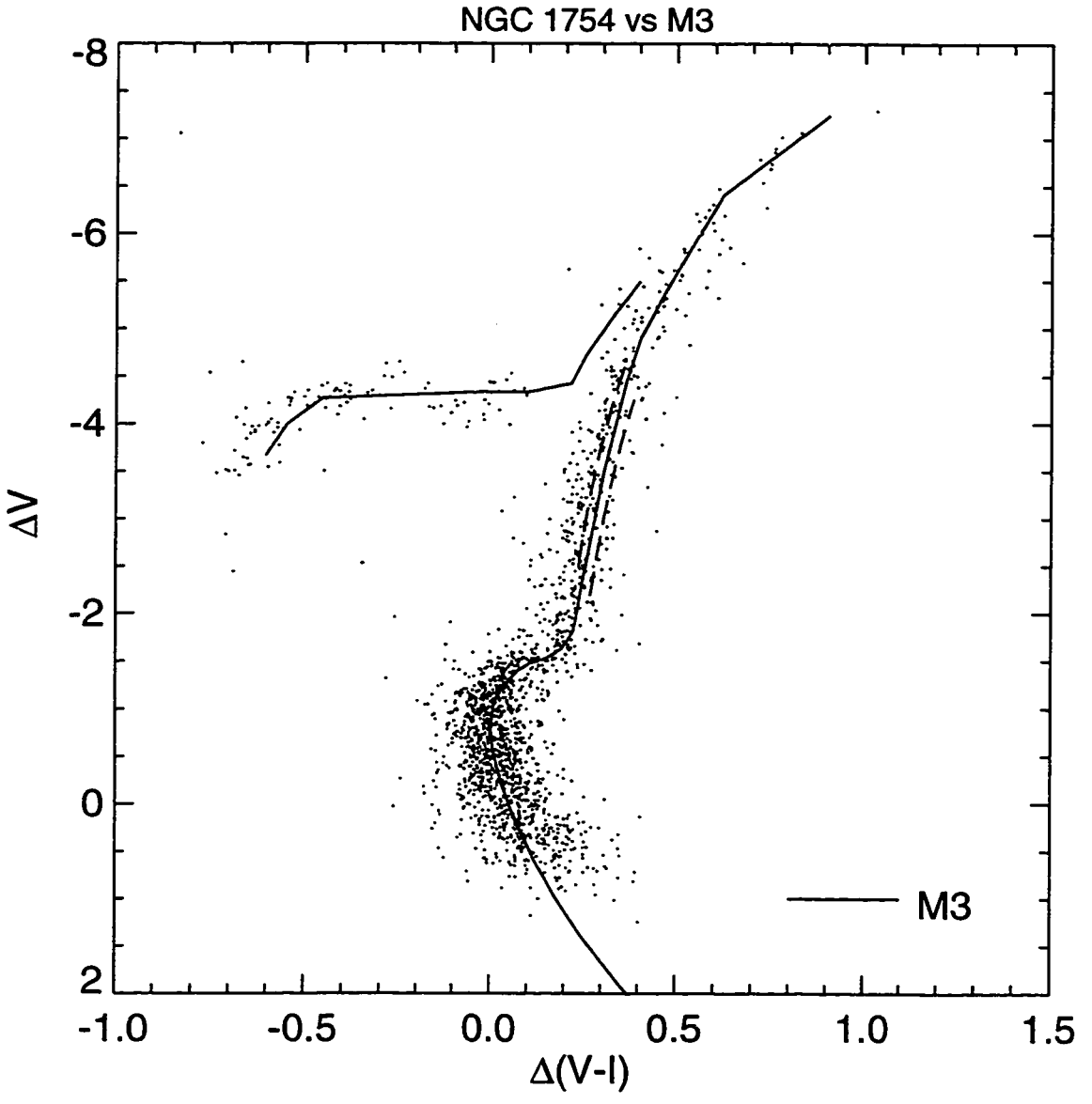

Figure 3.1a: The color-magnitude diagram of NGC 1754 shifted to match a fiducial sequence of the Milky Way globular cluster M3, as discussed in the text. The dashed line to the blue of the M3 RGB shows the location it would have if M3 were 2 Gyr older, while the line to the red shows the RGB of a cluster 2 Gyr younger than M3. The locations of these lines were calculated from the models of VandenBerg (1997).

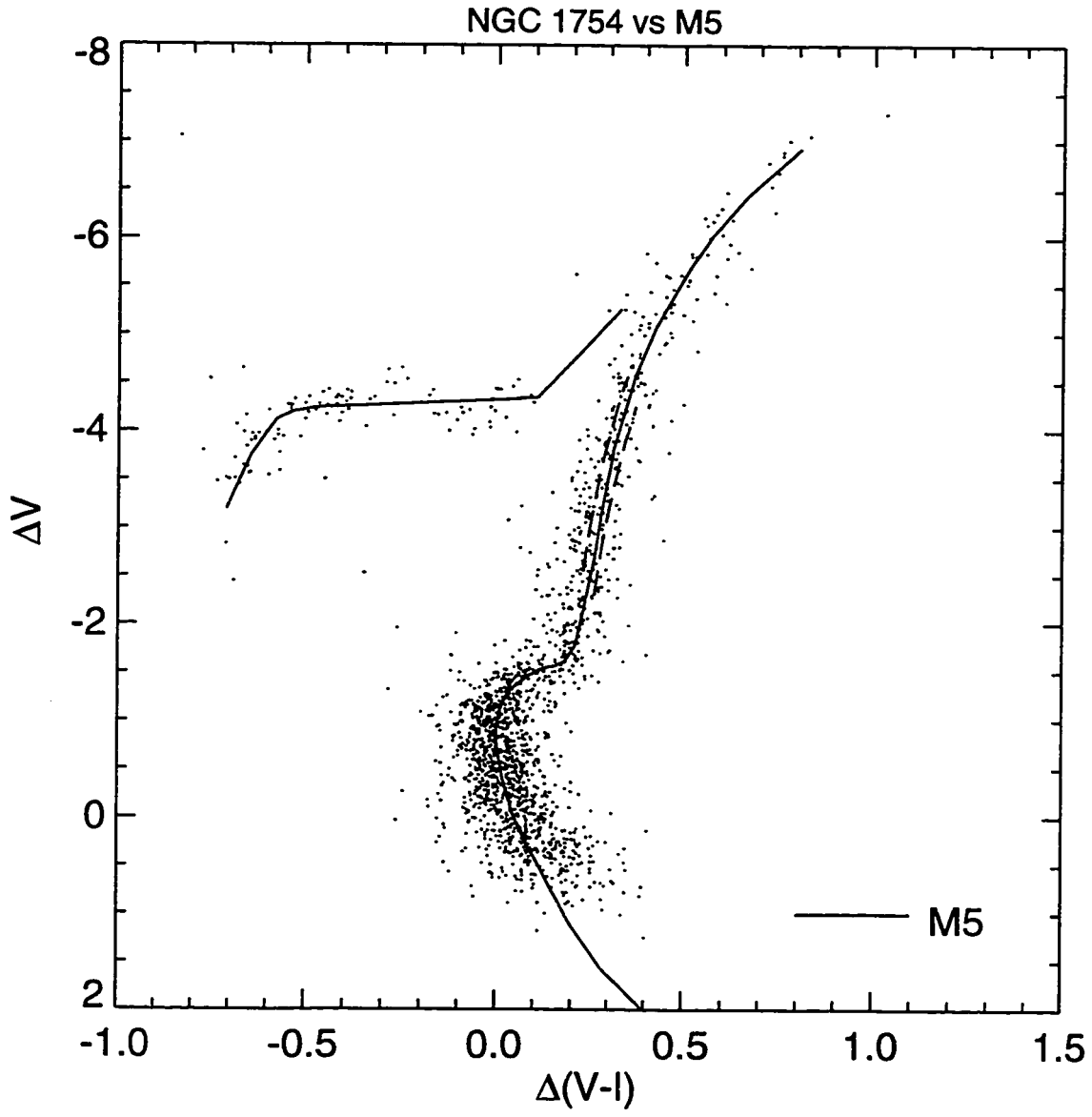

Figure 3.1b: The color-magnitude diagram of NGC 1754 shifted to match a fiducial sequence of the Milky Way globular cluster M5.

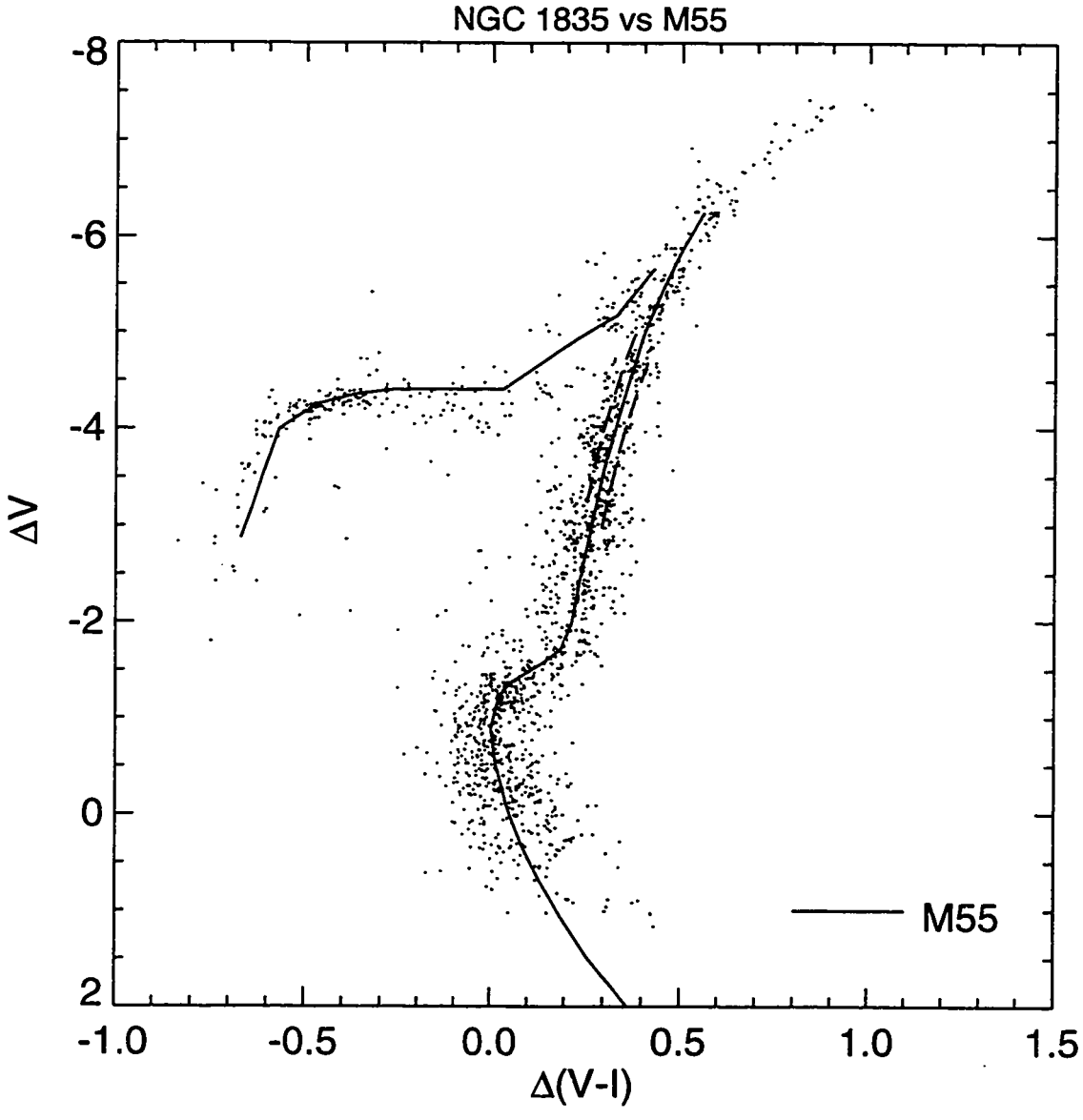

Figure 3.1c: The color-magnitude diagram of NGC 1835 shifted to match a fiducial sequence of the Milky Way globular cluster M55.

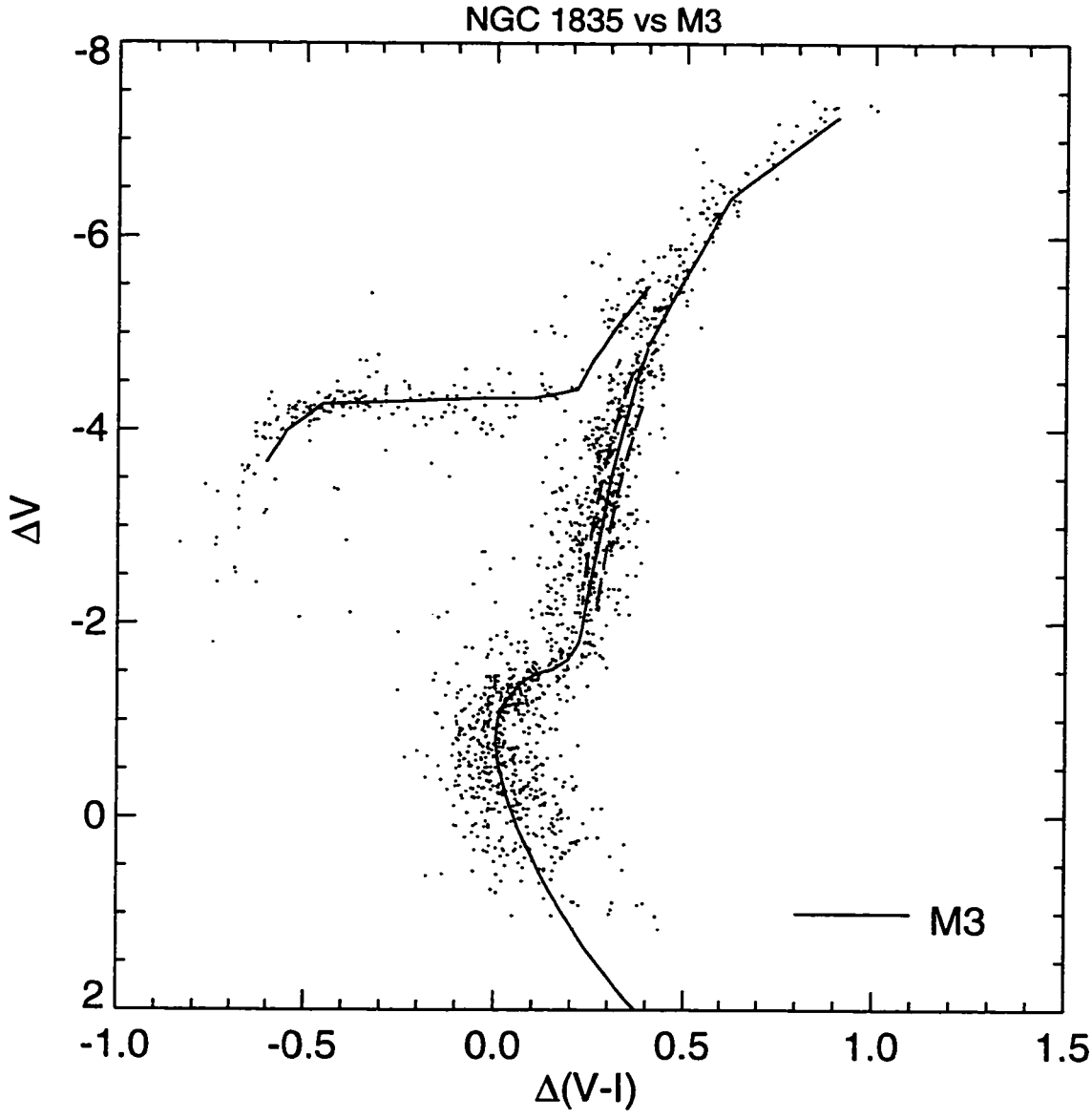

Figure 3.1d: The color-magnitude diagram of NGC 1835 shifted to match a fiducial sequence of the Milky Way globular cluster M3.

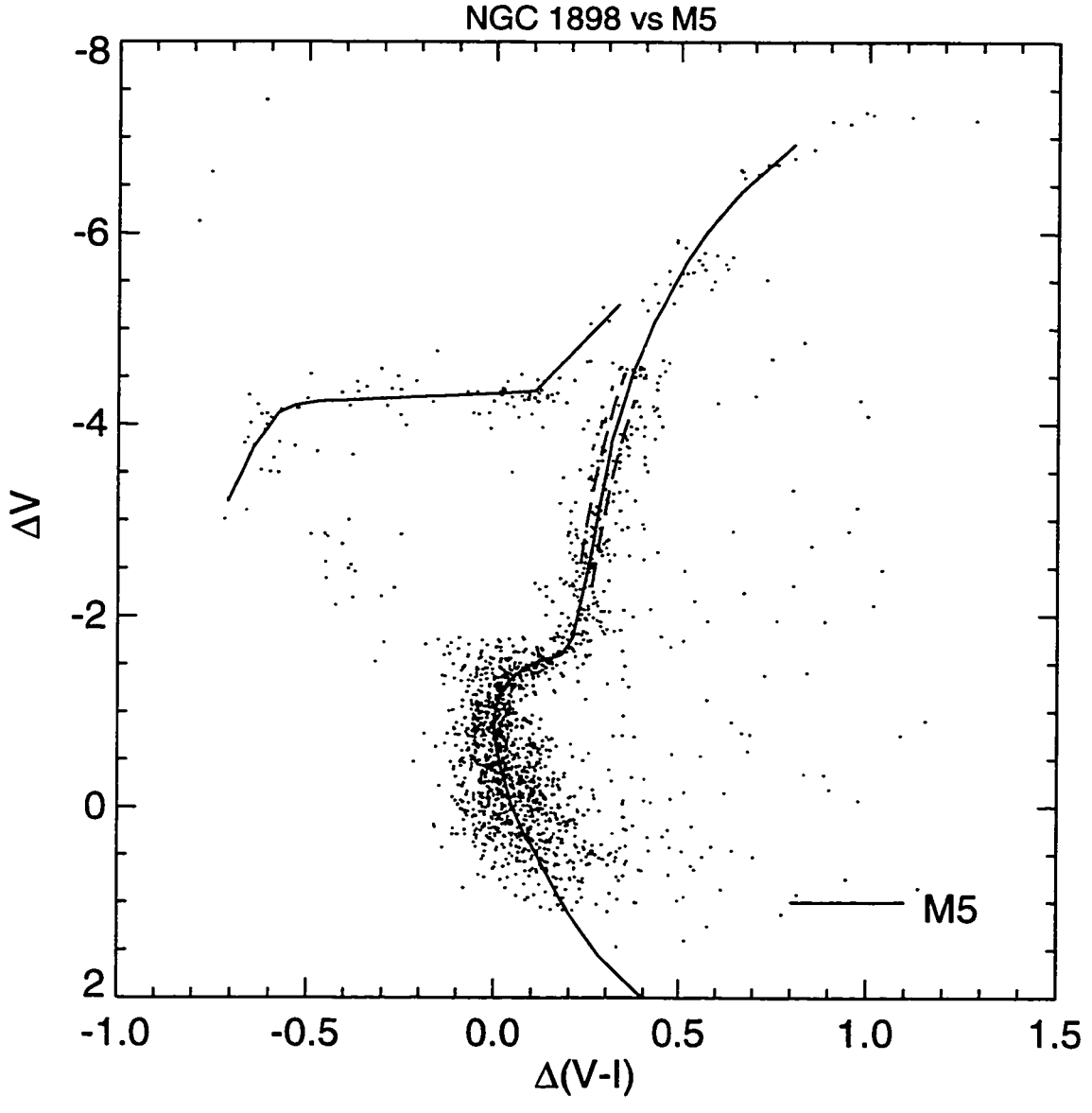

Figure 3.1e: The color-magnitude diagram of NGC 1898 shifted to match a fiducial sequence of the Milky Way globular cluster M5.

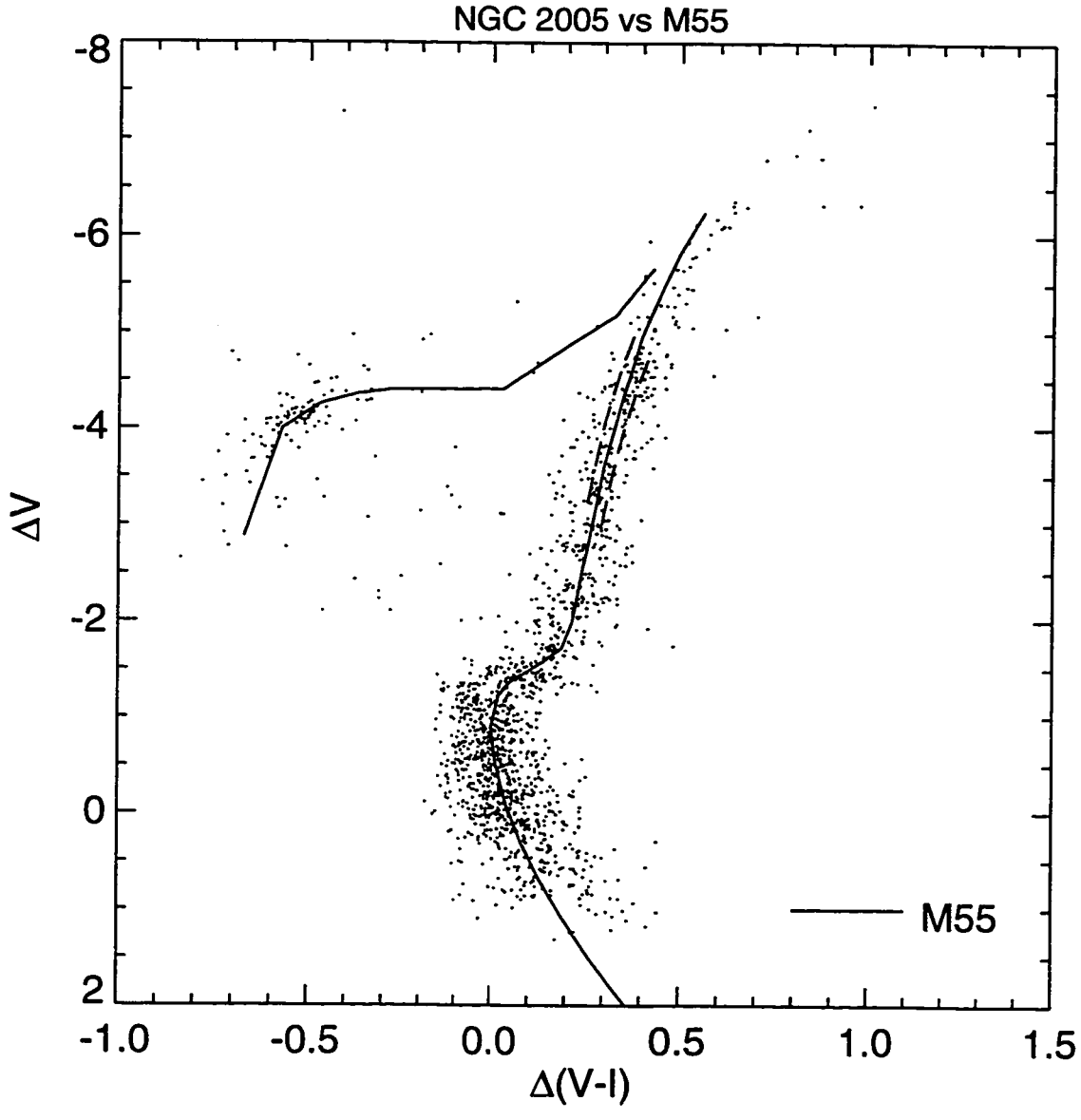

Figure 3.1f: The color-magnitude diagram of NGC 2005 shifted to match a fiducial sequence of the Milky Way globular cluster M55.

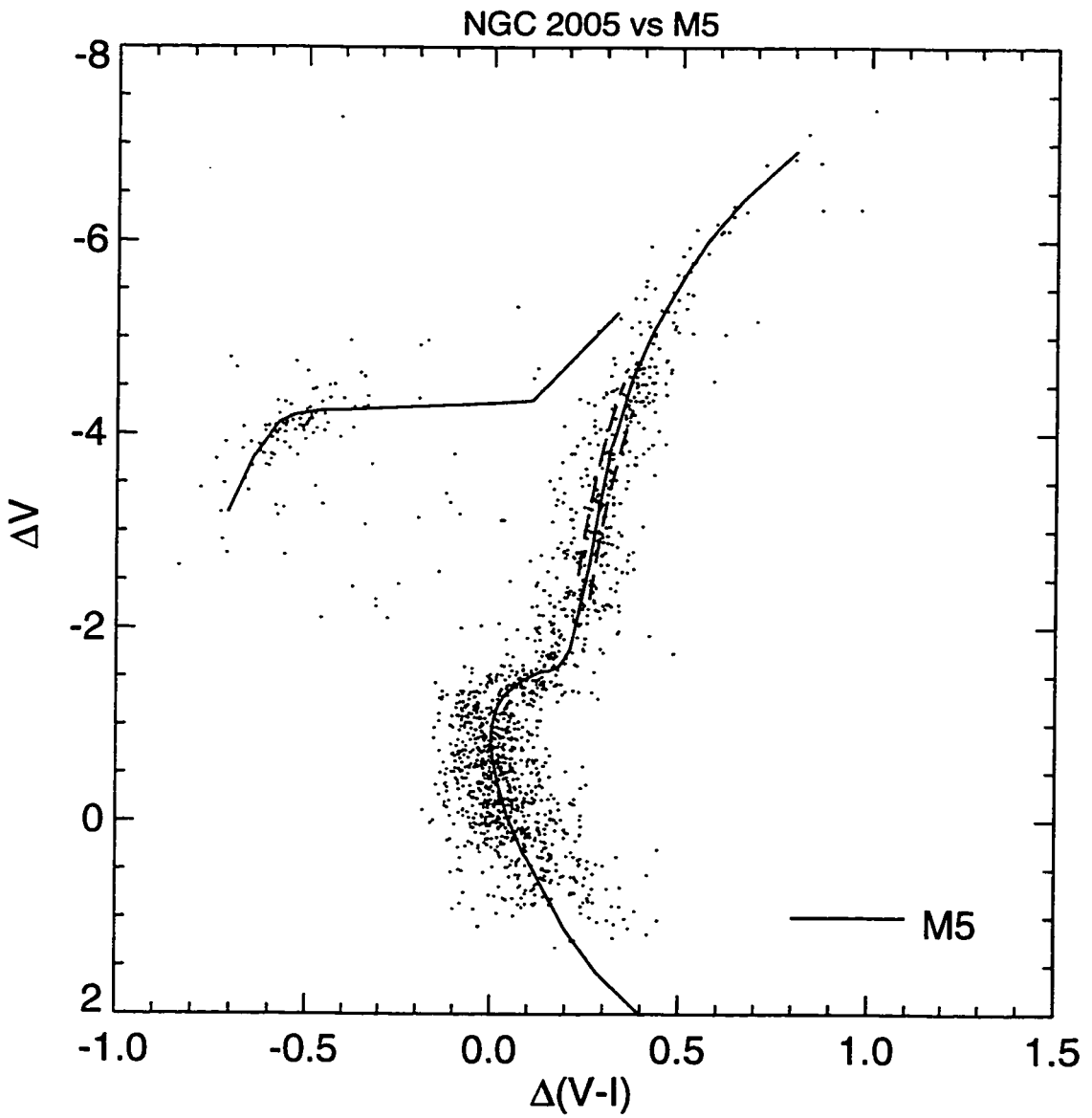

Figure 3.1g: The color-magnitude diagram of NGC 2005 shifted to match a fiducial sequence of the Milky Way globular cluster M5.

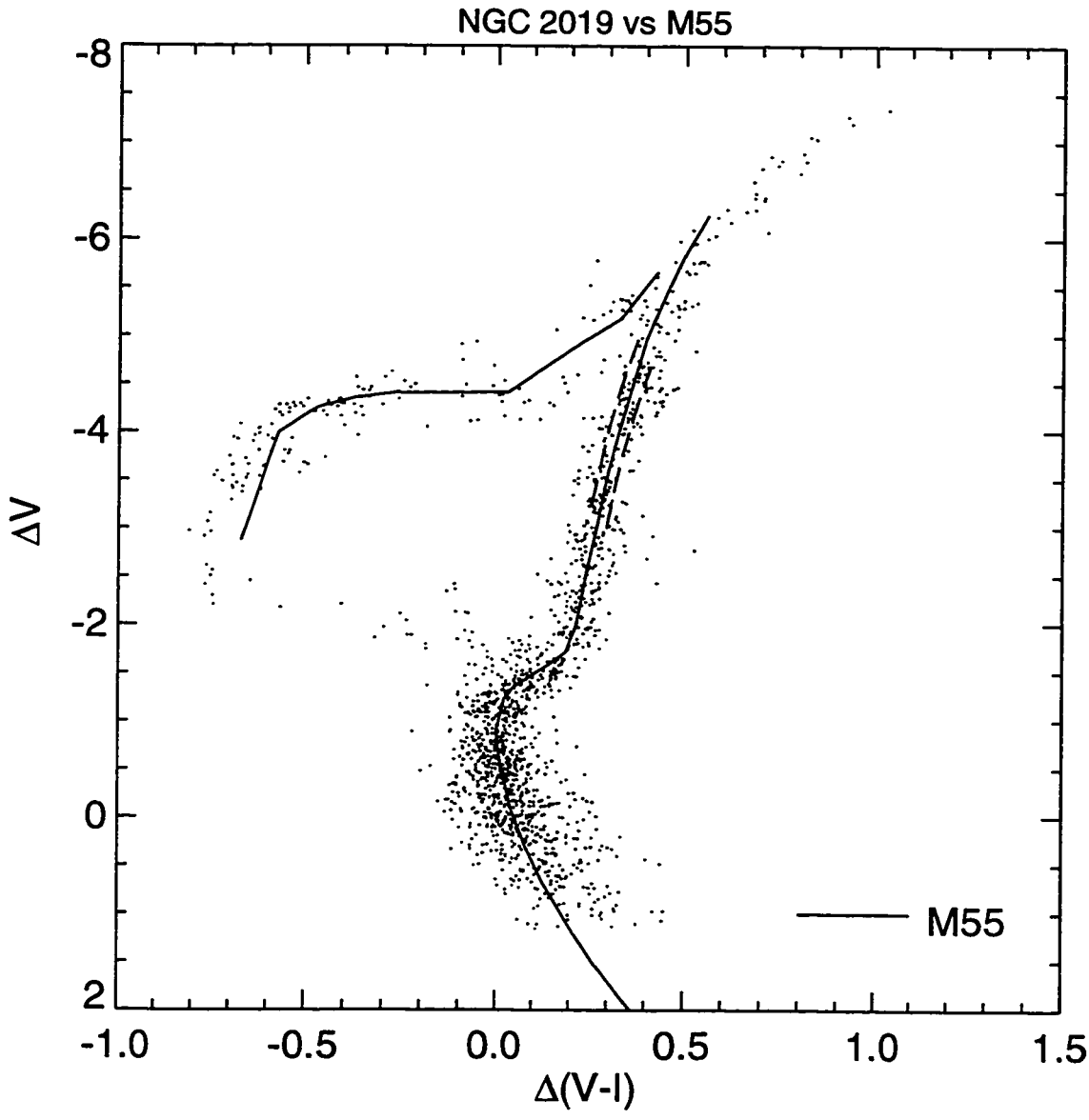

Figure 3.1h: The color-magnitude diagram of NGC 2019 shifted to match a fiducial sequence of the Milky Way globular cluster M55.

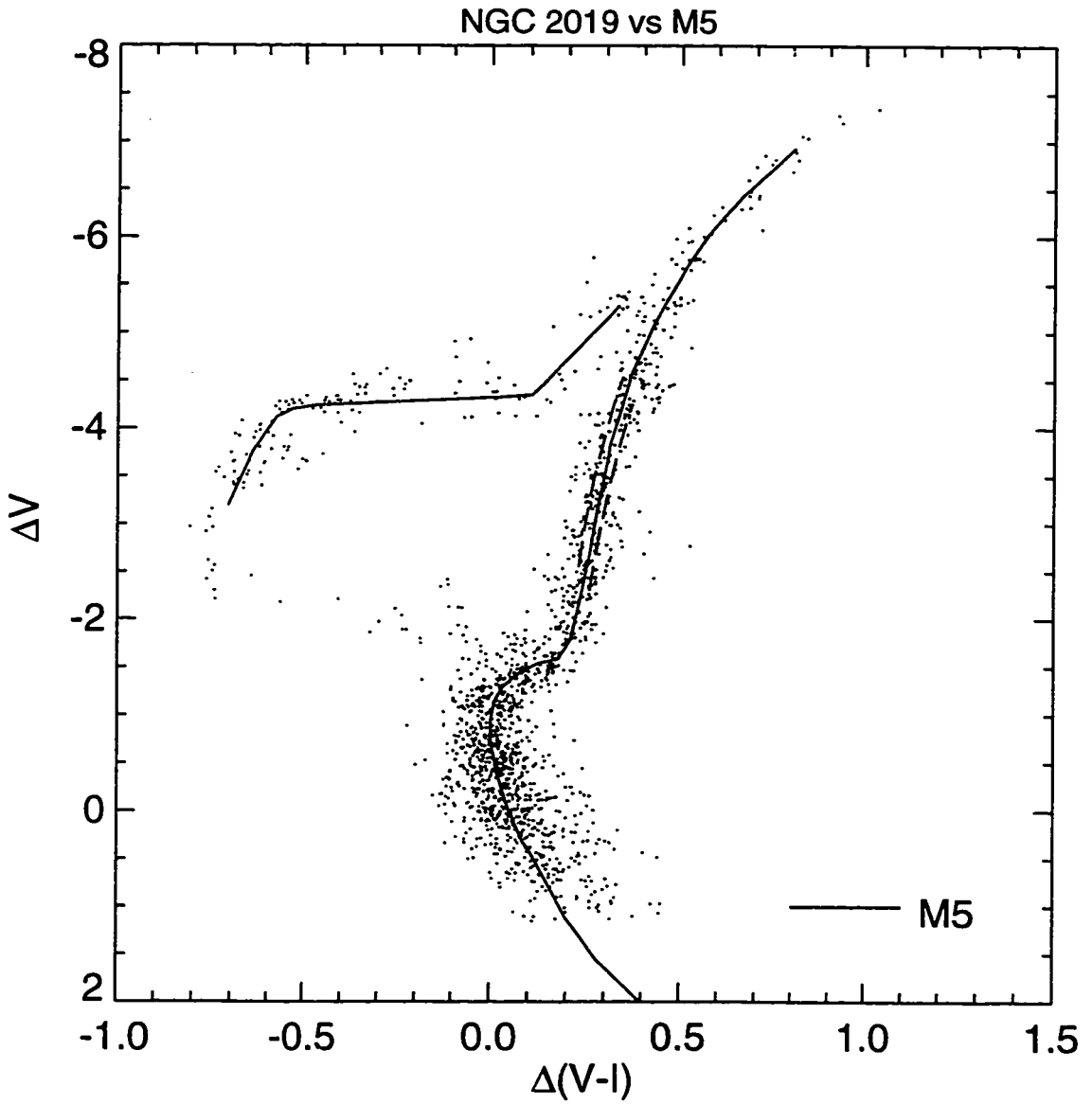

Figure 3.1i: The color-magnitude diagram of NGC 2019 shifted to match a fiducial sequence of the Milky Way globular cluster M5.

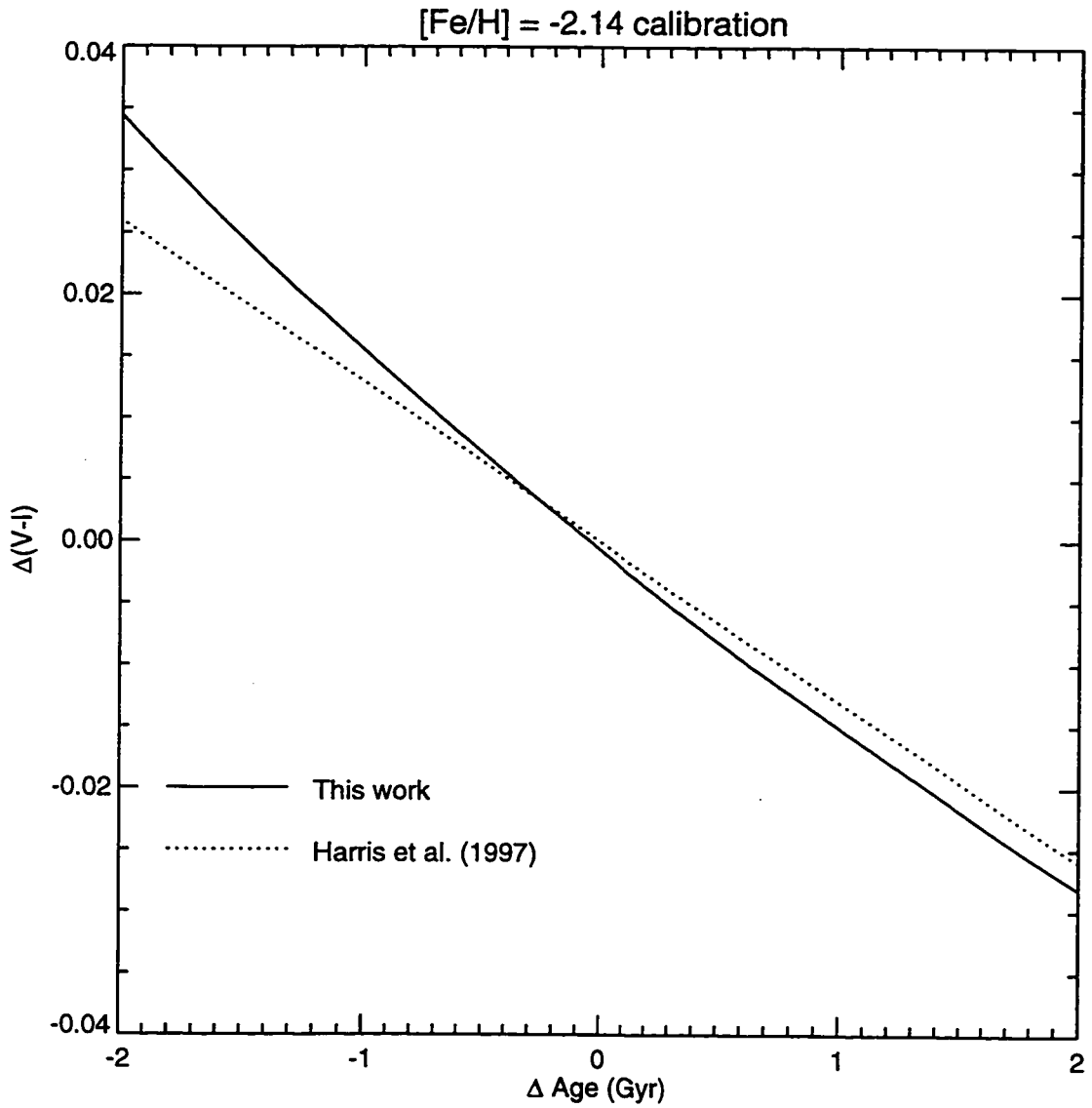

Figure 3.2: Calibration of age difference as a function of color offset of the RGB compared to the calibration of Harris et al. (1997) for the example of [Fe/H]= -2.14. The calibration differences are small compared to the precision of the age measurements.

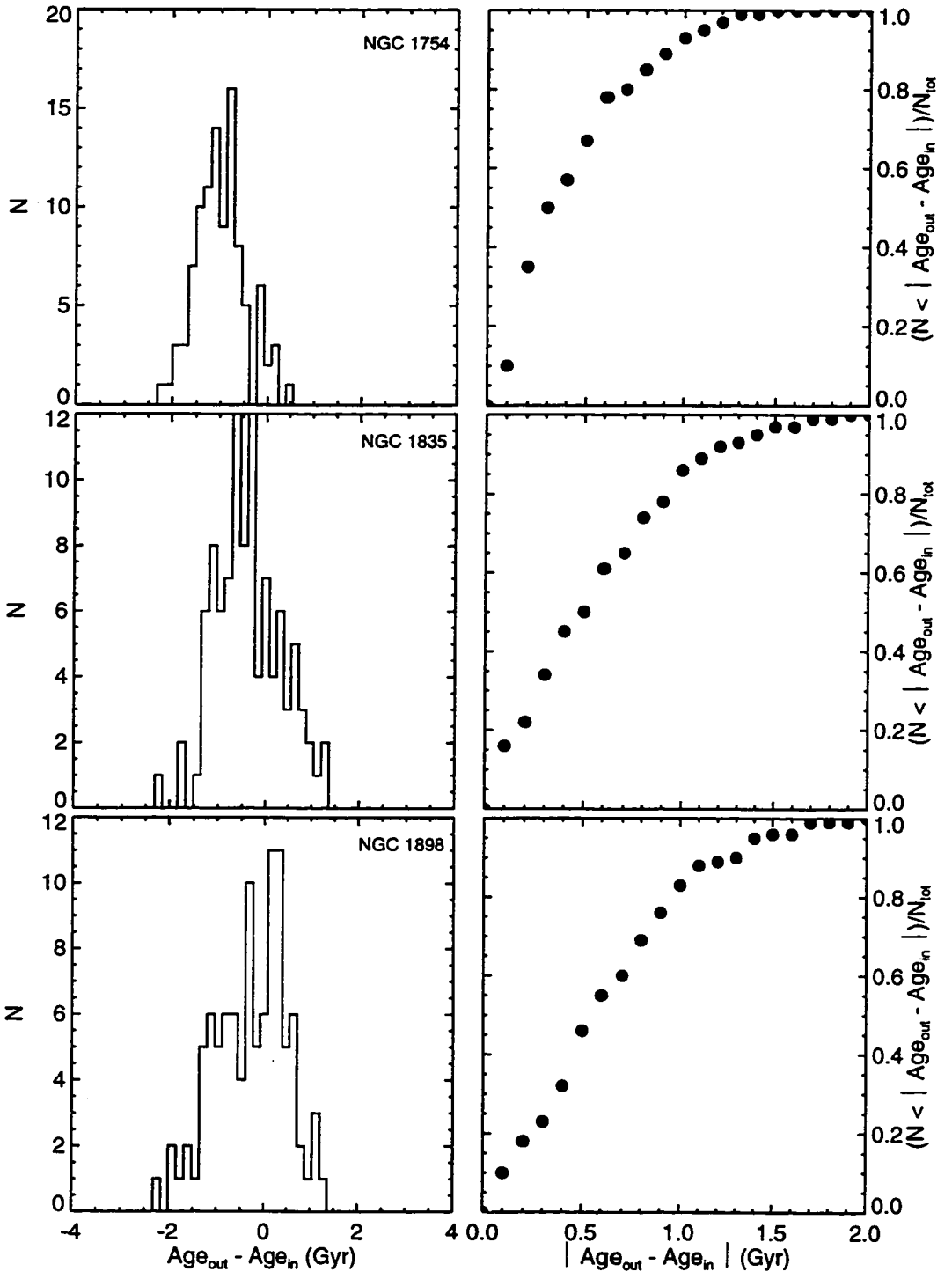

Figure 3.3a: Plots of the distribution of errors in the relative age measurement and cumulative distribution of errors around the mean calculated from the Monte Carlo experiments described in the text, for the clusters NGC 1754, NGC 1835, and NGC 1898. 70% of the cumulative distributions are enclosed within $\lesssim \pm 1$ Gyr. However, each cluster shows a bias of 0-1 Gyr towards measuring younger relative ages.

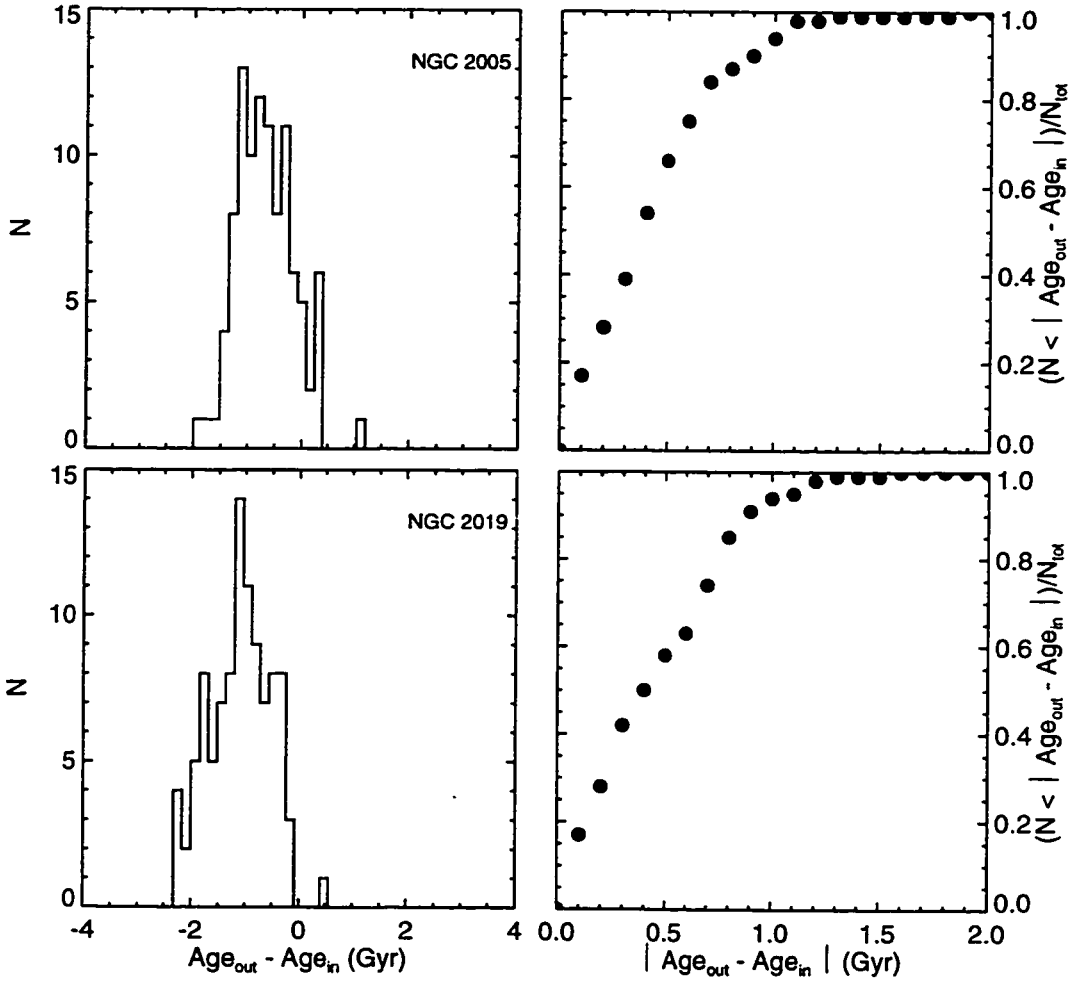

Figure 3.3b: Statistics from Monte Carlo experiments for the clusters NGC 2005 and NGC 2019.

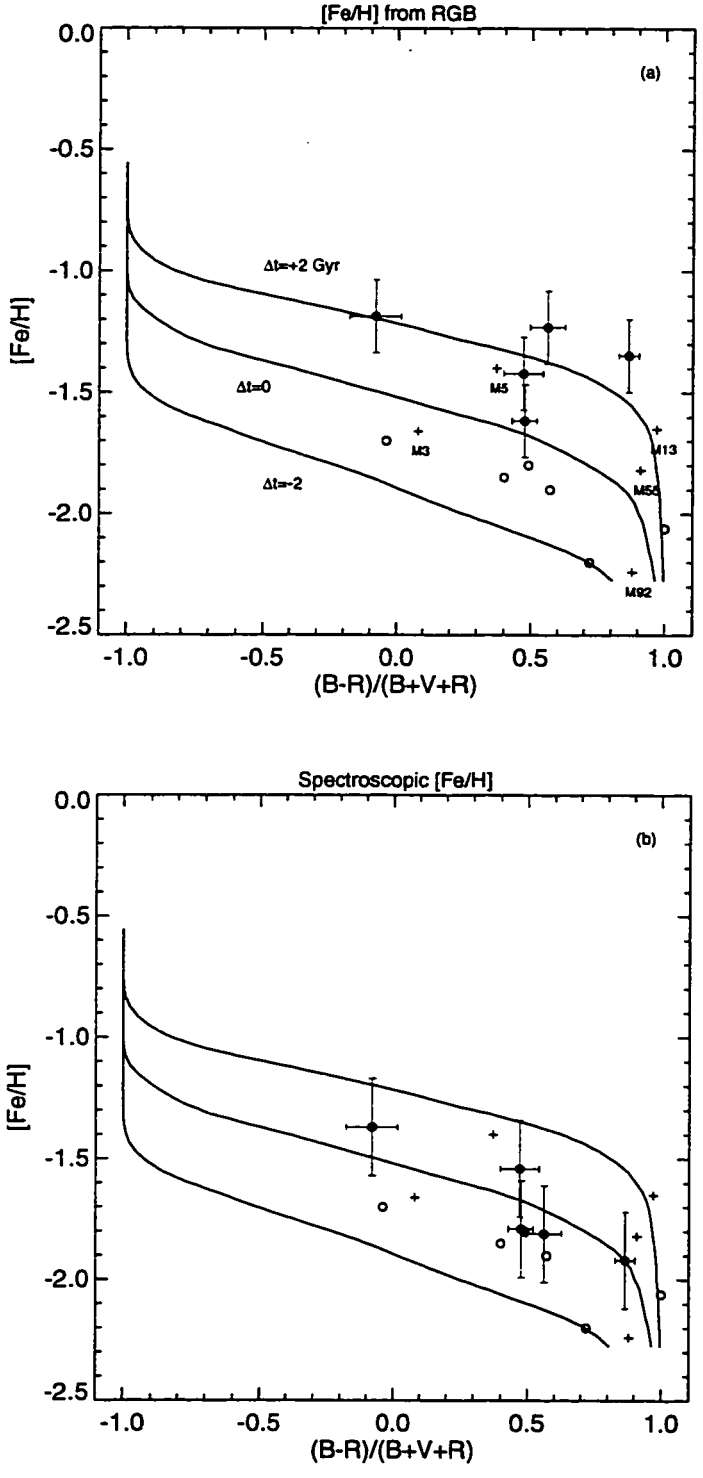

Figure 3.4: Comparison of the horizontal branch morphologies of the LMC clusters of this study (filled circles), LMC clusters from Walker (1992b) (open circles), and Milky Way comparison clusters used in this study (crosses) using the the CMD-based abundances (*a*) and the spectroscopic abundances of Olszewski et al. (1991) (*b*). The solid lines are HB evolutionary tracks from Lee et al. (1994) showing age differences of ± 2 Gyr.

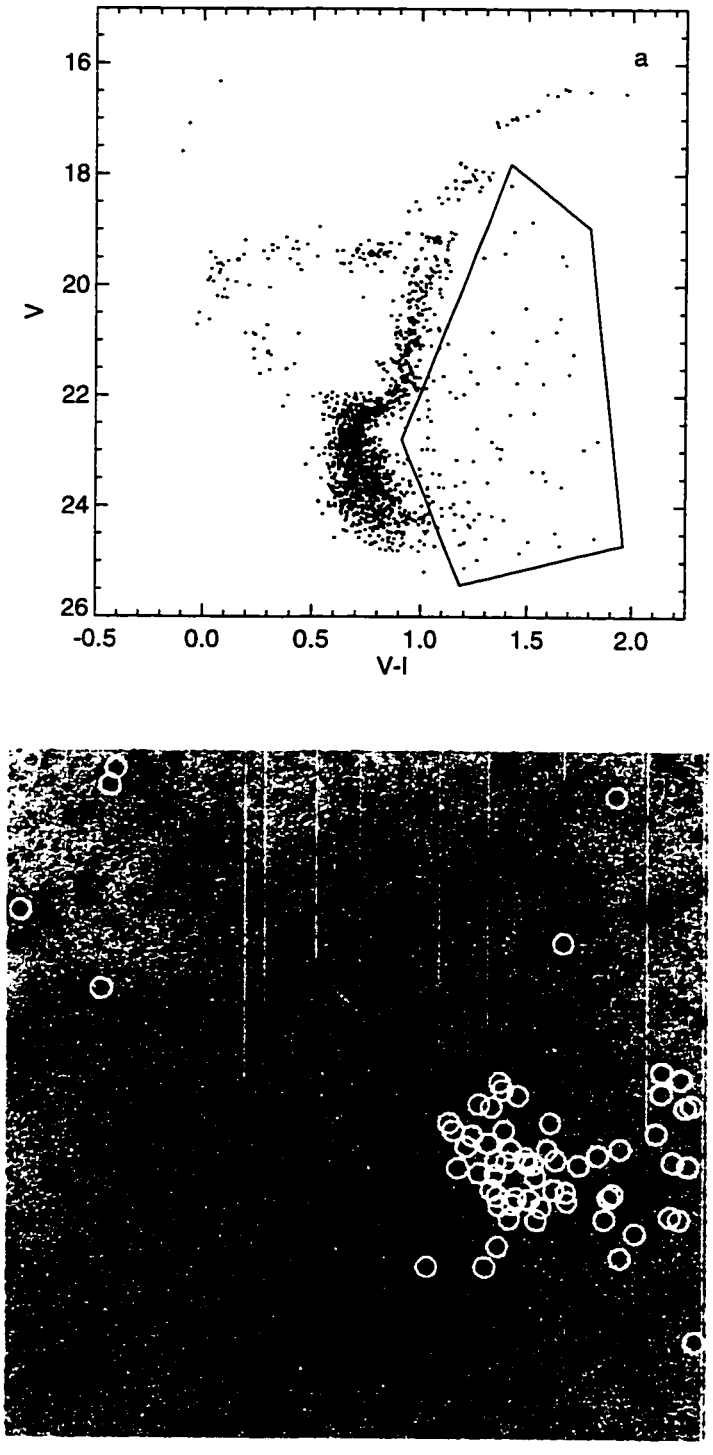

Figure 3.5: (*a*) The peculiarly red stars in the color-magnitude diagram of NGC 1898 were selected within the bounding polygon shown and their positions displayed on the image in (*b*). The selected stars are heavily concentrated towards a region of the image with noticeably lower star density, and are therefore very likely highly reddened.

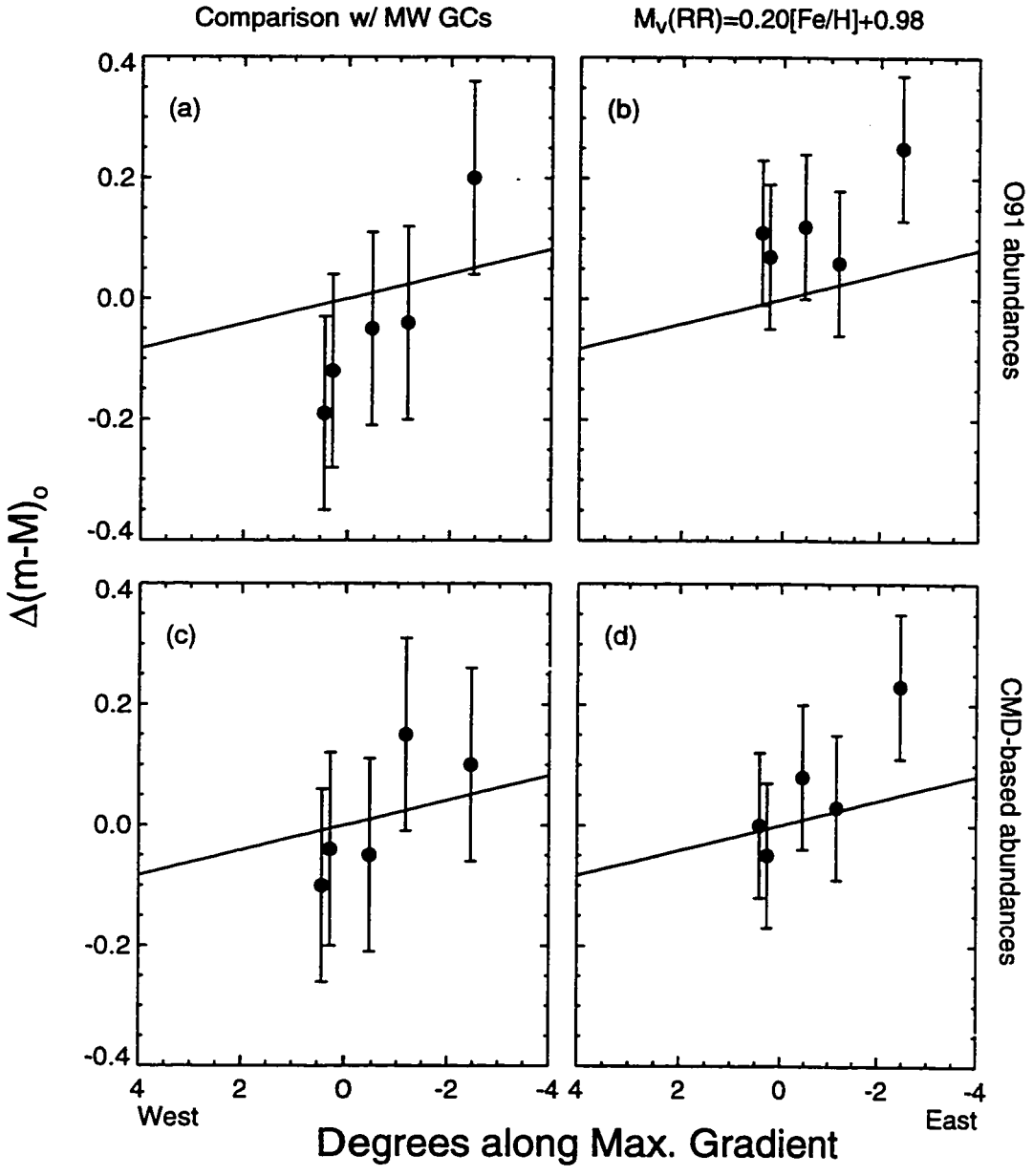

Figure 3.6: Comparison of the distance moduli of the LMC clusters implied by two different methods using two sources of abundances with the model of the tilt of the plane of the LMC of Caldwell & Coulson (1986). (*a*) and (*b*) incorporate the spectroscopic abundances of Olszewski et al. (1991) while (*c*) and (*d*) use the CMD-based abundances. (*a*) and (*c*) show the distances implied by the comparison to Milky Way clusters while (*b*) and (*d*) show the moduli implied by the horizontal branches, assuming $M_V(\mathrm{RR}) = 0.20[\mathrm{Fe/H}] + 0.98$ (Chaboyer et al. (1996). A modulus of 18.5 has been subtracted from (*a*) and (*c*) and 18.37 from (*b*) and (*d*) to show the consistency with the distances implied by LMC RR Lyrae observations and the adopted zero points of the $M_V(\mathrm{RR}) - [\mathrm{Fe/H}]$ relation.

Chapter 4

ANALYSIS OF FIELD STAR COLOR-MAGNITUDE DIAGRAMS

> The random sample represented by the nearby stars certainly includes a large range of masses, possibly some variety in initial composition, and most likely a great mixture of stellar ages. A great variety of evolutionary tracks therefore is involved ... and their disentanglement seems somewhat hopeless.
>
> – M. Schwarzschild 1965, Structure and Evolution of the Stars (New York: Dover), p. 2

4.1 Introduction

Like that of the nearby stars referred to by Martin Schwarzschild, color-magnitude diagrams of the field stars of the LMC are represented by a superposition of evolutionary tracks of a wide range in age, mass, and almost certainly chemical composition. These stars comprise the biggest fossil record of the star formation history in the LMC, making their analysis of strong interest for mapping the LMC's evolution. However, extracting the star formation history from the field star color-magnitude diagrams indeed appears to be a daunting if not entirely hopeless task. Luckily, modern tools now allow astronomers to attack the problem with brute force on a scale that Schwarzschild could not have done. The recent explosion in papers on the star formation histories of the Magellanic Clouds and of other Local Group galaxies (see Chapter 1) is witness to both the increasing power of telescopes used to gather color-

magnitude diagrams of these galaxies and the speed with which theoretical models can be compared with the observations.

In this Chapter, we describe the approach used to extract the star formation histories from the field star CMDs (Figs. 2.8) and the results of our analysis. We begin the discussion by showing what can be learned from a simple comparison of the CMDs with stellar evolutionary tracks. We then show comparisons of our NGC 1754 field star color-magnitude diagram with two sample model star formation histories similar to ones discussed in the literature. These preliminary analyses are used to motivate our method for fully exploring the parameters that affect the extracted star formation histories. This method, which is fairly automated, provides a "best-solution" star formation history for each field, allows us to easily see the effects of varying the input parameters on the star formation history, and allows us to calculate errors on the best-fit parameters through Monte Carlo simulations.

4.2 Preliminary Analysis of the Field Star Color-Magnitude Diagrams

4.2.1 Comparison with Stellar Isochrones

Throwing out the assumption of coevality that was made for the analysis of the clusters, we find that the distribution of stars in the field star CMDs is, to a first approximation, governed by the star formation rate as a function of time, SFR(t), the chemical evolution history, Z(t), the initial mass function (IMF), the reddening, $E(B-V)$, and the true distance modulus, $(m\text{-}M)_o$. Because of the degenerate and non-trivial effects that these parameters have on the observed colors and magnitudes, it is impossible to derive their quantities from a by-eye comparison with stellar models. However, useful limits can be set on some of the parameters from such a comparison.

Figs. 4.1 show the NGC 1754 field star CMD overlaid with Bertelli et al. (1994; hereafter B94) isochrones of two different metallicities, one similar to the metallicity of the young LMC stellar population and the other similar to that of an old metal-

poor population. The isochrones have been shifted to a distance modulus of 18.5 and a reddening of $E(B-V) = 0.12$. Even if the reddening and distance modulus were varied, it is clear that neither set of isochrones can simultaneously match the upper main sequence and the giant branch. In addition, the metal-poor isochrones fall on the blue edge of the lower main sequence when the old isochrones are made to fit the RGB, while the metal-rich isochrones fall on the red edge of the lower MS when they are forced to fit the upper MS. These comparisons give good evidence that a range of metallicities is represented by the field star CMDs.

We can also get some handle on the range of possible reddenings by assuming that the LMC distance modulus falls in the range $(m\text{-}M)_o = 18.4 - 18.7$ (Schommer, Olszewski, & Aaronson 1984, Feast & Catchpole 1997) and then trying fits of the isochrones to different features of the CMDs. By trying fits to the upper and lower MS and the giant branch with the isochrones described in the previous paragraph, we find likely ranges of $E(B-V)$ of 0.04–0.12 for all of the fields.

4.2.2 Two Simple Star Formation Histories

As discussed in Chapter 1, there is some disagreement between past studies of the star formation history of the LMC. At the heart of the disagreement are the conflicting results from the studies of Bertelli et al. (1992; hereafter B92) and Holtzman et al. (1997; hereafter H97). These studies observed fields in nearly the same location of the LMC but differed in the telescopes used and in their theoretical approaches. B92 used the CTIO 4-m to observe three fields, one of which is near the cluster NGC 1866. They pioneered the use of ratios of star counts in carefully selected areas of their CMDs to solve for the strength, time of onset, and duration of an assumed burst in the past star formation rate, finding a preferred model where the star formation rate increased by a factor of ten ~4 Gyr ago. Gallagher et al. (1996) reported on *HST* WFPC2 data of a similar field near NGC 1866, which H97 used to explore the LMC star formation history. Analyzing the luminosity function of these data, H97

found that the recent burst of star formation activity suggested by B92 is $\sim$3 times weaker when considered from the WFPC2 data.

To explore the possibilities raised by these two studies and to learn how best to proceed with a full analysis of our CMDs, we tested two simple model star formation histories against our NGC 1754 field star CMD. Model 1 is similar to the star formation history preferred by B92. It consists of constant star formation until 4 Gyr ago, after which the SFR increases by a factor of 10. Model 2 consists of purely constant star formation from 15 Gyr ago to the present. Model 2 was originally motivated by the finding of Gallagher et al. (1996) that constant star formation fits their NGC 1866 field HST data better than a model incorporating a strong recent star formation burst, but it is also qualitatively similar to the preferred model of H97. In both models, we used an abundance of Z = 0.0004 for ages older than 4 Gyr, while for younger ages we used Z = 0.008, which is similar to the abundance of the young LMC stellar population. We also include the cluster contamination as a component to the star formation history, since for these tests we did not use the cleaned CMDs. Figs. 4.2 show a schematic of the star formation histories represented by Models 1 and 2.

To compare the model star formation histories with the NGC 1754 field star CMD, we constructed model CMDs using the Bertelli et al. (1994; hereafter B94) isochrones. These isochrones are well-suited for our purposes because they model every post-main sequence evolutionary phase, incorporate the recent OPAL opacities (Rogers & Iglesias 1992), and are calculated for V and I, our observed passbands. Their main drawback is that they are difficult to interpolate, as they are not tabulated according to common evolutionary points. We found it necessary to interpolate the isochrones because we needed the ability to select stars of random masses and ages that are not included in the coarse grid of B94. We performed the interpolation by breaking the isochrones into segments which appeared to correspond to common features. Each of these segments was then broken into an equal number of mass points, between which we linearly interpolated to create the new isochrone of the desired age.

For each model star formation history, we selected ~50000 stars with masses randomly chosen from a Salpeter mass function ($N(m) \propto m^{-2.35}$) and with ages distributed according to the profiles shown in Figs. 4.2. For the sake of speed, we lumped ages together onto a number of single isochrones, spaced closely enough to form a grid generally finer than the typical photometric photometric errors. While doing this will not model the fine scale structure of the CMD correctly, the resolution afforded is sufficient for the simple tests described here. $V-I$ colors and V magnitudes were then calculated for the selected stars through the interpolated isochrones. Figs. 4.2 also show the resulting model CMDs.

To account for the observational errors, we used the results of an artificial star experiment similar to the ones described in section 2.5 of Chapter 2. Because the model stars were all drawn from the B94 isochrones, we used those isochrones to define the artificial star set for the experiment. The artificial stars were chosen from a grid encompassing the full set of isochrones, including all ages and metallicities. Enough stars were selected to adequately model the photometric errors as a function of $V - I$ and V.

Figs. 4.3 show the input and recovered artificial star CMDs. These CMDs were used to directly simulate the errors in the CMDs of Models 1 and 2. First, we placed the stars from Figs. 4.2 on the same grid used to select the artificial stars. For each grid box containing model stars, we then calculated the two-dimensional histogram of the recovered $V-I$ and V of all of the artificial stars originally placed in the box. This distribution accounts for both photometric scatter and incompleteness, as artificial stars not recovered were not added to the histogram. Each histogram was then scaled by the number of model stars in the box. The final distribution was normalized to unit area, yielding the probability distribution for observing stars in the $(V - I, V)$ plane for the given model star formation history.

In Figs. 4.4, we compare Models 1 and 2 to the field star CMD of NGC 1754. The figures show the residuals obtained when the model CMDs, which have been scaled

to contain the same total number of stars as are in the observed CMD, are subtracted from the binned observed CMD. Bright shadings are used to represent regions where too many stars are predicted by the models while the dark shadings represent an excess of observed stars compared to the models. Both images are scaled to the same levels. The most striking feature of both residual maps is the presence of adjacent dark and bright stripes running along the lower main sequence. As this feature mimics the step function used to describe the chemical evolution in our model star formation histories, we quite possibly are using too simplistic a model for the chemical evolution. The pattern of the residuals suggests that we have included too many metal-poor stars and not enough metal-rich ones. This comes as no surprise, since we used a population II-like abundance of Z=0.0004 up to the relatively young age of 4 Gyr. The feature could also be produced by or contributed to by an error in the assumed reddening of $\sim$0.1 magnitudes or a large error in the distance modulus. Other features in the residuals are more subtle, but still evident. Model 1, which included a strong recent burst of star formation, predicts too many blue main sequence stars. A similar feature is seen in the Model 2 (constant star formation) residuals, but it is weaker. While a fairly large error in the reddening could be partly responsible for this feature, it suggests that the strong star formation burst found by B92 is not seen in the NGC 1754 field CMD.

What have we learned from the tests of the two model star formation histories? While we showed that at least one of our fields does not seem to be represented by strong recent star formation activity in the LMC, we did not produce a model star formation history that fits our observations well. However, the ways in which our test models did not fit the data point to several areas for improvement. For instance, we found that the step function used to model the chemical evolution was overly simplistic. While we could add a single intermediate step in the chemical evolution model, as was done by H97, a better approach would be to adopt a chemical evolution model based more firmly on observations, such as the abundance distribution of LMC

clusters. In addition, errors in the assumed reddening and distance modulus can affect the star formation history that is derived for an observed CMD. We need to explore the effects of varying the reddening and distance modulus in the models and, if possible, solve for their probable values. Finally, we need to explore a much larger range of SFR(t) than was done in Models 1 and 2.

4.3 Automated Method for Extracting Star Formation Histories

4.3.1 Basic Description

For the full analysis of the field star CMDs, we would like to produce "best-fit" solutions of the star formation histories with as high as possible resolution in age and allowing the reddenings, distance moduli, and IMFs to vary. Within each age bin of the solutions, we want to allow the SFR to take on a number of possible values. If we were to continue the approach of constructing template star formation histories as done in the previous section and by some other studies (Gallart et al. 1996, Aparicio, Gallart, & Bertelli 1997), the number of models we would need to construct would be exceedingly large. For example, if we wished to extract a star formation history containing a modest number of 10 age bins spanning the range of 10 Myr – 15 Gyr with 5 possible values for the SFR within each bin, and we wished to test a small number of different IMFs, reddenings, and distance moduli, we would need to construct $> 10^7$ model star formation histories. As each model needs to contain at least as many individual stars as the observed CMD, our available computing resources would be greatly overmatched.

A much faster and more convenient approach is to treat SFR(t) as a free parameter for which we find the best solution for a given input model. The number of model star formation histories we need to construct is then vastly decreased, and is simply equal to the number of combinations of IMFs, reddenings, and distance moduli we wish to test times the number of age bins in the solution. An additional advantage

of this approach is that a fit parameter can be used to test the goodness-of-fit of the models and errors can be calculated from statistical arguments or through Monte Carlo simulations. An implementation of such an approach was first discussed by Dolphin (1997), who used χ^2 as the fit parameter and singular value decomposition (SVD; Press et al. 1992) to solve for the best-fit star formation history from a suite of models with a number of different IMFs, reddenings, distance moduli, and abundances. Dolphin (1997) applied the method to simulated CMDs to test the accuracy with which the input parameters could be recovered, but did not apply the method to actual observations.

We used the principles of this automated approach to construct a method to extract the star formation histories from our field star CMDs. The method consists of four basic steps, which we describe in the following sections.

4.3.2 Construction of the Model Star Formation Histories

As was done in section 4.2.2, the B94 isochrones were used to select stars to represent the CMDs of the model star formation histories. Because we included a detailed chemical evolution history, we needed to interpolate the isochrones in metallicity as well as age. Because the selection by eye of points on the isochrones separating equivalent evolutionary phases was a cumbersome process as well as being subject to error in judgement, we chose instead to break the isochrones into segments based on the characteristic evolutionary phases listed in Tables 7–12 of B94, an electronic copy of which was kindly provided by G. Bertelli. This approach had the advantages of being faster and is based on fundamental properties of the isochrones, but suffered occasionally from problems that rational judgement could easily avoid.

Fig. 4.5 shows two sample isochrones with ages of 100 Myr and 1 Gyr and [Fe/H]$\sim$-0.4, with the evolutionary points of B94's Tables 7–12 overplotted. Isochrones with a large difference in age are shown to emphasize the changes that occur in position of the phases. With our interpolation technique, each of the segments lying between

consecutive evolutionary points was broken into a number of mass bins. A new isochrone could then be interpolated point-by-point from adjacent isochrones, with the segments ensuring that the isochrone shape was preserved. We encountered a few problems, however. A problem of a minor nature was that we discovered that the $V-I$ and V for the masses of the evolutionary phases listed in B94's Tables 7–12 were often inconsistent with those tabulated in the isochrones. Instead of using $V-I$ and V from Tables 7–12, we therefore used the $V-I$ and V from the isochrones for the points nearest the masses in the Tables. Another small difficulty is that the number of evolutionary points listed in B94's Tables 7–12 occasionally changes for isochrones of different ages and different metallicities, as is the case for the isochrones shown in Fig. 4.5. For isochrones affected by these changes, we used our best judgement in deciding the correct mapping. A more serious problem is that large changes in the curvature of the isochrones do not always correspond with evolutionary points listed in the tables. Fig. 4.6 illustrates this problem. The solid lines are isochrones with log ages of 8.0 and 8.1 years and [Fe/H]$\sim$-0.4, while the dotted line is an interpolated isochrone with log age of 8.05. While the interpolated isochrone faithfully reproduces the shape of the adjacent ones over most of the isochrone, even on the blue loop, it deviates on the asymptotic giant branch. This is because there is no evolutionary point in Table 10 of B94 designating the finish of the blue loop and the start of the AGB. Figs. 4.7 show sample interpolated isochrones from the set of isochrones of all metallicities. Separate panels are shown for $M_V > 0$ and $M_V < 0$ so that the details may be seen clearly. While the interpolated isochrones have a number of areas where they deviate from the correct shape, the deviations occur primarily in short-lived phases of stellar evolution. We therefore did not attempt to correct the problems, as few of the stars in our observed CMDs will occupy these phases.

Using our interpolation technique, we constructed a finely spaced grid of isochrones to enable us to simulate stars of random ages and a wide selection of metallicities. We interpolated the B94 isochrones onto a grid of log ages ranging from 6.6 to 10.2 with

steps of 0.0024 log yrs and -1.33 $\leq$ [Fe/H] $\leq$ -0.3 with steps of 0.0015 dex (converted from Z using $Z_{\odot}$=0.02 and assuming a solar abundance set). The lower end of the metallicity scale was chosen to be equal to the average abundance of the metal-poor globular clusters studied in Chapter 3 while the upper end was chosen to equal the metallicity of the young LMC population (Olszewski et al. 1996). Provided a list of stars of given masses, ages, and metallicities, we could then calculate $V-I$ and V for the stars by looking up the appropriate isochrone in the grid and interpolating from the mass.

We simulated the CMDs of star formation histories using reddenings of $E(B-V)$=0.04$-$0.12 with steps of 0.02, distance moduli of 18.4$-$18.7 with steps of 0.1, and IMF slopes of x=1.5, 2.0, 2.35, and 3.00, where the IMF is given by the proportionality $N(m) \propto m^{-x}$. The combinations of parameters are summarized in Table 4.1. The ranges of $E(B-V)$ were chosen to span the likely range for these fields, the distance moduli include both the "short" and "long" distance scales, and the IMFs were picked to span the range of a number of derivations of the IMF in the LMC. The chemical evolution model adopted was linear in age with a slope of -0.073 dex Gyr^{-1} and a zero point of -0.3 dex. This model, shown in Fig. 4.8, agrees with the chemical evolution suggested by LMC clusters (Olszewski et al. 1996), with ours having a slightly higher metallicity at older ages that reflects our readjustment of the abundances of the inner globular clusters over Olszewski et al. (1991). For each of these models, we simulated separate CMDs within 36 logarithmic age bins with log widths of $\sim$0.08, or 20% of the age of the bin. We chose to use logarithmic age bins to compensate for the fact that isochrones are spaced more closely together at larger ages, decreasing the resolution with which one can discriminate between populations of different ages. The number of bins was chosen to approximately match the resolution with which we could hope to extract the star formation history from the observed CMDs.

Within each age bin, we then selected 20000$-$30000 stars with randomly distributed ages and masses, with limits on the ages imposed by the bin edges and

limits on the masses set approximately equal to the maximum and minimum masses of stars on the isochrones within the age bin. The number of stars was chosen to greatly exceed the number expected in the observed CMDs so as to limit counting statistics in the models, yet be smaller than the number of artificial stars available for simulating the errors. In order to increase the sampling of stars with higher masses, we selected the masses from a flat MF (x=0.0) but assigned each star a weight as if it were selected from the desired IMF of the model. After all stars were selected, we calculated the total mass in stars within each age bin, adding to this total the integral of the IMF over the range $0.08 \leq M \leq 120$ $M_{\odot}$ but excluding the mass range occupied by the simulated stars. The total mass represented in the age bin was then used to calculate the star formation rate within each age bin.

Photometric errors were applied to the model CMDs through the use of the artificial star results described in Chapter 3. For each star in the simulated CMD, we randomly selected a nearby artificial star. If the artificial star was not recovered during photometry, we removed the star from the simulated CMD. Otherwise, the star was moved according to the photometric shifts experienced by the artificial star. To increase the number of artificial stars from which we could simulate the errors, we allowed the program to pick artificial stars of a restricted range in magnitude but of any color. Because stars experience systematic photometric shifts that depend on color, we corrected for the different systematic shifts before moving the model stars.

We stored the simulated CMDs as density histograms by binning the output CMDs in bins of 0.0625 in $V-I$ and 0.2 in V. At this stage, the weights to bring the CMDs into keeping with the desired IMF were applied and the histograms were scaled so that each age bin represents a star formation rate of 1 $M_{\odot}$ yr^{-1}. Figs. 4.9 shows a sample raw simulated CMD, the simulated CMD with photometric errors, and the binned CMD density histogram, all summed over the 36 age bins.

4.3.3 Comparison of Model CMDs with Observed CMDs

For this work, we chose to use a parametric fitting technique, such as that of Dolphin (1997) and Ng (1998), to compare the fit of our models to the observations. However, a χ^2 parameter is not ideal for our application, as χ^2 is highly sensitive to outlying points. We instead chose to minimize the following parameter, which is derived from the Lorentzian distribution (Press et al. 1992):

$$P_{\rm Lor} = \sum_i \log\left(1 + \frac{1}{2}\left(\frac{O_i - M_i(\vec{x})}{\sigma_i}\right)^2\right)$$

where O_i are the observed number of stars in the CMD at grid point i, $M_i(\vec{x})$ is the number of stars predicted at grid point i by the model with parameters $\vec{x}$, and σ_i is the uncertainty in the number of stars at i, which we calculated from the models assuming Poisson statistics. The Lorentzian, with its large tails, is much less sensitive to outliers than χ^2. We expect to find outliers when comparing our observations to the models for several reasons. A primary reason is that the model isochrones used to generate the model CMDs do not perfectly describe the process of stellar evolution, especially for the evolved phases. In addition, we are assuming that a single reddening, distance modulus, and IMF is appropriate for all of the stars in a single CMD, and that all stars of a single age have the same metallicity, while in reality there will likely be some spread in these quantities. As long as the bulk of the stars are described by our single parameters, the remaining stars may be treated as outliers. For the NGC 1916 field, the assumption of a single reddening is clearly strongly violated, so that differential reddening must be included for a viable model fit. Finally, it is unlikely that we have exactly reproduced the photometric errors through our artificial star tests, and there could be significant "tails" in the photometric distributions that we have not modeled correctly.

4.3.4 Method for Solution of SFR(t)

For each model with different $E(B-V)$, distance modulus, and IMF we solved for SFR(t) by finding the linear combination of the 36 CMDs representing different ages that best matched the distribution of stars in the observed CMD. Because our models are normalized to represent a star formation rate of 1 $M_\odot$ yr^{-1}, this linear combination will produce SFR(t) in units of $M_\odot$ yr^{-1} over the area of the field. A partial code for producing the solutions was kindly provided by A. Dolphin, which we rewrote and amended for our purposes. The program finds the best match by minimizing $P_{\rm Lor}$, using the *Numerical Recipes* routine **amoeba** (Press et al. 1992), which is an implementation of the downhill simplex method (Nelder & Mead 1965). Given a starting guess at the correct values of the fitted parameters and the likely scale of the parameters, **amoeba** searches the N-dimensional parameter space for a minimum in the surface, stopping when small changes in the parameters change the value of the function by less than a given amount, which we set to be slightly larger than the machine precision. Because **amoeba** stops when a minimum is found, the minimum may not be the desired global minimum. To more thoroughly search the $P_{\rm Lor}$ surface for a global minimum, **amoeba** was restarted several times with the new input guess and scale of the parameters set equal to the previous output. After 4-5 restarts, **amoeba** returned to the same minimum as the previous run, indicating that no other nearby minimum exists. In this fashion, we established solutions of SFR(t) for each model with different $E(B-V)$, distance modulus, and IMF. Within each IMF, the best overall model was chosen as the one with the lowest value of $P_{\rm Lor}$.

4.4 Tests

We tested the ability of the method to solve for SFR(t) and identify the correct $E(B-V)$ and $(m\text{-}M)_o$ by producing a CMD representing a simple star formation history and running it through the solution procedure. The test case was constructed

by taking a model with a uniform star formation rate and adjusting the star formation rate in each age bin by a randomly selected amount. To avoid using pre-existing knowledge of the star formation history to our advantage during the solution, the input star formation history was kept secret until after the solutions were made. Choosing $E(B-V) = 0.08$, (m-M)$_o$ = 18.5, and x = 2.35 for the IMF slope, we simulated a CMD for the test case by selecting 1000 stars in each age bin from the interpolated B94 isochrones, to which we applied the completeness fractions and photometric errors derived for the NGC 1754 WF frames. We binned this simulated CMD to the resolution of the models. We also smoothed both the test CMD and the model CMDs with a Gaussian having a dispersion of one bin width, as we found that this limited the stochastic effects imposed by the binning. Fig. 4.10 shows the input star formation history for the test case.

Making a starting guess at the star formation rate in each bin, we used 4 iterations of amoeba to find the best-fit coefficients of the models in each of the 36 age bins and each value of $E(B-V)$ in the range 0.04–0.12, (m-M)$_o$ in the range 18.4-18.7, and x = 2.35. Fig. 4.11 shows the computed $P_{\rm Lor}$ surface as a function of $E(B-V)$ and (m-M)$_o$. The minimum of the surface occurs at $E(B-V) = 0.08$ and (m-M)$_o$ = 18.5, in agreement with the input values. Fig. 4.12a shows the star formation history derived for the minimum $P_{\rm Lor}$, compared with the input. While qualitatively similar, the output is clearly very noisy, mimicking a "bursting"-type star formation history. As the problem appears to be one of age resolution, we redid the solutions after grouping several age bins of the models together. Figs. 4.12b-d show the best-fit solutions to the star formation history after grouping every 2, 3, and 4 models together. These solutions agree much better with the input model, although the young and old age bins still show signs of excessive noise.

Two factors contribute to the limiting age resolution of the star formation history solutions: the number of stars that fall within each age bin and the spacing of the models in the CMD. The first factor is a function mainly of the number of stars

in the observed CMD while the second is a function of the age of the models and the photometric errors. Grouping the models together has the effect of reducing the contribution of both factors; the number of stars within each age bin is increased while the spacing between the models also increases. To describe the effects that the number of stars and the model spacing have on the errors in the solution, we ran repeated tests using the model star formation history described above with varying numbers of stars in the simulated CMDs. Table 4.2 lists the parameters of the tests and the number of runs for each test. We used these runs to calculate the dispersion in the recovered star formation rate as a function both of age and number of stars in the age bins. Fig. 4.13 shows the median uncertainty and dispersion about the median uncertainty of the recovered star formation rates over all age bins. The uncertainty in the star formation rates increases exponentially with decreasing numbers of stars per age bin. Fig. 4.6 shows that the dispersion about the median uncertainty for a given number of stars per age bin is due to the effect of the isochrone spacing. At the youngest and oldest ages, the uncertainty in the recovered star formation rate is higher than for intermediate ages, where model isochrones of similar ages are more easily distinguishable. We will bear these effects in mind when discussing the age resolution of the star formation histories derived for the observed CMDs.

4.5 Results for Field Star CMDs and Error Analysis

4.5.1 SFR(t), Best-Fit Parameters, and Errors

The SFR(t) solutions were made following the procedure outlined in section 4.3.4. As was done for the tests described in section 4.4, we binned the observed CMDs to the same resolution as the models and smoothed both the observed and model color-magnitude grids with a Gaussian having a 1-pixel dispersion. We produced separate solutions for each combination of the parameters listed in Table 4.1 and for 18, 12, and 9 age bins. For NGC 1835 and NGC 2005, we found that we needed to add

additional values of the reddening and distance modulus to bracket the full range of best-fit solutions. For each IMF, we found the reddening and distance modulus that best match the observed CMD by choosing the minimum of the $P_{\rm Lor}$ surface, as was done for the test. A sample surface is shown in Fig. 4.14. While the minimum $P_{\rm Lor}$ is well-defined, its value is not as low as those found during the tests, a sign that the model isochrones as input do not agree perfectly with the observations.

Tables 4.3 list the derived star formation rates, $E(B-V)$'s, (m-M)$_o$'s, and numbers of stars in each age bin of the star formation history solutions for the 18, 12, and 9 age bins used and the Salpeter IMF. As was shown by the tests performed in section 4.4, the age resolution of the derived star formation histories is a function of age and the number of stars within each age bin. The oldest age bins are well-populated for all the solutions, so we think we can usefully resolve changes in the star formation rate in these bins even for the solutions containing 18 age bins. Because the youngest age bins contain very few stars, the errors in their derived star formation rates will be large. However, as seen in Tables 4.3, the youngest age bins contain few stars even after the bins are broadened, which decreases the effect of the isochrone spacing on the errors. It therefore seems likely that the young bins contain few stars simply because there has been little star formation in these fields over the past $\sim$100 Myr.

We calculated the errors in SFR(t), $E(B-V)$, and (m-M)$_o$ through Monte Carlo simulations using bootstrapped samples of the observed CMDs. We ran 25 simulations for each value of the IMF and produced solutions having 18, 12, and 9 age bins covering the span 0$-$15 Gyr. For each run of the simulations, we resampled the observed CMDs and produced solutions of SFR(t) for each value of $E(B-V)$ and (m-M)$_o$, exactly as was done for the analysis of the true observed CMDs. We chose the best-fit solution from the set by picking the minimum of the $P_{\rm Lor}$ surface. Tables 4.4 list the dispersions of the minimum $P_{\rm Lor}$, $E(B-V)$, (m-M)$_o$, and SFR(t) for each simulation. The variations of the errors with age and number of stars per bin roughly agree with the expectations based on our tests.

Figs. 4.15 show the best-fit star formation histories and errors for each cluster. We show both the 18- and 12-bin solutions to show that the main features are not transient ones due to noise. We only show the solutions obtained for the Salpeter IMF, putting aside for now the effect that varying the IMF has on the derived star formation histories. We found that it was difficult to decide which IMF produced the best fit from our fit parameter, $P_{\rm Lor}$, alone. Figs. 4.16 show the minimum values of $P_{\rm Lor}$ obtained for each IMF, with dispersions in $P_{\rm Lor}$ from the Monte Carlo simulations. While the IMF of x=3.0 appears to be the worst fit in all cases, we can not distinguish between the fits of x=1.5, 2.00, and 2.35

There are several common features in the derived star formation histories shown in Figs. 4.15. All of the fields show significant star formation in the last 3-4 Gyr with roughly the same amplitude, with NGC 1754 proceeding at a rate $\sim 2-3$ times lower than the rest. The star formation has the appearance of a burst in all of the fields, and appears to be in decline over the last $\sim 0.5-1$ Gyr. In the NGC 1754 field, the last large peak in the star formation rate occurred ~ 0.5 Gyr ago, while in the bar fields it occurred ~ 1 Gyr ago. The NGC 1754 field appears to agree with the result of H97, who found an increase in the recent star formation rate by a factor of ~ 3. However, we find that the star formation has not uniformly increased, but has done so steadily up until the recent decline. We do not find evidence for the short burst of star formation ~ 2 Gyr ago found by Gallagher et al. (1996).

While the NGC 1754 field seems to only recently have formed a large number of stars, star formation in the bar fields was active as long ago as $\sim 6-8$ Gyr. Because this star formation appears restricted to the bar, we suggest that the period of 4-8 Gyr ago marks the formation epoch of the bar. This is in contradiction to the suggestion that the bar formed $1-2$ Gyr after the LMC disk (Elson, Gilmore, & Santiago 1997). Our results also do not fully agree with those of Hardy et al. (1984), who found that no significant star formation has occurred in the bar before 3 Gyr ago.

4.5.2 Contribution of the Clusters

An encouraging feature of each of the star formation histories of Figs. 4.15 is a significant number of stars in the last age bin, where we expect the contaminating globular cluster stars to be found. How much of the old stellar populations of Figs. 4.15 can be attributed to the clusters spilling into the WF frames? While we found we could not cleanly subtract the cluster stars from the field star CMDs, we can use the estimates of their numbers derived previously to address the question. Table 4.5 compares the number of cluster stars in the WF frames estimated from the King model fits to the number of stars in the last age bin of the star formation histories of Figs. 4.15. We find that the cluster stars contribute significantly to each field, while in the NGC 1754 and NGC 1898 fields they dominate the oldest bin.

We would also like to know whether the cluster stars are restricted to the oldest age bin of Figs. 4.15, or whether they spill over into nearby age bins. We addressed this question by examining the radial profiles of the distribution of stars likely to have contributed to each age bin. Assuming that the field stars are uniformly distributed across the field while the cluster stars are not, we should find that the older stars increase in number towards the cluster center. Starting with the oldest age bin, we selected stars from the observed CMDs having the same distribution over $V-I$ and V and the same number of stars as the model. We then removed the selected stars from the observed CMD and repeated the process with the next age bin. Figs. 4.17 show the completeness-corrected radial profiles for the selected stars in each age bin. Because the isochrones blend on the main sequence, it is impossible to perfectly discriminate between the cluster stars and field stars on the basis of age. Consequently, the non-uniform distribution of the cluster stars will partially contribute to all of the age bins, although this contribution will decrease for the younger ages. We find exactly this trend in all of the fields, with the stars in the oldest age bins having a detectable component of non-uniformly distributed stars but with the uniformly

distributed component dominating in the younger bins. For the NGC 1835, NGC 2005, and NGC 2005 fields we also find that the cluster contribution appears small compared to the field star contribution, as expected from the King model fits. It thus seems reasonable to expect that the cluster contamination appears mainly in the oldest age bin of Figs. 4.15.

4.5.3 Goodness of Fit of the Model Star Formation Histories

So far, we have implicitly assumed that the best-fit model star formation histories provide good fits to the observations. However, our models make a number of simplifications over what is realistically expected; e.g. we assumed uniform reddening, no binary stars, and a simple linear chemical evolution law. We will now discuss how badly the models fail to fit the observations and where the largest improvements can be made, and try to give a sense for how the results will be affected by improvements in the models.

To get an idea of whether the star formation histories shown in Figs. 4.15 provide sensible matches to the data, we overlaid isochrones representing peaks in the derived star formation histories on the field star CMDs. Figs. 4.18 show the ages at which the isochrones were chosen and the corresponding matches with the CMDs. The inability to tell by eye whether the chosen peaks in the star formation rate correspond to increases in the stellar density in the CMD reinforce the need for an automated technique to derive the star formation histories. We can tell, however, that there is a clear difference between the NGC 1754 CMD and the CMDs of the bar fields. While the NGC 1754 field appears to have a single old turnoff, the bar fields have many stars $\sim$0.5 magnitude brighter than the oldest turnoff, which we interpret as the 4-8 Gyr population in Figs. 4.15. Overlaying the isochrones also shows that our adopted chemical evolution model does not provide an ideal match to the CMDs, especially for the bar fields. The most striking disagreement is that the red giant branches of the older isochrones fall too far to the blue to match the observed giant branch. While the

observed giant branch could be fit by older isochrones if the distance modulus were decreased, it would then be difficult to match the blue envelope of the upper main sequence, which is reproduced well with the current models. A possible explanation is that the metallicity of the model old populations is too metal rich. Because the globular cluster sequences, which have a mean abundance equal to the abundance of the oldest bin in our models, fall roughly at the same locations as the field star RGBs, this would mean that the globular cluster abundances are too metal-rich by $\sim$0.5 dex. As the globular cluster abundances were measured from the slopes of the RGBs, which are empirically calibrated with Milky Way clusters using high-dispersion spectroscopic abundances, we would be surprised if they were found to be so grossly incorrect. A second possibility, however, is that the B94 isochrones do not correctly predict the color of the red giant branch for low metallicities. As discussed in Chapter 3, the color of the RGB depends on relatively poorly understood physics, and so could be in error. The error in the color of the RGB implied by our comparison is a rather large $\sim$0.08 magnitudes, which is almost as difficult to swallow as our abundances being grossly in error.

In Figs. 4.19 we show the residuals produced by the models of Figs. 4.15. The residuals are shown as fractions of the observed star density in the CMDs. The greyscale stretches from -1 to 1; white pixels are regions where too many stars are predicted by the models, black pixels represent an excess of observed stars, and grey pixels represent the regions where the models closely match the observations. The residuals show that over large areas of the CMDs, the models reproduce the observations fairly well. However, as expected from the comparisons with isochrones, there are several areas where the fits are poor, most notably the area of the red giant branch, the horizontal branch and red clump stars, and a small section of the upper main sequence. The poor fits in these regions are again caused by either the inadequacy of the B94 isochrones or by the incorrect chemical evolution model.

To get an idea of the formal goodness-of-fit of the models, we show the comparison

of the observed and model luminosity functions in Figs. 4.20. The errors in the points include both Poisson counting statistics and the uncertainties in the derived star formation rates of the models. The use of luminosity functions smooths over many of the disagreements between the models and observations, and the χ^2 and Kolmogorov-Smirnov statistics show that the distributions are, in some cases, roughly similar. In agreement with the inspection of the residuals, however, the luminosity functions indicate that the models for the bar fields contain too many old and intermediate age stars.

What are the possible effects of the disagreements between the models and observations on the derived star formation histories? To address this question, we studied the effects that varying the reddening, distance modulus, and IMF have on the derived star formation histories. While we did not model the effect of varying the metal abundance in each age bin, changing the abundances should have effects similar to changing the reddening and distance modulus.

Fig. 4.21 shows the star formation history derived for NGC 1835 for the best-fit $E(B-V) = 0.04$ and $(m\text{-}M)_o = 18.5$ and for other values of the reddening. While varying $E(B-V)$ by 0.02 magnitudes has a relatively small effect on the derived star formation history, increasing the reddening by 0.04 or 0.06 magnitudes raises the contribution of the young stars while decreasing the intermediate-age star formation. A similar and stronger effect is achieved by raising the distance modulus by 0.2 magnitudes, shown in Fig. 4.22. Throughout the variation of the parameters, the star formation in the oldest bin remained relatively unchanged, perhaps because our parameter set does not allow us to explore the effect of large decreases in $E(B-V)$ or $(m\text{-}M)_o$.

Fig. 4.23 shows the effect of varying the IMF on the derived star formation history of the NGC 1835 field. As the IMF is made shallower, more faint stars are needed to match the observed CMD, increasing the contribution of the older models. At an IMF slope of x=1.5, the old stellar populations dominate the star formation history.

For an IMF slope of x=3.0, the relative contribution of the younger stars increases, as expected. In Fig. 4.24, we show the effect of varying the IMF for the NGC 1754 field, which has a qualitatively different star formation history than the bar fields. We note that changing the IMF for this field does not produce a strong intermediate-age component to the star formation history.

While these explorations show that large variations in the input parameters can have a strong effect on the relative contributions of stellar populations of various ages, the main features of Fig. 4.15, such as the recent increase in the star formation rate and the existence of a 4–8 Gyr population in the bar fields remained intact. We thus feel comfortable that the qualitative features of our derived star formation histories are robust to errors in the input parameters and to the inadequacies of the B94 isochrones.

4.6 Summary

Martin Schwarzschild led off this Chapter with a remark concerning the hopelessness of disentangling the color-magnitude diagram of stars that contain a wide mix of ages and compositions. While modern computational power no longer makes the problem unapproachable, assumptions still need to be made to make it tractable. We have assumed throughout that the field star CMDs can be parametrized by a single reddening, distance modulus, and IMF; that the CMDs contain no binary stars; that the IMF does not vary in time; and that a simple linear chemical evolution law describes the enrichment history.

We first approached the problem by gauging what can be learned about the parameters by simply comparing the field star CMDs with stellar isochrones. We then constructed two simple model star formation histories, one having a strong recent burst in the star formation rate and the other representing constant star formation, and compared the models to our observations for the NGC 1754 field. From this

simple comparison we learned that the strong burst of star formation did not seem to be implied by the data, but that a number of our assumptions, such as the chemical evolution law, were overly simple. We quickly discovered that to achieve more detailed knowledge of the evolution of the fields, we need to use a more automated approach than constructing individual model star formation histories and comparing them to the observations.

Based on the updated work of Dolphin (1997), we developed a program to solve for the star formation history given a set of input parameters. With this method, we could restrict the number of models we needed to construct by producing CMDs of stars falling in 36 logarithmic age bins and then solving for the linear combination of the component CMDs that produced the best match to the observations. We constructed separate models to simulate CMDs having $E(B-V)$'s ranging from 0.02 to 0.12, $(m\text{-}M)_o$ from 18.4 to 18.7, and IMF slopes of x=1.5, 2.0, 2.35, and 3.0. By minimizing the Lorentzian fit parameter and using Monte Carlo simulations to investigate the errors, we produced a best-fit star formation history with small errors in $E(B-V)$ and $(m\text{-}M)_o$, although we found we could not easily distinguish between the different IMFs. The errors in the derived star formation rates depend both on the number of stars found per age bin of the models and on age. With our CMDs, we found we could usefully solve for the star formation rates with a resolution of 0.16-0.24 in log age.

Our results show that star formation has been active in the parts of the LMC sampled by our fields over the past 3 Gyr, but that activity has declined in the last 0.5−1 Gyr. This apparent decline could simply be evidence that the stars formed in the past 1 Gyr are not thoroughly mixed; the crossing time in the bar is ∼80 Myr, implying a mixing time of a few hundred million years. We find a strong qualitative difference between the bar fields (NGC 1835, NGC 1898, NGC 2005, and NGC 2019) and the NGC 1754 field, which lies outside the bar, in that the bar fields have enhanced star formation in the age range 4−8 Gyr while the NGC 1754 field does not. On the

basis of this difference, we suggest that the LMC bar formed 6–8 Gyr ago, with the age derived from the isochrones of B94. The star formation history derived for the NGC 1754 field is consistent with the finding of H97 that star formation in the LMC disk over the past 3–4 Gyr has been enhanced by a factor 3 over star formation occurring >4 Gyr ago, although it has not been uniform, as supposed in H97's simpler analysis.

We tested the goodness-of-fit of our model star formation histories as carefully as possible. We find that either our adopted chemical evolution model fails at the oldest ages and that our measurements of the globular cluster abundances are incorrect, or that the B94 isochrones do not faithfully produce the color of the red giant branch at low metallicities. Nevertheless, by examining the variation in the star formation rates with changes in the input parameters, we feel that the qualitative nature of our results are robust against the possible errors.

Table 4.1: Parameters of Model Star Formation Histories[a]

$E(B-V)$	$(m-M)_o$	IMF x	Fields Modelled
0.02	18.4-18.7	1.5	NGC 1835
0.04	18.3	1.5	NGC 2005
0.04	18.4-18.7	1.5	all
0.06	18.3	1.5	NGC 2005
0.06	18.4-18.7	1.5	all
0.08	18.3	1.5	NGC 2005
0.08	18.4-18.7	1.5	all
0.10	18.3	1.5	NGC 2005
0.10	18.4-18.7	1.5	all
0.12	18.3	1.5	NGC 2005
0.12	18.4-18.7	1.5	all
0.02	18.4-18.7	2.0	NGC 1835
0.04	18.3	2.0	NGC 2005
0.04	18.4-18.7	2.0	all
0.06	18.3	2.0	NGC 2005
0.06	18.4-18.7	2.0	all
0.08	18.3	2.0	NGC 2005
0.08	18.4-18.7	2.0	all
0.10	18.3	2.0	NGC 2005
0.10	18.4-18.7	2.0	all
0.12	18.3	2.0	NGC 2005
0.12	18.4-18.7	2.0	all

Table 4.1: Cont.: Parameters of Model Star Formation Histories

$E(B-V)$	$(m-M)_o$	IMF x	Fields Modelled
0.02	18.4-18.7	2.35	NGC 1835
0.04	18.3	2.35	NGC 2005
0.04	18.4-18.7	2.35	all
0.06	18.3	2.35	NGC 2005
0.06	18.4-18.7	2.35	all
0.08	18.3	2.35	NGC 2005
0.08	18.4-18.7	2.35	all
0.10	18.3	2.35	NGC 2005
0.10	18.4-18.7	2.35	all
0.12	18.3	2.35	NGC 2005
0.12	18.4-18.7	2.35	all
0.02	18.4-18.7	3.0	NGC 1835
0.04	18.3	3.0	NGC 2005
0.04	18.4-18.7	3.0	all
0.06	18.3	3.0	NGC 2005
0.06	18.4-18.7	3.0	all
0.08	18.3	3.0	NGC 2005
0.08	18.4-18.7	3.0	all
0.10	18.3	3.0	NGC 2005
0.10	18.4-18.7	3.0	all
0.12	18.3	3.0	NGC 2005
0.12	18.4-18.7	3.0	all

[a] A chemical evolution law of $[Fe/H] = -0.073(\frac{Age}{10^9 yr}) - 0.3$ was used for all models

Table 4.2: Parameters of Test Star Formation History

$E(B-V)$	$(m-M)_o$	IMF x	# Stars bin^{-1}	# Stars bin^{-1} after completeness correction	# Runs
0.08	18.5	2.35	250	~185	10
0.08	18.5	2.35	500	~370	10
0.08	18.5	2.35	1000	~740	25
0.08	18.5	2.35	2000	~1480	10
0.08	18.5	2.35	3000	~2220	10

Table 4.3a: Derived Star Formation History: NGC 1754

$E(B-V)$	$(m-M)_o$	# age bins	$\log_{10}$ Age	# Stars bin^{-1}	SFR
0.06	18.5	18	7.42	0	0.0000
			7.57	0	2.7791E-06
			7.73	64	1.4895E-04
			7.89	0	0.0
			8.05	37	4.0401E-05
			8.21	1	1.1243E-06
			8.37	40	2.0397E-05
			8.52	62	2.1558E-05
			8.68	37	8.9741E-06
			8.84	306	5.0429E-05
			9.00	249	2.8403E-05
			9.16	327	2.7974E-05
			9.32	209	1.2796E-05
			9.48	462	2.1299E-05
			9.63	162	5.3881E-06
			9.79	197	4.9002E-06
			9.95	253	4.7808E-06
			10.11	2479	3.6479E-05
0.06	18.5	12	7.46	8	2.7476E-05
			7.69	79	1.3380E-04
			7.93	11	1.0617E-05
			8.17	0	0.0
			8.41	80	2.4512E-05
			8.64	84	1.4733E-05
			8.88	419	4.1647E-05
			9.12	441	2.6771E-05
			9.36	416	1.5786E-05
			9.59	484	1.1608E-05
			9.83	12	1.8919E-07
			10.07	2886	3.0008E-05
0.06	18.5	9	7.50	0	1.6508E-06
			7.81	96	9.0202E-05
			8.13	23	1.0407E-05
			8.45	55	1.1475E-05
			8.76	336	3.2880E-05
			9.08	574	2.8009E-05
			9.40	680	1.7859E-05
			9.71	44	6.3135E-07
			10.03	3102	2.5626E-05

Table 4.3b: Derived Star Formation History: NGC 1835

$E(B-V)$	$(m-M)_0$	# age bins	$\log_{10}$ Age	# Stars bin^{-1}	SFR
0.04	18.5	18	7.42	0	6.0478E-06
			7.57	0	0.0
			7.73	0	1.9055E-06
			7.89	0	8.9792E-07
			8.05	29	4.3015E-05
			8.21	0	0.0
			8.37	0	2.5364E-07
			8.52	149	7.2823E-05
			8.68	235	8.1063E-05
			8.84	229	5.8894E-05
			9.00	1184	2.1879E-04
			9.16	642	9.4709E-05
			9.32	587	6.5352E-05
			9.48	605	4.9161E-05
			9.63	903	5.8213E-05
			9.79	1468	7.4723E-05
			9.95	0	0.0
			10.11	5483	1.7142E-04
0.04	18.5	12	7.46	0	0.0
			7.69	0	5.6442E-07
			7.93	28	3.6853E-05
			8.17	3	2.9179E-06
			8.41	50	2.1294E-05
			8.64	354	8.7919E-05
			8.88	616	9.6411E-05
			9.12	1315	1.3562E-04
			9.36	770	5.1880E-05
			9.59	1394	6.3437E-05
			9.83	1254	4.0046E-05
			10.07	5721	1.2734E-04
0.04	18.5	9	7.50	0	0.0
			7.81	20	2.6579E-05
			8.13	2	1.2246E-06
			8.45	137	3.9394E-05
			8.76	575	8.4591E-05
			9.08	1606	1.3162E-04
			9.40	1226	5.7555E-05
			9.71	1752	4.9820E-05
			10.03	5836	1.0313E-04

Table 4.3c: Derived Star Formation History: NGC 1898

$E(B-V)$	$(m-M)_o$	# age bins	$\log_{10}$ Age	# Stars bin^{-1}	SFR
0.06	18.4	18	7.42	0	0.0
			7.57	18	8.8100E-05
			7.73	59	1.9203E-04
			7.89	48	1.0452E-04
			8.05	137	2.0320E-04
			8.21	0	0.0
			8.37	55	3.8028E-05
			8.52	145	7.0193E-05
			8.68	227	7.9456E-05
			8.84	237	6.2563E-05
			9.00	865	1.6474E-04
			9.16	774	1.1811E-04
			9.32	1084	1.2548E-04
			9.48	0	0.0
			9.63	2764	1.8972E-04
			9.79	1453	8.3194E-05
			9.95	0	0.0000E+00
			10.11	3293	1.2095E-04
0.06	18.4	12	7.46	14	6.3915E-05
			7.69	5	1.3817E-05
			7.93	175	2.4086E-04
			8.17	19	1.5487E-05
			8.41	142	6.4109E-05
			8.64	240	6.3457E-05
			8.88	616	9.5908E-05
			9.12	1300	1.3184E-04
			9.36	1364	9.7174E-05
			9.59	2436	1.2101E-04
			9.83	44	1.5350E-06
			10.07	3802	9.9020E-05
0.06	18.4	9	7.50	0	0.0
			7.81	167	2.2613E-04
			8.13	59	3.7918E-05
			8.45	226	6.8974E-05
			8.76	491	7.3826E-05
			9.08	1607	1.2991E-04
			9.40	2261	1.1404E-04
			9.71	1513	4.6493E-05
			10.03	3831	7.8215E-05

Table 4.3d: Derived Star Formation History: NGC 2005

$E(B-V)$	$(m-M)_o$	# age bins	$\log_{10}$ Age	# Stars bin^{-1}	SFR
0.06	18.45	18	7.42	6	4.8338E-05
			7.57	28	1.3762E-04
			7.73	20	6.8084E-05
			7.89	0	2.6168E-08
			8.05	29	4.5870E-05
			8.21	84	8.9075E-05
			8.37	197	1.4820E-04
			8.52	100	5.0603E-05
			8.68	346	1.2437E-04
			8.84	491	1.2301E-04
			9.00	781	1.4019E-04
			9.16	1127	1.5704E-04
			9.32	669	7.2332E-05
			9.48	1499	1.2626E-04
			9.63	1653	1.0553E-04
			9.79	2105	1.0687E-04
			9.95	162	6.3587E-06
			10.11	3082	9.7924E-05
0.06	18.45	12	7.46	37	1.6272E-04
			7.69	7	1.6645E-05
			7.93	30	4.1562E-05
			8.17	125	9.6756E-05
			8.41	210	9.4478E-05
			8.64	405	1.0478E-04
			8.88	763	1.1670E-04
			9.12	1554	1.5244E-04
			9.36	1341	9.0516E-05
			9.59	3602	1.6389E-04
			9.83	226	7.1378E-06
			10.07	3378	7.5259E-05
0.06	18.45	9	7.50	41	1.1826E-04
			7.81	0	0.0
			8.13	164	9.8842E-05
			8.45	265	7.5607E-05
			8.76	840	1.2424E-04
			9.08	1873	1.5273E-04
			9.40	1735	8.0826E-05
			9.71	3765	1.0761E-04
			10.03	4192	7.4426E-05

Table 4.3e: Derived Star Formation History: NGC 2019

$E(B-V)$	$(m-M)_o$	# age bins	$\log_{10}$ Age	# Stars bin^{-1}	SFR
0.06	18.5	18	7.42	3	2.3351E-05
			7.57	5	2.6169E-05
			7.73	0	0.0
			7.89	4	9.9922E-06
			8.05	122	1.9828E-04
			8.21	63	7.1391E-05
			8.37	284	2.2204E-04
			8.52	225	1.2089E-04
			8.68	377	1.4283E-04
			8.84	471	1.2479E-04
			9.00	1339	2.5445E-04
			9.16	1422	2.0964E-04
			9.32	619	6.9481E-05
			9.48	2313	2.0373E-04
			9.63	59	3.9894E-06
			9.79	3080	1.6144E-04
			9.95	77	3.1596E-06
			10.11	2305	7.3667E-05
0.06	18.5	12	7.46	0	0.0
			7.69	14	3.5781E-05
			7.93	55	7.8645E-05
			8.17	133	1.0943E-04
			8.41	397	1.8719E-04
			8.64	413	1.1258E-04
			8.88	1107	1.7858E-04
			9.12	2136	2.2182E-04
			9.36	1446	1.0164E-04
			9.59	2394	1.1418E-04
			9.83	2280	7.4408E-05
			10.07	2706	6.0961E-05
0.06	18.5	9	7.50	0	2.1811E-06
			7.81	0	0.0
			8.13	258	1.7210E-04
			8.45	451	1.4348E-04
			8.76	906	1.4104E-04
			9.08	2699	2.2401E-04
			9.40	2137	1.0542E-04
			9.71	3352	9.8589E-05
			10.03	3234	5.7802E-05

Table 4.4a: Dispersions in Derived Parameters: NGC 1754

$\sigma_{P_{Lor}}$	$\sigma_{E(B-V)}$	$\sigma_{(m-M)_o}$	# age bins	$\log_{10}$ Age	σ_{SFR}
0.07	0.01	0.05	18	7.42	8.0016E-05
				7.57	1.6070E-04
				7.73	8.2110E-05
				7.89	5.2147E-05
				8.05	2.0089E-05
				8.21	3.1473E-05
				8.37	2.5283E-05
				8.52	2.3833E-05
				8.68	1.3280E-05
				8.84	1.3967E-05
				9.00	9.0920E-06
				9.16	8.1498E-06
				9.32	7.4369E-06
				9.48	1.1524E-05
				9.63	9.6743E-06
				9.79	5.2884E-06
				9.95	4.2624E-06
				10.11	3.1761E-06
0.04	0.01	0.05	12	7.46	1.5948E-04
				7.69	7.4927E-05
				7.93	3.7926E-05
				8.17	2.5056E-05
				8.41	2.7524E-05
				8.64	1.3111E-05
				8.88	5.3803E-06
				9.12	5.1347E-06
				9.36	6.3707E-06
				9.59	1.0943E-05
				9.83	1.3434E-05
				10.07	2.1333E-06
0.06	0.01	0.05	9	7.50	8.5681E-05
				7.81	4.3180E-05
				8.13	1.3958E-05
				8.45	8.6834E-06
				8.76	7.5887E-06
				9.08	4.0187E-06
				9.40	2.3925E-06
				9.71	2.8652E-06
				10.03	8.7736E-07

Table 4.4b: Dispersions in Derived Parameters: NGC 1835

$\sigma_{P_{Lor}}$	$\sigma_{E(B-V)}$	$\sigma_{(m-M)_o}$	# age bins	$\log_{10}$ Age	σ_{SFR}
0.06	0.01	0.05	18	7.42	1.1261E-04
				7.57	4.8035E-05
				7.73	1.7181E-04
				7.89	2.9839E-05
				8.05	9.5973E-05
				8.21	8.5427E-06
				8.37	1.2938E-05
				8.52	2.9623E-05
				8.68	3.2404E-05
				8.84	3.5401E-05
				9.00	2.5273E-05
				9.16	2.0741E-05
				9.32	2.7457E-05
				9.48	2.9499E-05
				9.63	3.4743E-05
				9.79	3.3393E-05
				9.95	3.5146E-05
				10.11	1.1797E-05
0.06	0.01	0.05	12	7.46	2.3460E-05
				7.69	4.3172E-05
				7.93	2.7941E-05
				8.17	3.0187E-05
				8.41	1.9669E-05
				8.64	3.0518E-05
				8.88	2.8340E-05
				9.12	1.2129E-05
				9.36	1.5697E-05
				9.59	1.9326E-05
				9.83	1.8305E-05
				10.07	1.0628E-05
0.08	0.01	0.05	9	7.50	5.7747E-05
				7.81	3.9084E-05
				8.13	7.4174E-05
				8.45	1.6890E-05
				8.76	1.8678E-05
				9.08	9.7807E-06
				9.40	9.0753E-06
				9.71	1.4722E-05
				10.03	7.7568E-06

Table 4.4c: Dispersions in Derived Parameters: NGC 1898

$\sigma_{P_{Lor}}$	$\sigma_{E(B-V)}$	$\sigma_{(m-M)_o}$	# age bins	$\log_{10}$ Age	σ_{SFR}
0.06	0.01	0.05	18	7.42	2.4110E-04
				7.57	2.4255E-04
				7.73	2.4648E-04
				7.89	1.1133E-04
				8.05	9.4291E-05
				8.21	6.8403E-05
				8.37	5.0695E-05
				8.52	3.5939E-05
				8.68	2.6499E-05
				8.84	3.0870E-05
				9.00	2.6898E-05
				9.16	3.3158E-05
				9.32	4.0139E-05
				9.48	8.3338E-05
				9.63	6.5218E-05
				9.79	4.4882E-05
				9.95	2.9845E-05
				10.11	1.6001E-05
0.05	0.01	0.05	12	7.46	1.4784E-04
				7.69	1.9536E-04
				7.93	1.0591E-04
				8.17	4.5420E-05
				8.41	2.5766E-05
				8.64	1.9254E-05
				8.88	1.7318E-05
				9.12	1.9830E-05
				9.36	2.5159E-05
				9.59	2.0059E-05
				9.83	1.3562E-05
				10.07	8.7337E-06
0.06	0.01	0.05	9	7.50	1.3790E-04
				7.81	1.0671E-04
				8.13	4.4540E-05
				8.45	2.4293E-05
				8.76	1.8759E-05
				9.08	1.6869E-05
				9.40	3.1867E-05
				9.71	3.1451E-05
				10.03	6.5193E-06

Table 4.4d: Dispersions in Derived Parameters: NGC 2005

$\sigma_{P_{Lor}}$	$\sigma_{E(B-V)}$	$\sigma_{(m-M)_o}$	# age bins	$\log_{10}$ Age	σ_{SFR}
0.06	0.01	0.05 18	7.42	8.5572E-04	
				7.57	1.7598E-04
				7.73	8.2876E-05
				7.89	5.8866E-05
				8.05	6.2614E-05
				8.21	8.4364E-05
				8.37	7.9664E-05
				8.52	6.9887E-05
				8.68	3.1272E-05
				8.84	2.6248E-05
				9.00	1.7152E-05
				9.16	2.0050E-05
				9.32	3.7080E-05
				9.48	4.2654E-05
				9.63	6.2696E-05
				9.79	6.2927E-05
				9.95	1.5374E-05
				10.11	1.4323E-05
0.06	0.01	0.05 12	7.46	1.3061E-04	
				7.69	1.0052E-04
				7.93	4.3409E-05
				8.17	6.7668E-05
				8.41	4.7157E-05
				8.64	2.4893E-05
				8.88	1.6667E-05
				9.12	1.0092E-05
				9.36	1.6754E-05
				9.59	2.3949E-05
				9.83	2.6985E-05
				10.07	1.5712E-05
0.06	0.01	0.05 9	7.50	1.3016E-04	
				7.81	3.9535E-05
				8.13	6.5027E-05
				8.45	2.5993E-05
				8.76	1.8660E-05
				9.08	9.4358E-06
				9.40	1.3566E-05
				9.71	9.9098E-06
				10.03	1.0263E-05

Table 4.4e: Dispersions in Derived Parameters: NGC 2019

$\sigma_{P_{Lor}}$	$\sigma_{E(B-V)}$	$\sigma_{(m-M)_o}$	# age bins	$\log_{10}$ Age	σ_{SFR}
0.06	0.01	0.05	18	7.42	1.9088E-04
				7.57	3.0672E-04
				7.73	2.0260E-04
				7.89	4.6479E-05
				8.05	1.4322E-04
				8.21	9.4049E-05
				8.37	7.9462E-05
				8.52	6.2105E-05
				8.68	4.0938E-05
				8.84	6.4580E-05
				9.00	6.0505E-05
				9.16	2.8012E-05
				9.32	3.0848E-05
				9.48	5.3633E-05
				9.63	5.7923E-05
				9.79	6.4386E-05
				9.95	4.3079E-05
				10.11	2.0453E-05
0.05	0.01	0.05 12	7.46	1.1799E-03	
				7.69	1.2121E-04
				7.93	7.2012E-05
				8.17	2.8150E-04
				8.41	5.6305E-05
				8.64	2.4161E-05
				8.88	4.4089E-05
				9.12	3.3432E-05
				9.36	2.1338E-05
				9.59	2.9916E-05
				9.83	3.5475E-05
				10.07	1.4630E-05
0.07	0.01	0.05	9	7.50	1.1921E-04
				7.81	7.4017E-05
				8.13	1.0252E-04
				8.45	3.8040E-05
				8.76	2.5175E-05
				9.08	2.7703E-05
				9.40	1.6146E-05
				9.71	1.2426E-05
				10.03	1.4391E-05

Table 4.5: Comparison of Oldest Bin with Expected Cluster Contamination

Field	$\frac{N(\text{oldest bin})}{N(\text{total})}$	$\frac{N(\text{cluster stars})}{N(\text{total})}$
NGC 1754	0.51	0.40
NGC 1835	0.48	0.07
NGC 1898	0.29	0.23
NGC 2005	0.25	0.10
NGC 2019	0.18	0.08

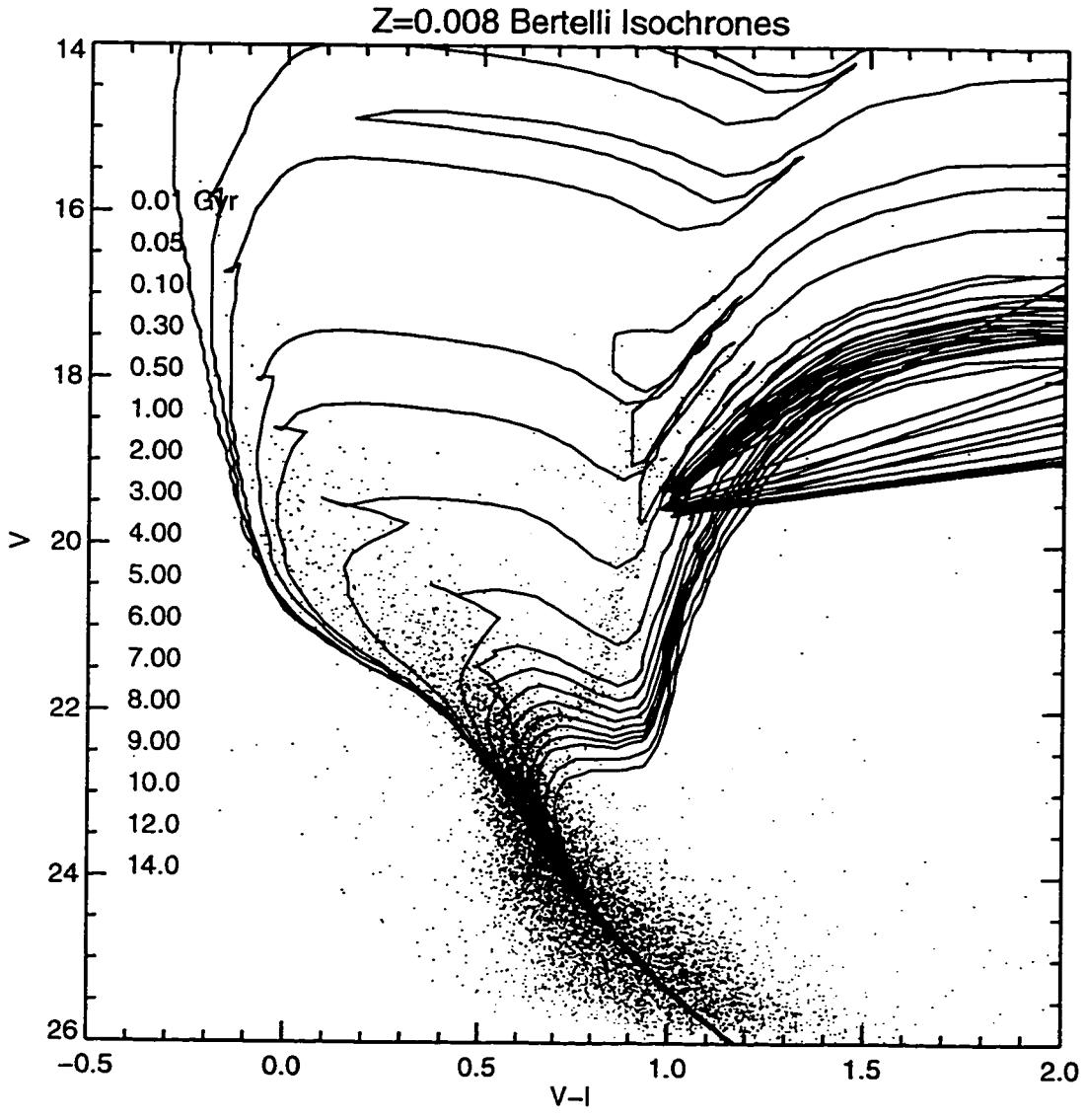

Figure 4.1a: Comparison of the NGC 1754 field star color-magnitude diagram with Bertelli isochrones of Z=0.008. The isochrones have been shifted to match using a distance modulus of 18.5 and $E(B-V) = 0.12$. While the young main sequence is fit well by these isochrones, the red giant branch is not.

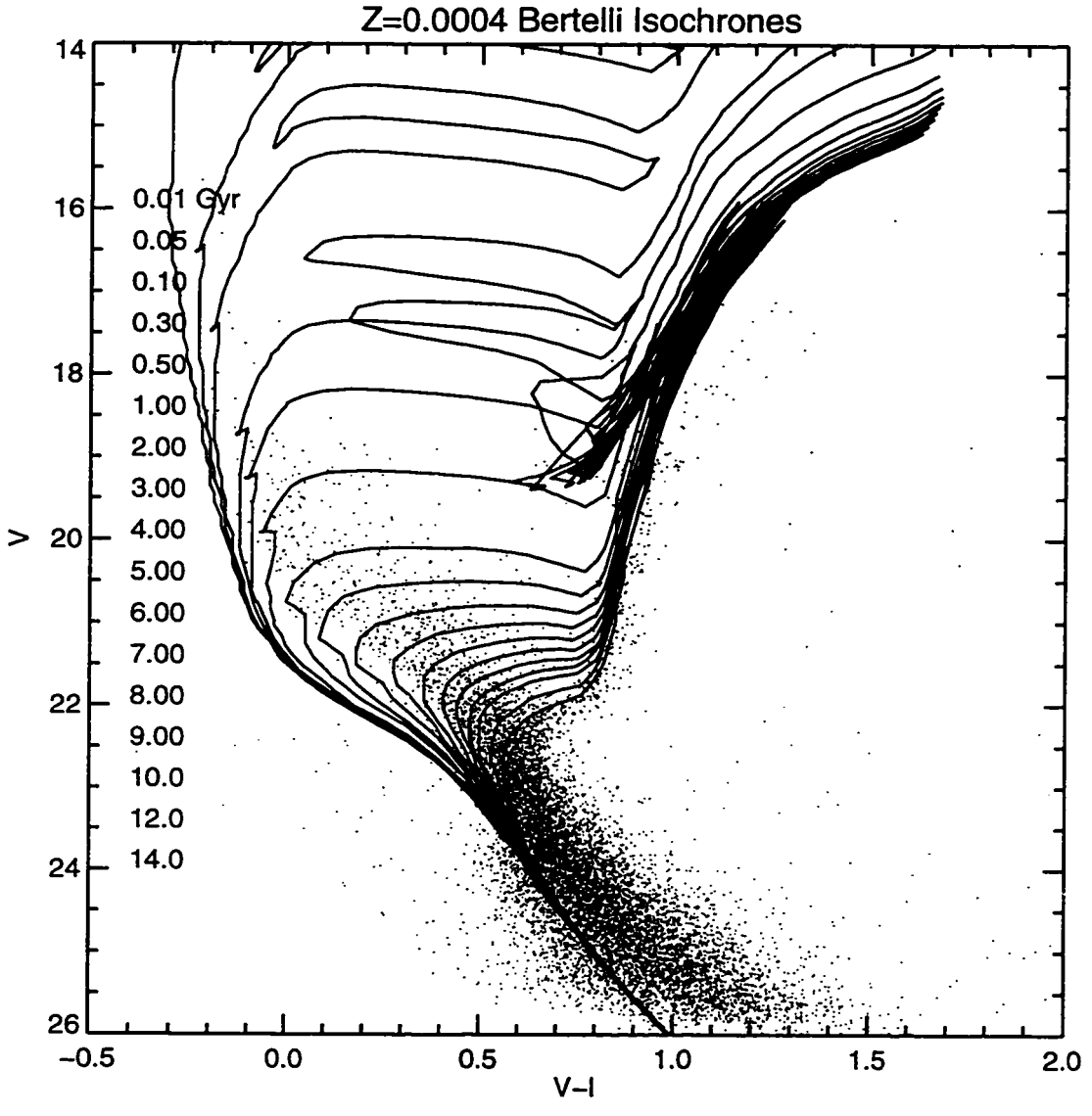

Figure 4.1b: Comparison of the NGC 1754 field star color-magnitude diagram with Bertelli isochrones of Z=0.0004. In contrast to *a*, the metal-poor isochrones fit well with the red giant branch but not with the young main sequence.

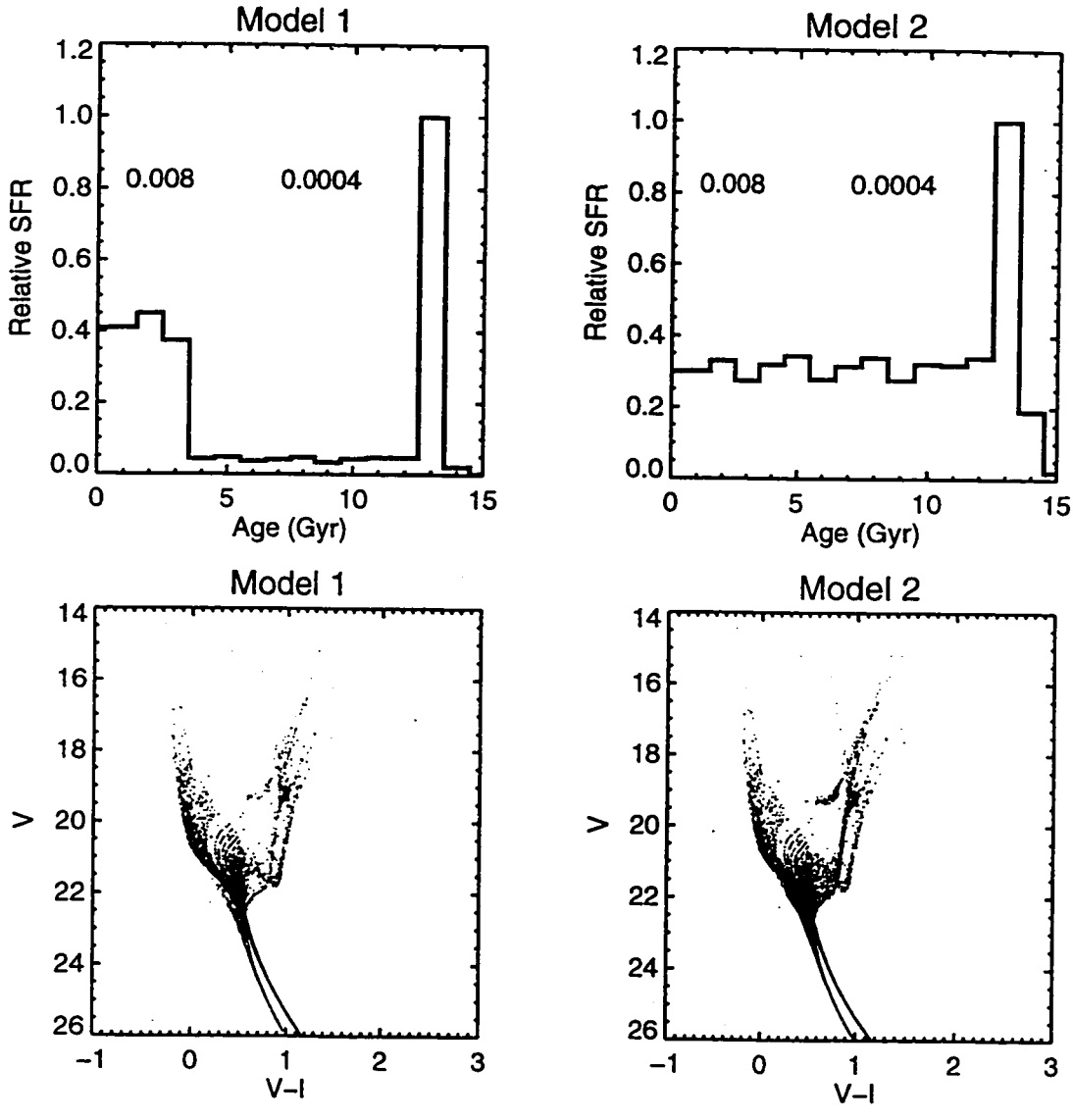

Figure 4.2: Schematics of star formation histories of Models 1 and 2 and the color-magnitude diagrams of the stars selected according to model profiles. An abundance of Z=0.0004 has been used for ages older than 4 Gyr, while Z=0.008 was used for the younger ages. The stars were sampled from interpolated Bertelli et al. (1994) isochrones.

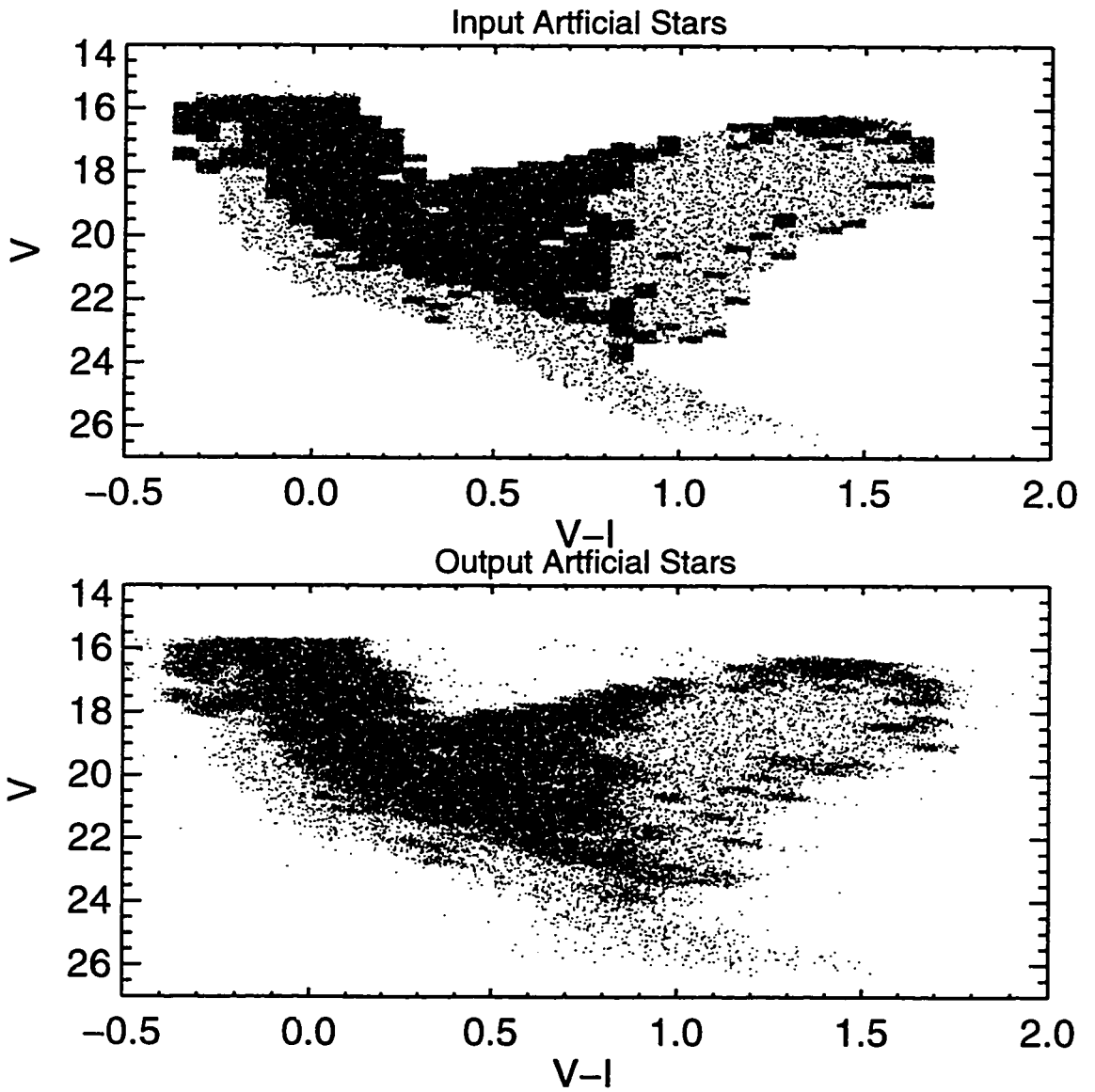

Figure 4.3: Input and recovered artificial star distributions used in comparing Models 1 and 2 with the field star color-magnitude diagram of NGC 1754.

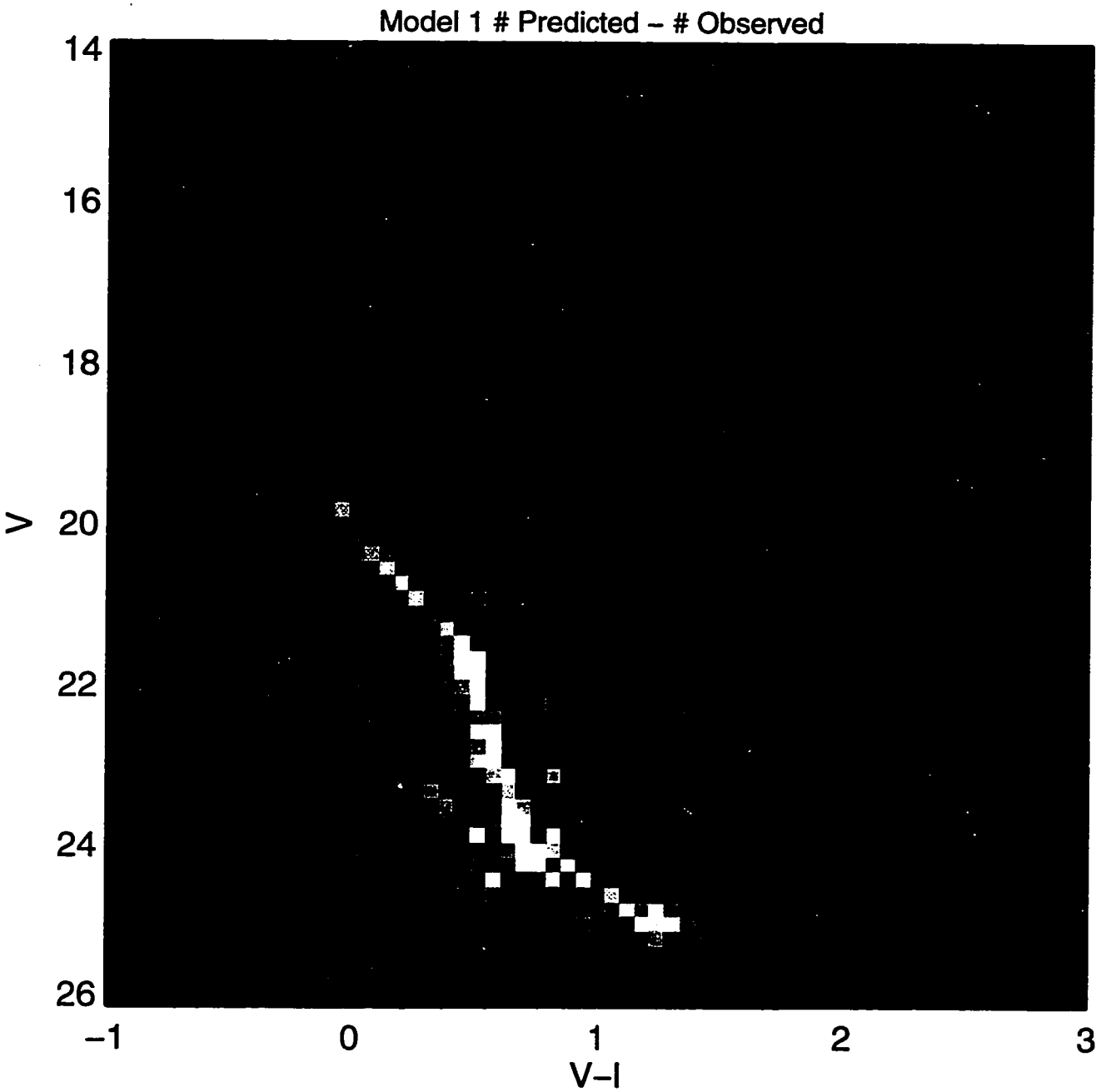

Figure 4.4a: Residuals of Models 1 and 2 after subtraction with the color-magnitude diagram of the NGC 1754 field. Bright pixels represent regions where too many stars were predicted while dark regions signify an excess of observed stars. See text for discussion.

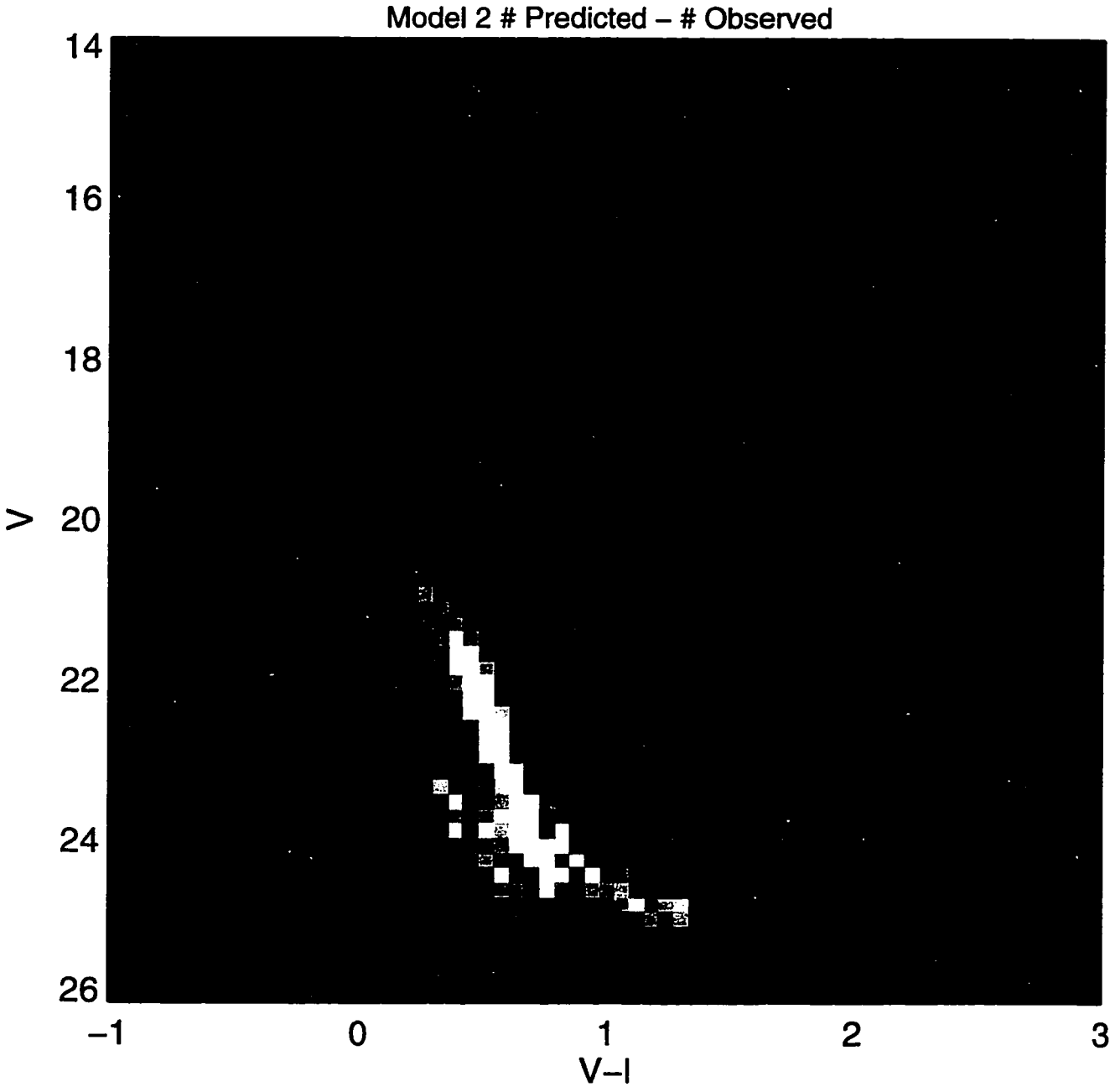

Figure 4.4b: Residuals of Model 2.

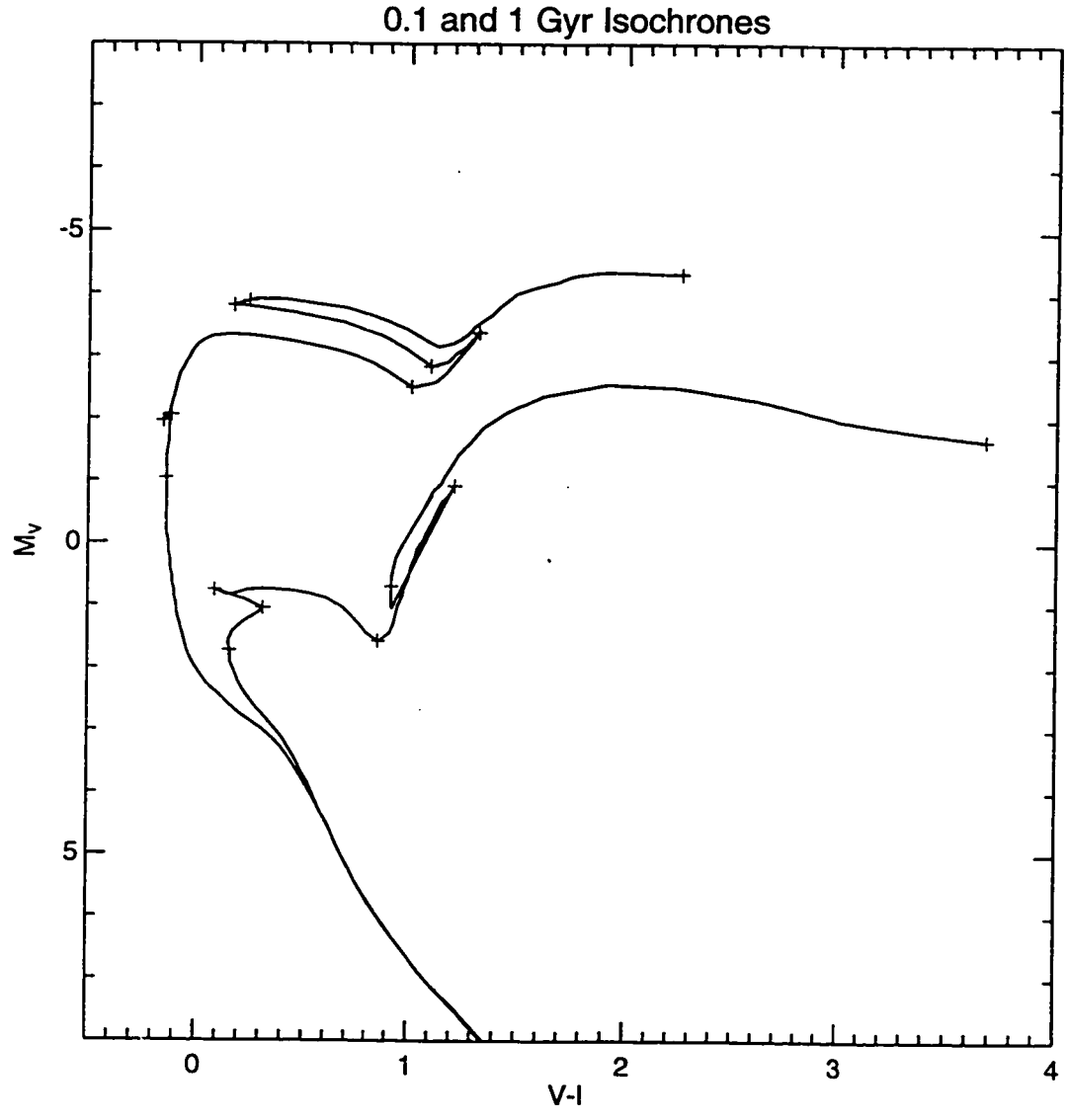

Figure 4.5: Evolutionary points from Table 7−12 of Bertelli et al. (1994) (crosses) for 0.1 and 1 Gyr isochrones with [Fe/H]~ -0.4. The common segments between the crosses were mapped to each other to interpolate isochrones of new ages and abundances.

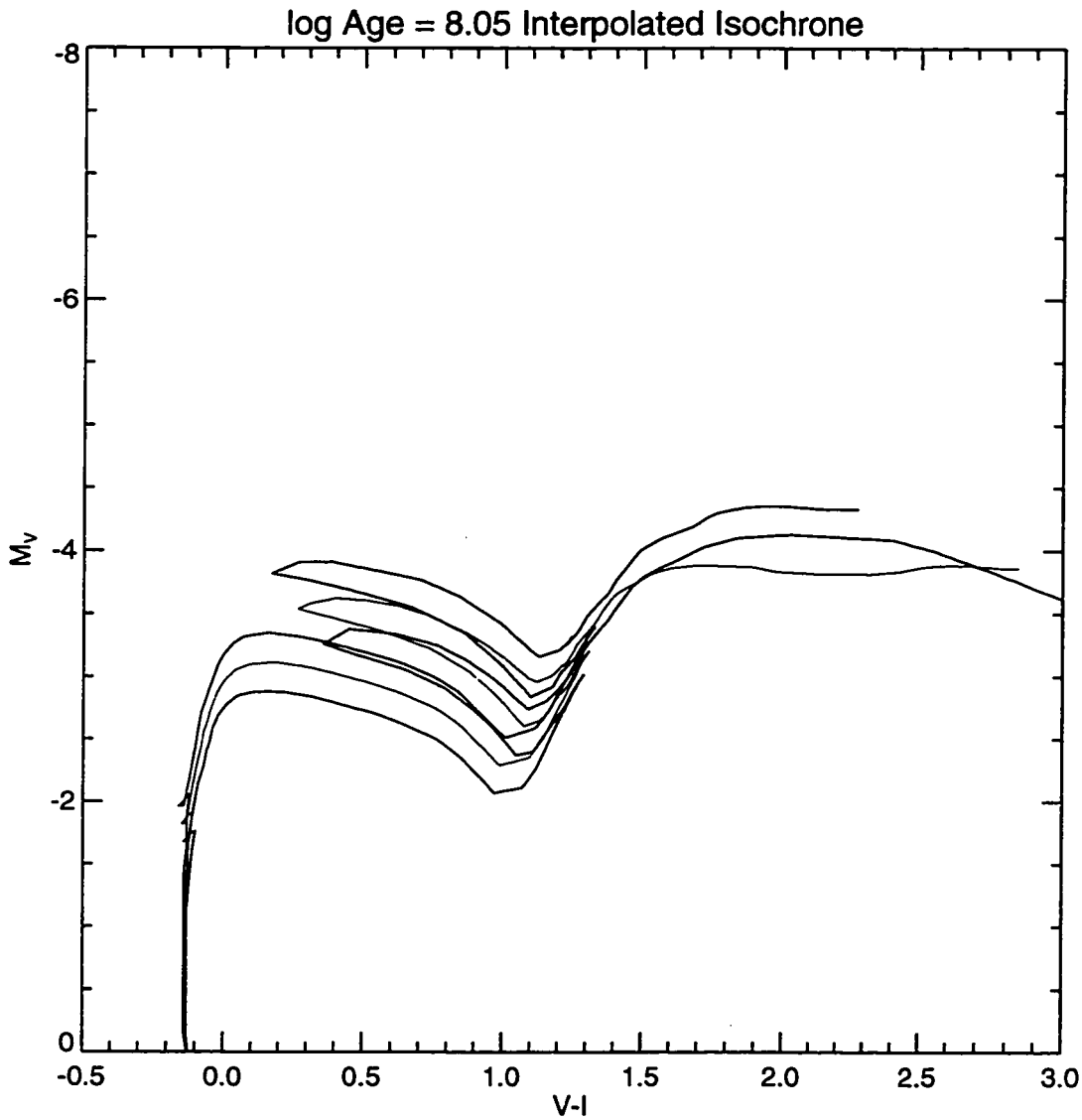

Figure 4.6: An interpolated isochrone with $\log_{10}$ Age = 8.05 and [Fe/H]~ -0.4 is shown with adjacent isochrones of $\log_{10}$ Age = 8.0 and 8.1. While the interpolation faithfully reproduces the shape of the isochrone over the majority of evolutionary phases, it fails on the asymptotic giant branch.

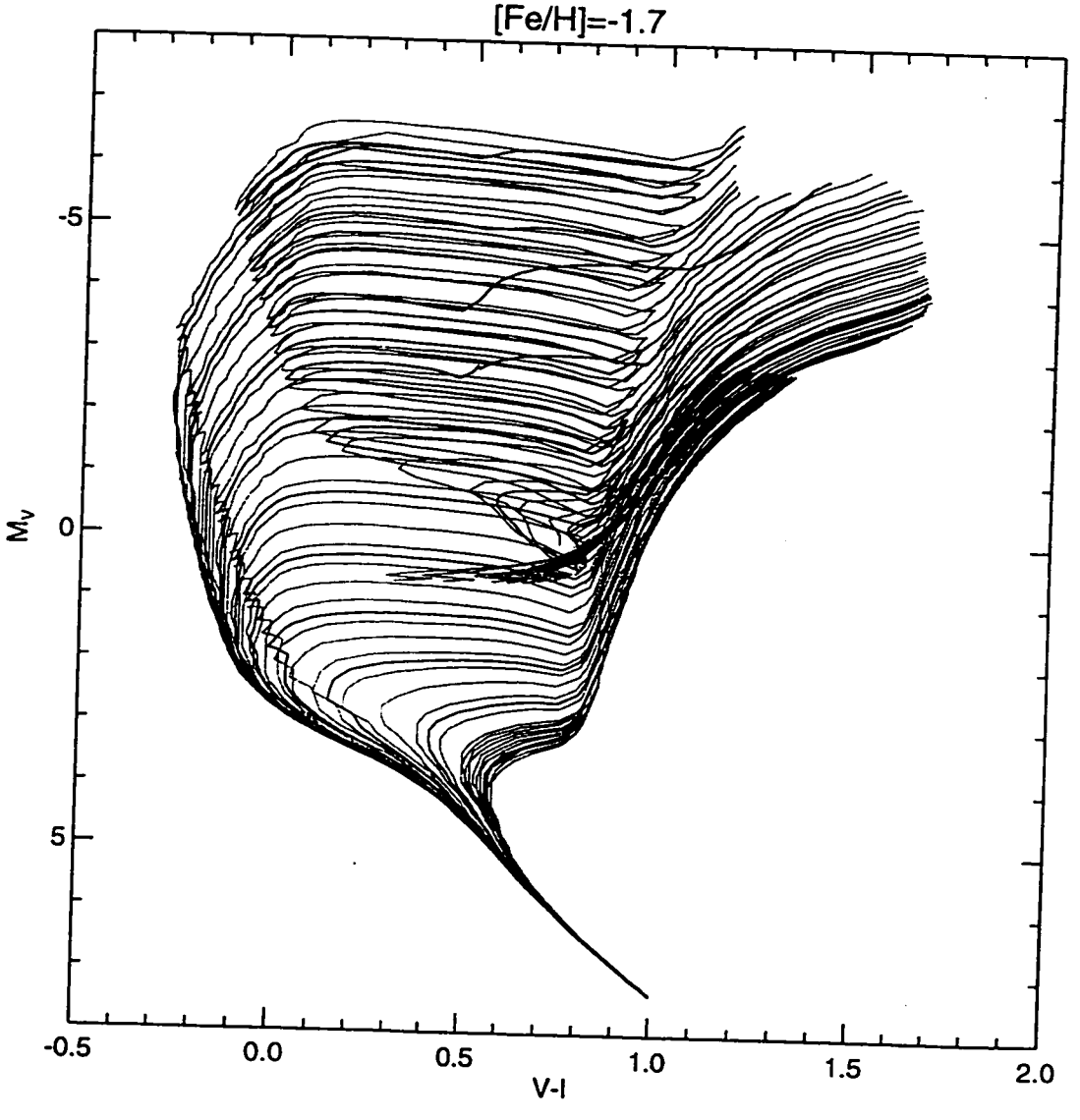

Figure 4.7a: Interpolated isochrones for [Fe/H]=−1.7. Narrow gray lines are the isochrones from Bertelli et al. 1994), while heavy dark lines are isochrones interpolated in age.

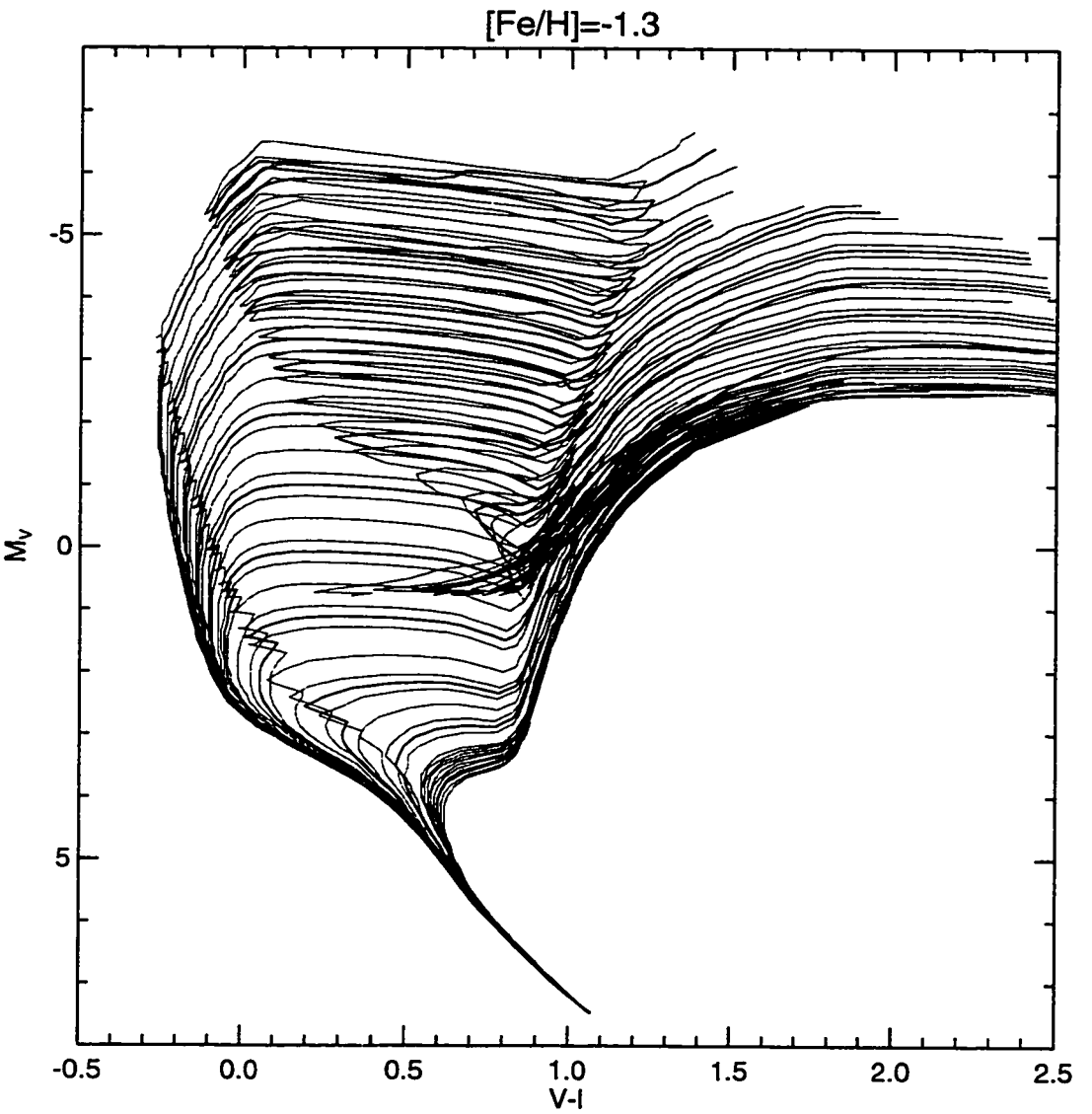

Figure 4.7b: Interpolated isochrones for [Fe/H]=−1.3.

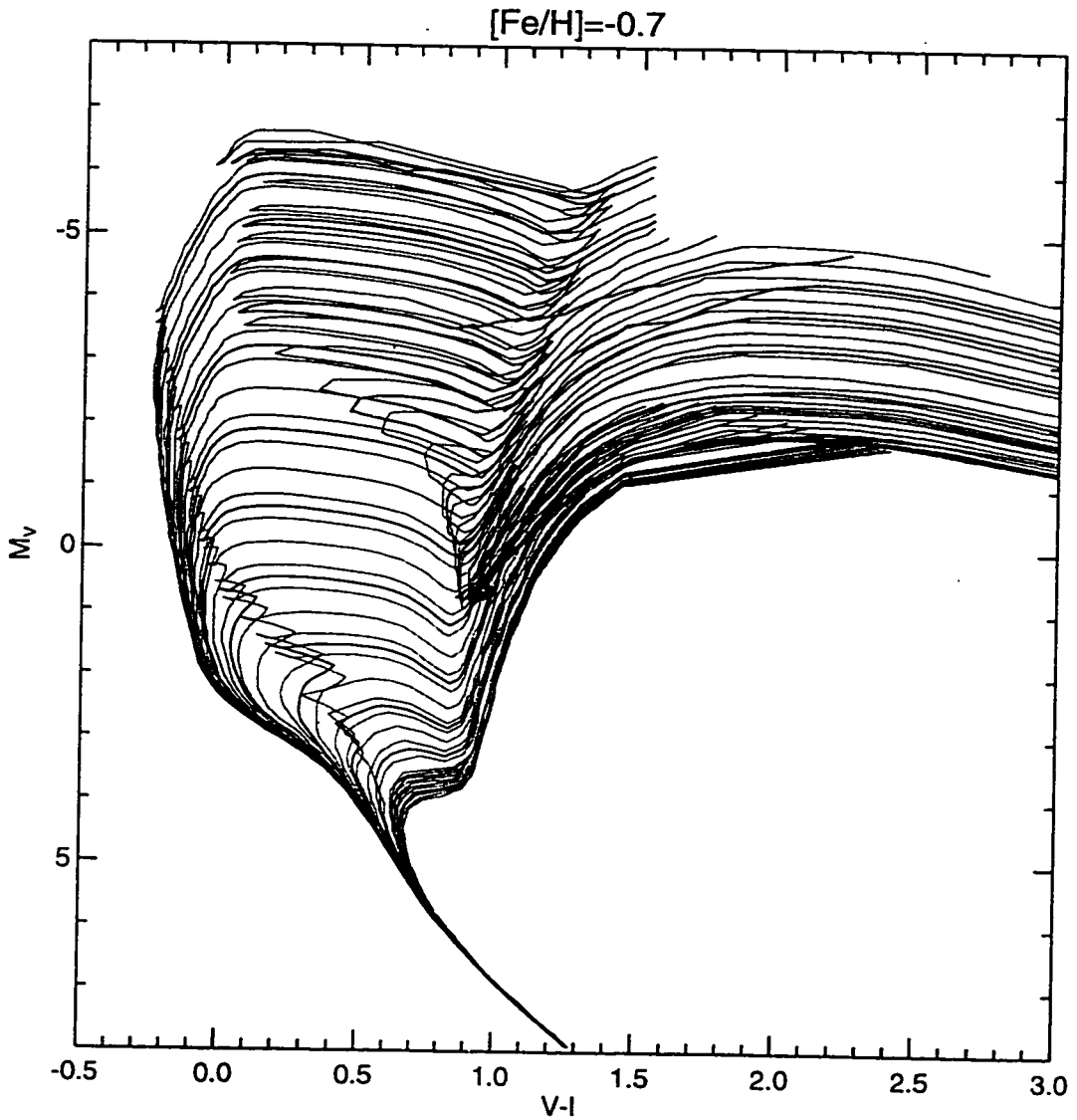

Figure 4.7c: Interpolated isochrones for [Fe/H]=−0.7.

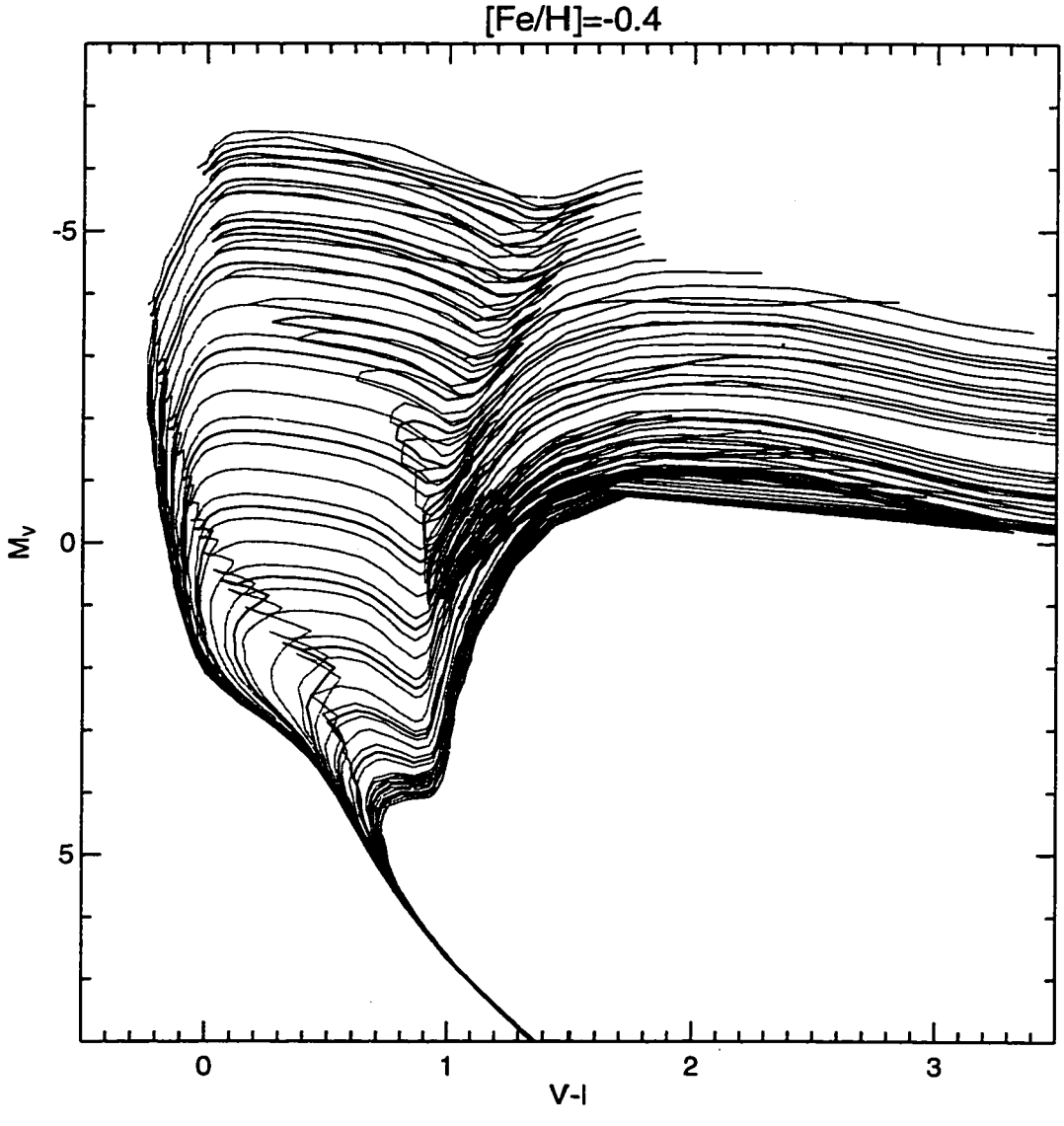

Figure 4.7d: Interpolated isochrones for [Fe/H]=−0.4.

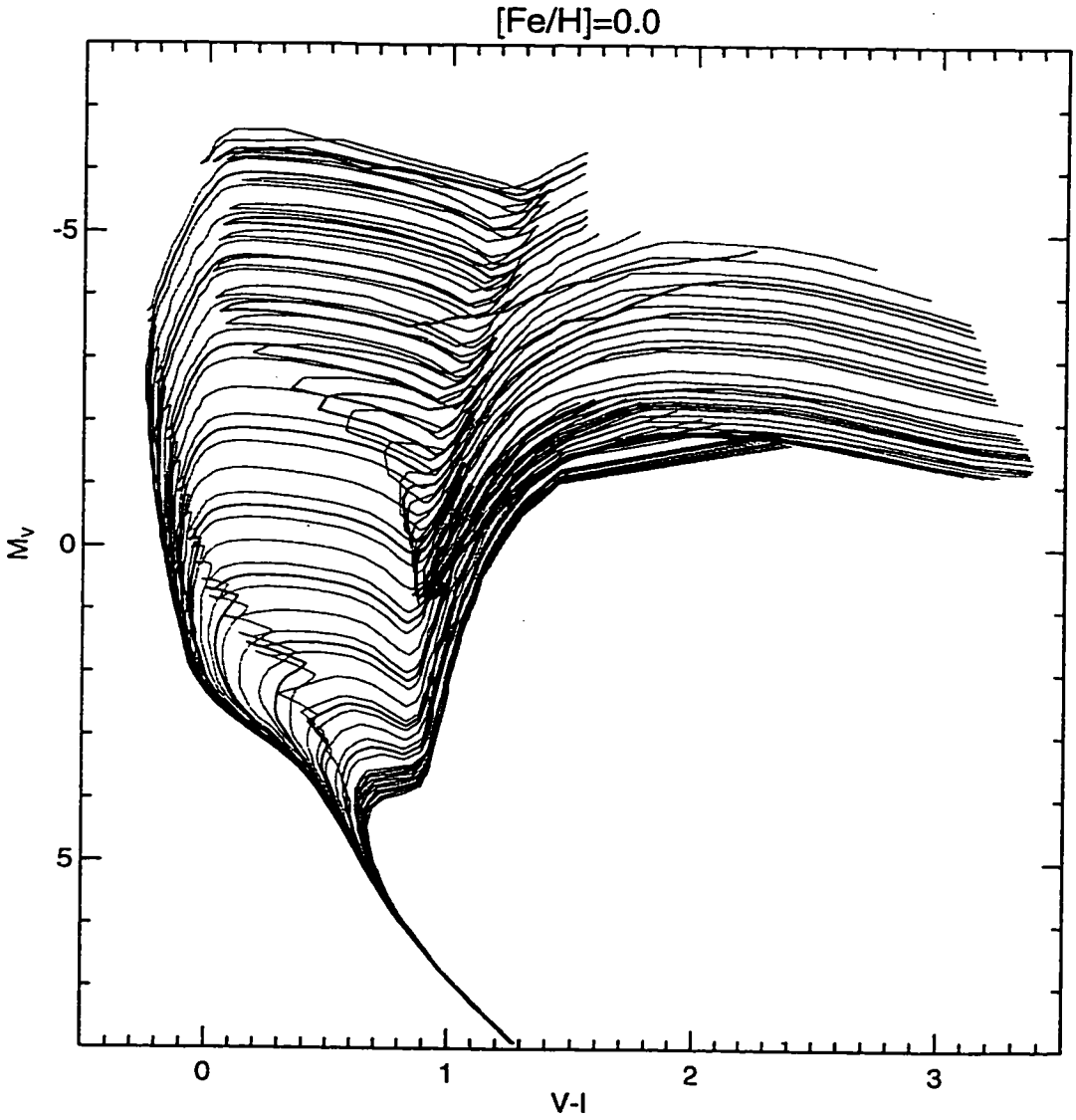

Figure 4.7e: Interpolated isochrones for [Fe/H]=0.0.

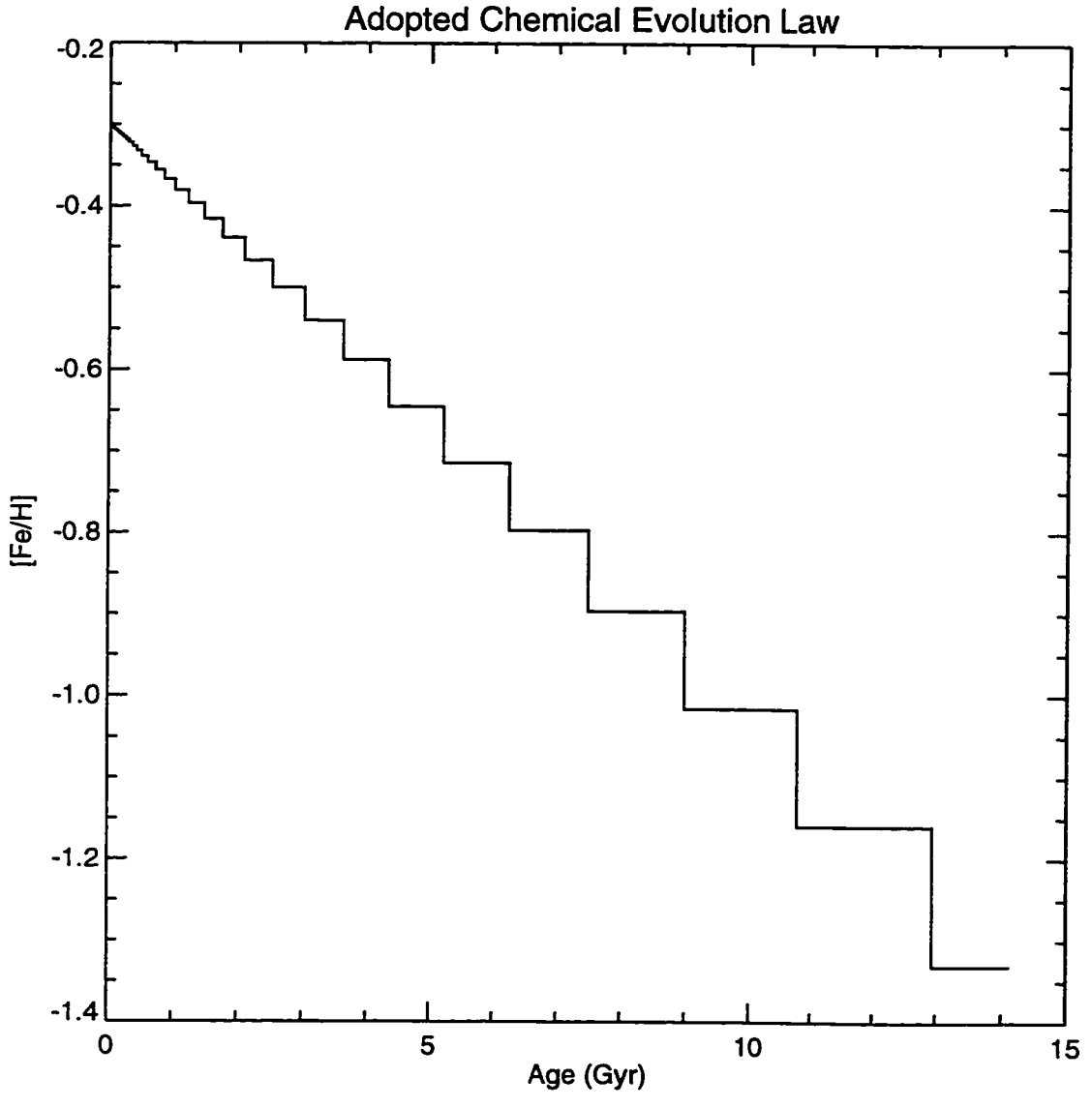

Figure 4.8: Chemical evolution model adopted for the analysis of the field star color-magnitude diagrams. The model was constructed from a linear fit to the ages and average abundances of the globular clusters studied in Chapter 3, the intermediate-age cluster ESO +121-SC03, and the young cluster population.

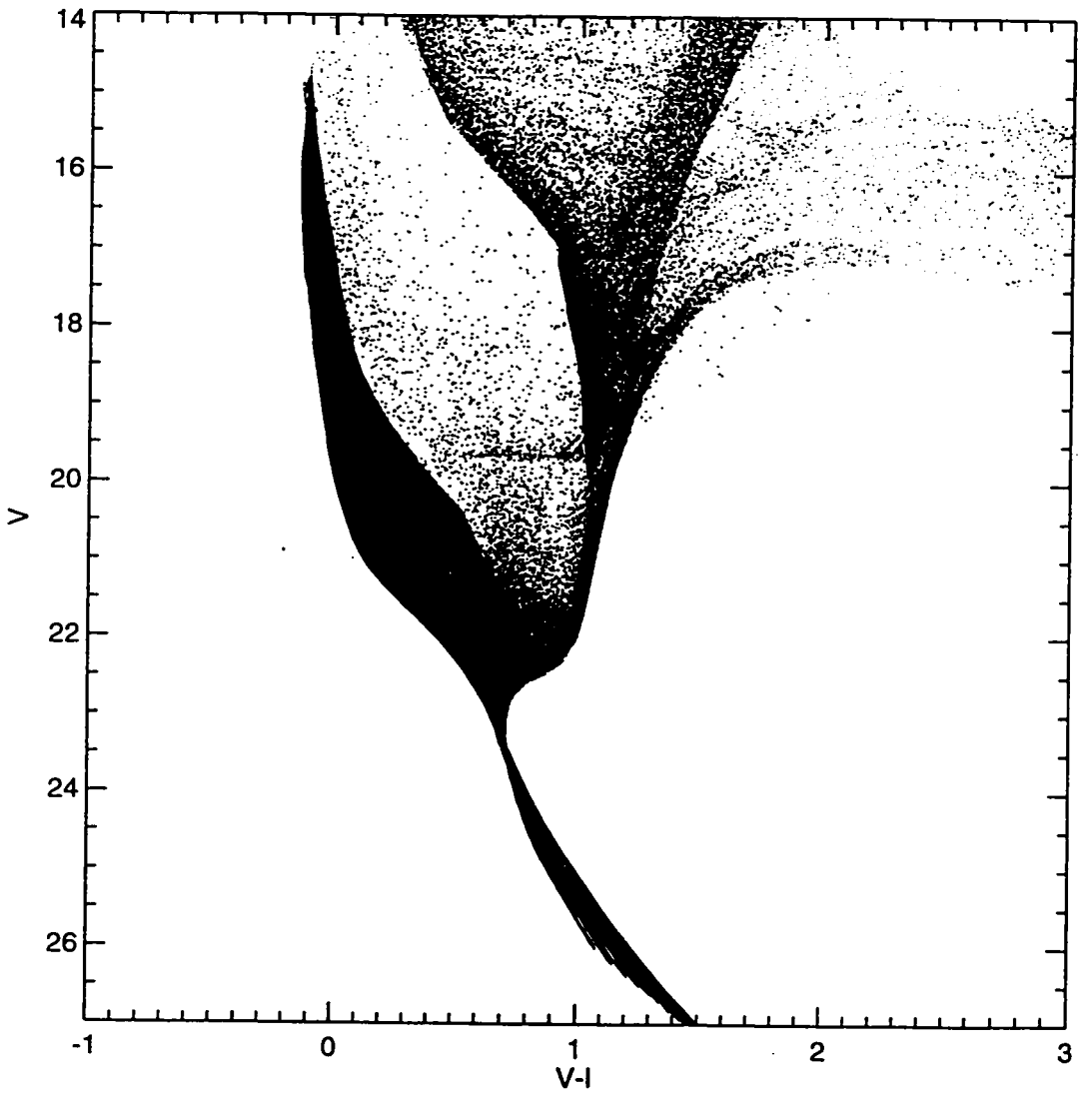

Figure 4.9a: Example color-magnitude diagram of stars selected to represent a model with a star formation rate of 1 $M_{\odot}yr^{-1}$ over 36 age bins, a flat IMF, $(m\text{-}M)_o = 18.3$, and $E(B-V)$=0.08.

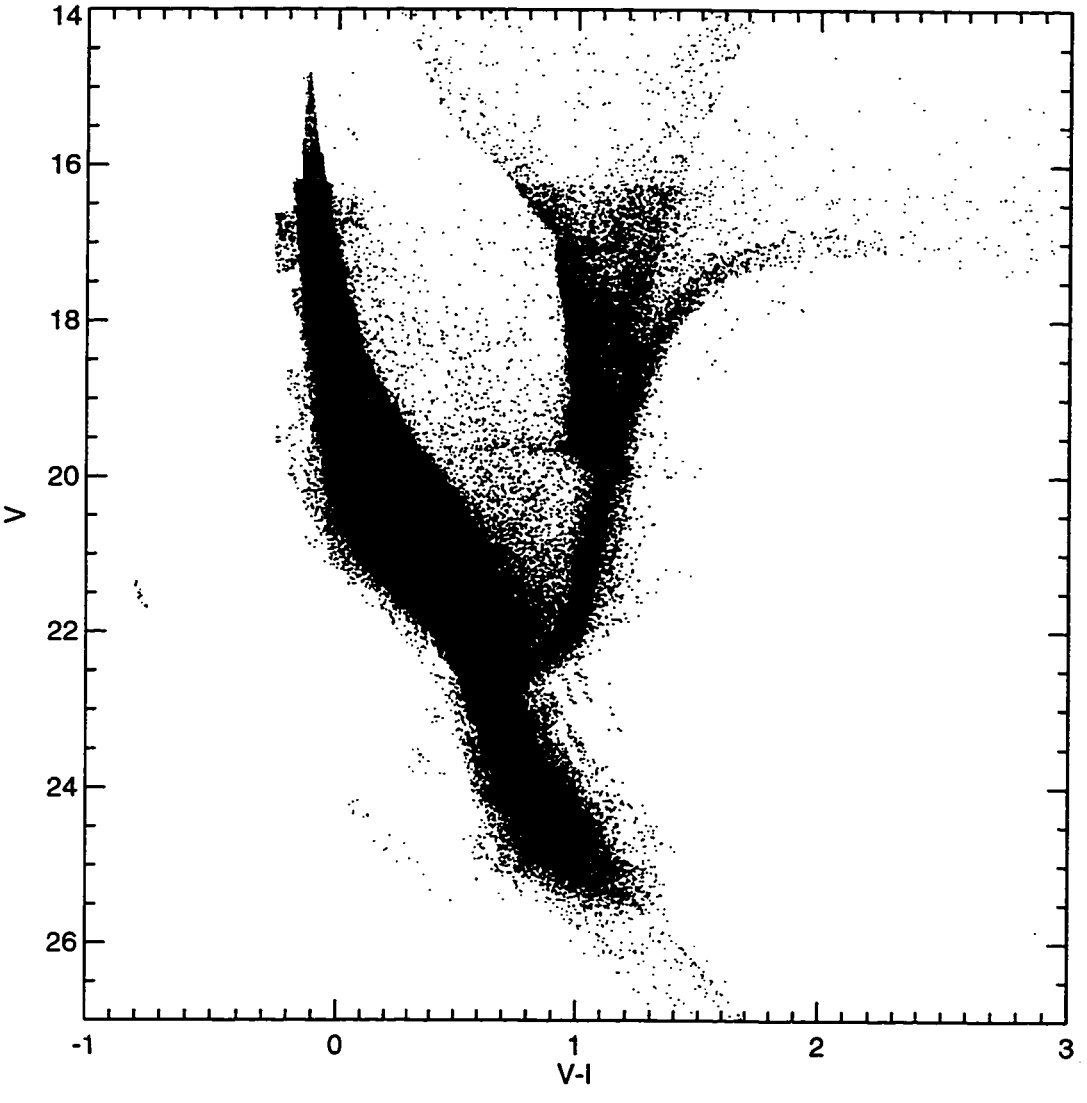

Figure 4.9b: Color-magnitude diagram of stars from *a* after photometric errors and incompleteness effects have been applied.

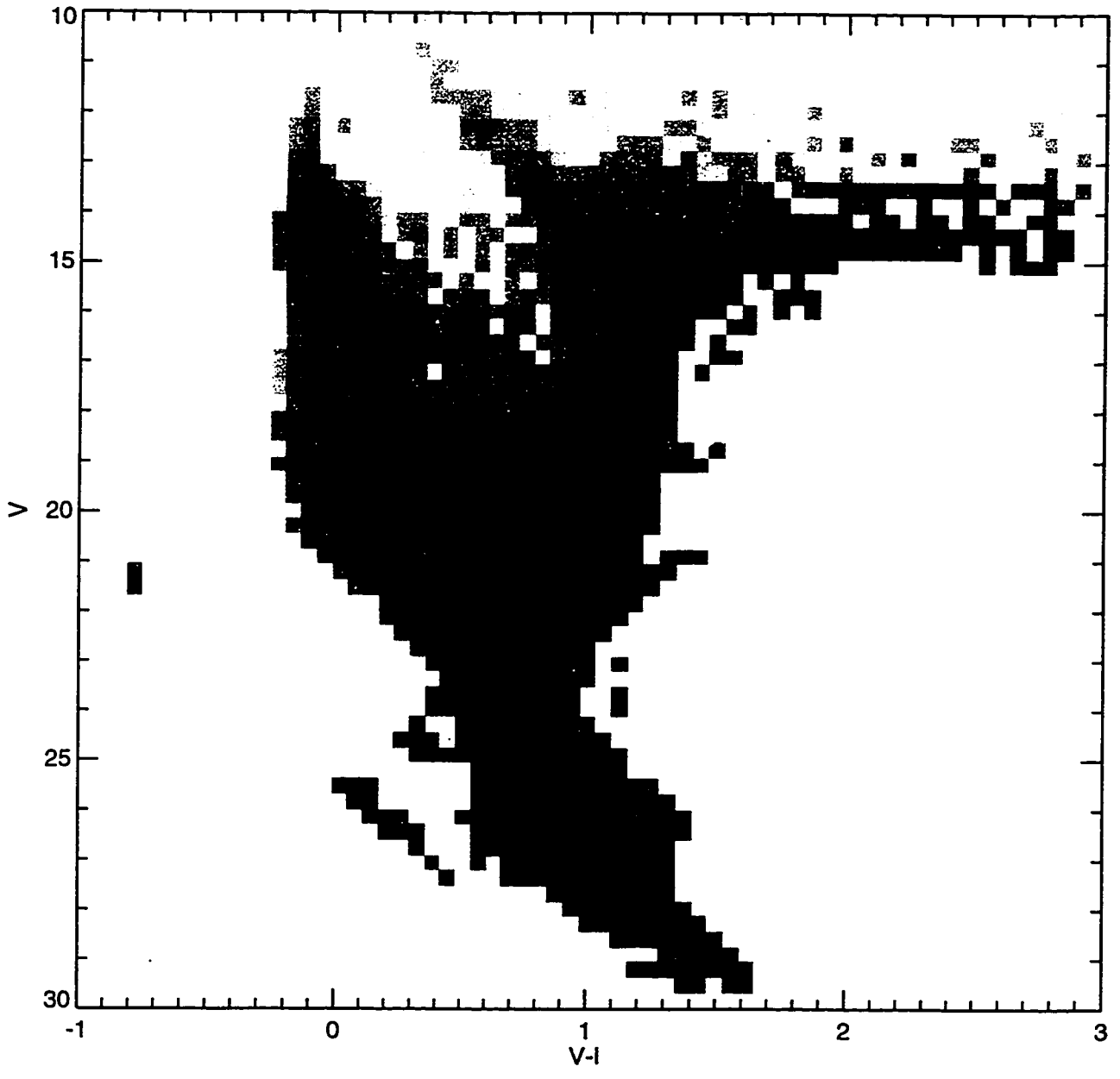

Figure 4.9c: Image showing the Hess diagram of the stars in *b*. Weights have been applied to correct the flat IMF from which the stars were selected to a Salpeter IMF. The scaling is logarithmic to bring out the less-populated evolutionary phases.

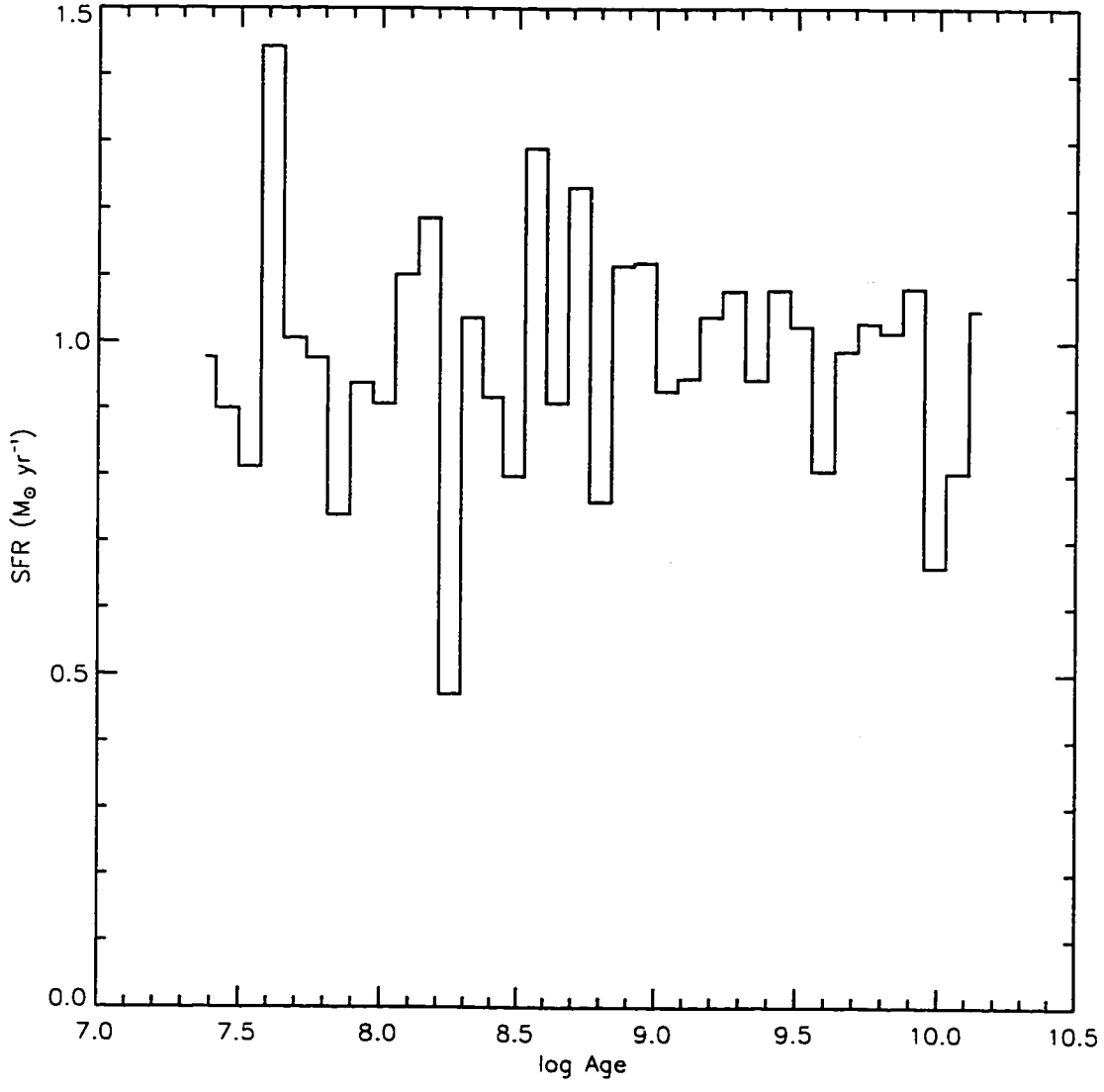

Figure 4.10: Input star formation history used in tests of the solution method described in the text.

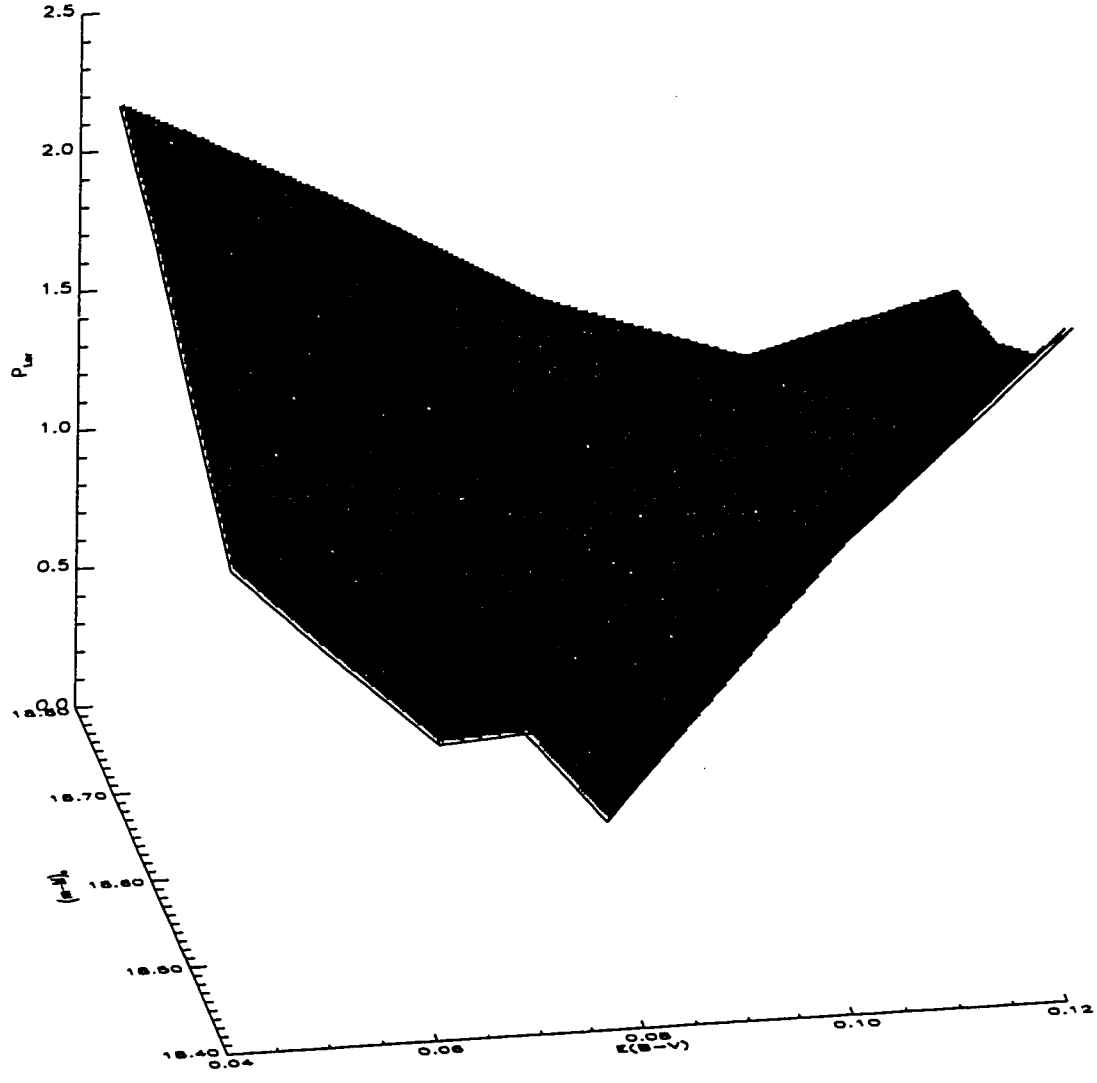

Figure 4.11: P_{Lor} surface used to select the best-fit parameters of the solution to the star formation history in Fig. 4.10. The minimum occurs at $E(B-V)$=0.08 and $(m\text{-}M)_o$=18.5, which were the input values.

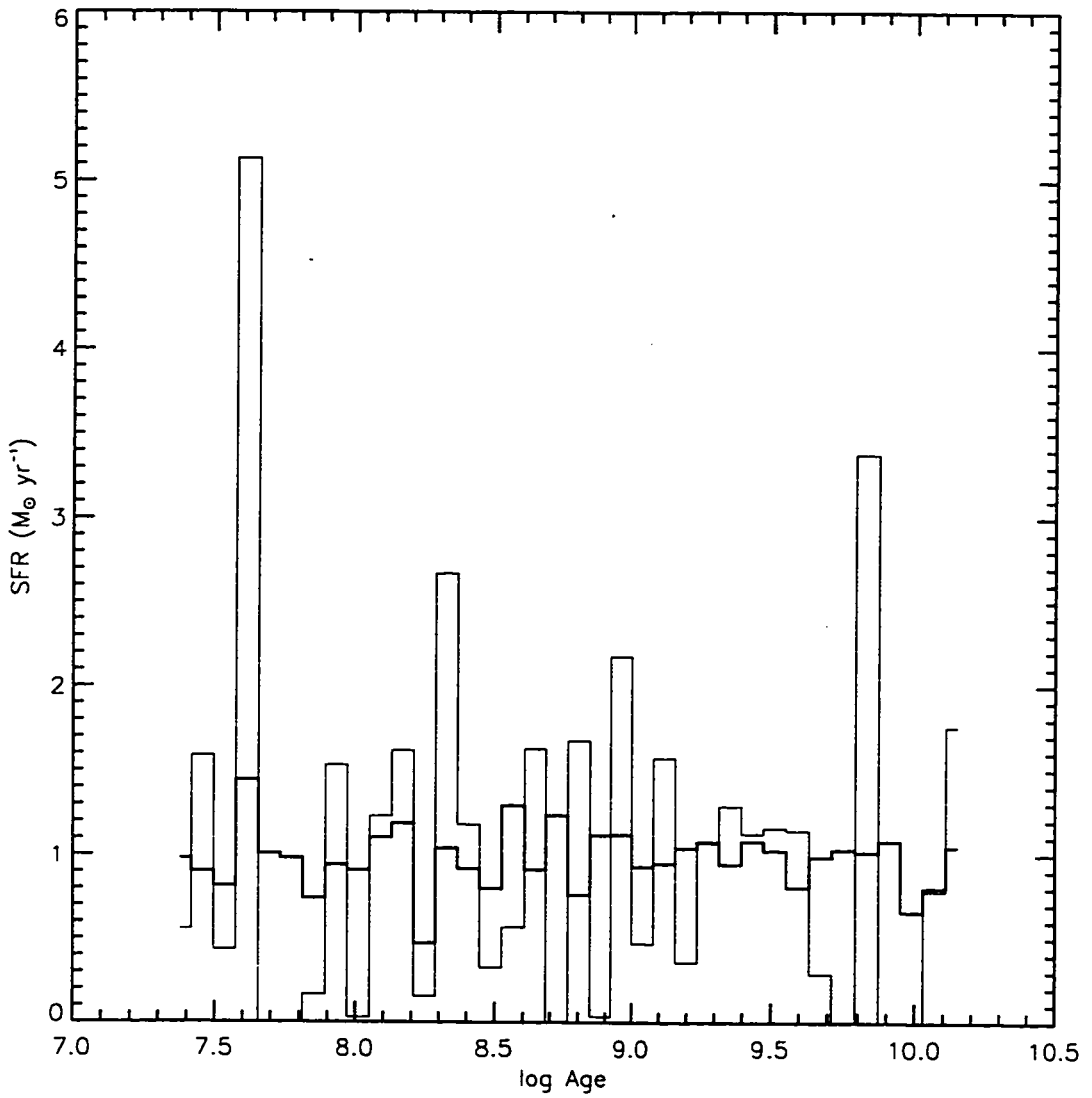

Figure 4.12a: Star formation history solved from a color-magnitude diagram with stars selected from the profile of Fig. 4.10, using 36 age bins in the solution. The noisy solution indicates that the achievable age resolution is lower than that which was attempted.

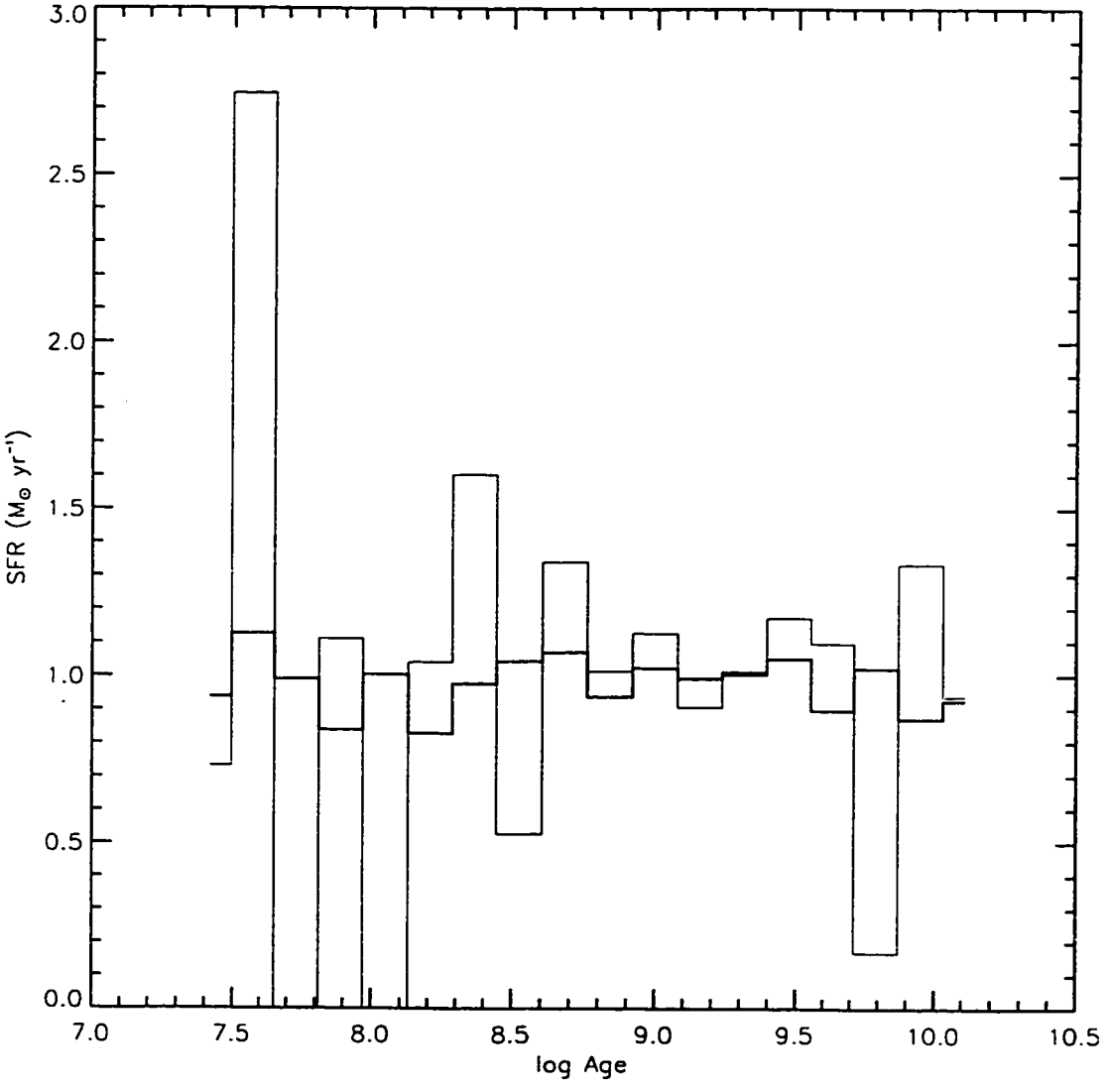

Figure 4.12b: Star formation history solution of same color-magnitude diagram as was used in *a*, after grouping every other model together.

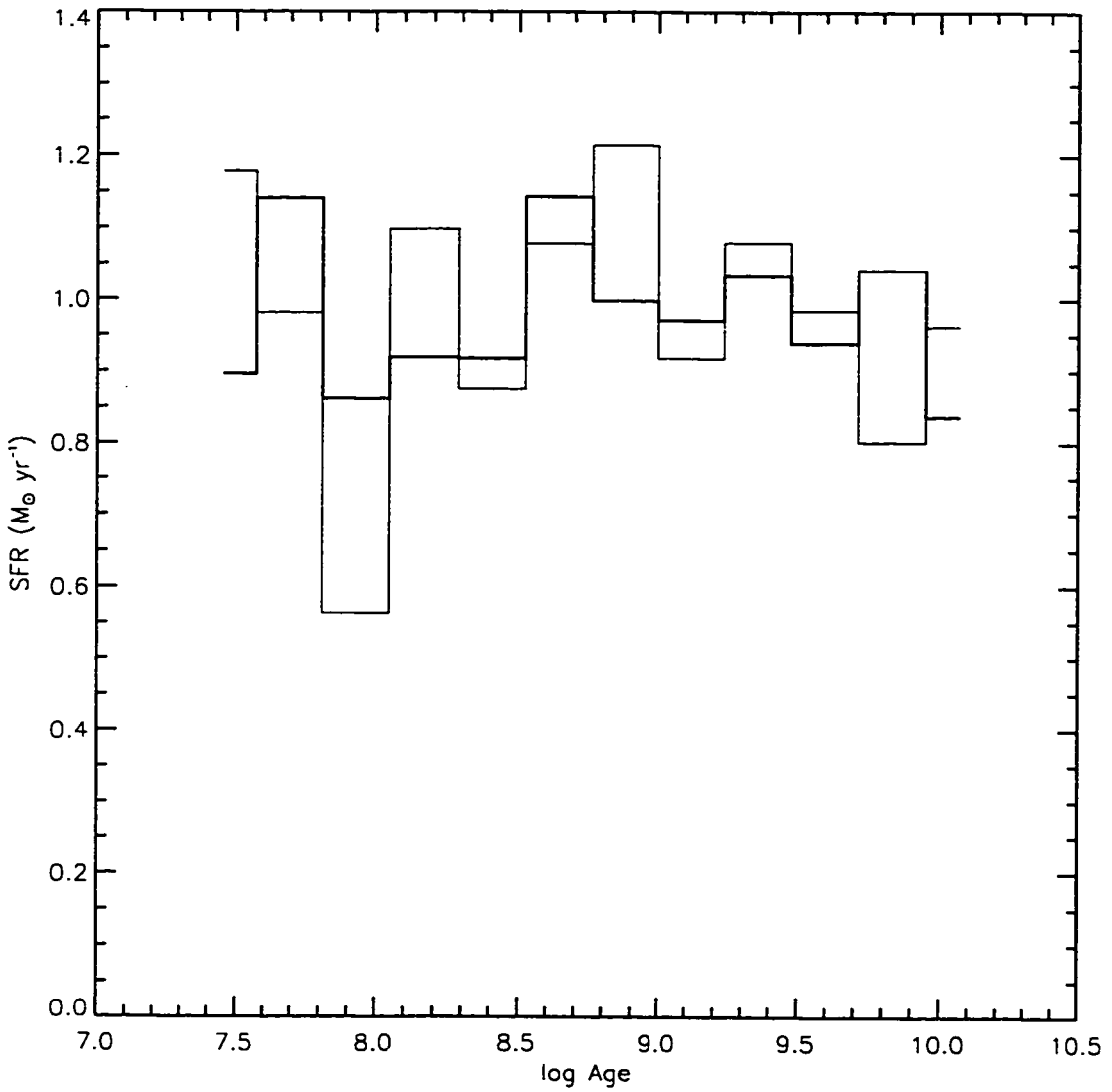

Figure 4.12c: Star formation history solution after grouping every three models together.

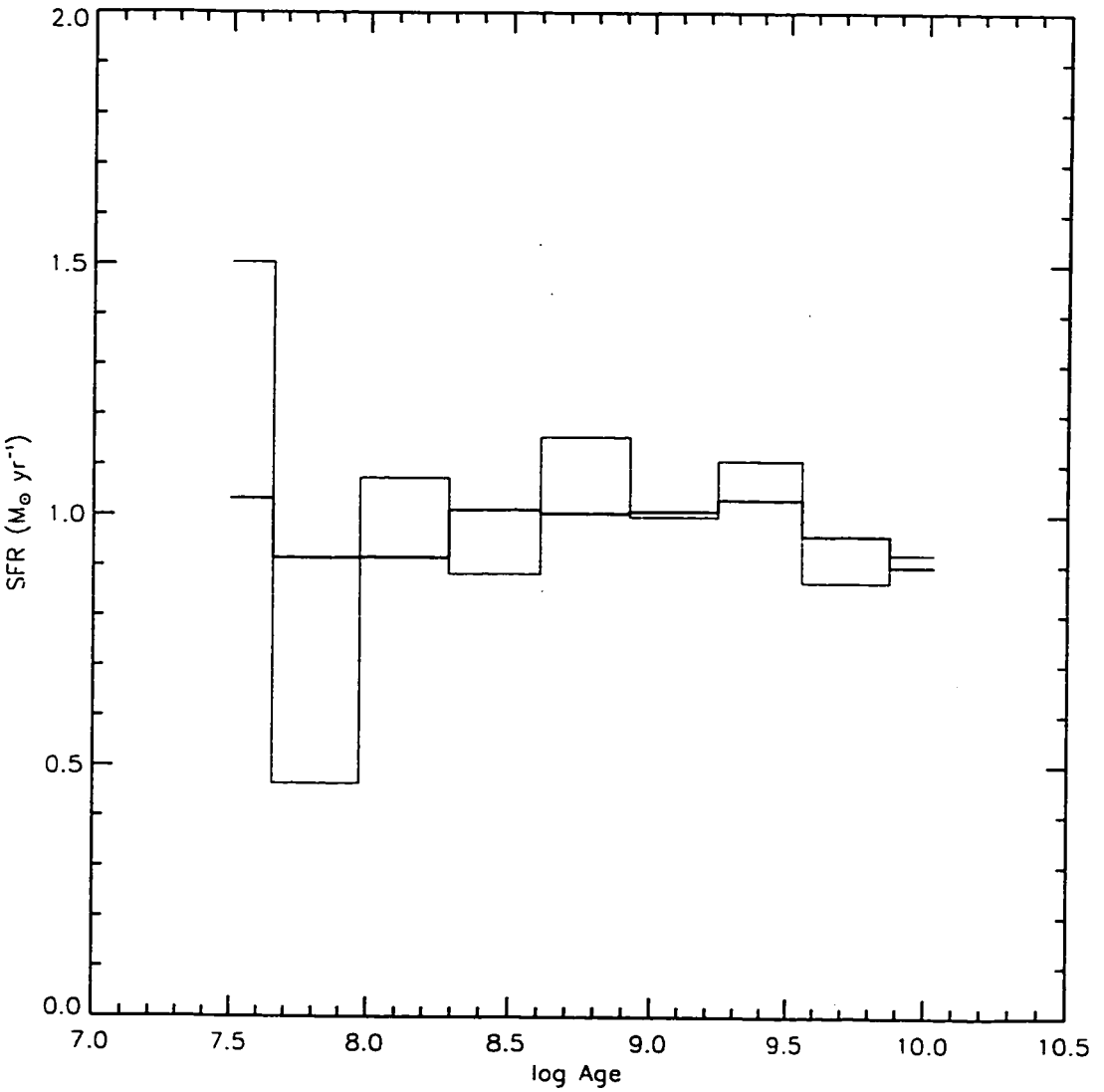

Figure 4.12d: Star formation history solution after grouping every four models together.

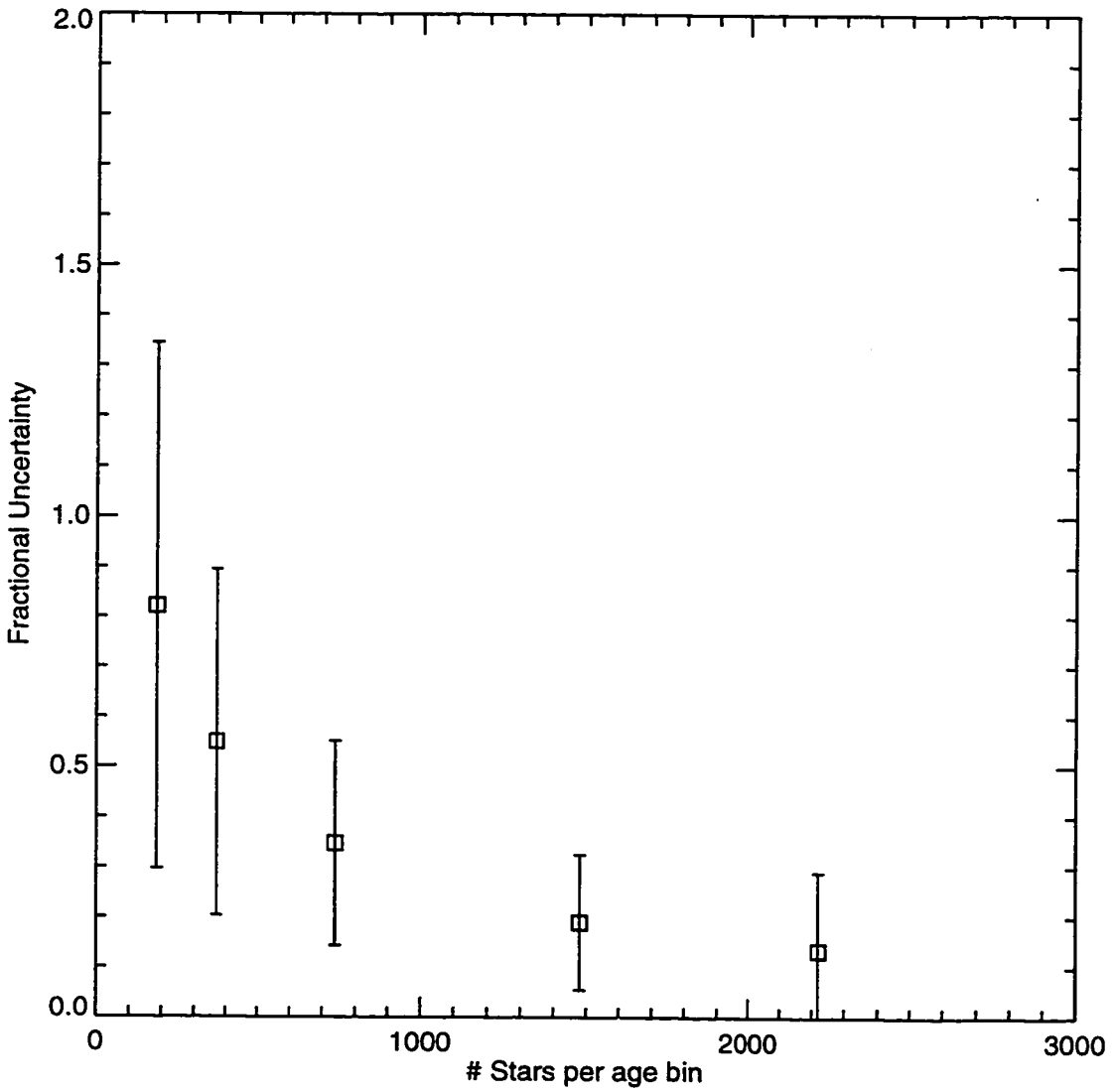

Figure 4.13a: Median uncertainty and dispersion about the median uncertainty in the star formation rate of repeated solutions made from color-magnitude diagrams with stars selected from the profile of Fig. 4.10. The figure shows the effect on the uncertainties as the number of stars in the color-magnitude diagram increases.

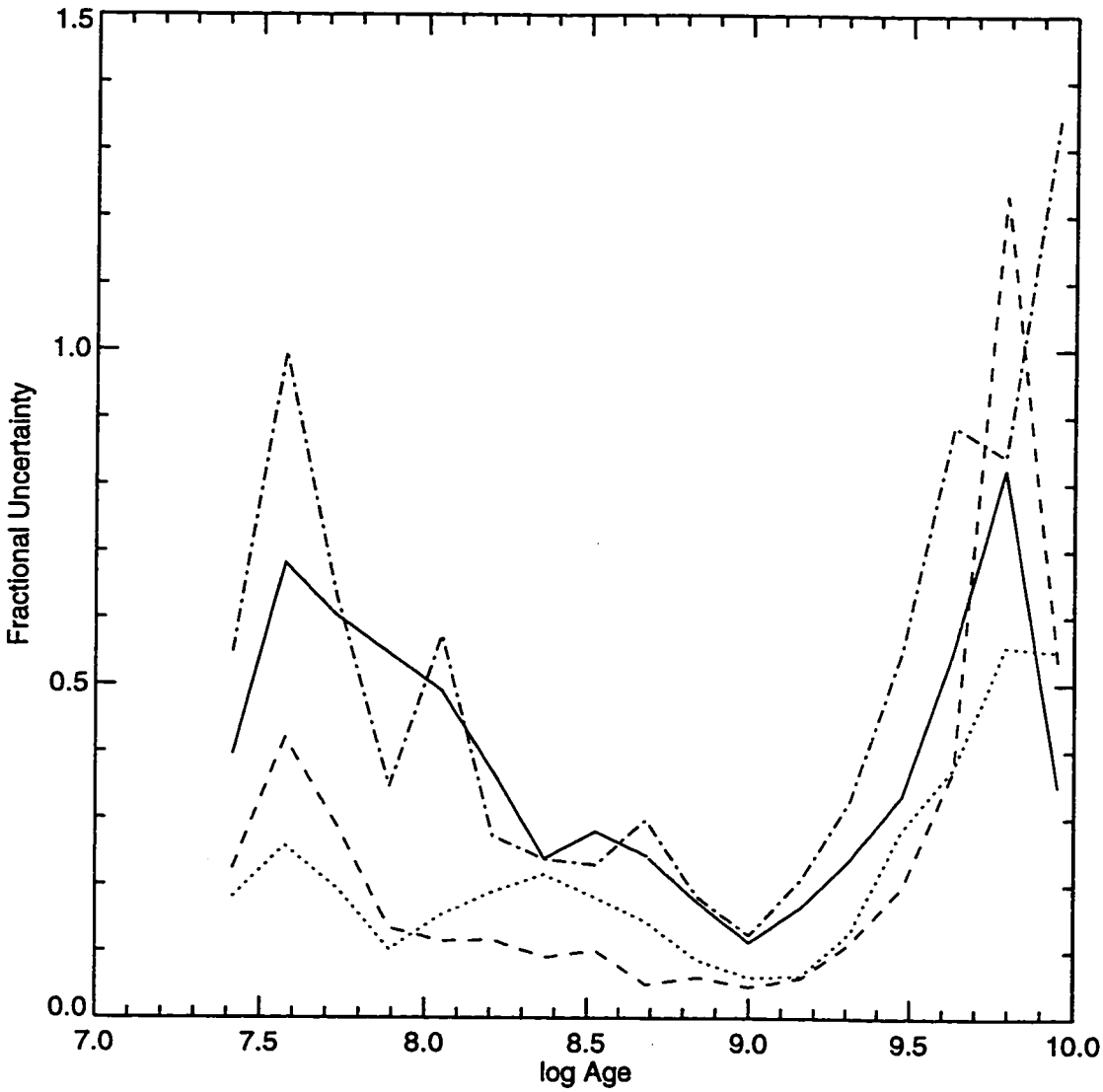

Figure 4.13b: Median uncertainty in the star formation rate from the solutions described in *a*, shown as a function of log Age. The dashed-dotted line represents the solutions made for the CMDs with 500 stars per age bin, the solid line for 100 stars per age bin, the dotted line for 2000 stars per age bin, and the dashed line for 300 stars per age bin.

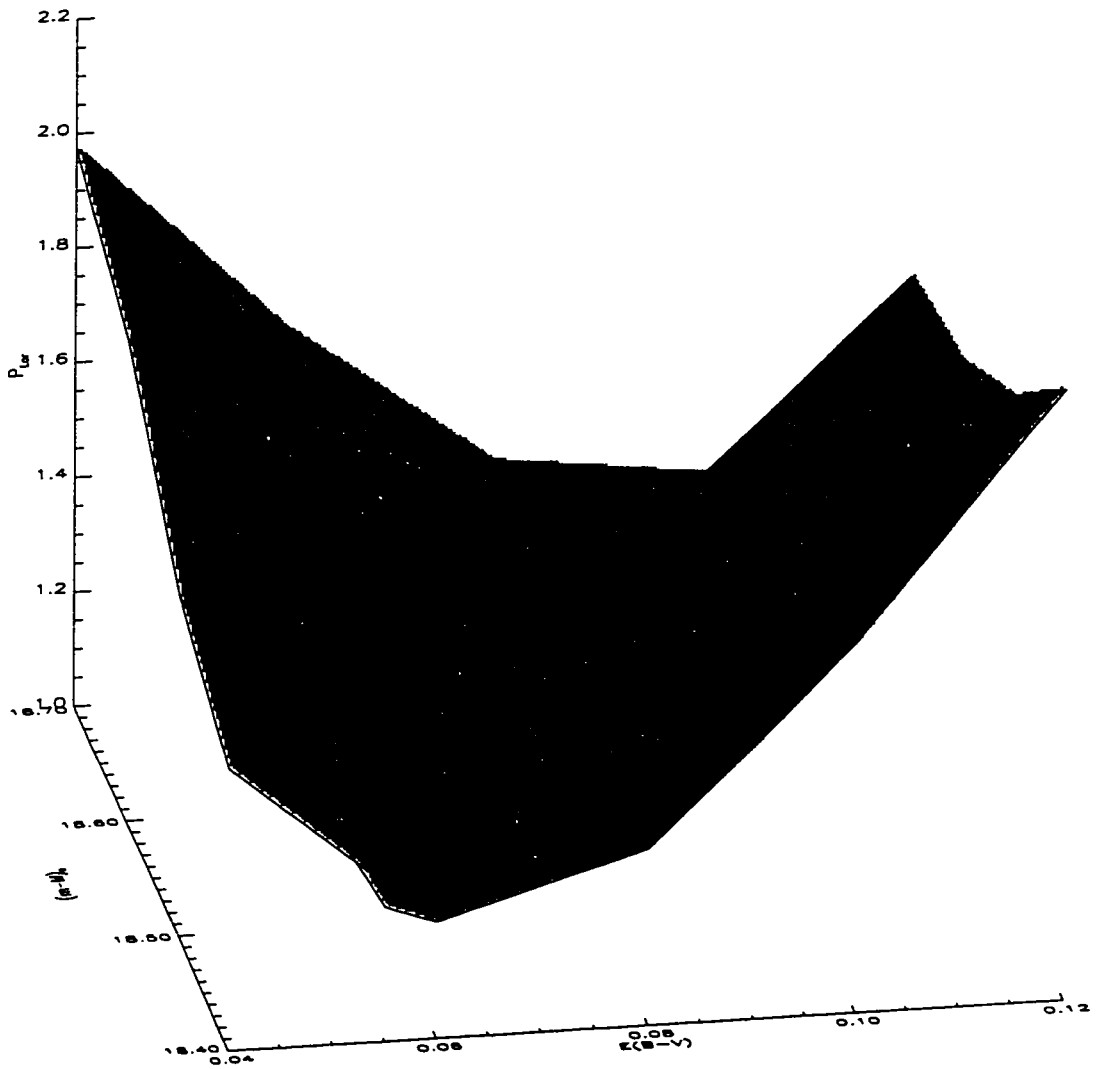

Figure 4.14: P_{Lor} surface for solutions of the star formation history of the NGC 1754 field for the Salpeter IMF. The minimum of the surface is at $E(B-V)$=0.06 and $(m\text{-}M)_o$=18.5.

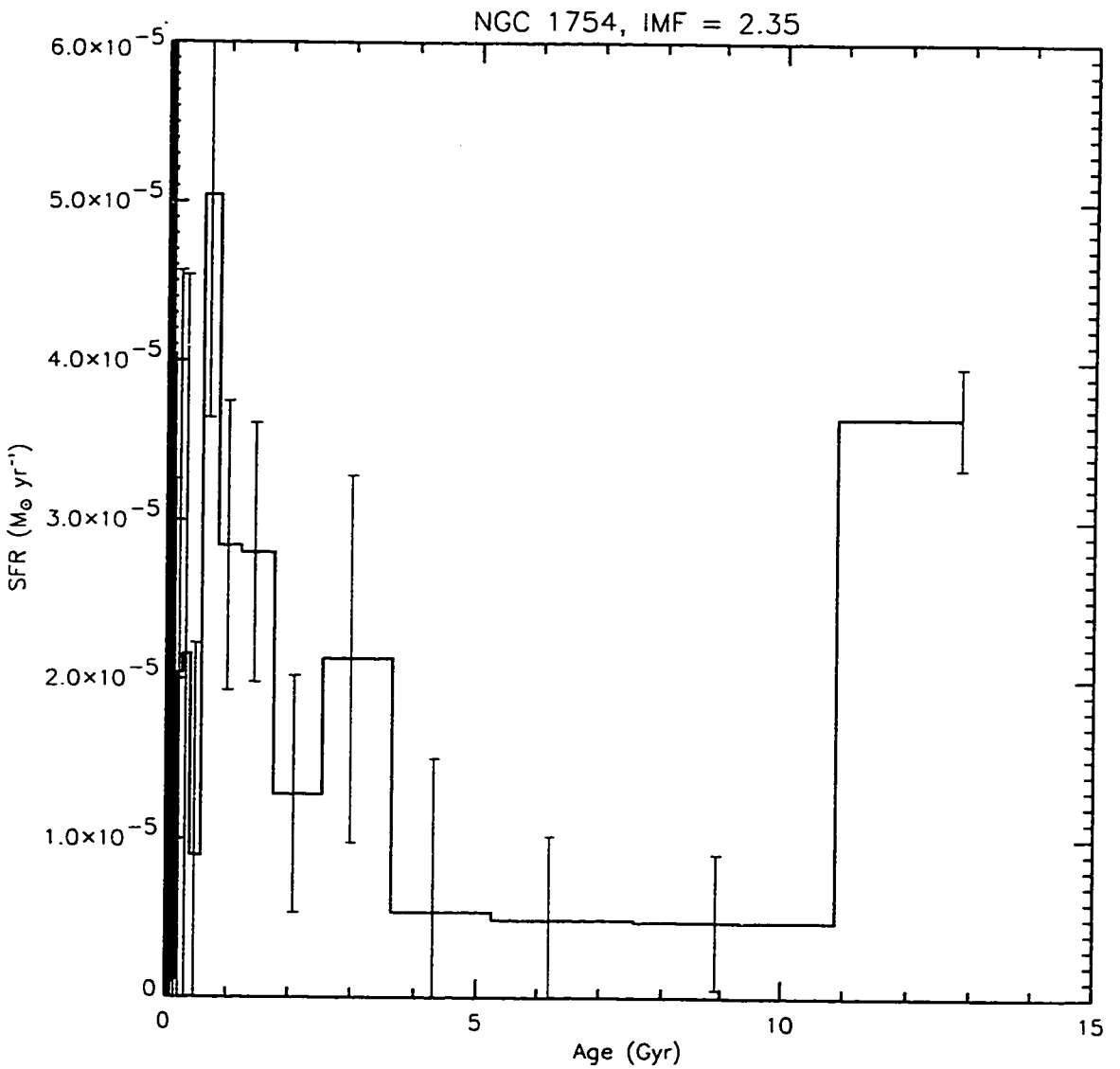

Figure 4.15a: Derived star formation history for the NGC 1754 field using 18 age bins in the solution and the Salpeter IMF. The error bars were calculated from the Monte Carlo simulations described in the text.

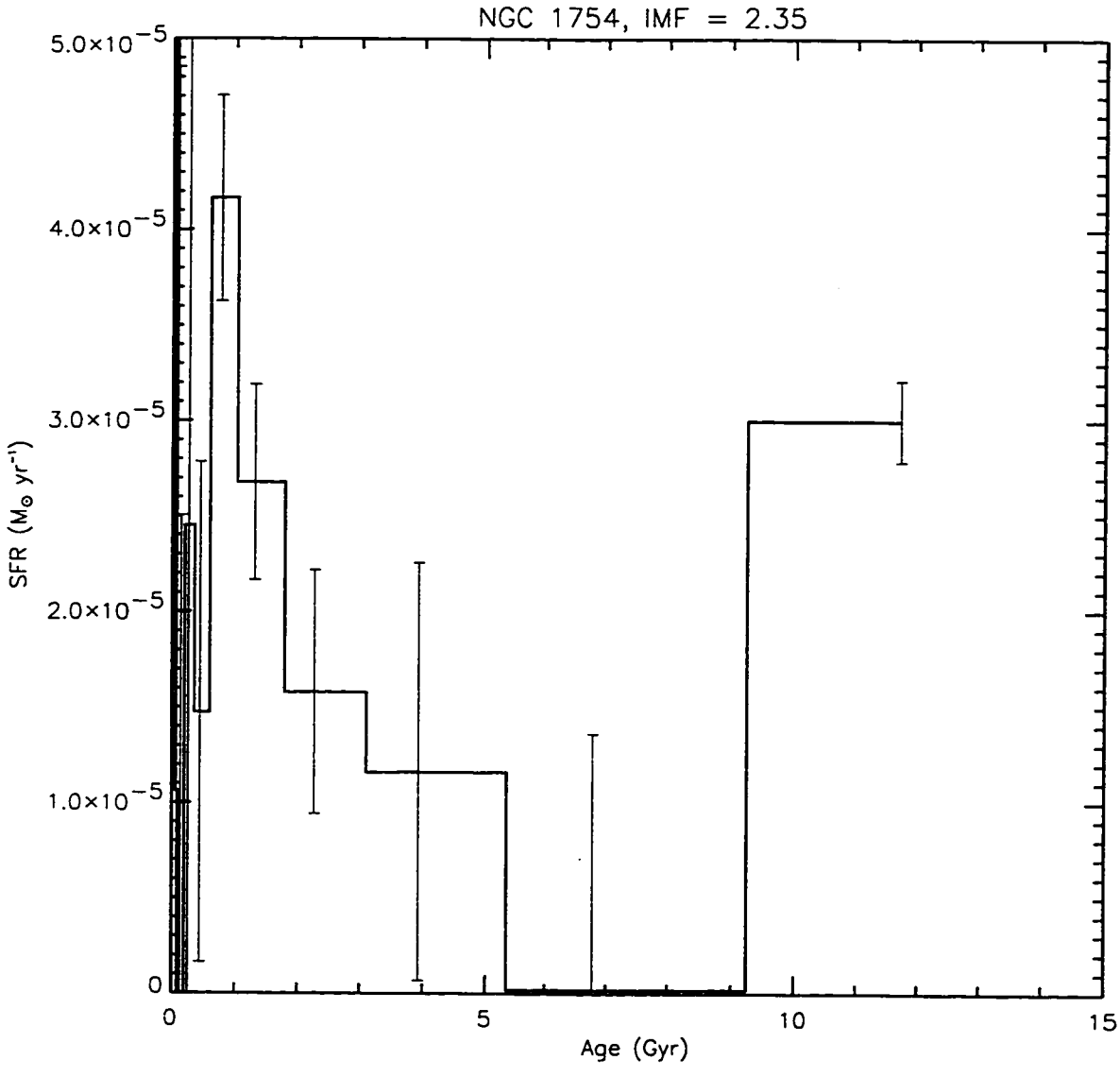

Figure 4.15b: Derived star formation history for the NGC 1754 field using 12 age bins in the solution and the Salpeter IMF.

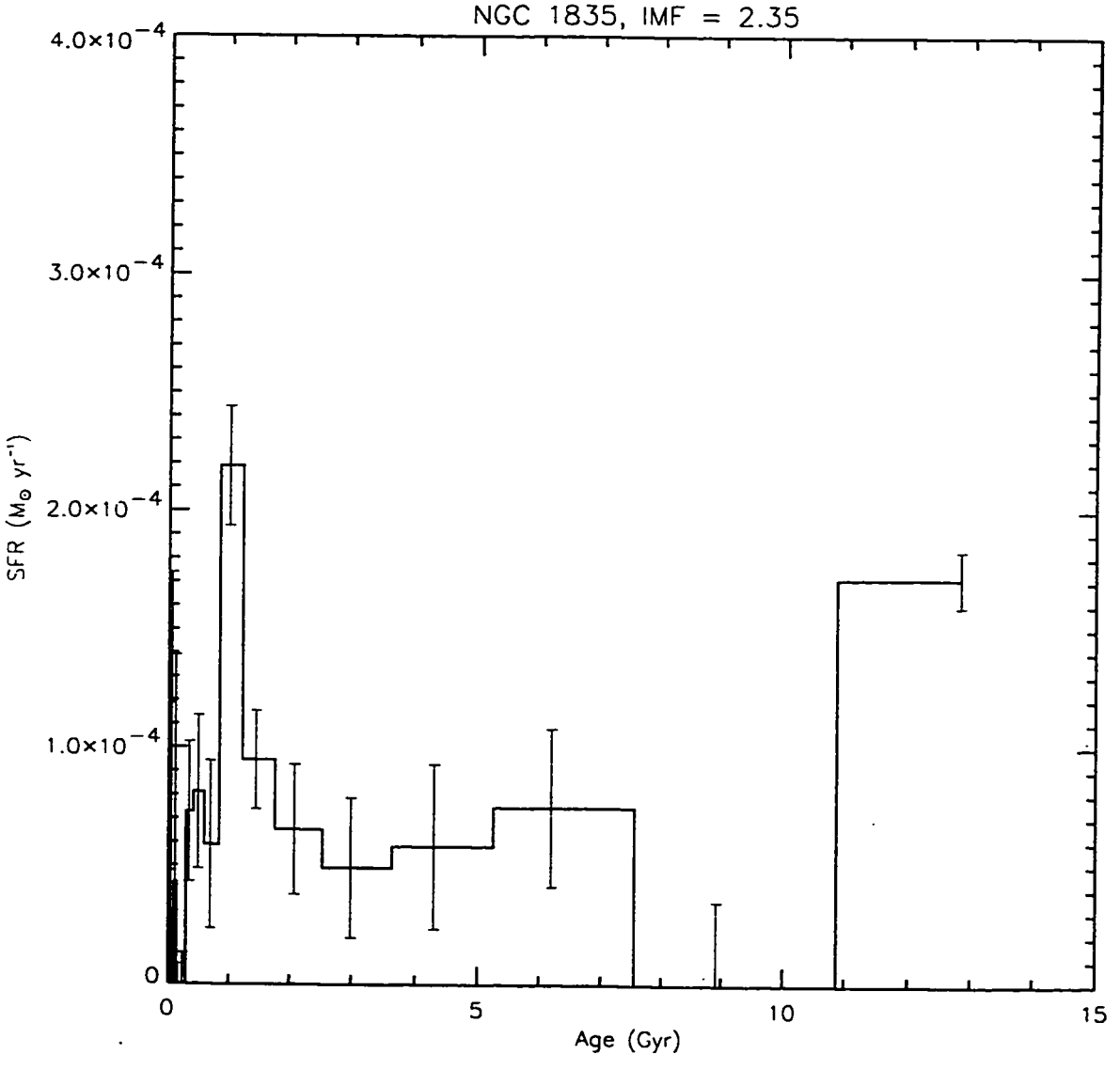

Figure 4.15c: Derived star formation history for the NGC 1835 field using 18 age bins in the solution and the Salpeter IMF.

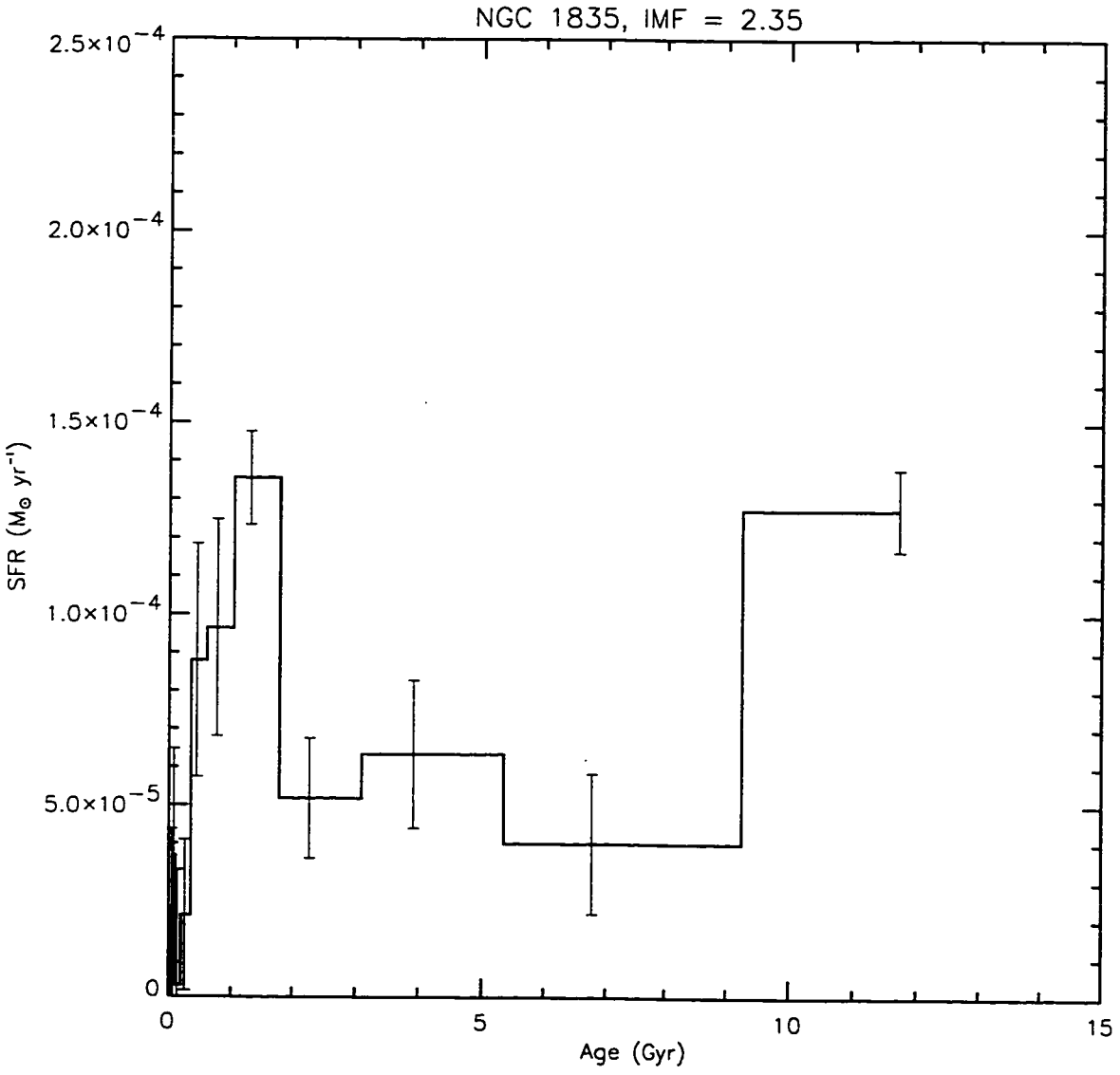

Figure 4.15d: Derived star formation history for the NGC 1835 field using 12 age bins in the solution and the Salpeter IMF.

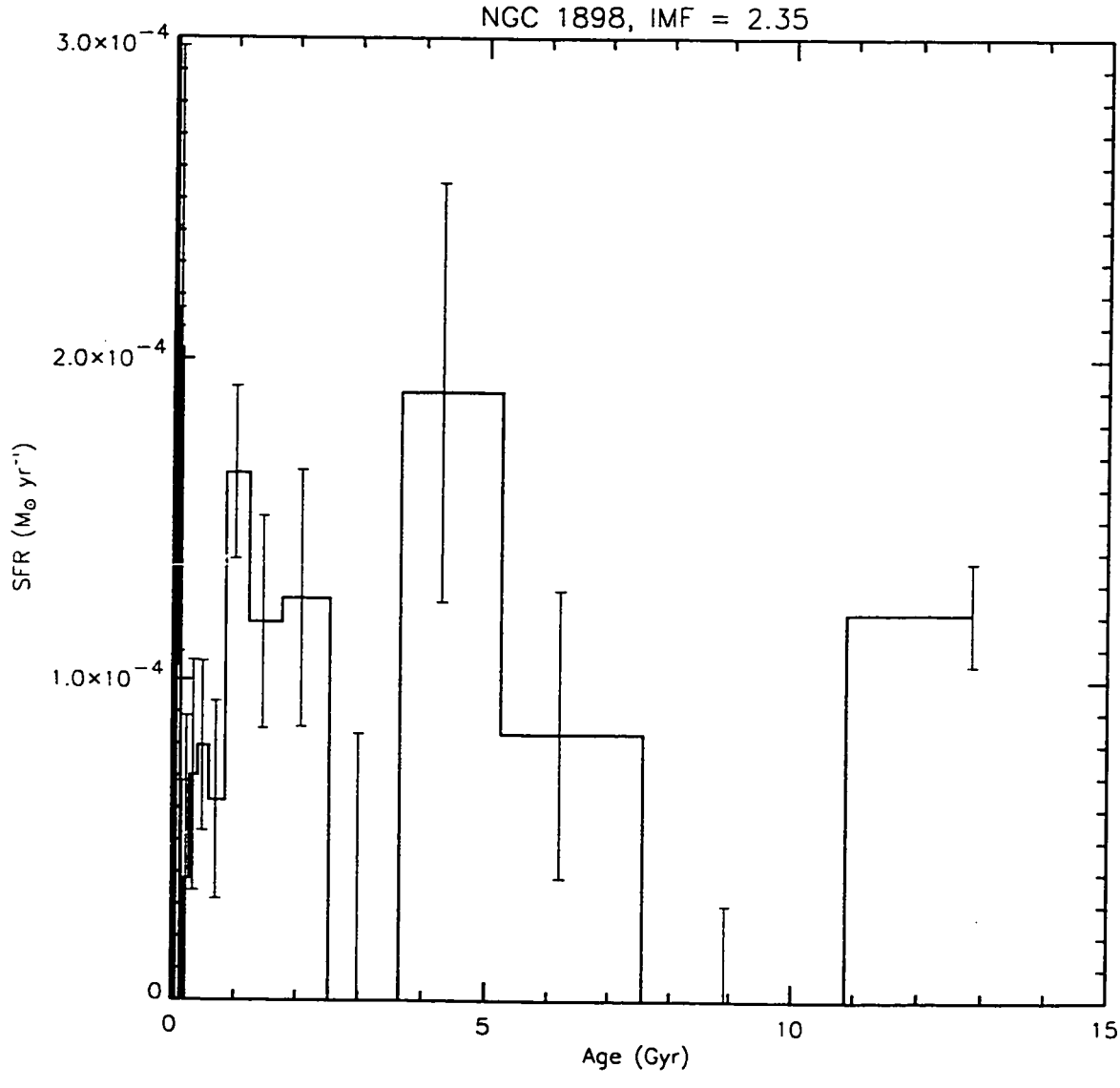

Figure 4.15e: Derived star formation history for the NGC 1898 field using 18 age bins in the solution and the Salpeter IMF.

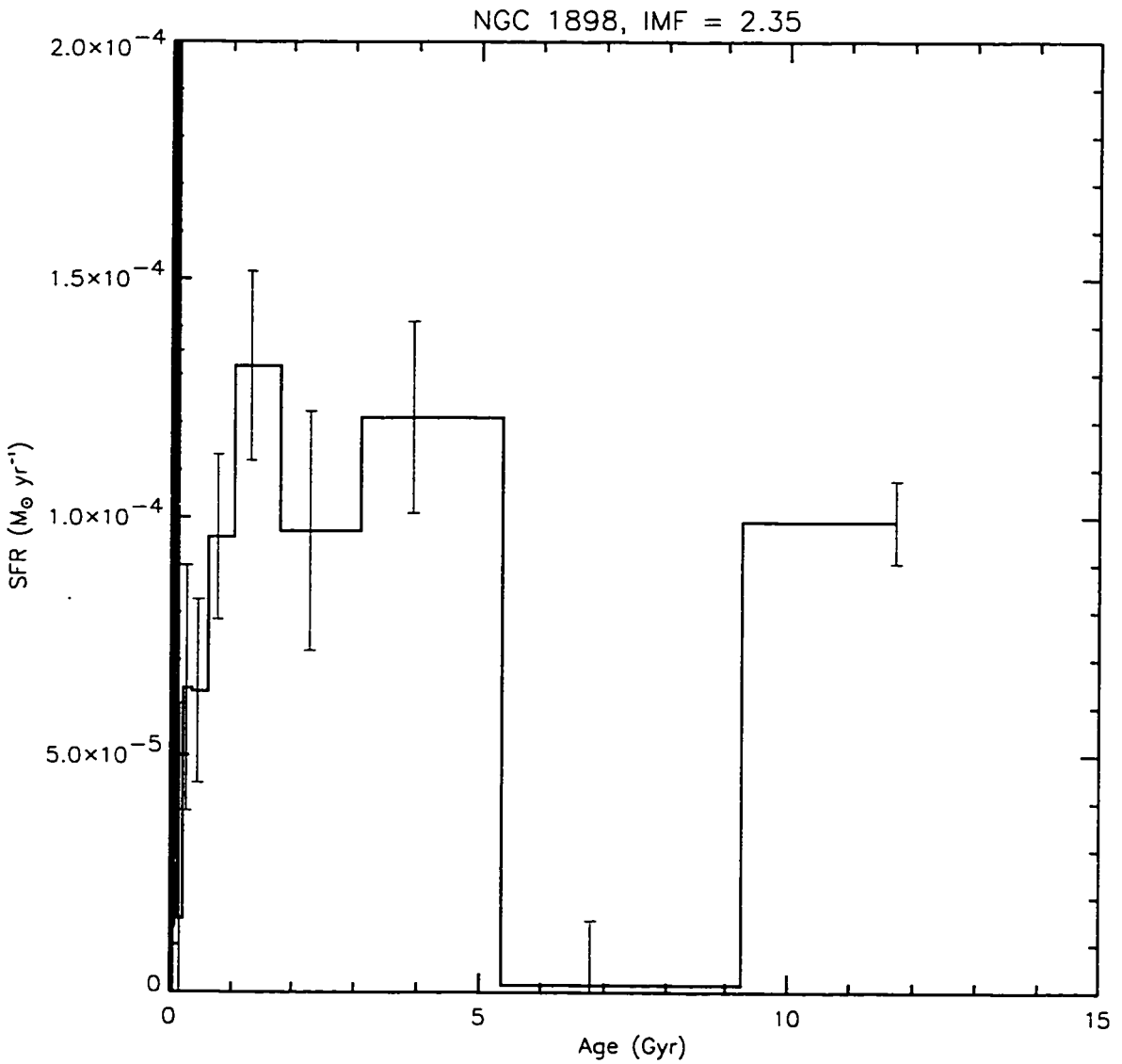

Figure 4.15f: Derived star formation history for the NGC 1898 field using 12 age bins in the solution and the Salpeter IMF.

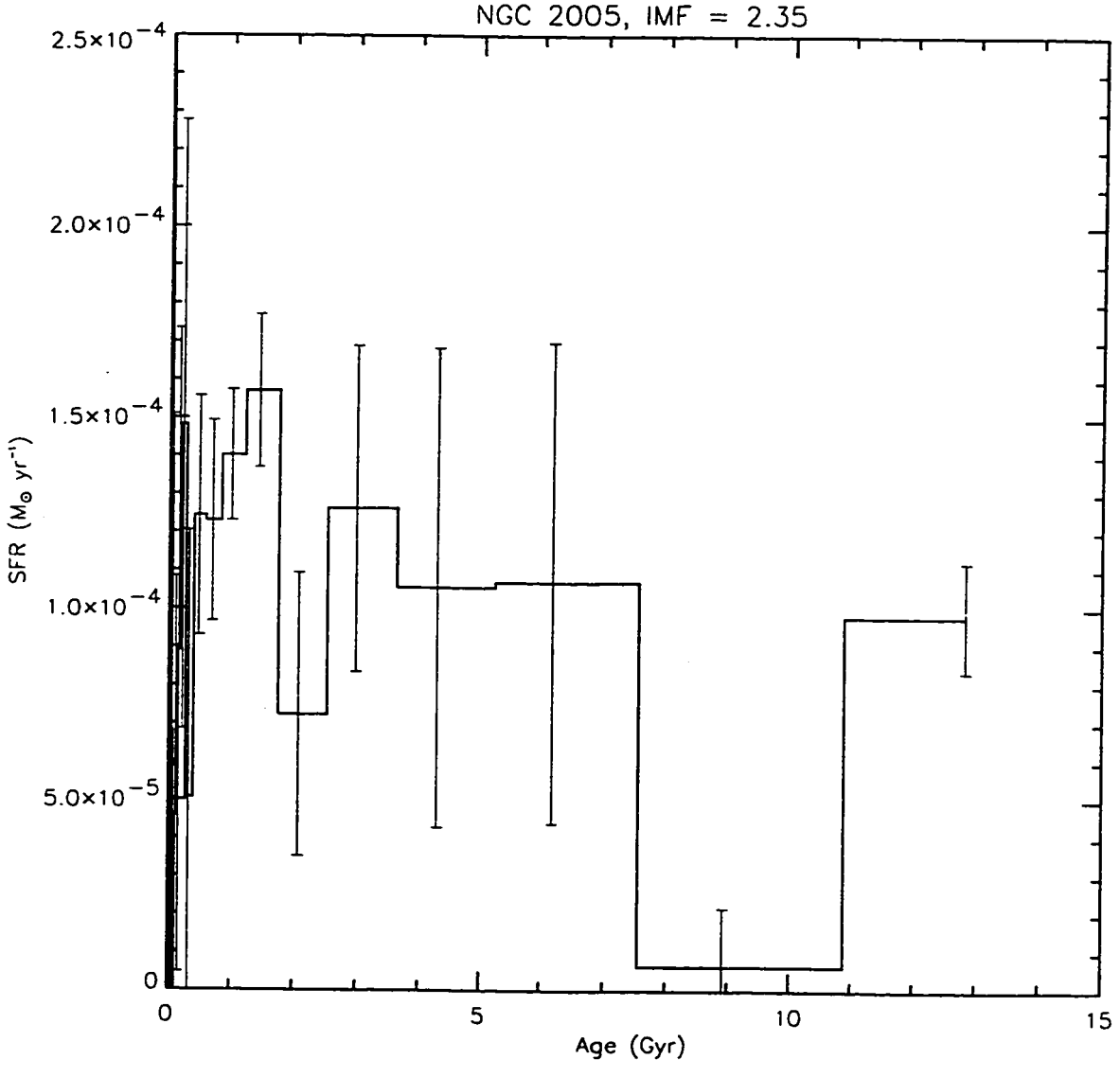

Figure 4.15g: Derived star formation history for the NGC 2005 field using 18 age bins in the solution and the Salpeter IMF.

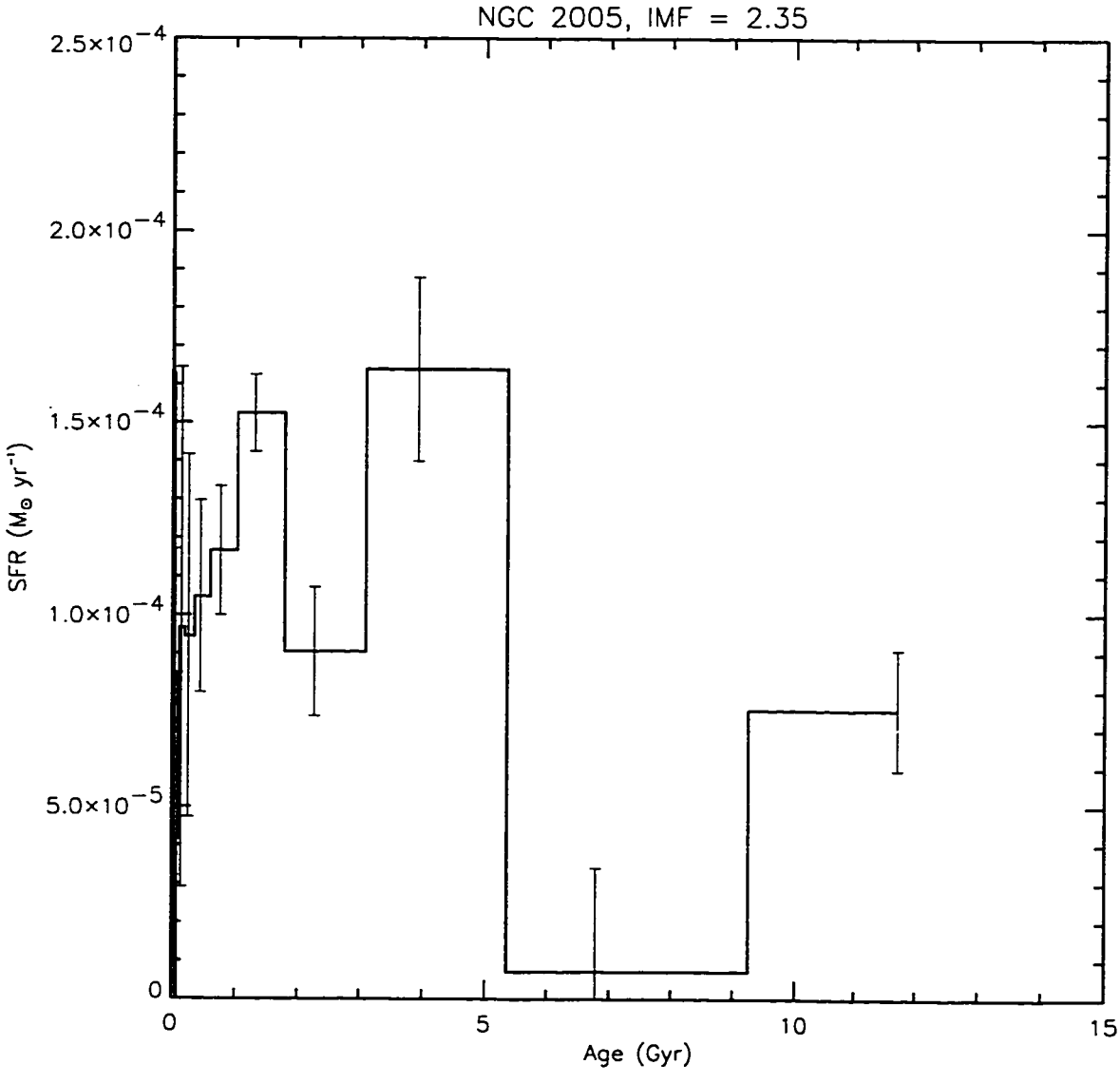

Figure 4.15h: Derived star formation history for the NGC 2005 field using 12 age bins in the solution and the Salpeter IMF.

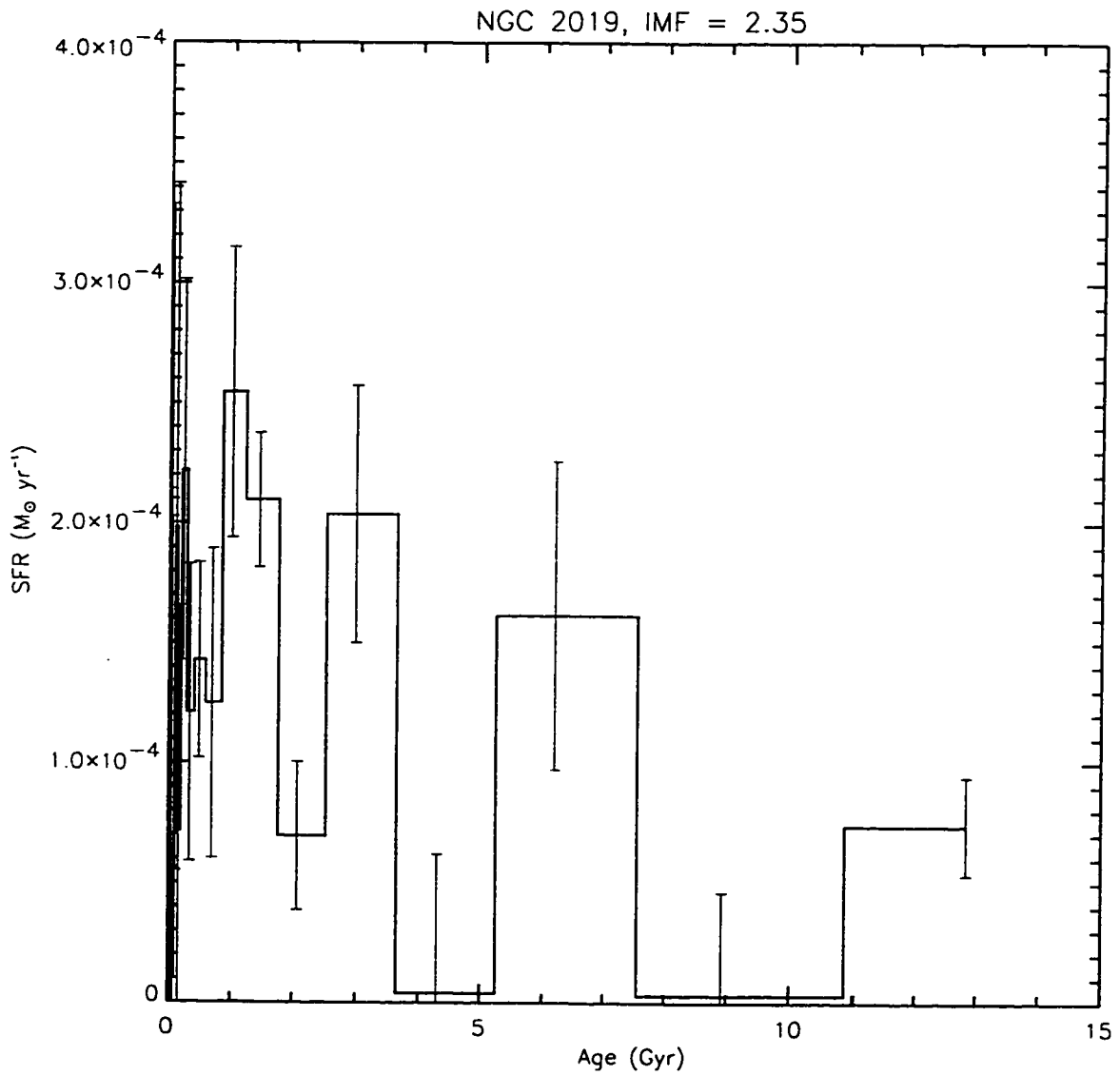

Figure 4.15i: Derived star formation history for the NGC 2019 field using 18 age bins in the solution and the Salpeter IMF.

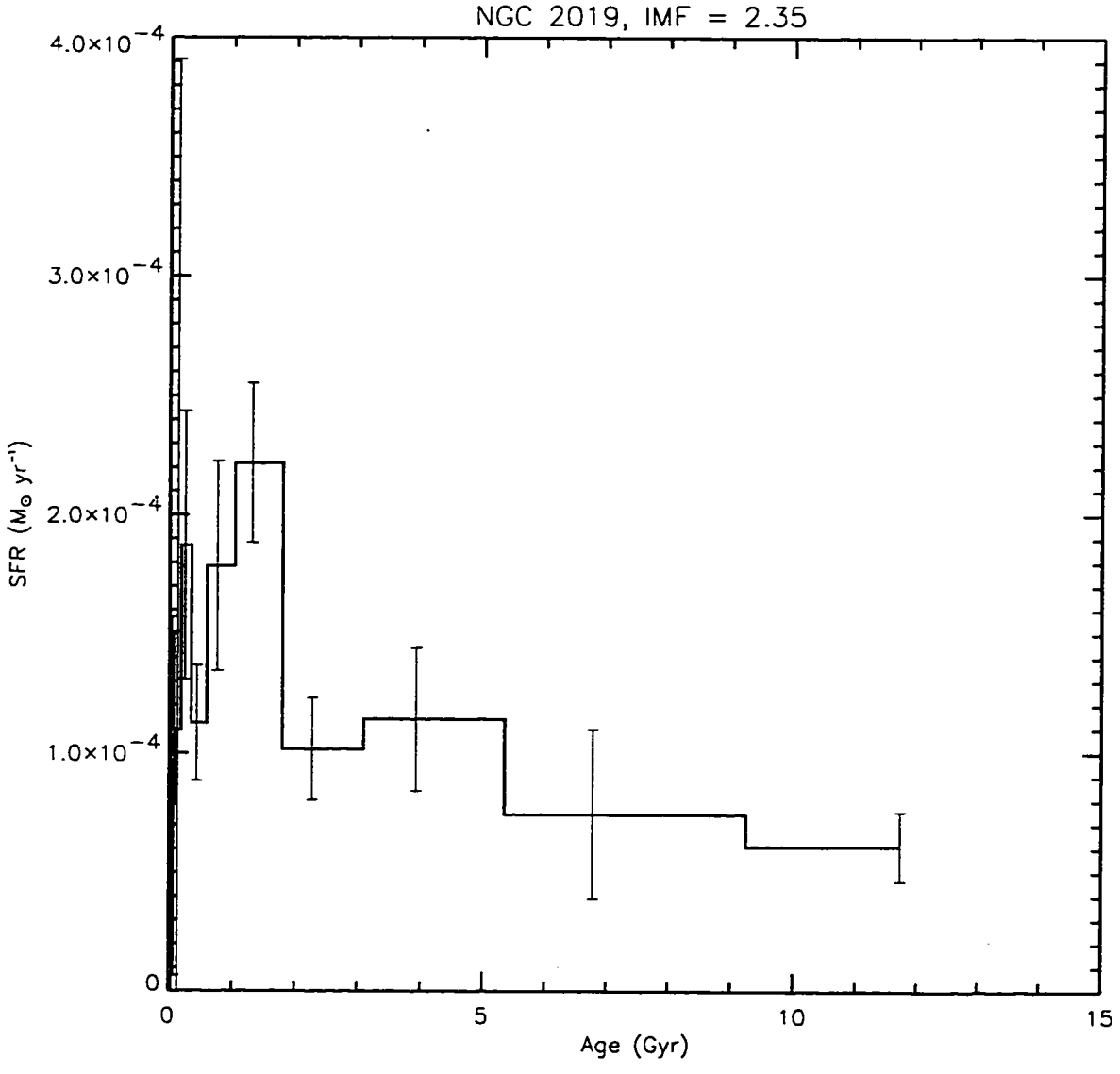

Figure 4.15j: Derived star formation history for the NGC 2019 field using 12 age bins in the solution and the Salpeter IMF.

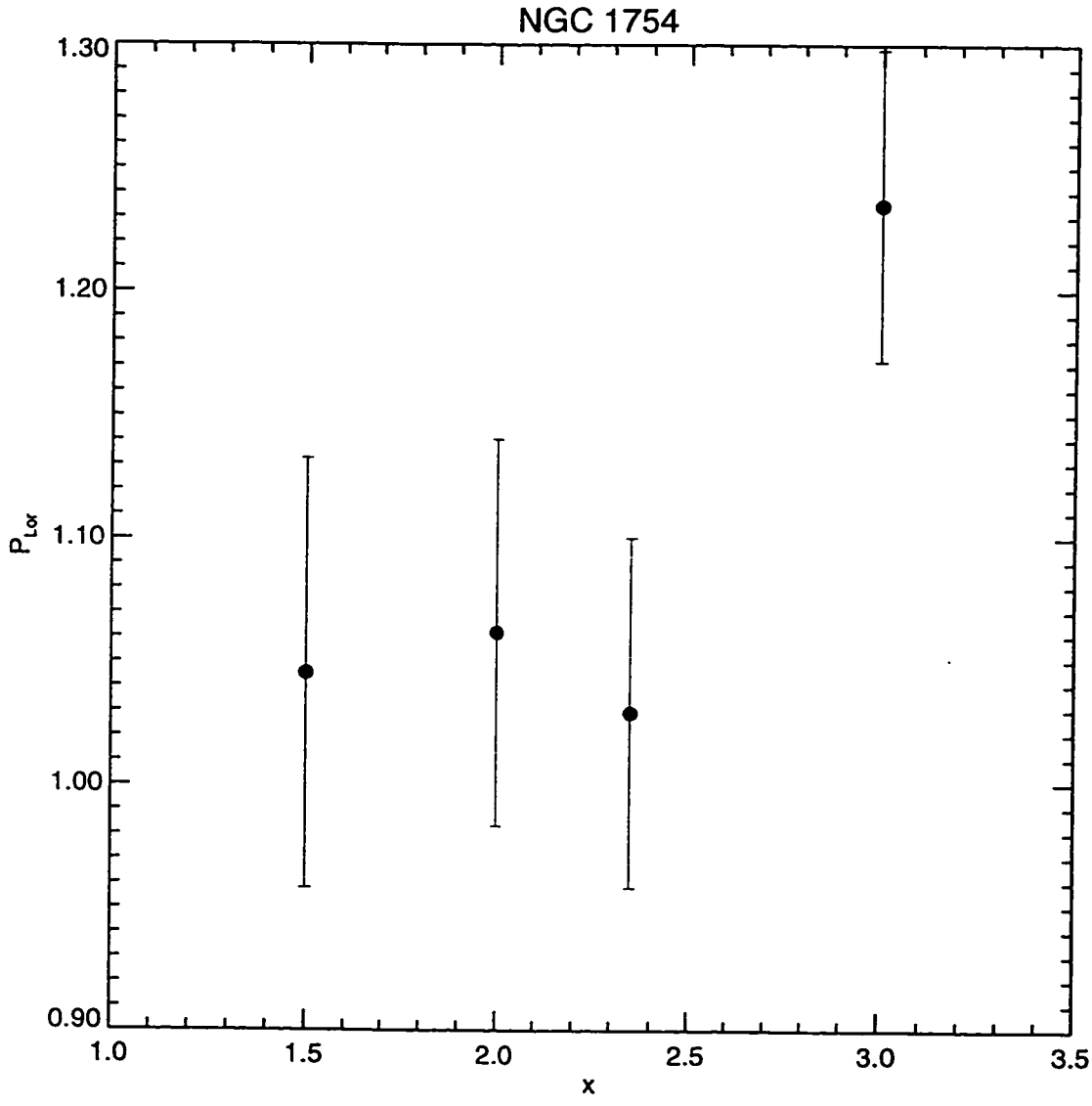

Figure 4.16a: The minimum $P_{\rm Lor}$ for each IMF used in the solutions for the NGC 1754 field. While x=3.0 produces the worst fit in each field, we were unable to distinguish between the fits of x=1.5, 2.0, and 2.35.

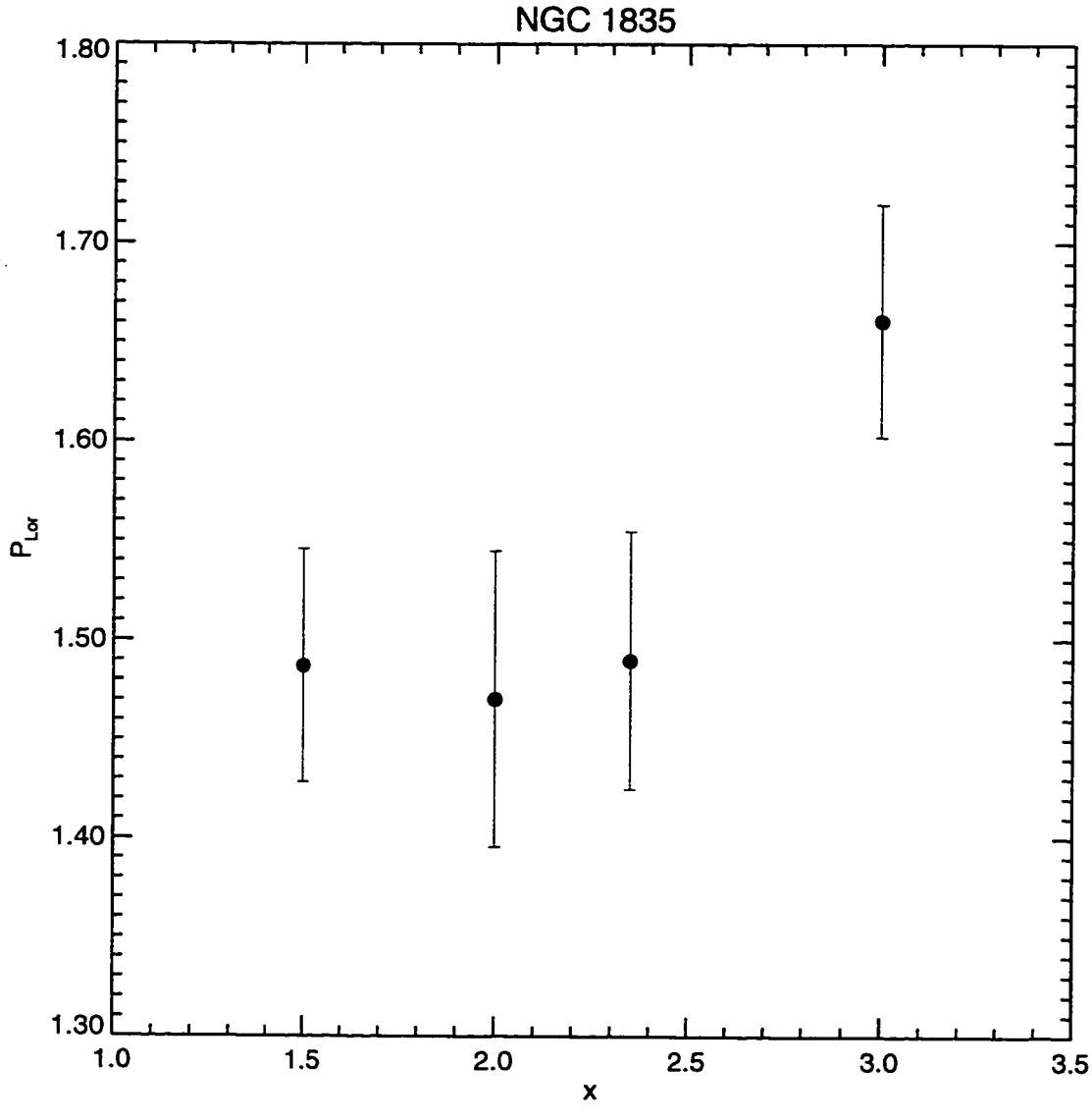

Figure 4.16b: The minimum $P_{\rm Lor}$ for each IMF used in the solutions for the NGC 1835 field.

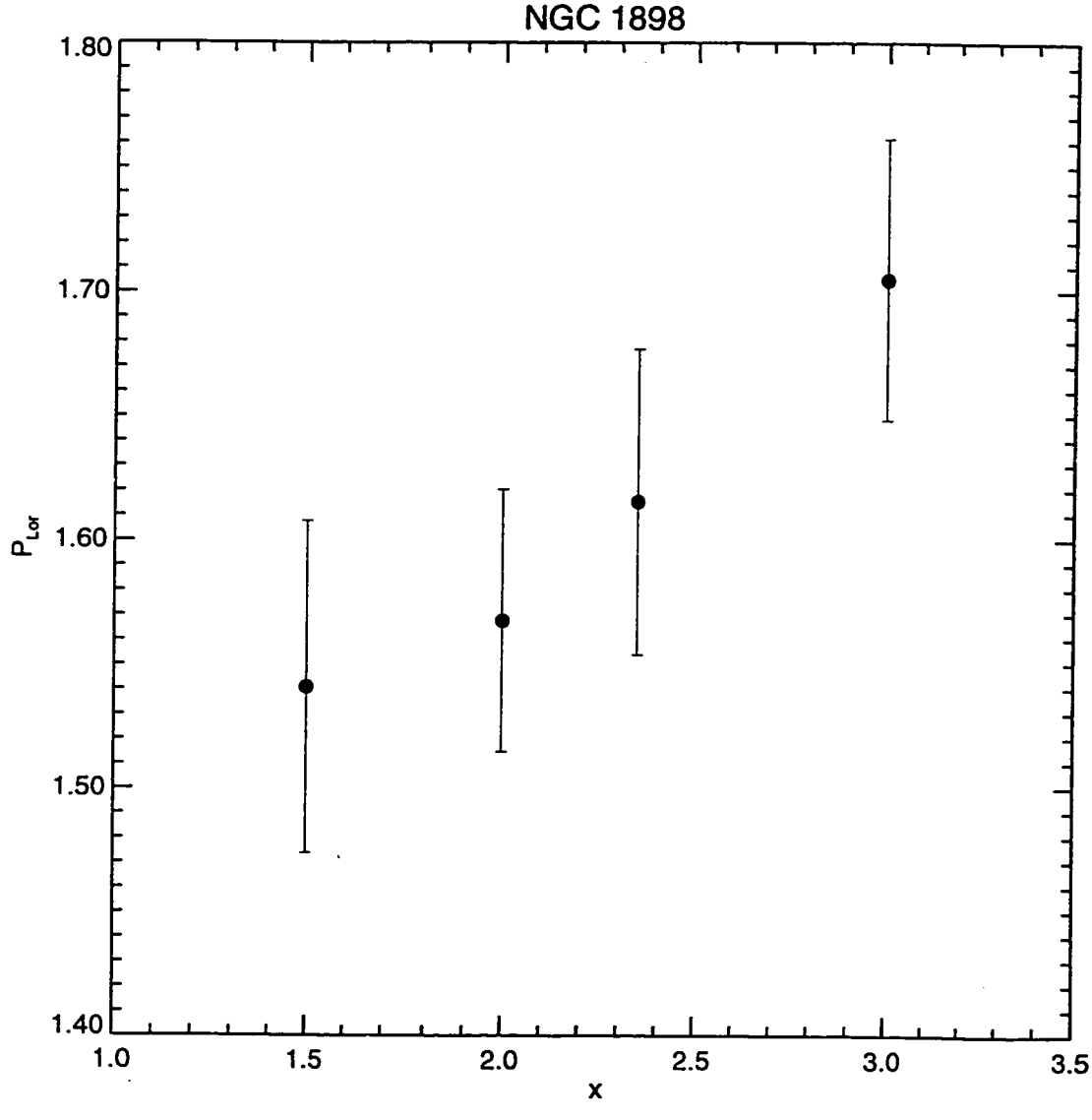

Figure 4.16c: The minimum $P_{\mathbf{Lor}}$ for each IMF used in the solutions for the NGC 1898 field.

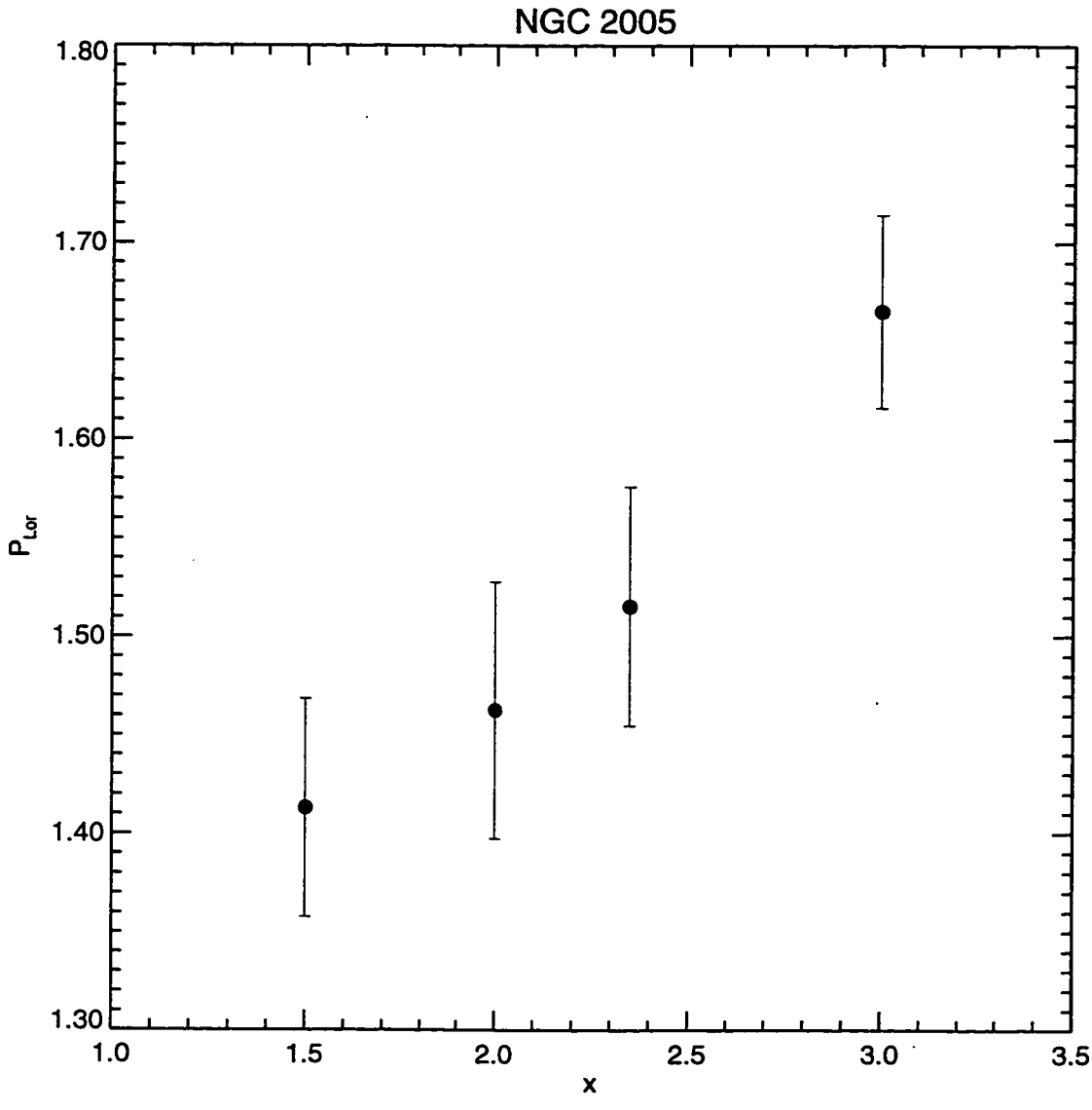

Figure 4.16d: The minimum P_{Lor} for each IMF used in the solutions for the NGC 2005 field.

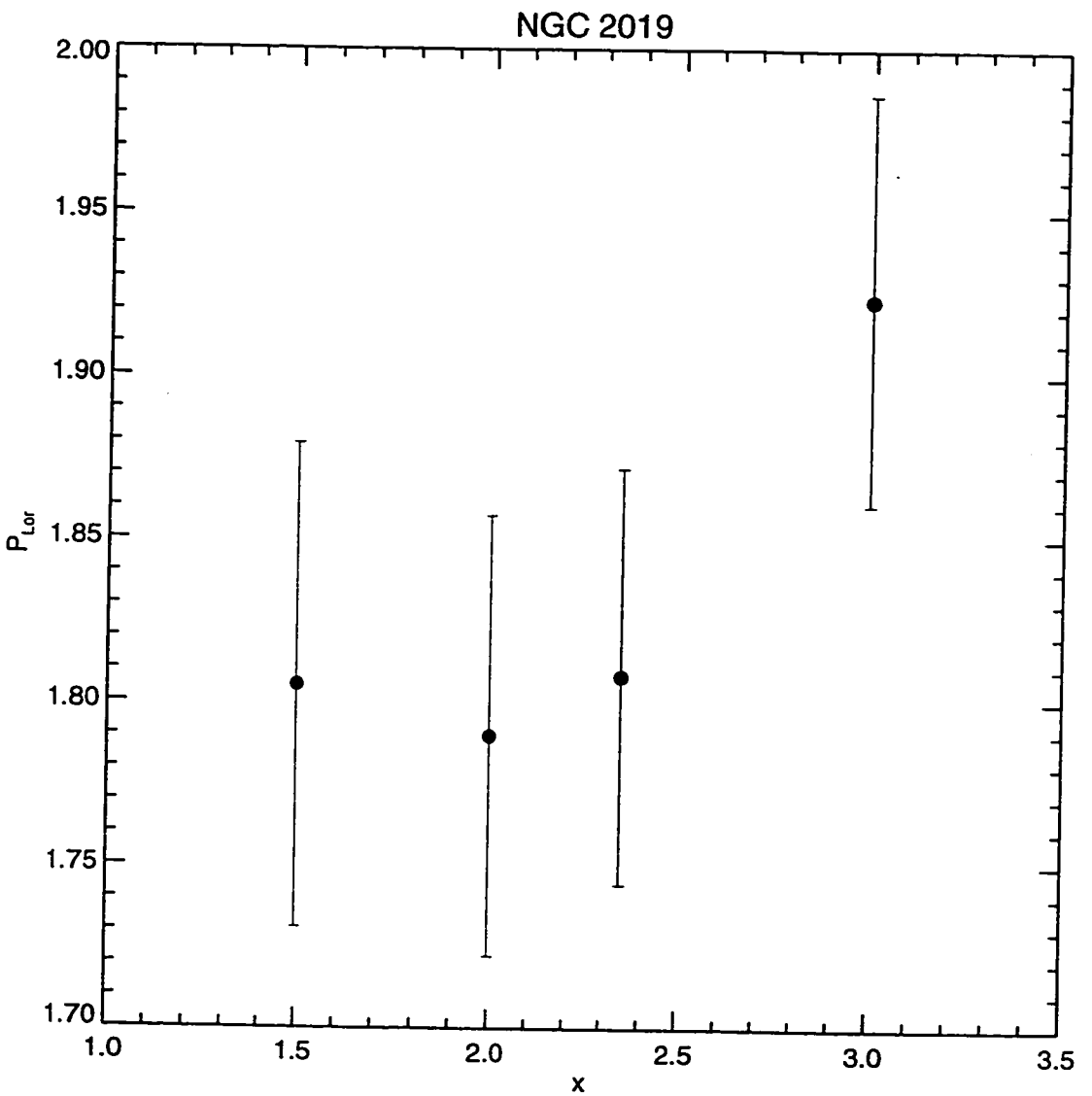

Figure 4.16e: The minimum P_{Lor} for each IMF used in the solutions for the NGC 2019 field.

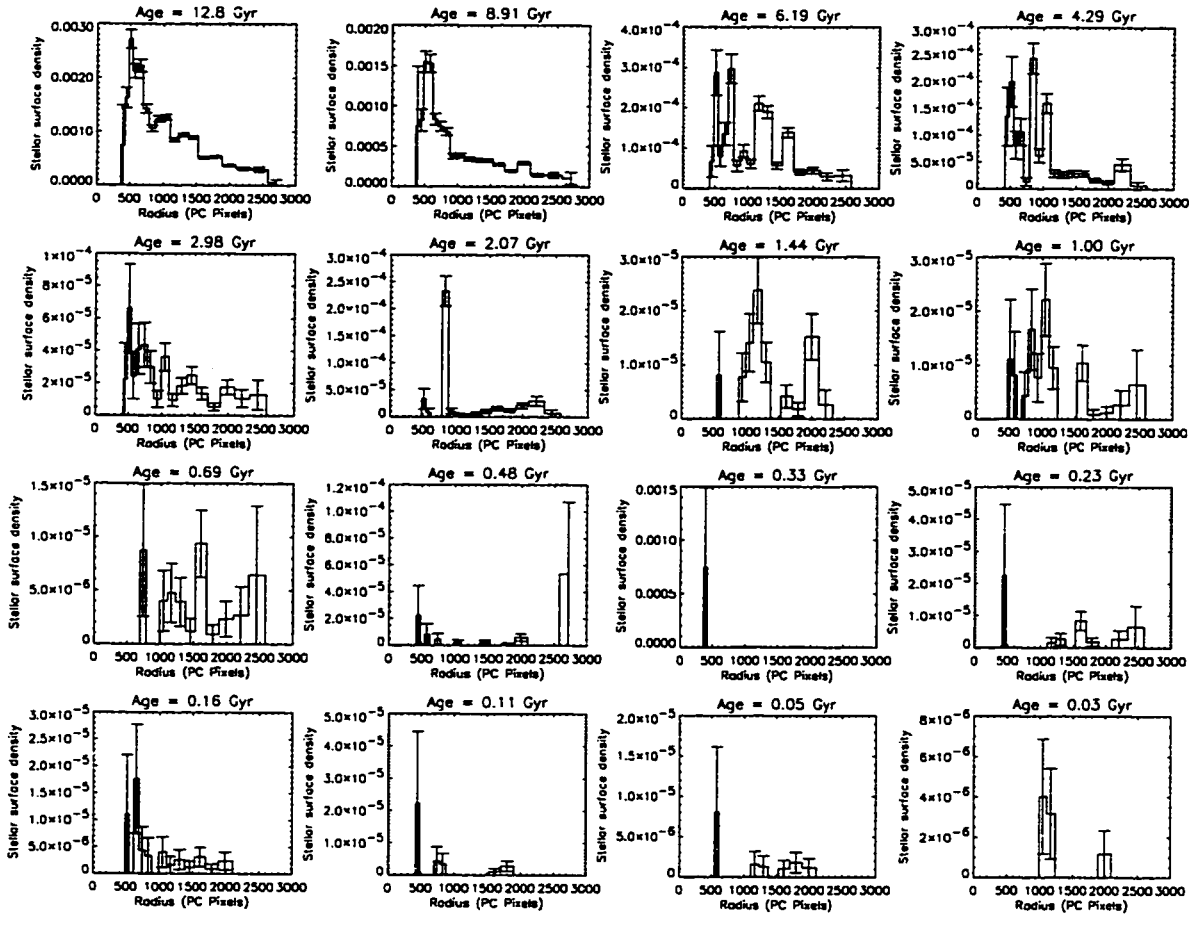

Figure 4.17a: Radial profiles of stars with $V - I$ and V distributed similarly to the color-magnitude diagrams of the solution, shown as a function of age for the NGC 1754 field. The figure shows that the older stars tend to be distributed more non-uniformly than the younger ones.

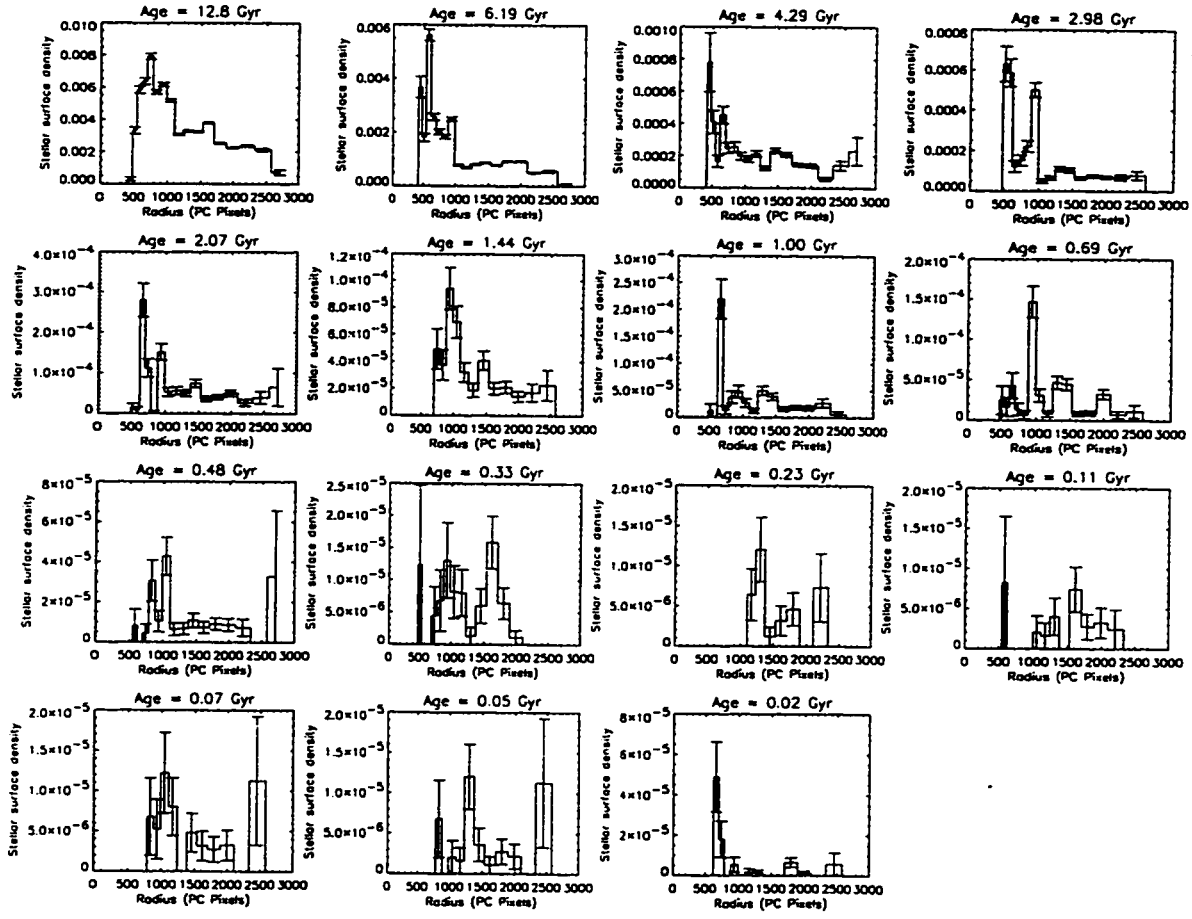

Figure 4.17b: Radial profiles of stars as a function of age in the NGC 1835 solution.

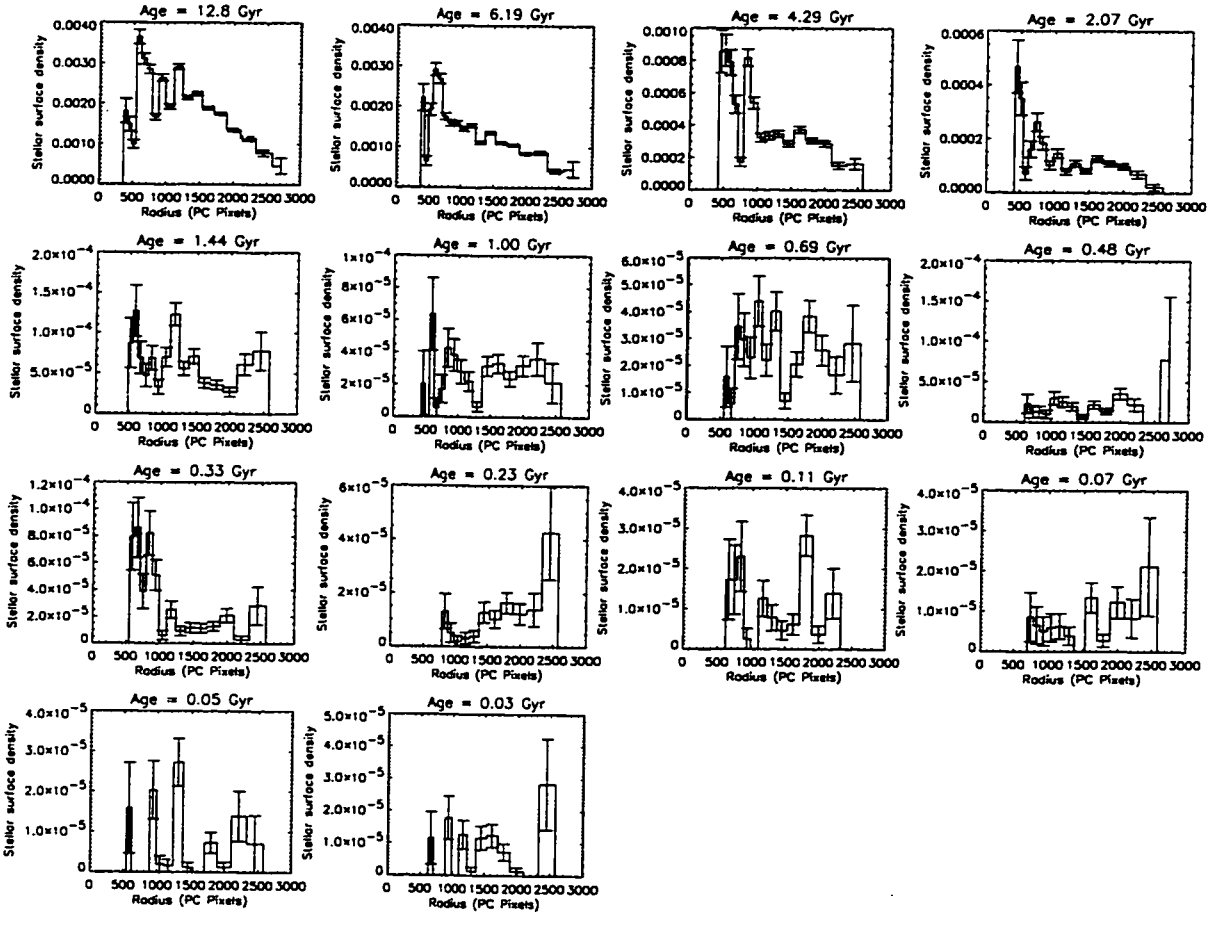

Figure 4.17c: Radial profiles of stars as a function of age in the NGC 1898 solution.

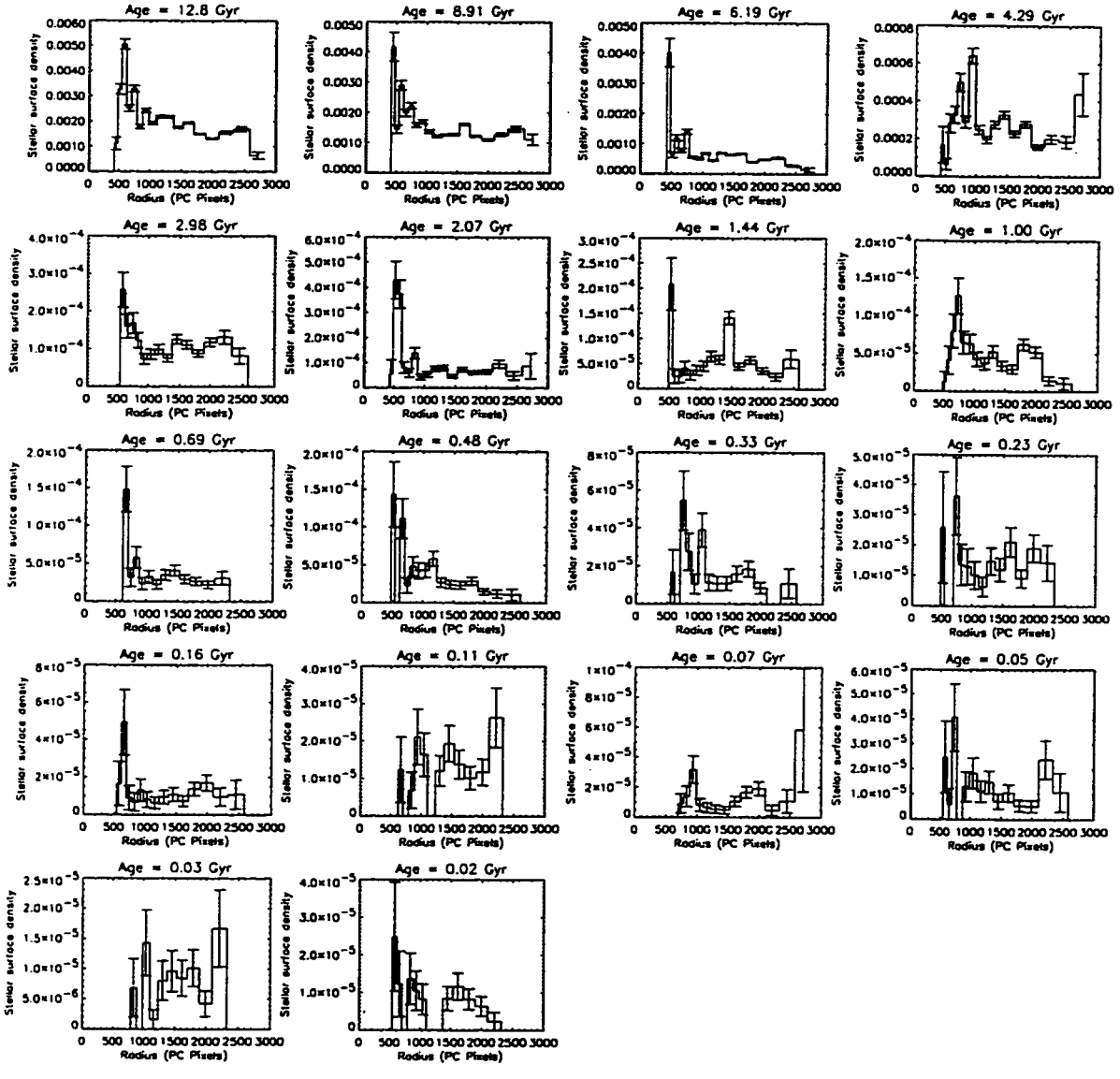

Figure 4.17d: Radial profiles of stars as a function of age in the NGC 2005 solution.

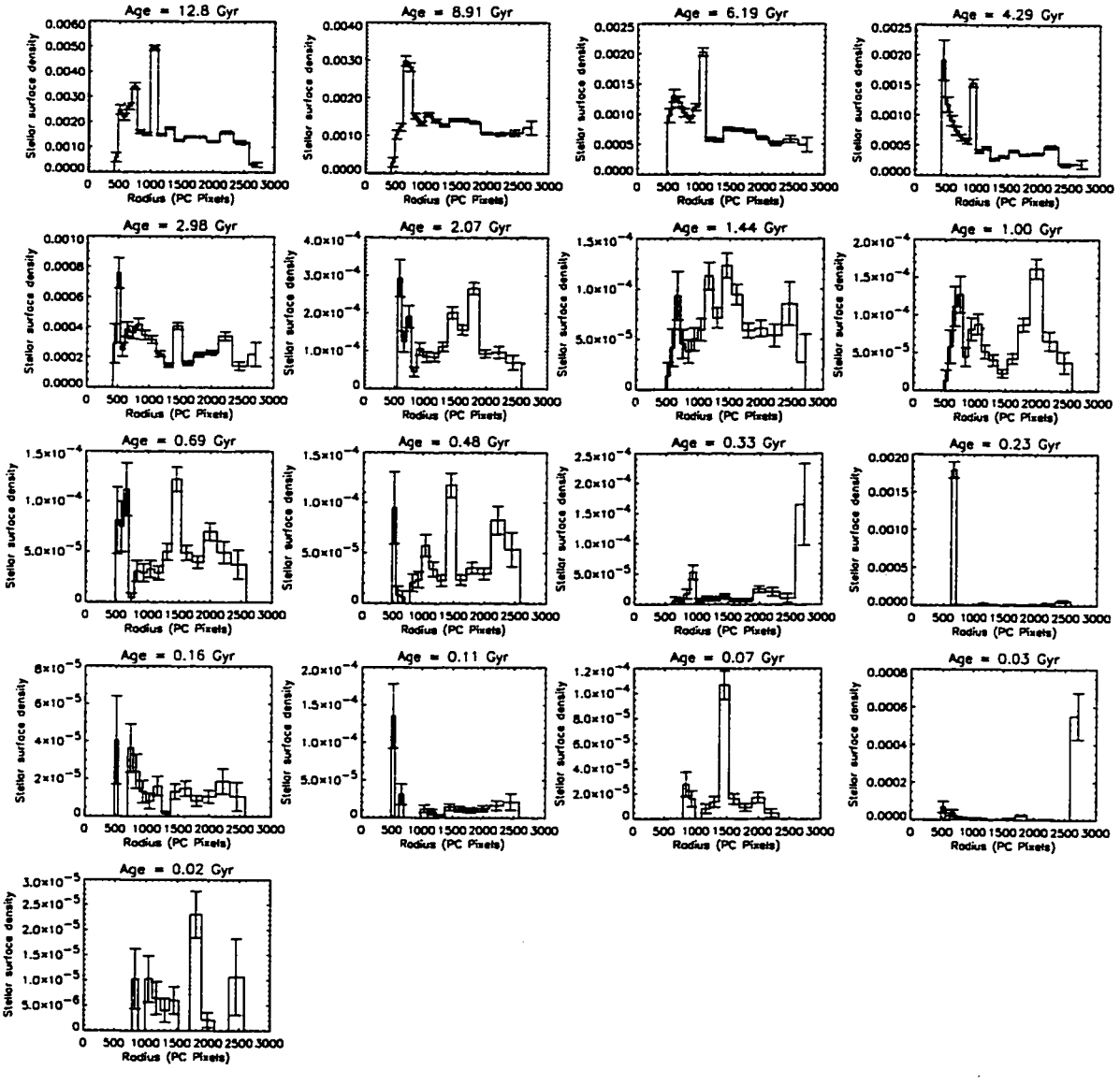

Figure 4.17e: Radial profiles of stars as a function of age in the NGC 2019 solution.

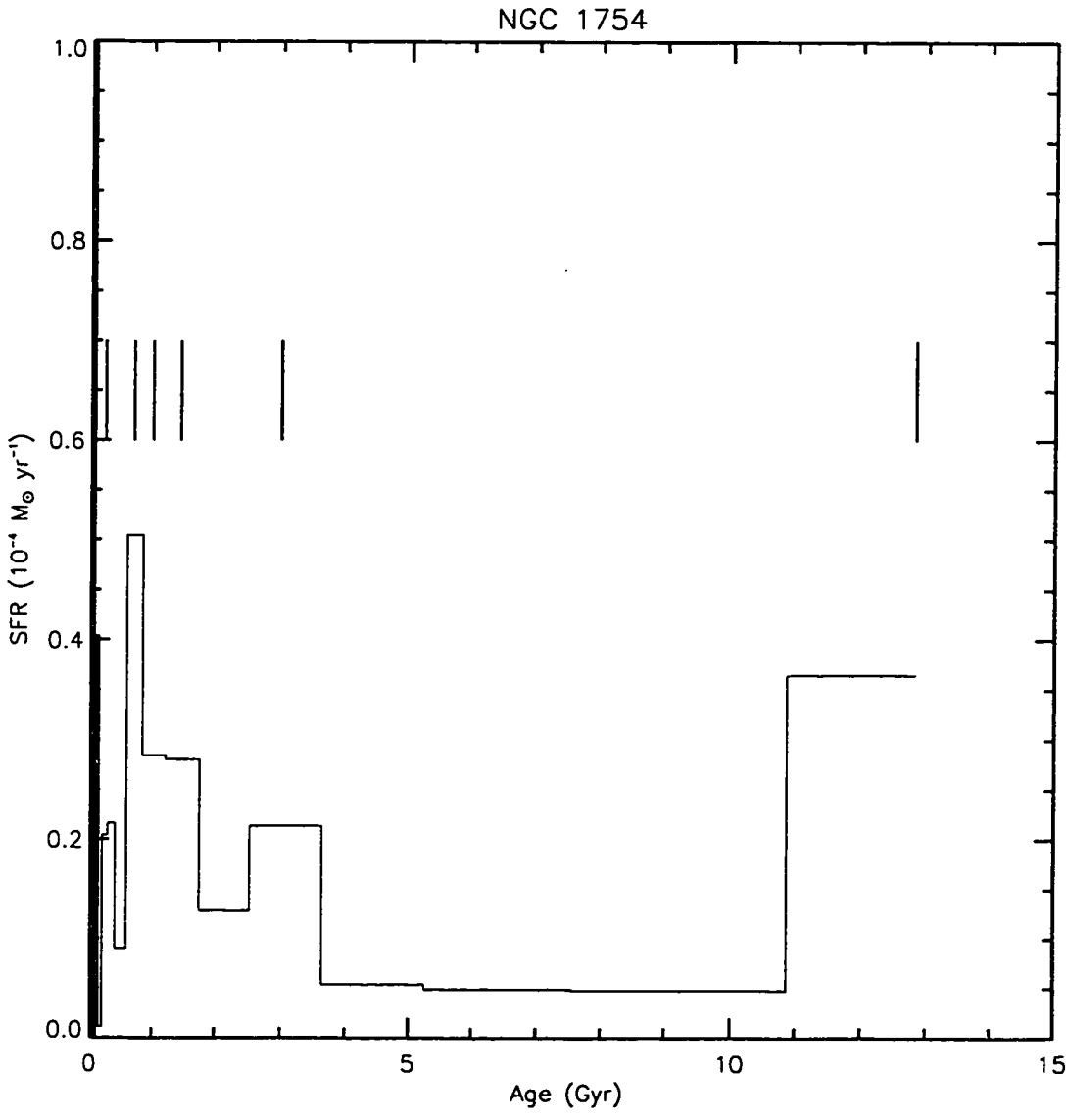

Figure 4.18a: The lines shown above the star formation history of the NGC 1754 field mark peaks which are investigated in *b*.

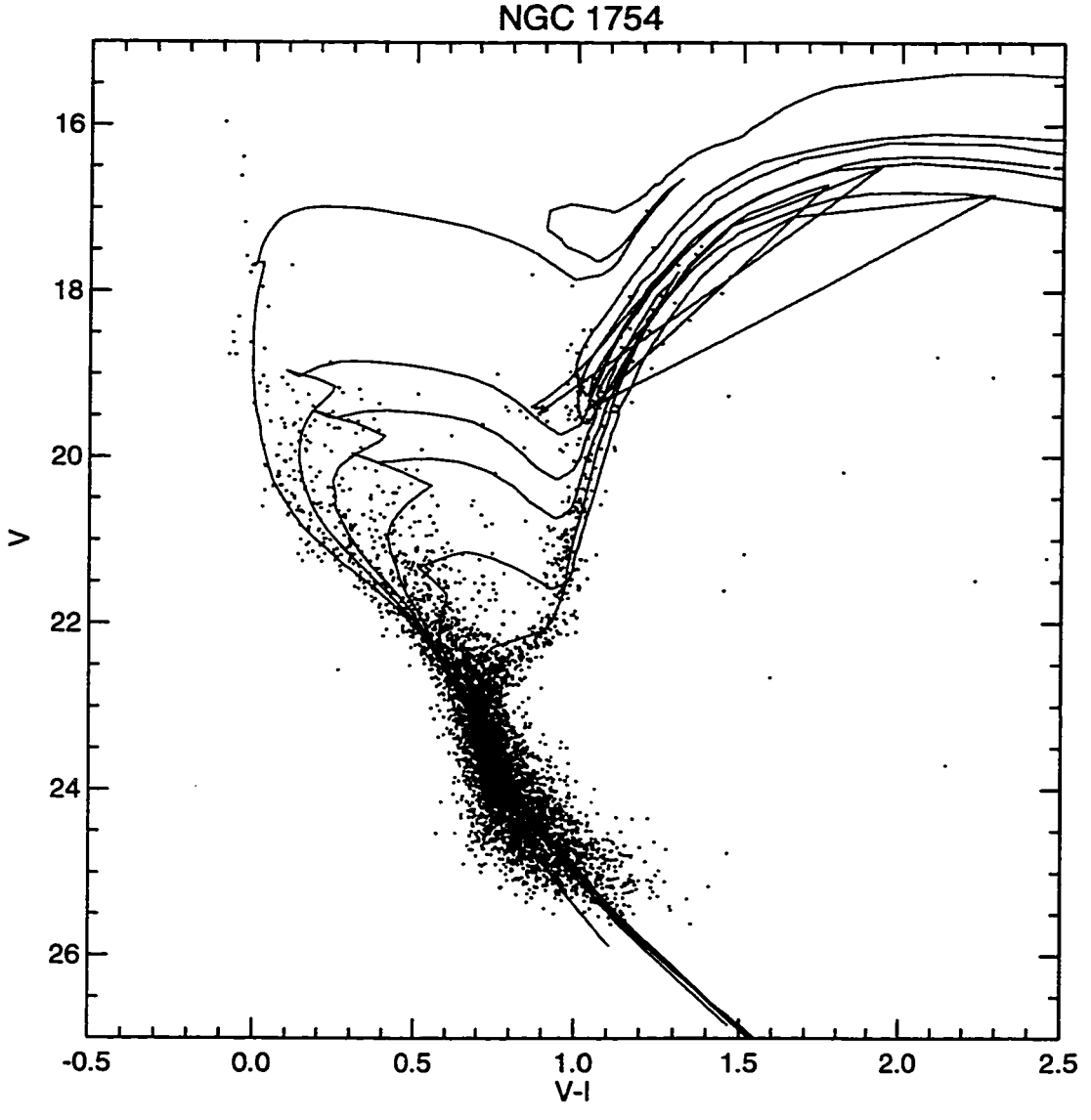

Figure 4.18b: Isochrones with the selected ages from *a* and abundances matching the chemical evolution law of Fig. 4.8 overlayed with the NGC 1754 field star color-magnitude diagram.

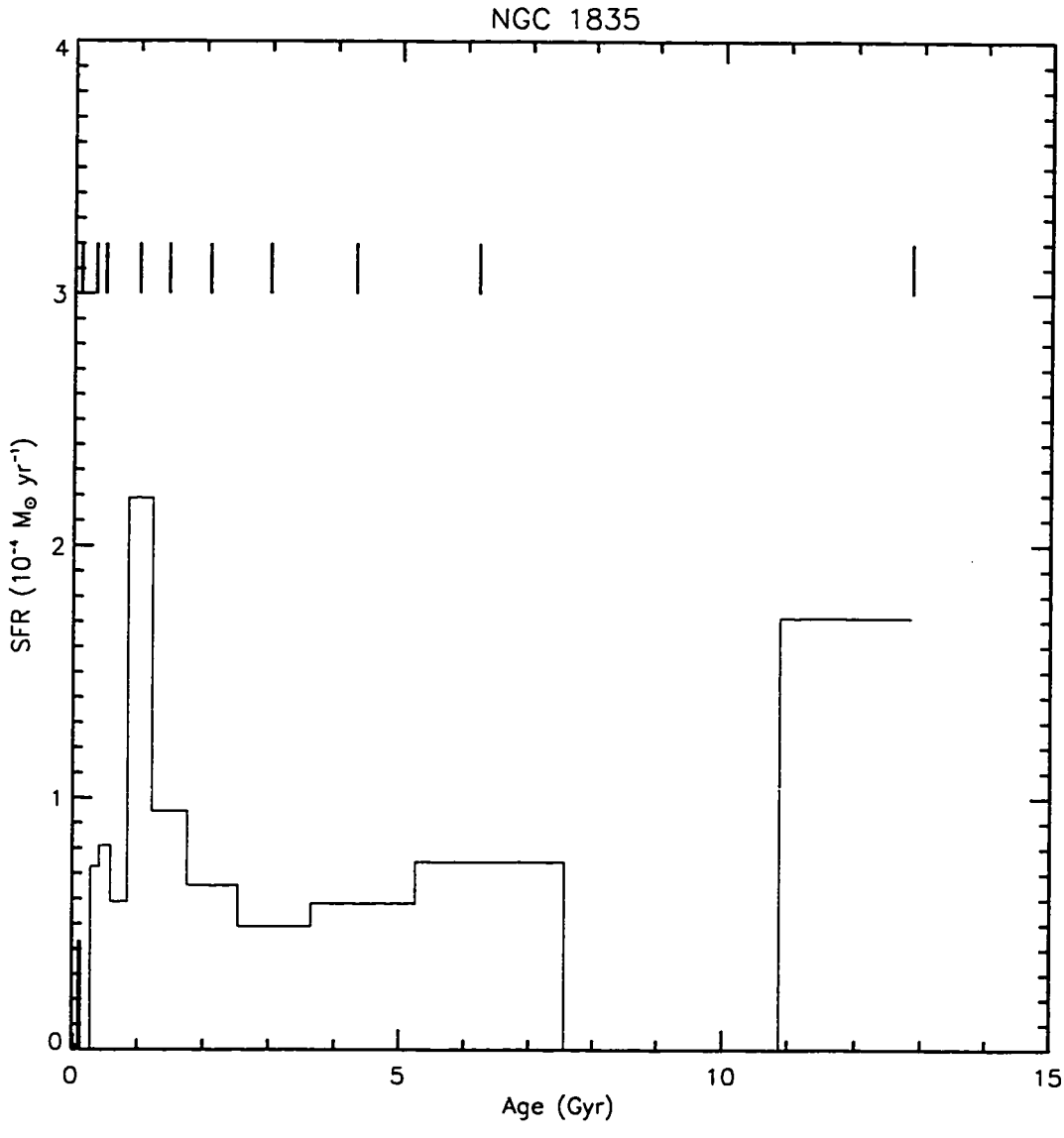

Figure 4.18c: Selected peaks for NGC 1835 star formation history.

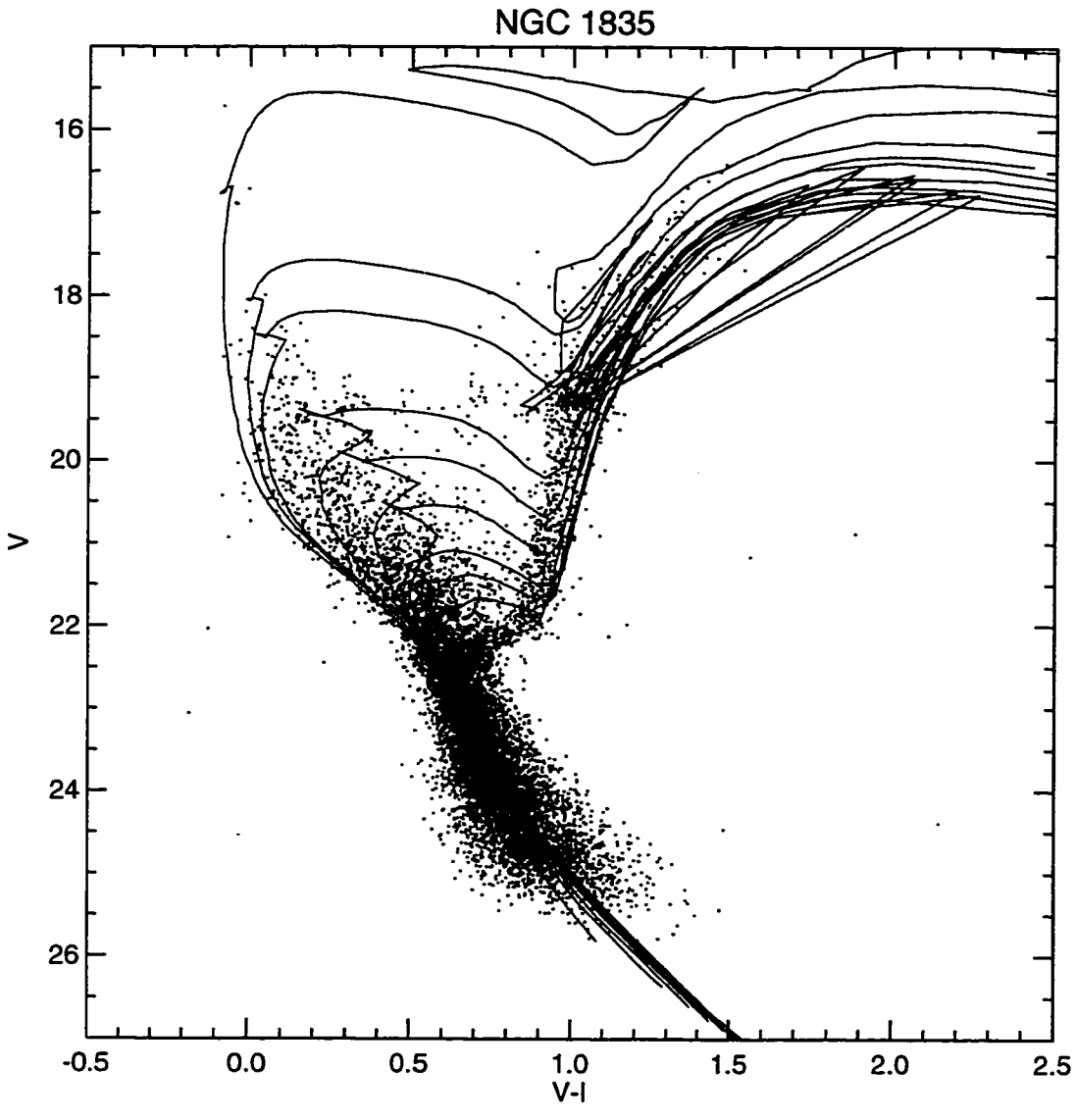

Figure 4.18d: Isochrones with ages of peaks in c shown with NGC 1835 field star CMD. The fact that the older isochrones fall too far red of the red giant branch is discussed in the text.

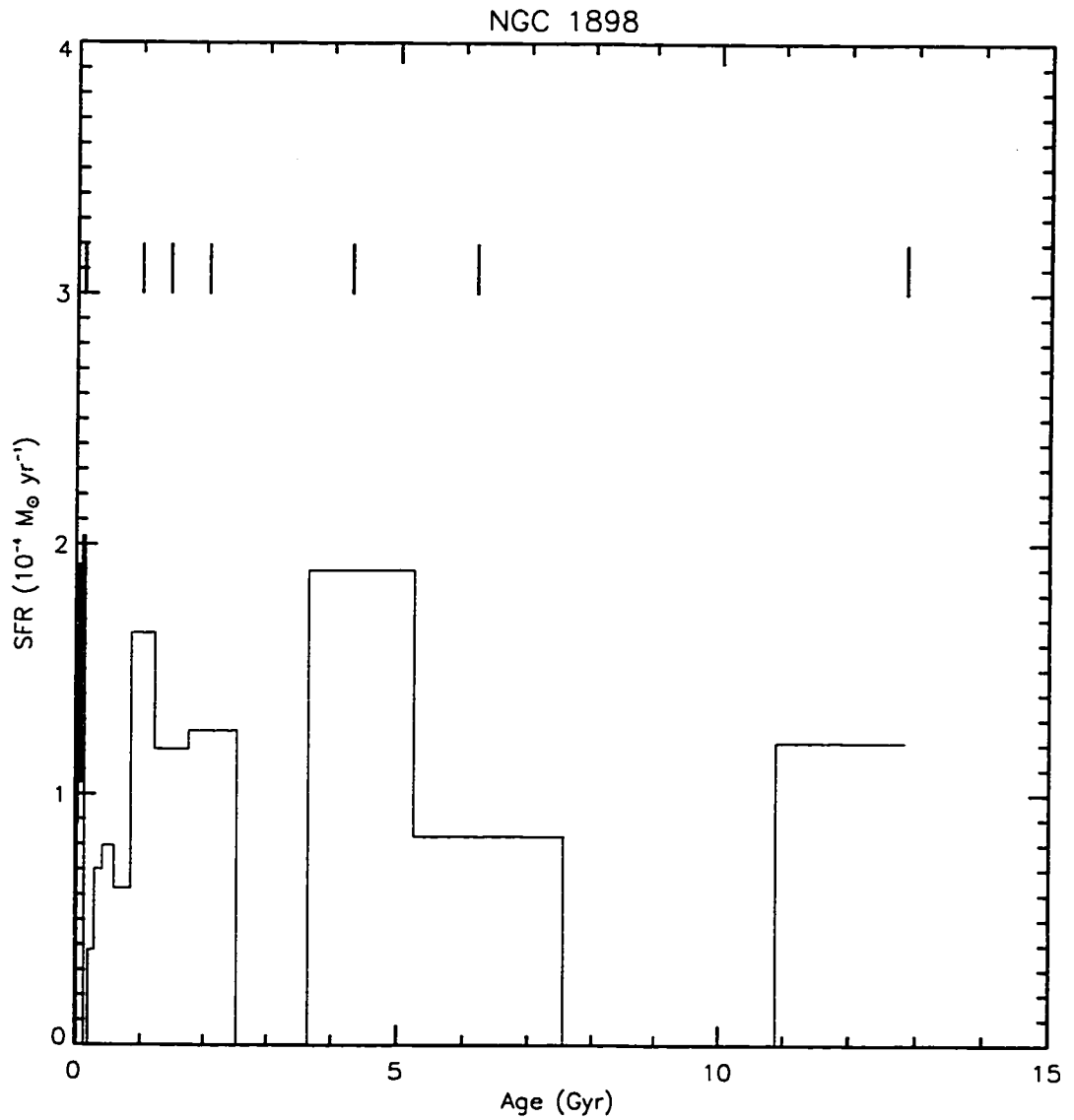

Figure 4.18e: Selected peaks for NGC 1898 star formation history.

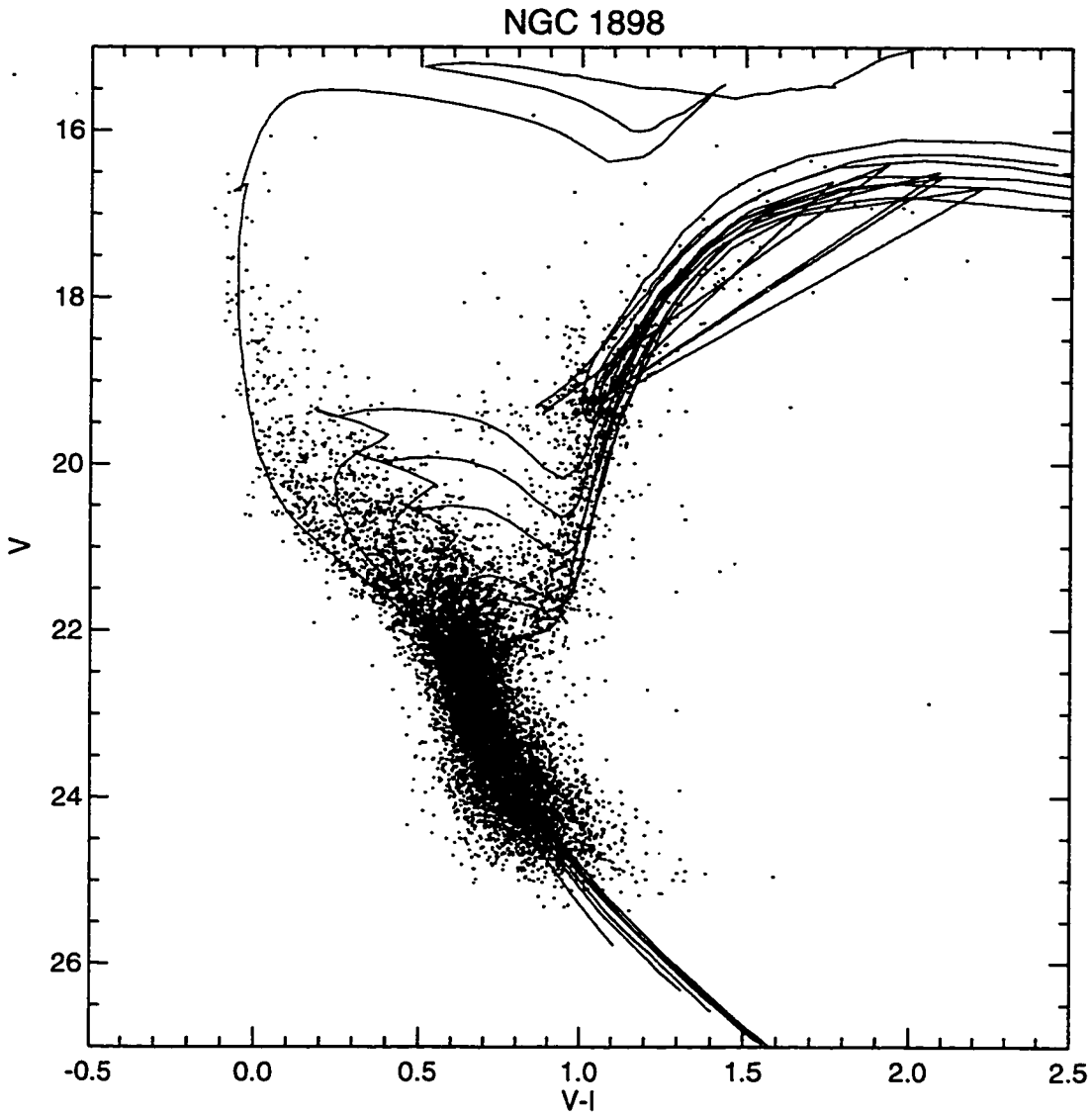

Figure 4.18f: Isochrones corresponding to peaks in e with NGC 1898 CMD.

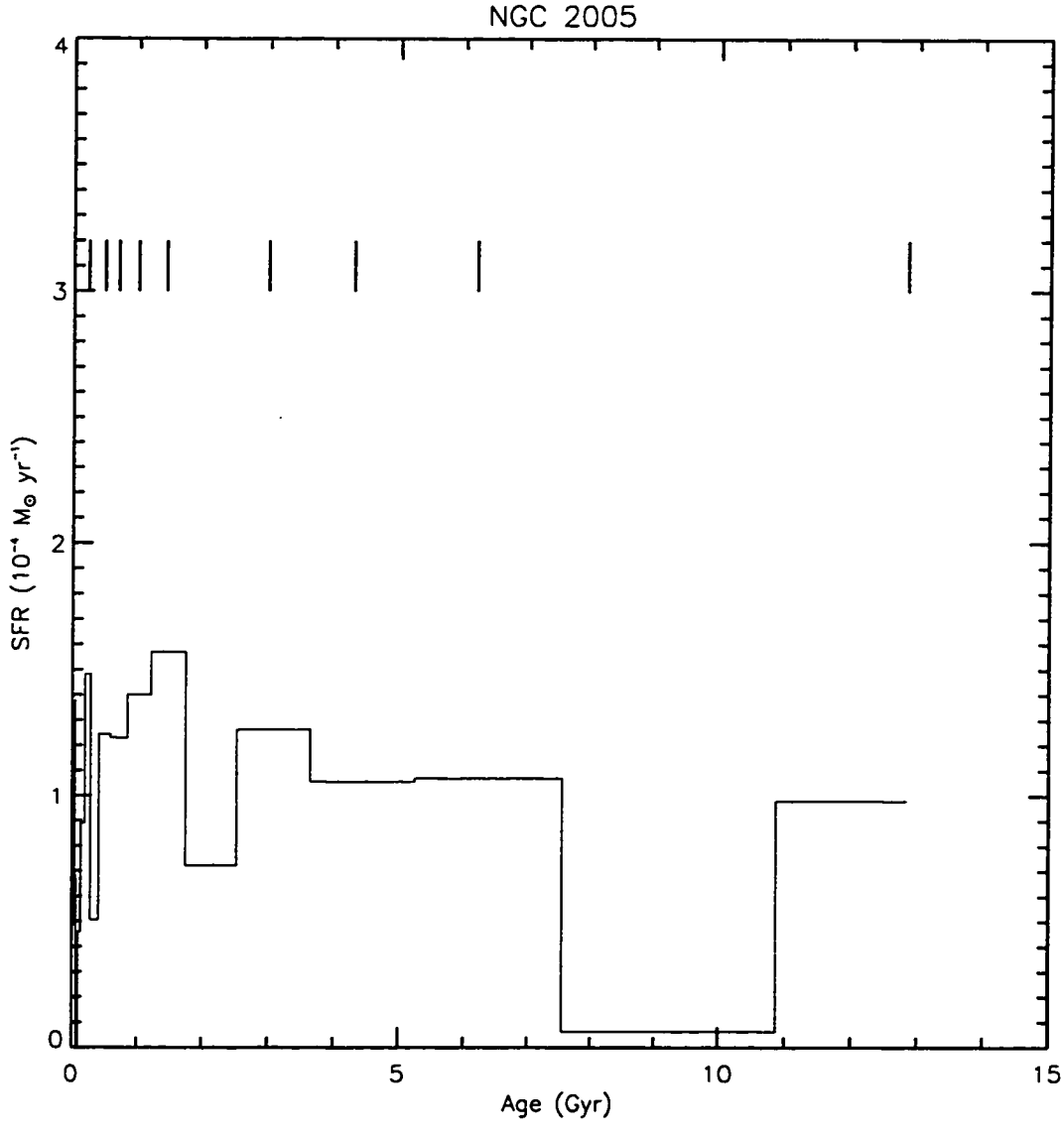

Figure 4.18g: Selected peaks for NGC 2005 star formation history.

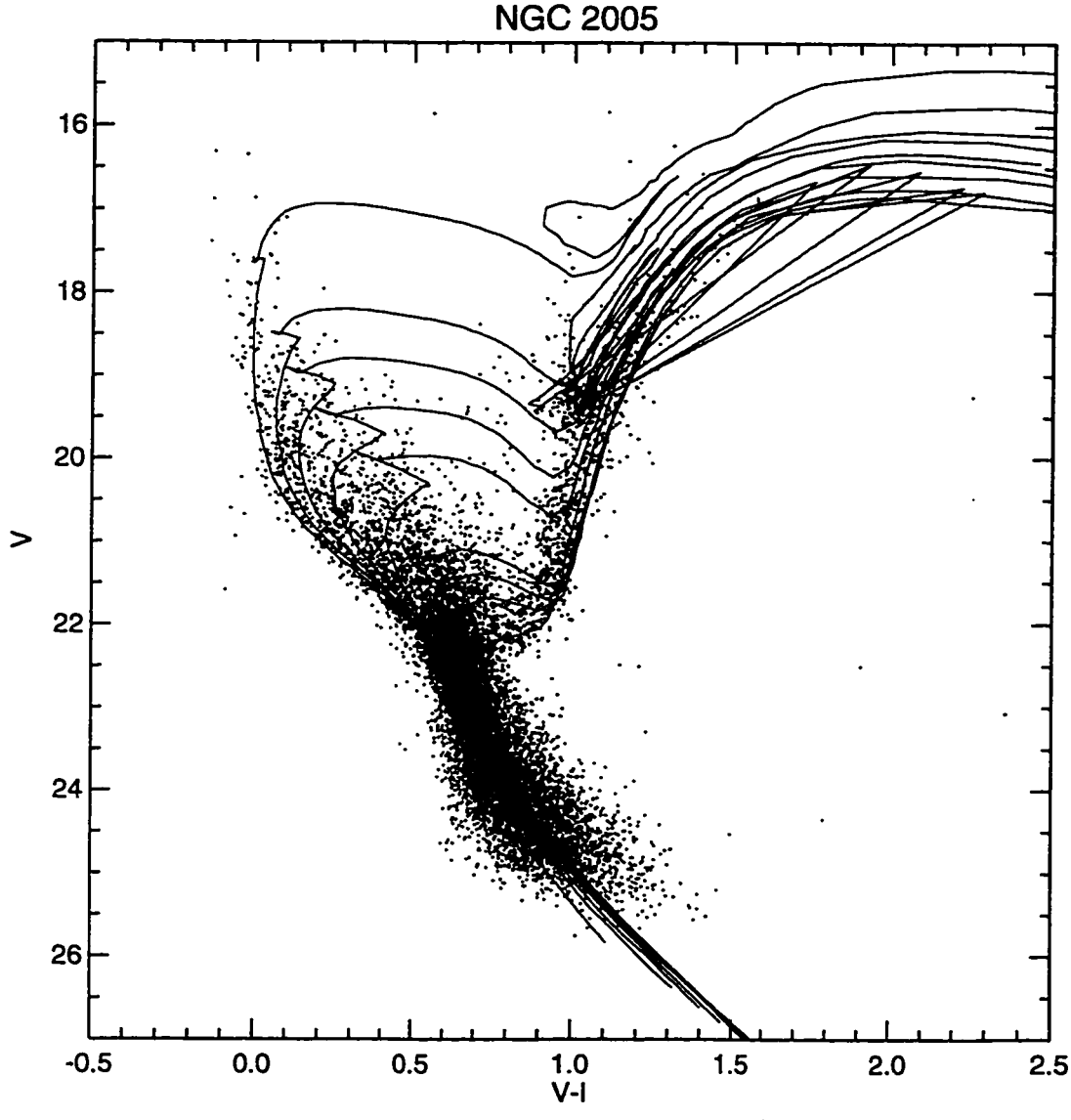

Figure 4.18h: Isochrones corresponding to peaks in e with NGC 2005 CMD.

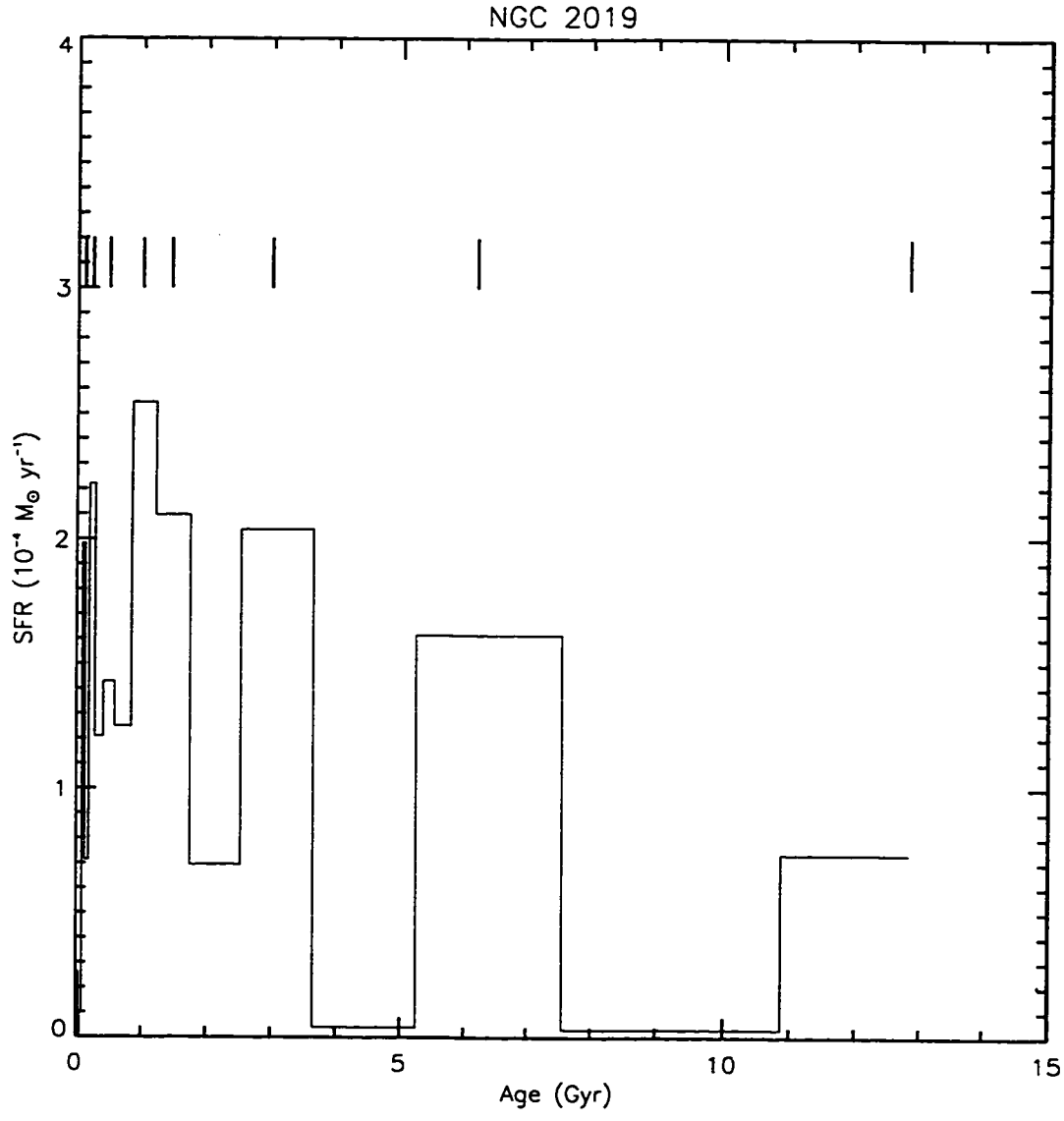

Figure 4.18i: Selected peaks for NGC 2019 star formation history.

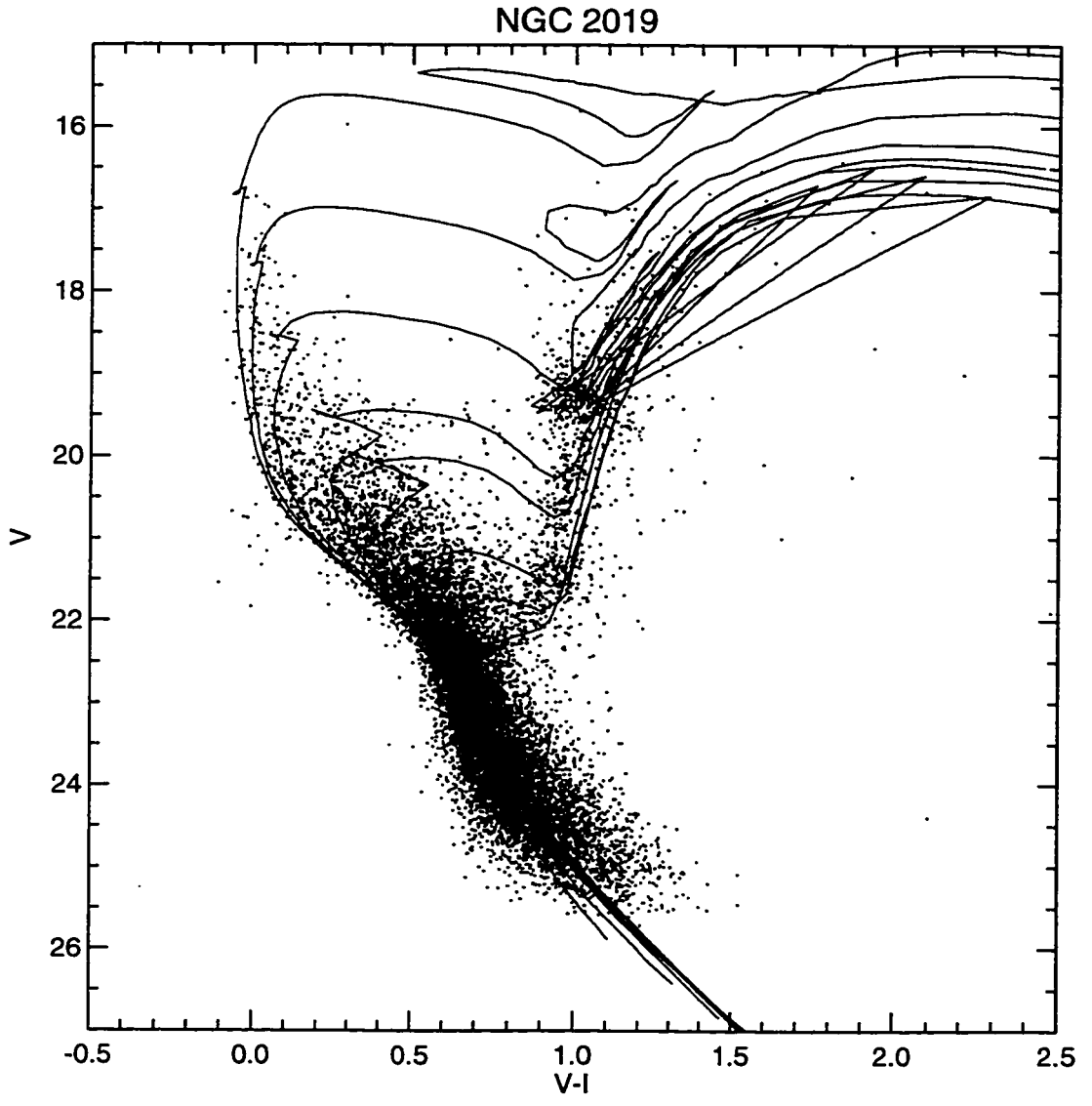

Figure 4.18j: Isochrones corresponding to peaks in e with NGC 2019 CMD.

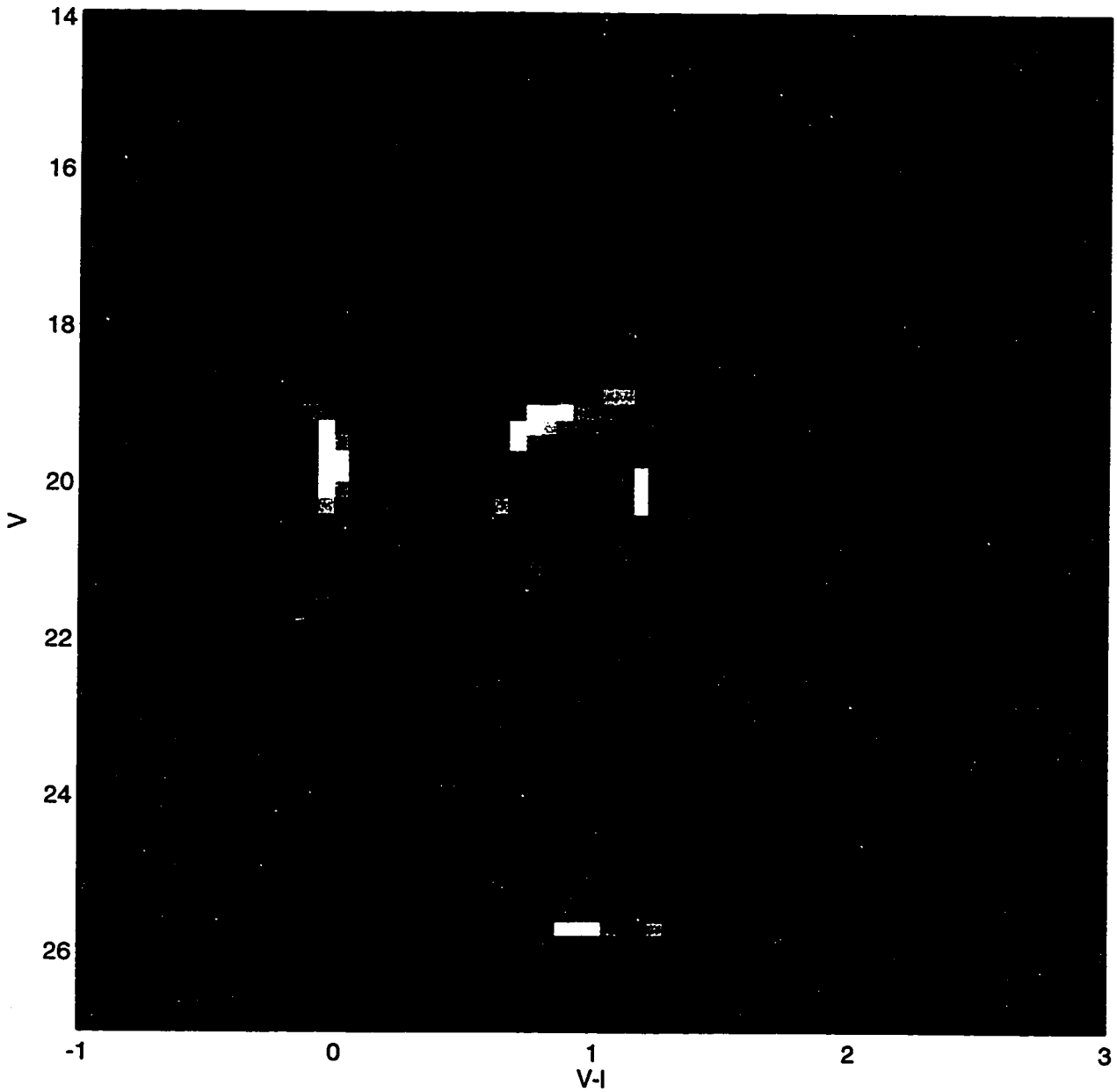

Figure 4.19a: Residuals of the best-fit model for the star formation history of the NGC 1754 field for a Salpeter IMF after subtraction of the observed CMD. Bright patches indicate an excess of predicted stars while dark patches are regions where there are more observed stars than predicted. Gray areas indicate good agreement between the models and observations. The residuals have been divided by the number of observed stars to remove the effect of the luminosity function. The grey levels have been stretched from -1 to 1.

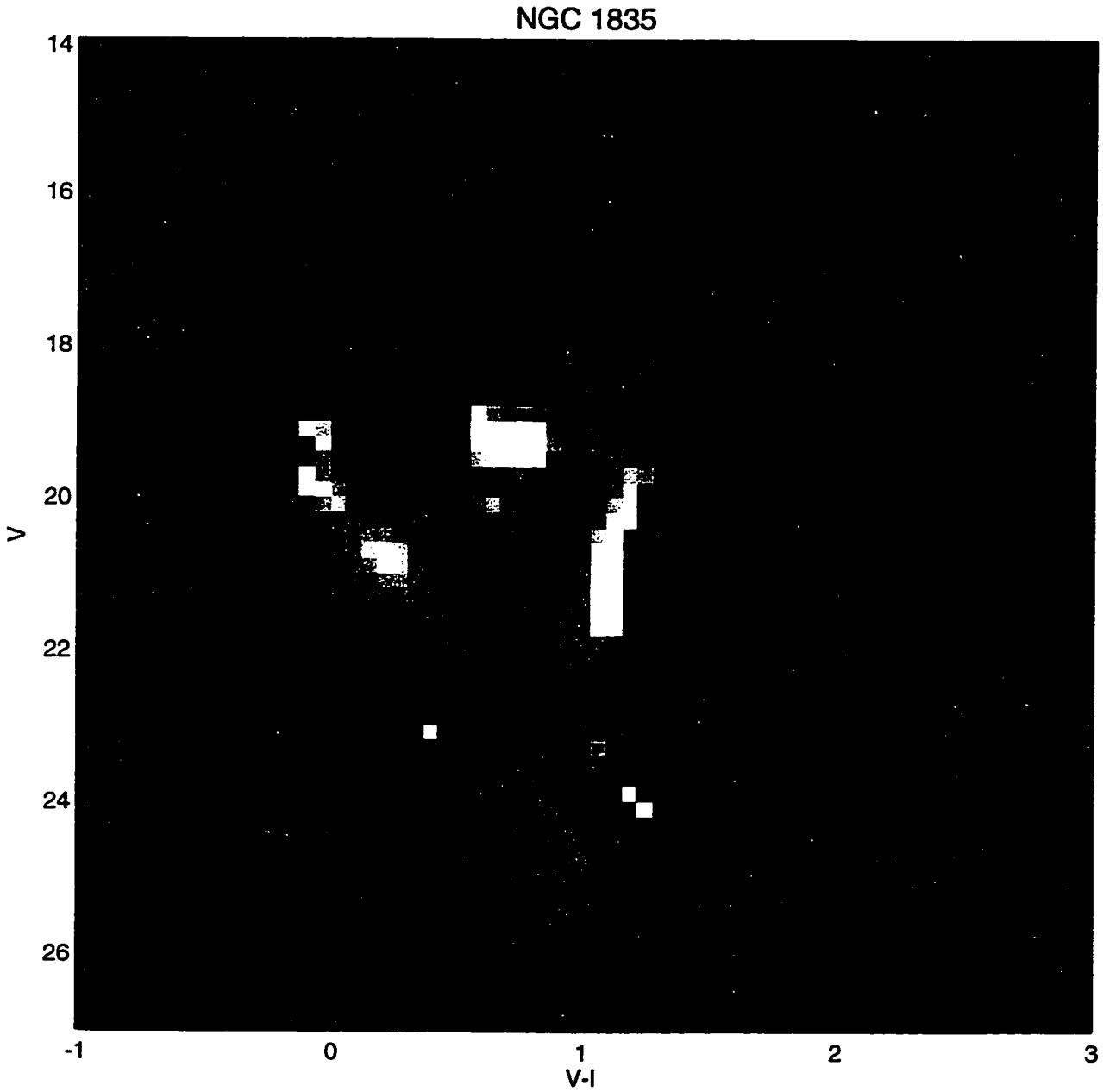

Figure 4.19b: Residuals of the best-fit model for the star formation history of the NGC 1835 field for a Salpeter IMF after subtraction of the observed CMD. The poor fit of the models on the red giant branch and red clump seen in Fig. 4.6d produces an obvious feature in the residuals.

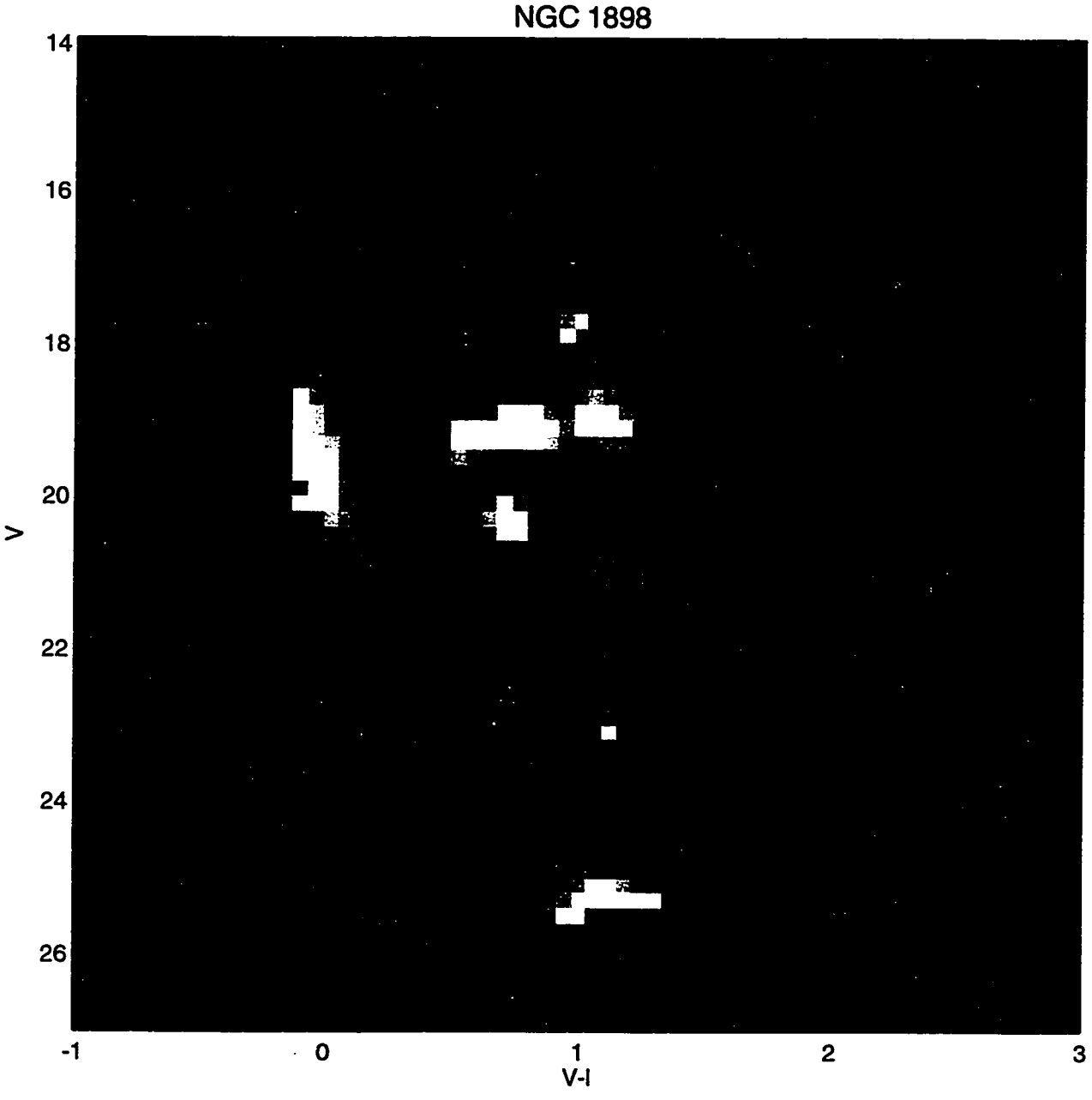

Figure 4.19c: Residuals of the best-fit model for the star formation history of the NGC 1898 field for a Salpeter IMF after subtraction of the observed CMD.

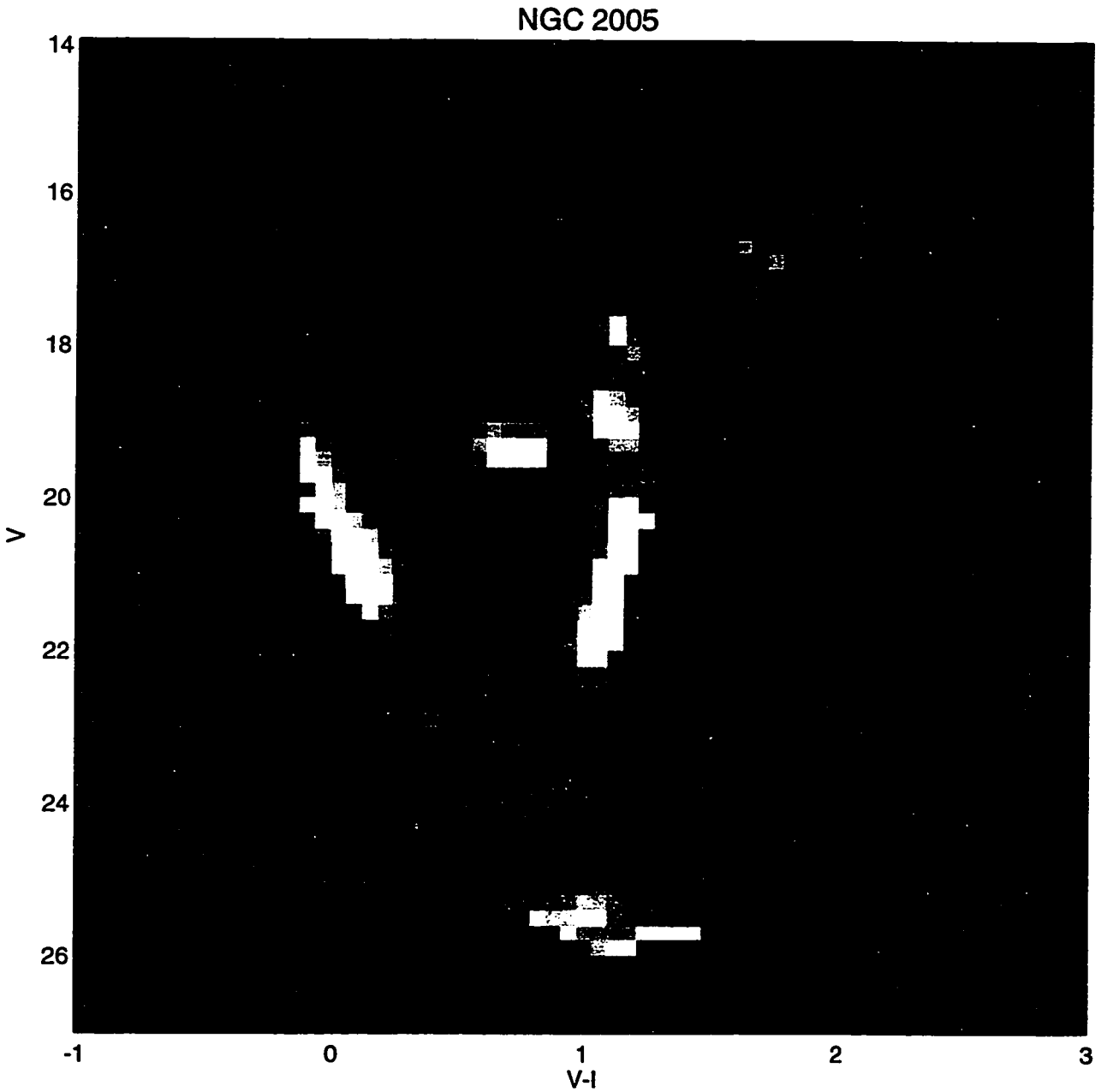

Figure 4.19d: Residuals of the best-fit model for the star formation history of the NGC 2005 field for a Salpeter IMF after subtraction of the observed CMD.

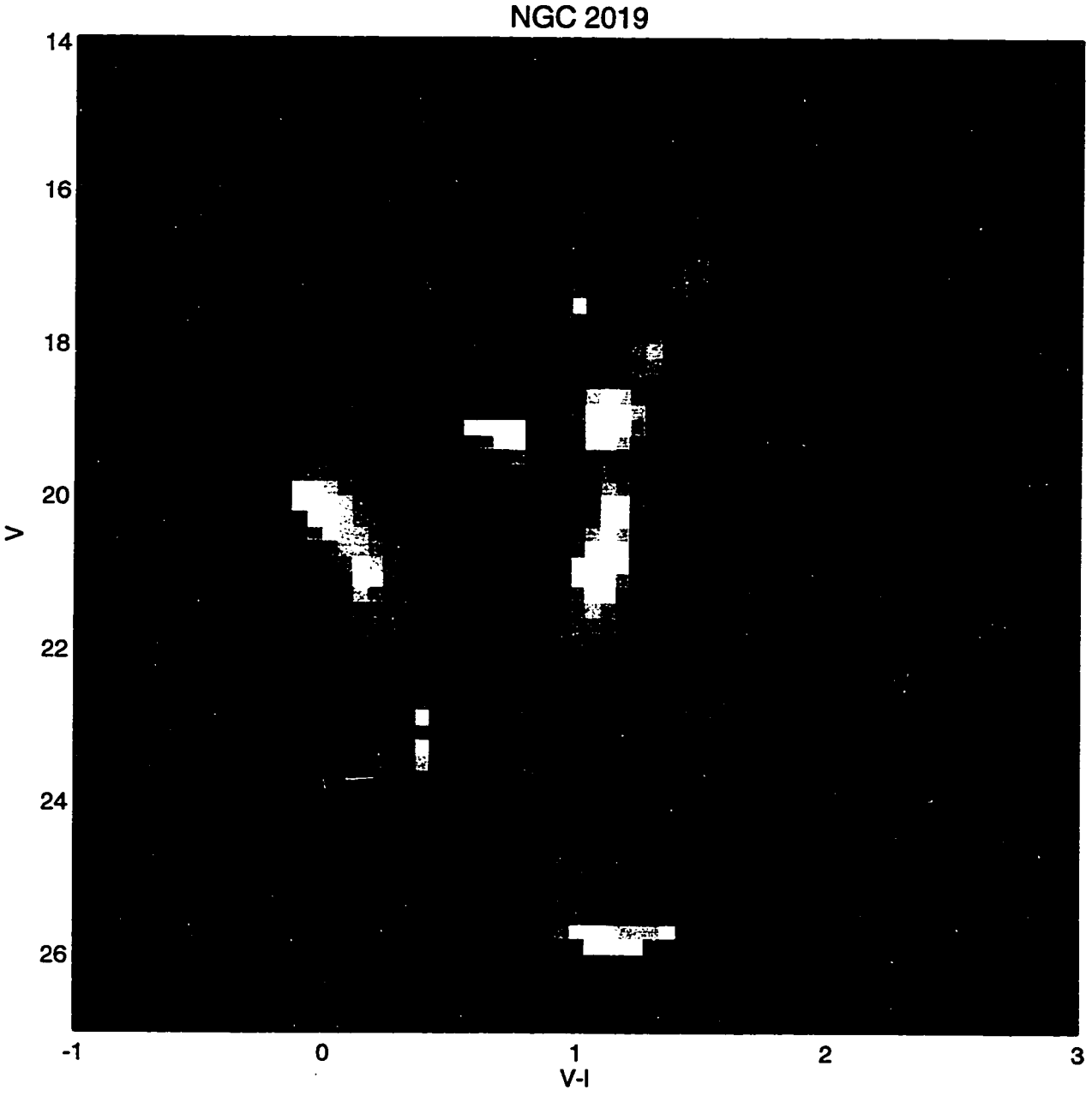

Figure 4.19e: Residuals of the best-fit model for the star formation history of the NGC 2019 field for a Salpeter IMF after subtraction of the observed CMD.

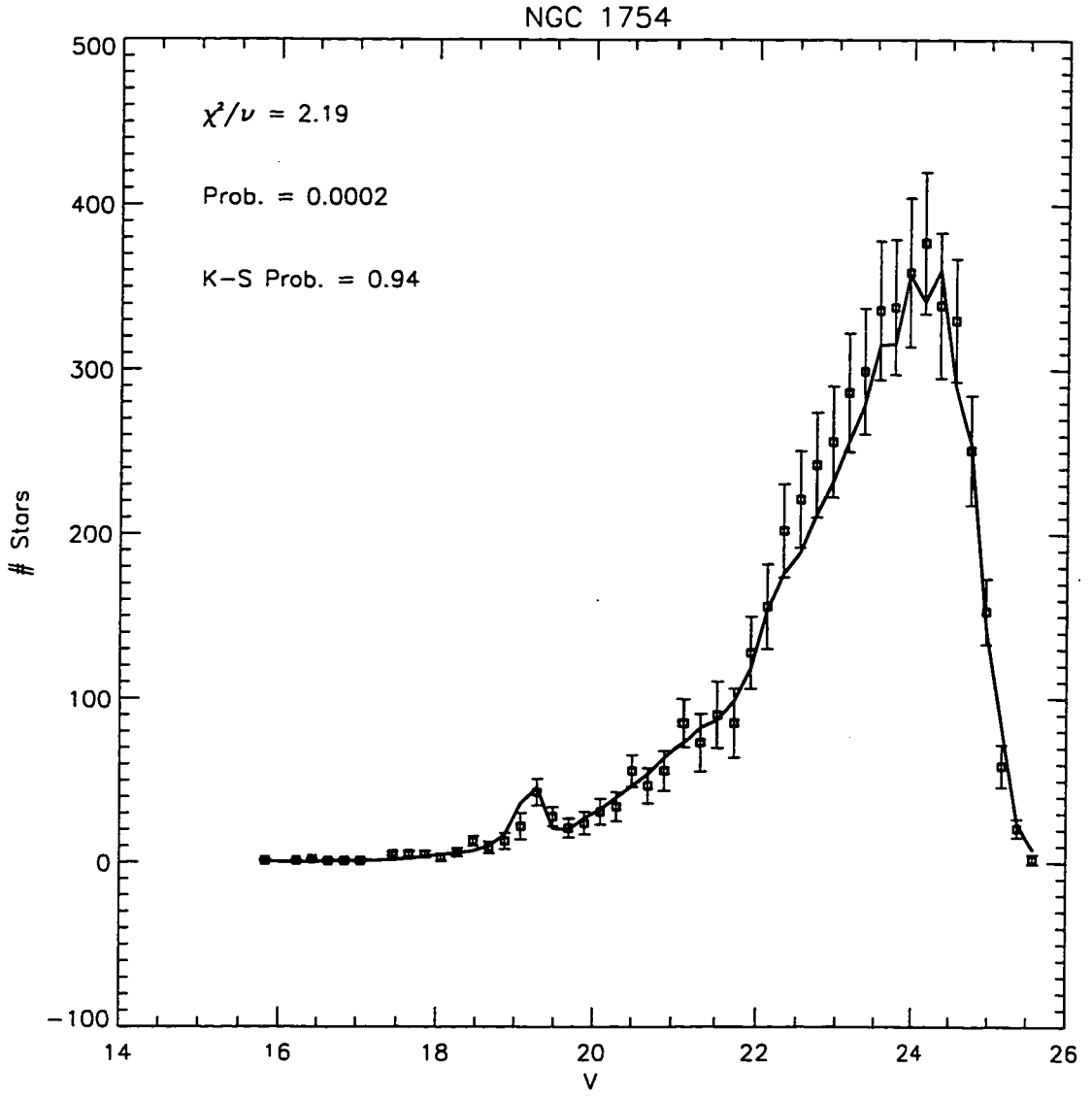

Figure 4.20a: Comparison of the observed luminosity function (squares) with the best-fit model for a Salpeter IMF (solid line) for the NGC 1754 field. The errors in the points are those due to Poisson number statistics and the errors in the derived star formation rates. The figure indiciates the χ^2 per degree of freedom for the fit, the probability that χ^2 would exceed the given value by chance, and the probability that the model and observed distributions are drawn from the same parent population, based on the Kolmogorov-Smirnov statistic.

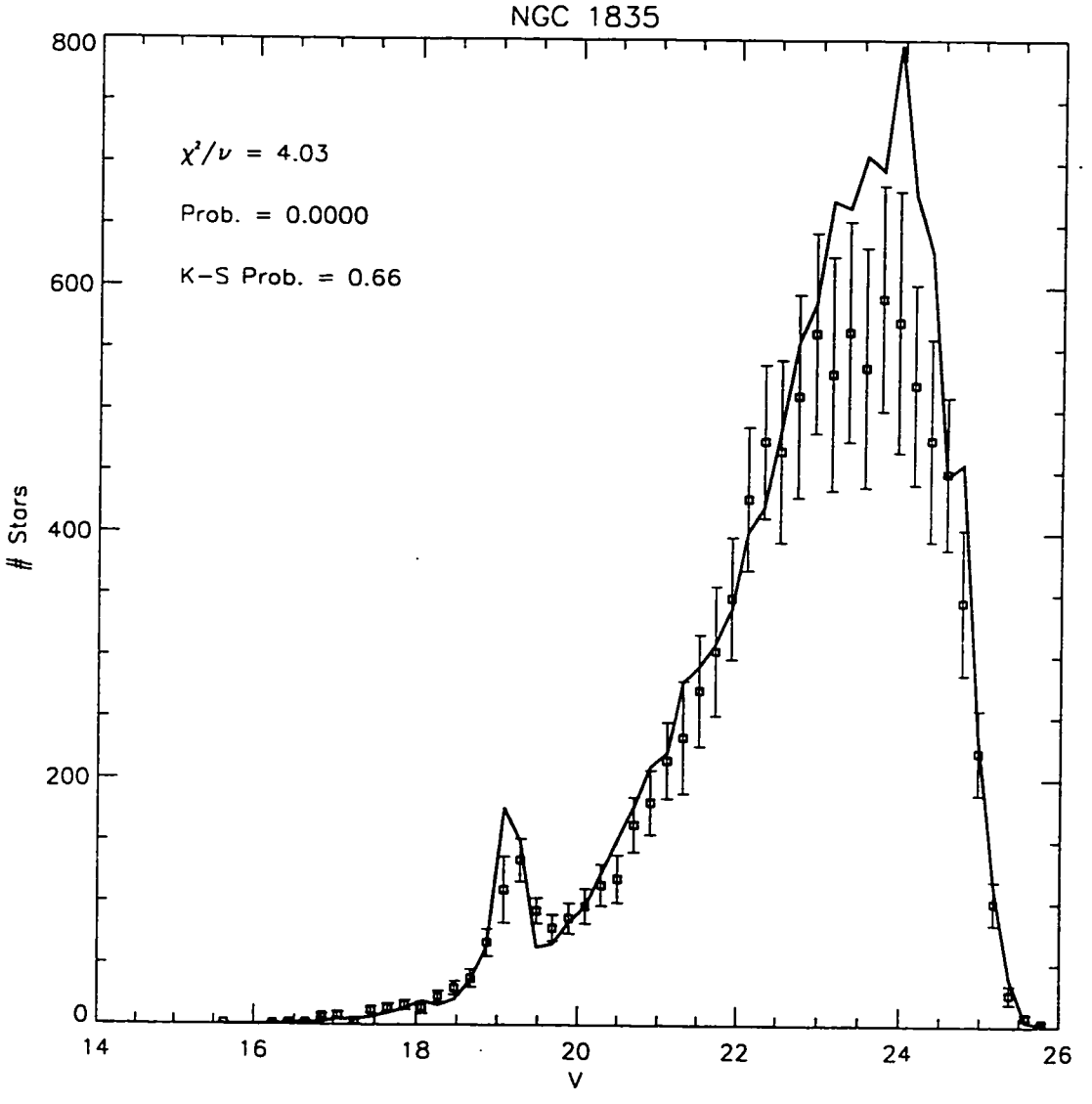

Figure 4.20b: Comparison of the observed luminosity function with the best-fit model for a Salpeter IMF for the NGC 1835 field.

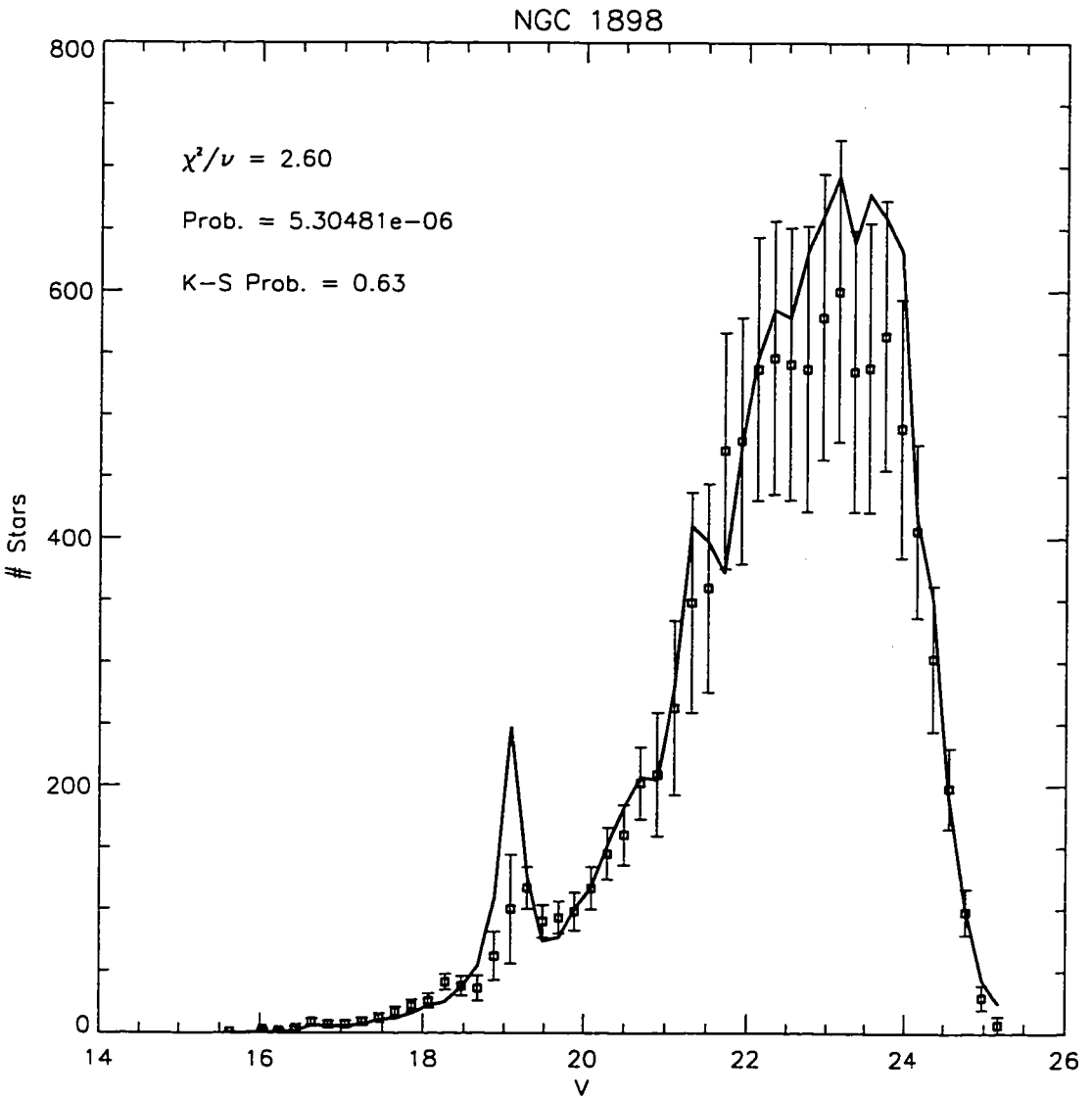

Figure 4.20c: Comparison of the observed luminosity function with the best-fit model for a Salpeter IMF for the NGC 1898 field.

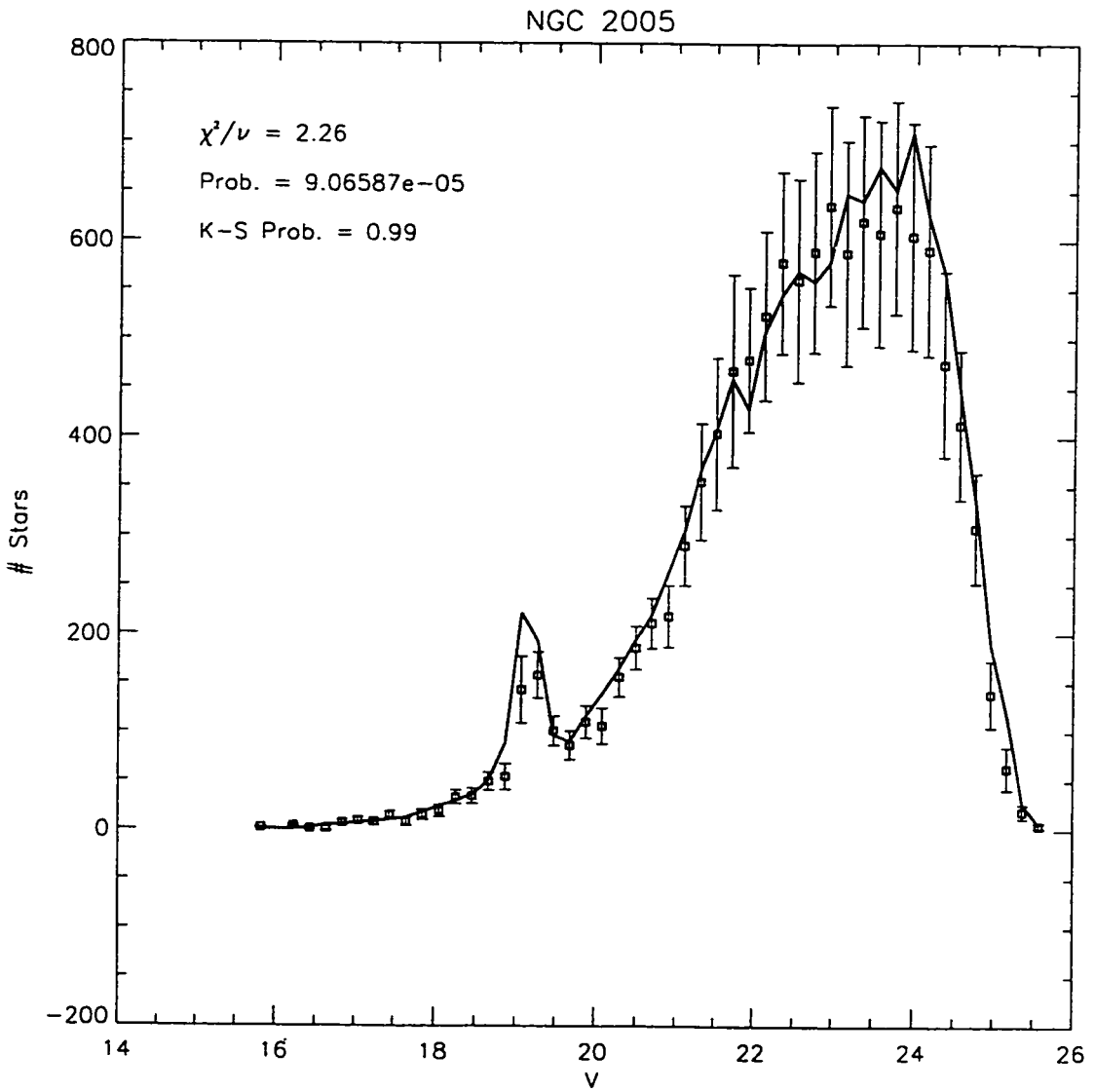

Figure 4.20d: Comparison of the observed luminosity function with the best-fit model for a Salpeter IMF for the NGC 2005 field.

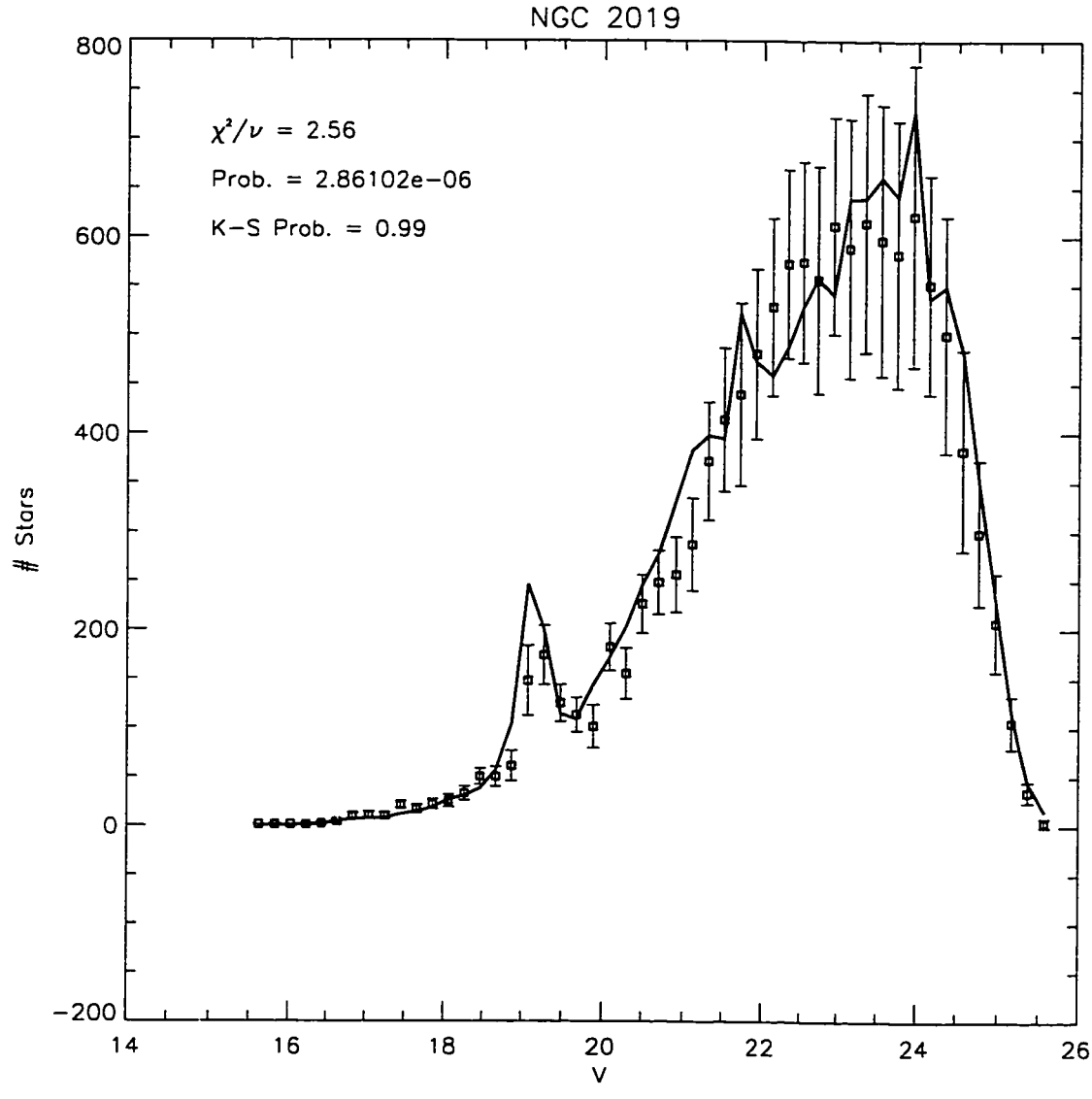

Figure 4.20e: Comparison of the observed luminosity function with the best-fit model for a Salpeter IMF for the NGC 2019 field.

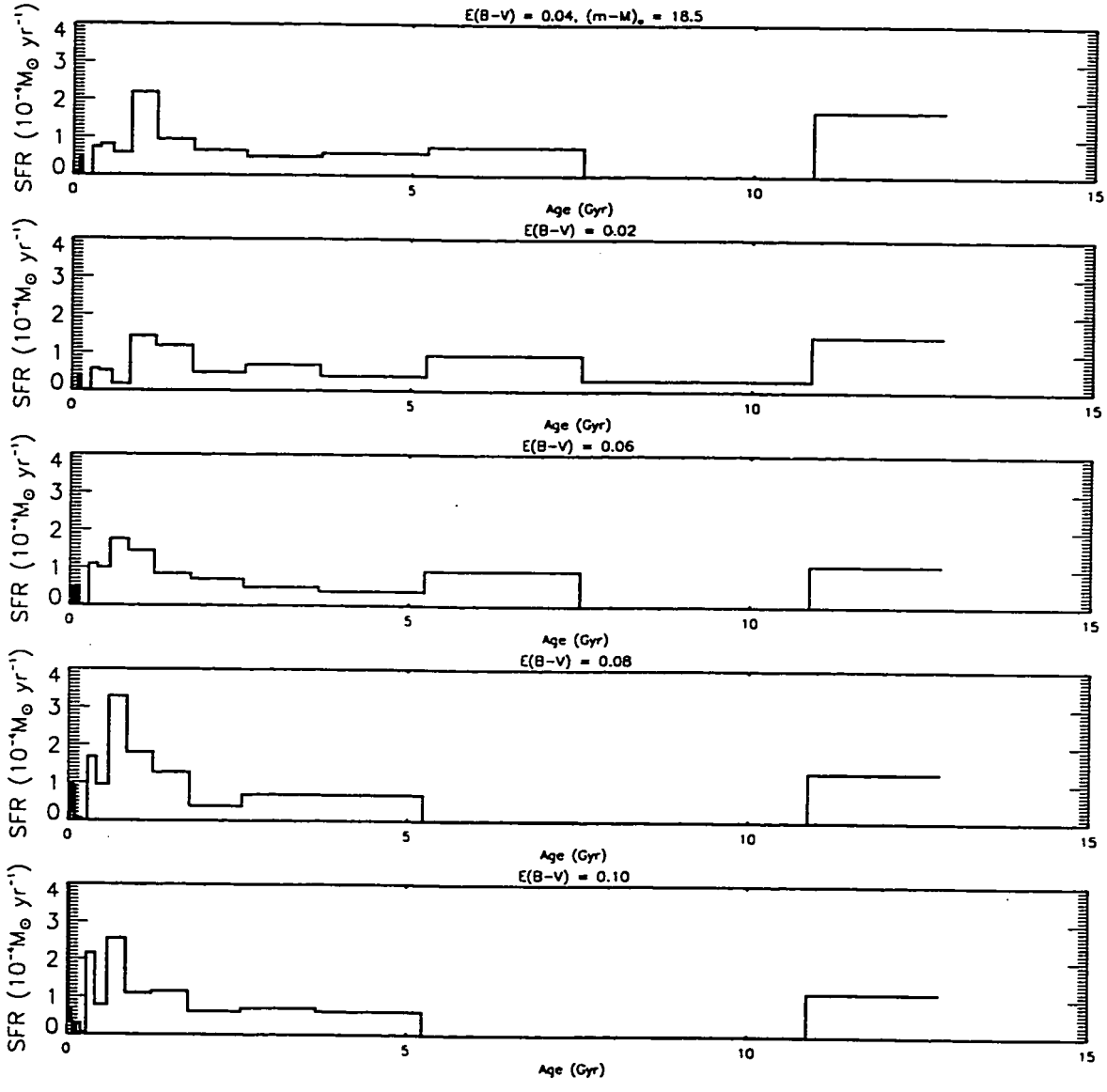

Figure 4.21: The figure shows the effect of varying the reddening on the derived star formation history for the NGC 1835 field. Raising the reddening increases the relative contribution of the young populations.

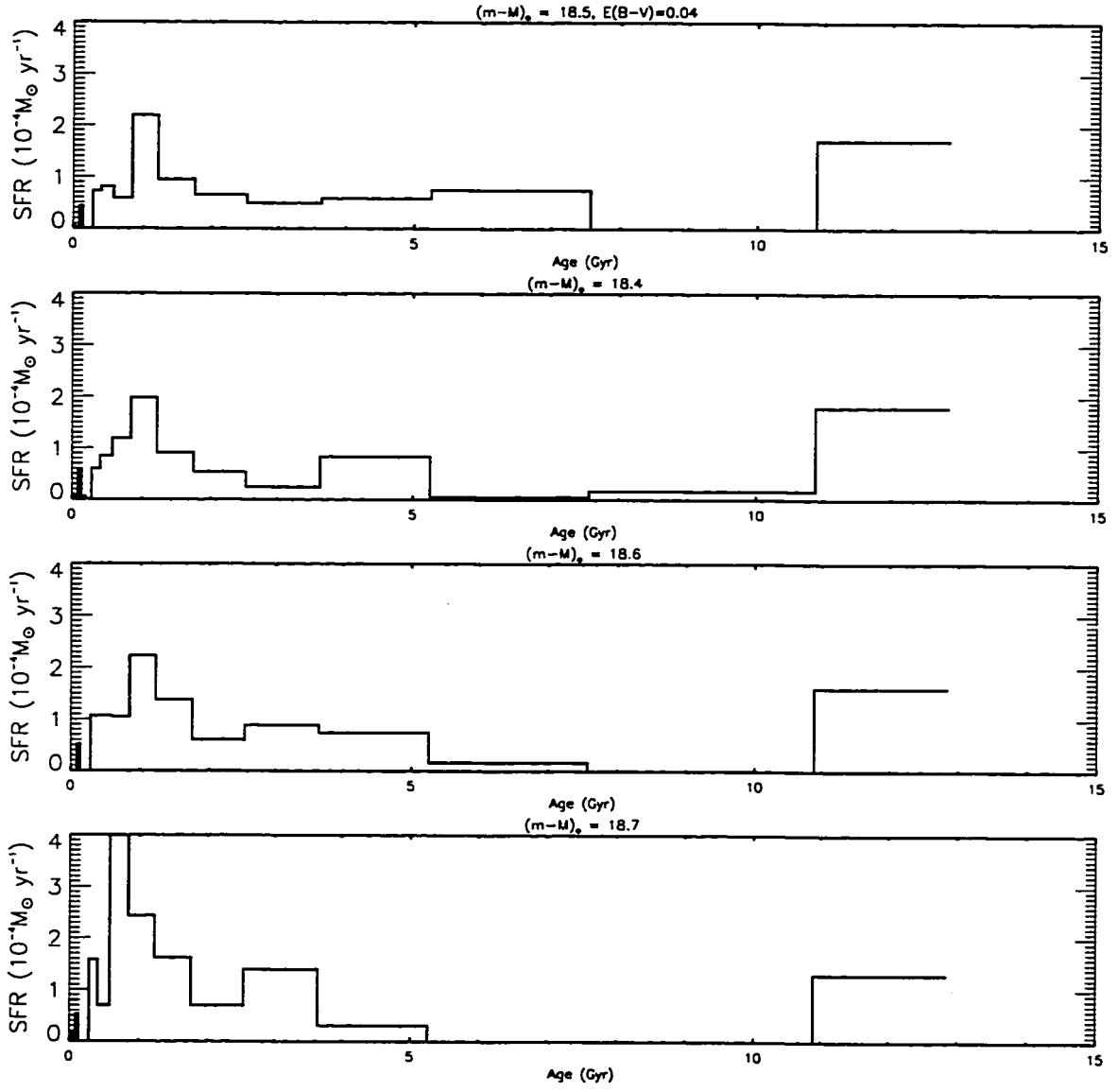

Figure 4.22: The figure shows the effect of varying the distance modulus on the derived star formation history for the NGC 1835 field. Raising the distance modulus increases the relative contribution of the young populations.

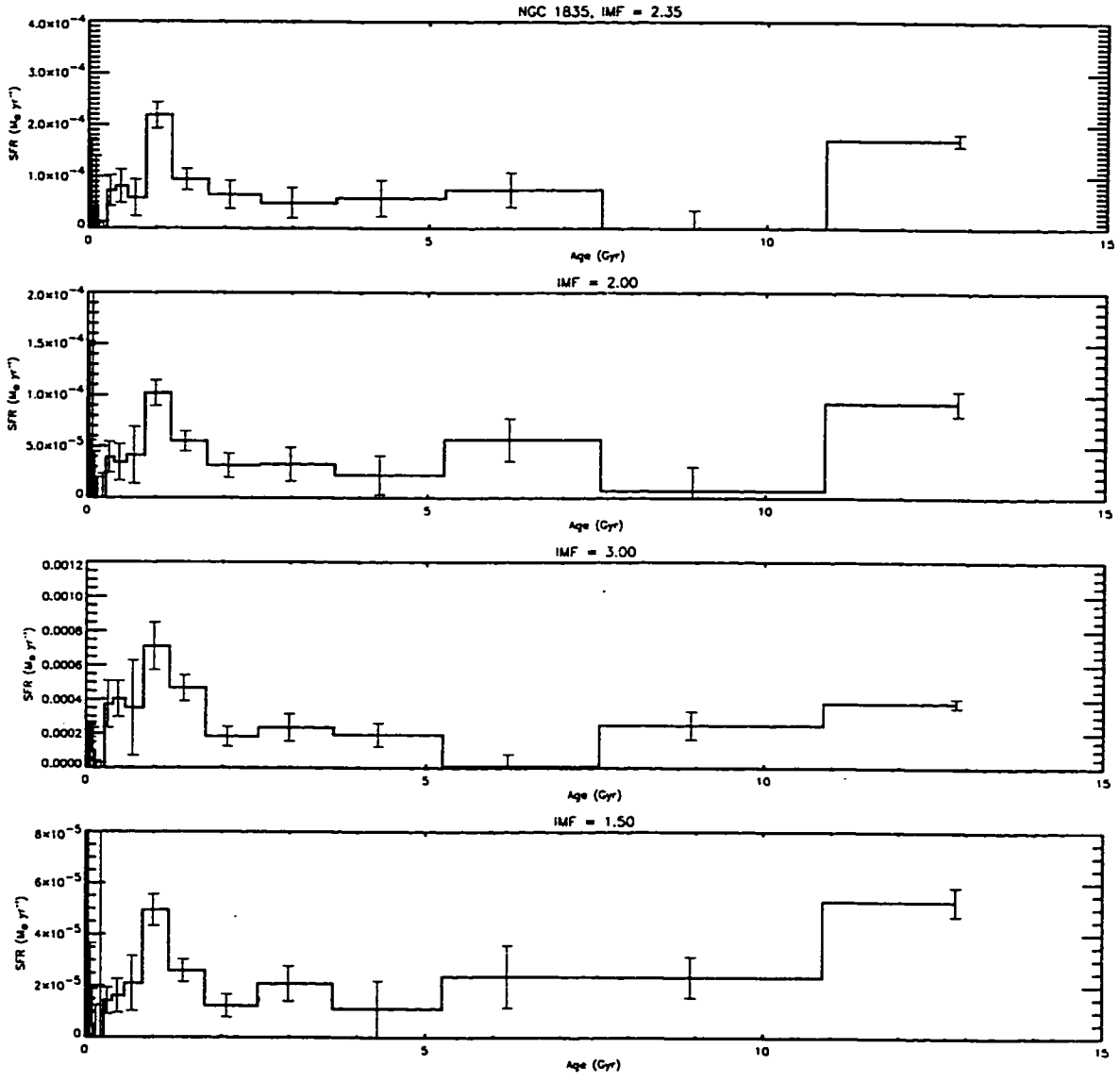

Figure 4.23: The figure shows the large effect that varying the IMF slope has on the derived star formation history for the NGC 1835 field. With a flatter IMF, the old populations contribute more in a relative sense.

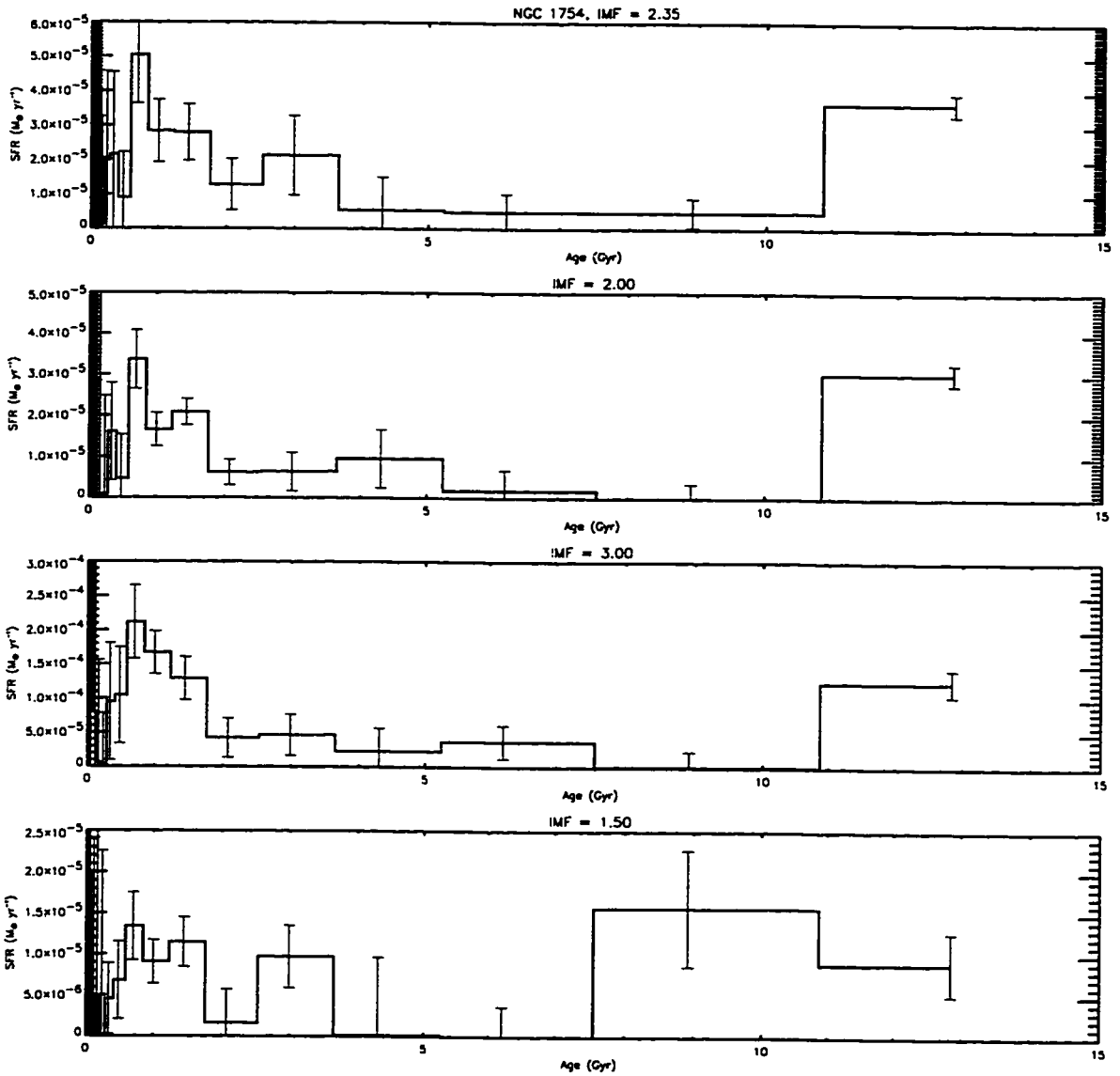

Figure 4.24: For the NGC 1754 field, varying the IMF does not have as drastic an effect as it did in Fig. 4.23. Even with the flatter IMFs, the field does not have significant star formation in the 4–8 Gyr range.

Chapter 5

THE FINAL CHAPTER

Although this is the Final Chapter of my dissertation, it is by no means the final chapter on the study of the formation and evolution of the Large Magellanic Cloud. Future observations of the globular clusters and field stars of the LMC and further understanding of stellar evolution will improve on the specific results obtained in this dissertation, while our general understanding of the formation and evolution and the LMC will continually be advanced by new ideas. However, I believe that our results have produced some new bits of information that are worth restating:

- The inner globular clusters of the LMC appear to be as old as the oldest clusters of the Milky Way, meaning that the LMC and Milky Way formed the first stellar generation during the same epoch. We base this conclusion mainly on the comparison of the LMC globular cluster color-magnitude diagrams with fiducial sequences of the Milky Way clusters M3, M5, and M55 (see Figs. 3.1a-i), but also on the comparison of the horizontal branch morphologies and CMD-based abundances of the clusters with HB evolutionary tracks (see Fig. 3.4a).

- Our analysis of the field star color-magnitude diagrams shows that areas of the LMC bar and a field $\sim 1°$ from the bar have been active in forming stars over the past 3–4 Gyr (see Figs. 4.15a-j), as suggested by many previous researchers. A new discovery is that there is a strong difference in the star formation histories of the bar fields and that of the disk field near NGC 1754. While the disk field shows that there was an 8–10 Gyr lull in star formation after the globular cluster formation epoch, the bar fields show that the bar was as active 4–8 Gyr

ago as it has been over the past 4 Gyr, suggesting that the bar is a long-lived feature. These results are fairly robust against errors in the parameters that we explored.

- The mismatch of the field star red giant branch with the metal-poor Bertelli et al. (1994) models implies that either the globular cluster abundances that we derived from the CMDs are too metal-rich by ~0.5 dex or that the isochrones do not correctly predict the color of the giant branch. Both possibilities are interesting. If the abundances are wrong, then it means that an unknown difference in the properties of the LMC and Milky Way clusters affects the slope of the red giant branch. If the models are incorrect, the absolute age-dating of old clusters using the Bertelli et al. models is strongly affected.

While I do not claim to be able to predict the directions of research that will most positively advance our understanding of the formation and evolution of the LMC, a number of ongoing and planned efforts point to studies that have been or will likely be undertaken within the next few years:

- Because of the metallicity dependence of the age indicators discussed in Section 6.2, our conclusions based on the cluster ages depend critically on the CMD-based abundances being correct. If we adopt the O91 spectroscopic abundances, for instance, our conclusions change considerably. Fig. 3.4b shows the comparison of the LDZ HB evolutionary tracks with our cluster data using the O91 abundances. The HB tracks imply, in this case, that the LMC clusters are indeed ~2 Gyr younger than the old Milky Way halo. However, we are then unable to build a consistent picture with the relative ages derived from the comparison to Milky Way clusters. Coupled with the better internal consistency weakly implied by the distance moduli (Figs. 3.6), we continue to prefer the CMD-based abundances for these LMC clusters. Nevertheless, it would clearly be extremely

valuable to have high-resolution spectroscopic abundances of several stars in each cluster available. This will soon be easily possible with the construction of 8-m class telescopes in the southern hemisphere.

- While some results on ages for the outer globular clusters were mentioned in Chapter 1, *HST* observations of all of the LMC globular clusters are necessary to derive ages from the unevolved main sequence. These observations have been taken for the outer clusters, and their analysis is underway (Johnson & Bolte 1997). The ages of these clusters will provide important additional constraints on the formation epoch of the LMC.

- Although we tried to understand the effects of errors in the assumed input parameters on the star formation histories we derived for the fields, it is difficult to estimate the effect of some our simplifying assumptions. A more thorough analysis will explore the effects of differential reddening (clearly very important for the NGC 1916 field), binary stars, and different chemical evolution histories. Continuing gains in computing speed will increase the number of parameters that can be varied and explored.

- The ongoing drift-scan survey of the LMC (Zaritsky et al. 1996) and the large number of field stars in the MACHO database (Alves et al. 1998) provide an excellent complement to deep *HST* imaging of small LMC fields. With an automated analysis technique, these observations can be used to describe the star formation history of the LMC in good detail over a huge range of locations, making it perhaps possible to link the star formation history with the dynamical history of the LMC. With the excellent number statistics of the color-magnitude diagrams, these observations will also almost certainly provide new constraints on stellar evolutionary theory, the possibility of which was hinted at in this dissertation. The analysis of these fields will hinge on having a fast method

to extract the star formation history and careful consideration of differential reddening, chemical evolution, and other model parameters.

BIBLIOGRAPHY

Alcaino, G., Liller, W., Alvarado, F., Kravtsov, V., Ipatov, A., Samus, N., and Smirnov, O.: 1996, *Astron. J.* **112**, 2020

Alves, D. et al.: 1997, *Bull. Am. Astron. Soc.* **191**, #115.01

Andersen, J., Blecha, A., and Walker, M.: 1984, *Mon. Not. R. Astron. Soc.* **211**, 695

Andersen, J., Blecha, A., and Walker, M.: 1985, *Astron. Astrophys.* **150**, L12

Aparicio, A., Gallart, C., and Bertelli, G.: 1997, *Astron. J.* **114**, 669

Bertelli, G., Bressan, A., Chiosi, C., Fagotto, F., and Nasi, E.: 1994, *Astron. Astrophys. Suppl. Ser.* **106**, 275

Bertelli, G., Mateo, M., Chiosi, C., and Bressan, A.: 1992, *Astrophys. J.* **387**, 320

Brocato, E., Castellani, V., Ferraro, F., Piersimoni, A., and Testa, V.: 1996, *Mon. Not. R. Astron. Soc.* **282**, 614

Buonanno, R., Corsi, C., Bellazzini, M., Ferraro, F. R., and Pecci, F. F.: 1997, *Astron. J.* **113**, 706

Buonanno, R., Corsi, C., Pecci, F., Richer, H., and Fahlman, G.: 1993, *Astron. J.* **105**, 184

Butcher, H.: 1977, *Astrophys. J.* **216**, 372

Caldwell, J. and Coulson, I.: 1986, *Mon. Not. R. Astron. Soc.* **218**, 223

Catelan, M., Sweigart, A. V., Borissova, J., and Spassova, N.: 1997, in P. Bradley and J. Guzik (eds.), *A Half Century of Stellar Pulsation Interpretations: A Tribute to Arthur N. Cox*, Vol. 135 of *ASP Conference Series*, ASP

Chaboyer, B. and Kim, Y.-C.: 1995, *Astrophys. J.* **454**, 767

Da Costa, G.: 1993, in G. Smith and J. Brodie (eds.), *The Globular Cluster-Galaxy Connection*, Vol. 48 of *ASP Conference Proceedings*, p. 363, ASP

Dean, J., Warren, P., and Cousins, A.: 1978, *Mon. Not. R. Astron. Soc.* **183**, 569

Demers, S. and Irwin, M.: 1991, *Astron. Astrophys. Suppl. Ser.* **91**, 171

Dolphin, A.: 1997, *New Astronomy* **2**, 397

Dottori, H., Bica, E., Claria, J., and Puerari, I.: 1996, *Astrophys. J.* **461**, 742

Elson, R., Gilmore, G., and Santiago, B.: 1997, *Mon. Not. R. Astron. Soc.* **289**, 157

Feast, M. and Catchpole, R.: 1997, *Mon. Not. R. Astron. Soc.* **286**, L1

Fernley, J. et al.: 1998, *Astron. Astrophys.* **330**, 515

Freeman, K. and Gascoigne, S.: 1977, *Proc. Astron. Soc. Aust.* **3**, 136

Gallagher, J. et al.: 1996, *Astrophys. J.* **466**, 732

Gallart, C., Aparicio, A., Bertelli, G., and Chiosi, C.: 1996a, *Astron. J.* **112**, 1950

Gallart, C., Aparicio, A., and Vílchez, J.: 1996b, *Astron. J.* **112**, 1928

Gascoigne, S.: 1966, *Mon. Not. R. Astron. Soc.* **134**, 59

Geha, M. et al.: 1998, *Astron. J.* **115**, 1045

Geisler, D., Bica, E., Dottori, H., Claria, J., Piatti, A., and J.F.C. Santos, J.: 1997, *Astron. J.* **114**, 1920

Gould, A.: 1995, *Astrophys. J.* **452**, 189

Gratton, R. and Ortolani, S.: 1987, *Astron. Astrophys. Suppl. Ser.* **71**, 131

Hardy, E., Buonanno, R., Corsi, C., Janes, K., and Schommer, R.: 1984, *Astrophys. J.* **278**, 592

Harris, W. et al.: 1997, *Astron. J.* **114**, 1030

Harris, W., Hesser, J., and Atwood, B.: 1983, *Publ. Astron. Soc. Pac.* **95**, 967

Hesser, J., Ugarte, P., and Hartwick, F.: 1976, *Astrophys. J., Suppl. Ser.* **32**, 283

Hodge, P.: 1960, *Astrophys. J.* **131**, 351

Hodge, P.: 1986, *Galaxies*, Harvard University Press, Cambridge

Hodge, P.: 1987, *Publ. Astron. Soc. Pac.* **99**, 730

Hodge, P.: 1988, *Publ. Astron. Soc. Pac.* **100**, 576

Holtzman, J. et al.: 1995a, *Publ. Astron. Soc. Pac.* **107**, 156

Holtzman, J. et al.: 1995b, *Publ. Astron. Soc. Pac.* **107**, 1065

Holtzman, J. et al.: 1997, *Astron. J.* **113**, 656

Jensen, J., Mould, J., and Reid, N.: 1988, *Astrophys. J., Suppl. Ser.* **67**, 77

Johnson, J. and Bolte, M.: 1997, *Bull. Am. Astron. Soc.* **189**, 7118

Kim, S. and Staveley-Smith, L.: 1997, in S. Holt and L. Mundy (eds.), *Star Formation Near and Far*, No. 393 in AIP Conference Proceedings, p. 582, AIP, AIP Press, New York

King, I.: 1966, *Astron. J.* **71**, 64

Landolt, A.: 1992, *Astron. J.* **104**, 340

Lee, Y.-W., Demarque, P., and Zinn, R.: 1994, *Astrophys. J.* **423**, 248

Lin, D. and Richer, H.: 1992, *Astrophys. J.* **388**, L57

Madore, B. and Freedman, W.: 1998, *Astrophys. J.* **492**, 110

Mandushev, G., Fahlman, G., Richer, H., and Thompson, I.: 1996, *Astron. J.* **112**, 1536

Mateo, M.: 1987, *Ph.D. thesis*, University of Washington

Mateo, M., Hodge, P., and Schommer, R.: 1986, *Astrophys. J.* **311**, 113

Mazzitelli, I., D'Antona, F., and Caloi, V.: 1995, *Astron. Astrophys.* **302**, 382

Mighell, K., Rich, R., Shara, M., and Fall, S.: 1996, *Astron. J.* **111**, 2314

Moore, B. and Davis, M.: 1994, *Mon. Not. R. Astron. Soc.* **270**, 209

Murai, T. and Fujimoto, M.: 1980, *Publ. Astron. Soc. Jpn.* **32**, 581

Nelder, J. and Mead, R.: 1965, *Computer Journal* **7**, 308

Ng, Y.: 1998, astro-ph/9803332

Olszewski, E., Schommer, R., Suntzeff, N., and Harris, H.: 1991, *Astron. J.* **101**, 515

Olszewski, E., Suntzeff, N., and Mateo, M.: 1996, *Annu. Rev. Astron. Astrophys.* **34**, 511

Panagia, N., Gilmozzi, R., Macchetto, F., Adorf, H.-M., and Kirshner, R. P.: 1991, *Astrophys. J.* **380**, L23

Penny, A.: 1975, *Mon. Not. R. Astron. Soc.* **172**, 65

Press, W., Teukolsky, S., Vetterling, W., and Flannery, B.: 1992, *Numerical Recipes*

in C, Cambridge University Press, Cambridge, second edition

Quinn, T., Katz, N., and Efstathiou, G.: 1996, *Mon. Not. R. Astron. Soc.* **278**, L49

Reid, N. and Freedman, W.: 1994, *Mon. Not. R. Astron. Soc.* **267**, 821

Rogers, F. and Iglesias, C.: 1992, *Astrophys. J., Suppl. Ser.* **79**, 507

Sarajedini, A.: 1994, *Astron. J.* **107**, 618

Sarajedini, A., Chaboyer, B., and Demarque, P.: 1997, *Publ. Astron. Soc. Pac.* **109**, 1321

Sarajedini, A., Lee, Y.-W., and Lee, D.-H.: 1995, *Astrophys. J.* **450**, 712

Schechter, P., Mateo, M., and Saha, A.: 1993, *Publ. Astron. Soc. Pac.* **105**, 1342

Schommer, R., Olszewski, E., and Aaronson, M.: 1984, *Astrophys. J.* **285**, L53

Schommer, R., Olszewski, E., Suntzeff, N., and Harris, H.: 1992, *Astron. J.* **103**, 447

Schwarzschild, M.: 1965, *Structure and Evolution of the Stars*, Dover, New York

Shapley, H.: 1930, *Star Clusters*, No. 2 in Harvard Observatory Monographs, McGraw-Hill, New York

Smecker-Hane, T.: 1997, in S. Holt and L. Mundy (eds.), *Star Formation Near and Far*, No. 393 in AIP Conference Proceedings, p. 571, AIP, AIP Press, New York

Sonneborn, G., Fransson, C., Lundqvist, P., Cassatella, A., Gilmozzi, R., Kirshner, R. P., Panagia, N., and Wamsteker, W.: 1997, *Astrophys. J.* **477**, 848

Stetson, P., VandenBerg, D., and Bolte, M.: 1996, *Publ. Astron. Soc. Pac.* **108**, 560

Stryker, L.: 1983, *Astrophys. J.* **266**, 82

Stryker, L.: 1984, *Astrophys. J., Suppl. Ser.* **55**, 127

Stryker, L., Nemec, J., Hesser, J., and McClure, R.: 1984, in S. van den Bergh and K. de Boer (eds.), *Structure and Evolution of the Magellanic Clouds*, No. 108 in IAU Symposium, p. 43, Reidel, Dordrecht

Suntzeff, N., Schommer, R., Olszewski, E., and Walker, A.: 1992, *Astron. J.* **104**, 1743

Sweigart, A. V.: 1997, *Astrophys. J.* **474**, L23

Testa, V., Ferraro, F., Brocato, E., and Castellani, V.: 1995, *Mon. Not. R. Astron.*

Soc. **275**, 454

Tolstoy, E. and Saha, A.: 1996, *Astrophys. J.* **462**, 672

Tsujimoto, T., Miyamoto, M., and Yoshii, Y.: 1988, *Astrophys. J.* **492**, 79

VandenBerg, D.: 1997, personal communication

VandenBerg, D., Bolte, M., and Stetson, P.: 1990, *Astron. J.* **100**, 445

Walker, A.: 1989, *Astron. J.* **98**, 2086

Walker, A.: 1990, *Astron. J.* **100**, 1532

Walker, A.: 1992a, *Astron. J.* **104**, 1395

Walker, A.: 1992b, *Astrophys. J.* **390**, L81

Walker, A.: 1992c, *Astron. J.* **103**, 1166

Walker, A.: 1993, *Astron. J.* **106**, 999

Walker, M.: 1972, *Mon. Not. R. Astron. Soc.* **156**, 459

Walker, M.: 1979, *Mon. Not. R. Astron. Soc.* **186**, 767

White, S. and Rees, M.: 1978, *Mon. Not. R. Astron. Soc.* **183**, 341

Whitmore, B. and Heyer, I.: 1997, Technical report, STScI, WFPC2 Instrument Science Report 97-08

Zaritsky, D., Harris, J., and Thompson, I.: 1997, *Astron. J.* **114**, 1002

Zinn, R. and West, M.: 1984, *Astrophys. J., Suppl. Ser.* **55**, 45

VITA

Knut Anders Grova Olsen was born on May 6, 1970 in Oslo, Norway to Bjorn Reino Olsen and Marie Louise Grova Olsen. He quickly established himself as a night person by insisting on staying awake all night and sleeping during the day, a schedule his parents were not immediately fond of. He also early became part of the jet-set, moving to the United States twice before settling there permanently at the age of 7. On his second trip he took fancy to a telescope he saw in a toy store, and a few years later his parents gave him one for his birthday. His explorations of the Universe thus began and his interest in astronomy continued, despite the disappointment of realizing that a star in a telescope still just looks like a point. In high school and at Swarthmore College he became interested in physics, but decided that the real mysteries lie far away, and so majored in astrophysics, receiving his B.A. in 1992. He conducted his first astronomical research at Swarthmore with Professor John Gaustad, and liked it enough to apply to graduate school, which resulted in his move to Seattle, WA to enroll in the Astronomy Department at the University of Washington. As star formation had become his interest in College, he found a natural fit in Paul Hodge, who introduced him to the study of stellar populations in the Magellanic Clouds and who has made the past 6 years very enjoyable.

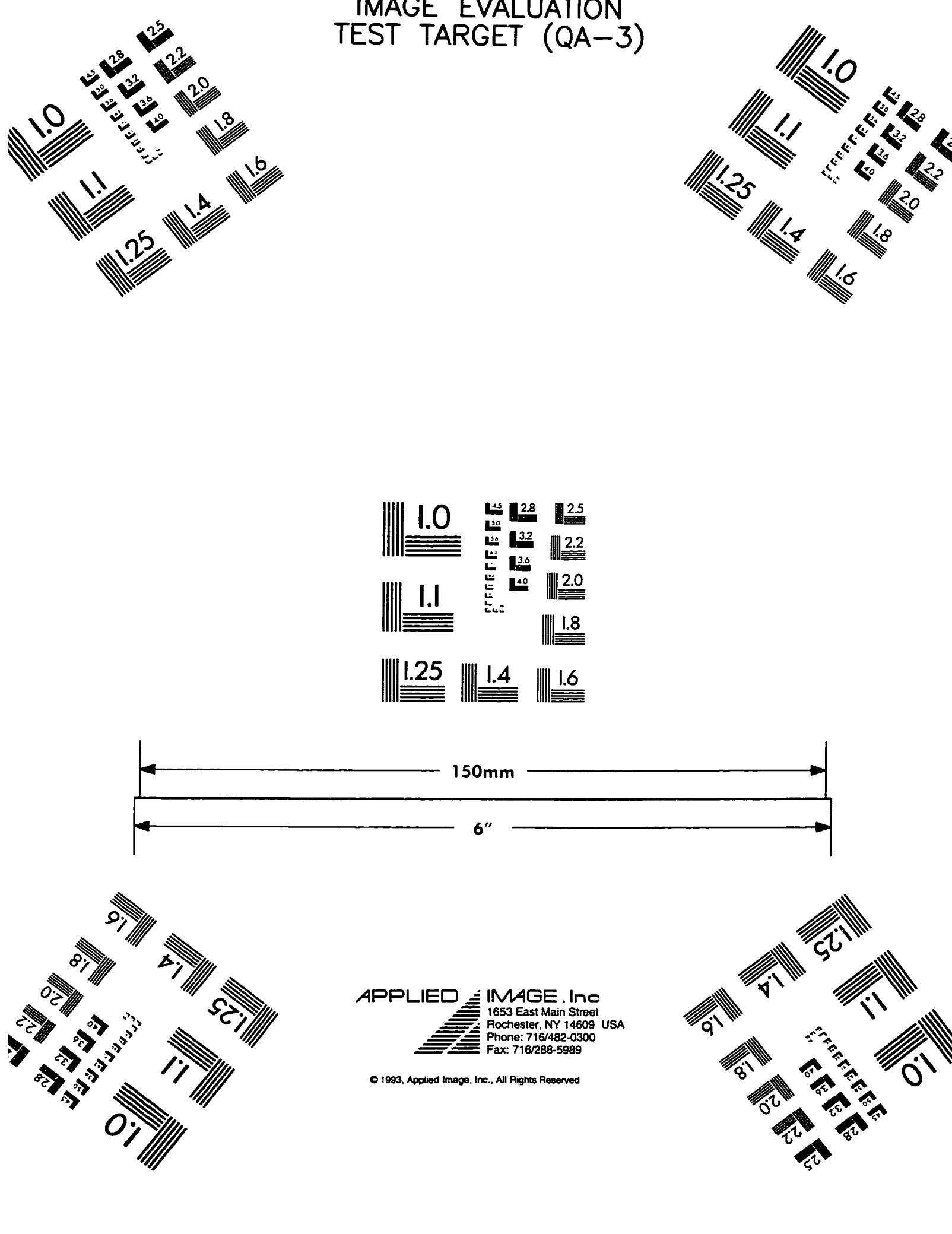
IMAGE EVALUATION
TEST TARGET (QA-3)
1.0
1.1
1.25
1.4
1.6
2.8
2.5
3.2
2.2
3.6
2.0
4.0
1.8
150mm
6"
APPLIED IMAGE, Inc
1653 East Main Street
Rochester, NY 14609 USA
Phone: 716/482-0300
Fax: 716/288-5989
© 1993, Applied Image, Inc., All Rights Reserved